Alteration and Fluid Characterization of the Hamlin Lake IOCG Occurrence, Northwestern Ontario, Canada

By
Nathan Forslund

2012
Lakehead University
955 Oliver Road
Thunder Bay, ON
P7B 5E1

Abstract

The Hamlin Lake area is located approximately 120km southwest of Thunder Bay, Ontario, in the Shebandowan Greenstone Belt of the Wawa Subprovince in the Superior Province. The area has been explored for its copper and gold mineralization for more than 50 years, but has only recently been treated as an iron-oxide copper gold (IOCG) occurrence. The aim of this study was to characterize the alteration at the occurrence through space and time, and to relate this paragenesis to the formation of mineralization.

Localized field mapping and re-logging of drill core established several relationships between styles of alteration. Rocks were examined in hand specimen and thin section, and minerals were examined with scanning electron microscope (SEM) to identify mineral assemblages and associations. Consistent variations in space could not be mapped, so textural relationships were used to relate the timing between six styles of alteration and the local brecciation that hosts the potential ore. These are: (1) sodic, (2) early potassic, (3) calcic(-iron), (4) late potassic, (5) carbonate, and (6) silicic.

Sodic alteration is largely composed of albitisation, and is occasionally conserved in fragments of the breccia. The early potassic stage of alteration consists of biotite and magnetite in the matrix of the breccia, which is cross-cut by epidote and sphene from the calcic(-iron) stage. Sodium cobaltinitrite staining was used to identify potassium feldspar alteration associated with mineralization of the late potassic stage. The mineralization in this stage is represented by the assemblage chalcopyrite + pyrite + magnetite. This first stage of mineralization was succeeded by carbonate precipitation, and finally by a second stage of mineralization associated with a vuggy quartz breccia.

The two phases of mineralization are primarily different in that stage I mineralization is associated with potassic alteration and iron-oxide mineralization, whereas stage II mineralization is associated with quartz and has a general lack of massive iron-oxide. The alteration leading up to the first stage of mineralization, and the stage I mineralization itself are consistent with the general alteration patterns observed in other magnetite-group IOCG deposits worldwide. The onset of carbonate alteration, followed by vuggy quartz with moderate- to high-sulfidation assemblages of stage II mineralization, is more typical of an epithermal environment.

Thermodynamic parameters of the mineralizing fluids were ascertained by the use of fluid inclusions. Fluid inclusions from the vuggy quartz associated with stage II mineralization were analyzed and suggest a low-salinity fluid with a temperature in the approximate range of 200° to 250°C responsible for mineralization.

Stable oxygen isotopes from chlorite, magnetite and sulphur isotopes from sulphides were measured to establish the source of the fluids responsible for the formation of the deposit. Oxygen from the magnetite of early mineralizing assemblages has a narrow range of values for $\delta^{18}O_{water}$ from +8.9‰ to +10.9‰. These are indicative of a deep-seated metamorphic or magmatic source for early fluids. Oxygen from chlorite associated with the later stages of mineralization have a wider range of $\delta^{18}O_{water}$ values (+0.4‰ to +5.9‰), which may suggest that meteoric or other crustally derived fluids played a role in stage II mineralization. δD values were

measured on the chlorite as well; however, these may have been reset by later metasomatic events. Sulphur isotope values from mineralization were measured ($\delta^{34}S$ -6.9‰ to +1.8‰), and indicated that an exotic sulphur source probably played a role in mineralization.

Acknowledgements

Now that this project is drawing to an end, I finally have the time to sit and reflect on all the people who helped to make it possible.

My sincerest gratitude goes out to Dr. Stephen Kissin, who provided his guidance and supervision. Not only has he supported me through this thesis project, but throughout my entire university career. I am also deeply grateful to Gord Maxwell and Bob Middleton, who granted me the opportunity to undertake this project. These people provided me the wind to my wings, without which the project would never have left the ground.

I would also like to thank the entire faculty of geology at Lakehead University; however, several people in particular are worthy of special acclaim. I must convey my utmost gratitude to Dr. Peter Hollings, who offered his insight and support on countless occasions, as if I were one of his own students. Dr. Andrew Conly deserves the highest appreciation for his undying patience and insight with respect to my constant barrage of questions on stable isotopes. Special thanks to Anne Hammond for the hard work and dedication she put into producing flawless thin sections, as well as for the time she spent helping me prepare samples. Finally, I must thank Al MacKenzie and Colleen Kurcinka for their help in learning to use the SEM and XRD.

Many other individuals were involved in the successful completion of this project, and I must extend my gratitude to all of them.

To Dr. Hamid Mumin for his helpful review, and for providing expert insight towards my interpretations and conclusions.

To Max Keogh of Xstrata Copper for his orientation to the Hamlin Lake geology, and for lending an ear to which I could share my thoughts.

To Dr. Balz Kamber and Dr. Thomas Ulrich at Laurentian University for their second to none laser ablation analyses, and insight toward its interpretation.

To the people at Queens Facility for Isotope Research for providing quality stable isotope data, and to Kerry Klassen for her swift and helpful responses to my questions regarding the data.

To my field assistants, Alex and Kyle, who followed me without complaint through wind and rain, even when encumbered with backpacks full of rocks.

Finally, no one supported me like my family and friends. For their enduring confidence and encouragement I cannot thank them enough.

Thanks to everyone,

Nathan

Table of Contents

Table of Contents continued

List of Figures

List of Figures continued

Chapter 7 – Discussion and Conclusions

List of Tables

List of Appendices

Chapter 1 – Introduction

1.1 Introduction

The Hamlin Lake area was initially explored as a potential volcanic hosted massive sulphide (VHMS) deposit based on extensive copper mineralization and regional chloritic and sericitic alteration in the host volcanic rocks (Shute, 2009). In 2006, an age date on molybdenite was obtained by East West Resource Corporation (2692 ±12 Ma) which was not consistent with the age of volcanic activity (2719.9 ±1.1 Ma; Hart and Metsaranta, 2009). This discovery led to a new interpretation of the Hamlin Lake mineralization as being iron oxide-copper-gold (IOCG) related, since a volcanogenic origin was no longer credible. A preliminary investigation of the occurrence as it fell into the IOCG classification was undertaken by Bennett (2007); however, many questions remained to be answered.

1.2 Objective

While the study of Bennett (2007) provided a good foundation, showing that the Hamlin Lake occurrence does fit the IOCG model, it left many questions unanswered regarding the formation of the deposit. The purpose of the present study is to utilize various methodologies to help in understanding the complex processes involved in the formation of the Hamlin Lake deposit.

Three questions were proposed. (1) What were the sources for the fluids responsible for ore formation? (2) How did these fluids evolve through time and space, ultimately producing an ore deposit? (3) Can this deposit be compared with other IOCG deposits worldwide and traced back to a unique formational model? Understanding these questions will ultimately improve our understanding of the Hamlin Lake occurrence, and could lead to further IOCG discoveries in the region.

The first question was addressed by using several stable isotope systems (sulphur, hydrogen and oxygen) that have characteristics dependant on the source of the element. Fluid inclusion geothermometry used in conjunction with a thorough alteration paragenetic study on drill core were used to address how this fluid evolved over time and space. The third question was theoretical and required comparison of the results of the first two problems with similar studies on better defined IOCG deposits around the world.

1.3 Iron Oxide-Copper-Gold deposits

The term IOCG was first used in the early 1990s when it was introduced to describe the world class Olympic Dam deposit in Australia (Hitzman *et al.,* 1992). Since then, other deposits around the world have been found to have the distinct features that make this a class of its own (Table 1.1). Often related to the porphyry copper-epithermal continuum, IOCG deposits are distinct due to their alkali-iron metasomatism and their abundance of hydrothermal iron oxides. Porphyry copper deposits exhibit a distinct potassic-phyllic-propyllitic alteration zoning, whereas epithermal deposits display lower

Table 1.1 - List of factors that characterize IOCG deposits (from Corriveau and Mumin, 2009).

•	Sulfide deficient, polymetallic, hydrothermal systems with zones > 15-20% of magnetite or hematite
•	Source of base (Cu, Fe, Ni, Pb, Zn), precious (Au, Ag, PGE), rare earth, strategic (Bi, Co, V) and nuclear metals (U) and industrial minerals (e.g. apatite and vermiclite)
•	Potentially very large tonnage / low to moderate grades
•	In any host rock but largely in continental volcano-plutonic arc and back-arc terranes
•	Associated with, but either proximal or distal to:
	-large-scale granitic to dioritic plutons (A to I types)
	-alkaline carbonatite stocks
	-crustal-scale fault zones and splays, commonly active during magmatism
	-along, adjecent to or at intersection of major faults
	-at or near volcano-sedimentary-plutonic unconformities/contact
•	Extensional episodes in or following compressional tectonic regimes
•	Mantle to surface "connection"
•	Archean to Phanerozoic in age (fertile 1.9-1.5 Ga age bracket)
•	Extensive and intensive diagnostic alteration and breccia
•	IOCG-porphry copper-epithermal continuum
•	Association of vein type U with IOCG
•	Potential continuum with other sedimentary- and volcanic- hosted deposit types, including other uranium deposit types

formational temperatures and near surface textures such as vugs and open-space filling (Mumin *et al.*, 2010).

1.3.1 IOCG characteristics

One of the most controversial aspects of IOCG deposits is the extreme diversity of deposit styles, including age, host rocks, mineralogy, geochemical signatures and even geologic setting (Williams *et al.*, 2005). With such a broad definition the obvious question is: what are some common characteristics between IOCG deposits that make them worthy of their own deposit type? As the name implies the most notable feature

that is common to these deposits is the association of iron oxides with Cu and Au mineralization. Other elements that are commonly enriched in these deposits include Ag, U, Ba, F and light rare earth elements (LREE).

Other common features include a strong spatial and temporal relationship with regional I-type to A-type granitic suites, and proximity to crustal scale faults or shear zones (Williams *et al.*, 2005). Respectively, these are responsible for driving and channeling the fluids involved, and they produce extensive alteration signatures, brecciation, and ore systems. Some deposits might even be in direct contact or even partly hosted by the intrusions, but this is not encountered in all cases as it is in some other types of hydrothermal ore deposits (e.g., porphyry and skarn type deposits). In rare cases (e.g., Wernecke Breccias in the Yukon) syn-mineralization intrusive suites have not been noted, and it is thought that fluid flow may have been triggered by magmatic events in the mantle or lower crust. For this reason the exposure of coeval regional scale intrusive bodies is not regarded as an essential characteristic for IOCG deposits.

In all cases the IOCG model should be considered as a non-genetic model, since there are several key knowledge gaps that pertain to their genesis. One such issue is the source for fluids, metals, and sulphur and the role of mixing between two or more fluids. Processes that control metal recharge and discharge, brecciation and alteration are also poorly understood, as are the thermodynamic conditions required for precipitation of abundant iron oxides over iron sulphides. Mantle and deep-seated crustal melts seem to play an important role in the formation of some IOCG deposits, but this role is poorly understood.

Table 1.2 – IOCG deposits with their ages and grades.

District	Age	Deposit/Prospect	Reserves/Production	References
Great Bear Magmatic Zone (Northwest Territorries, Canada)	1.88-1.84 Ga	Sue Dianne	10.1Mt @ 0.80% Cu, 3.1 g/t Ag, 0.07 g/t Au	Mumin *et al*. (2009)
		NICO	21.8Mt @1.08 g/t Au, 0.13% Co, 0.16% Bi	"
		Echo Bay	23.8 M oz. Ag, 4,187 tonnes Cu, 15 Mt U3O8	"
		Sloan	~100,000 t @8.4% Cu	"
Peruvian Coastal Belt (Peru) and Chilean Iron Belt (Chile)	97-177 Ma	Raul Condestable	32 Mt @ 1.7% Cu, 0.3 g/t Au, 6 g/t Ag	de Haller *et al.* (2006)
		Marcona	1.9 Gt @ 55% Fe, 0.12% Cu	Chen *et al.* (2010)
		Candelaria	470 Mt @ 0.95% Cu, 0.22 g/t Au, 3.1 g/t Ag	Marschik and Fontbote (2001)
		Mantoverde	440 Mt @ 0.56% Cu, 0.12 g/t Au	Rieger (2010)
Carajas Mineral Province (Para, Brazil)	~2.57 Ga	Alemao	219 Mt @ 1.4% Cu, 0.86 g/t Au	Grainger *et al.* (2008)
		Cristalino	500 Mt @ 1.0% Cu, 0.3 g/t Au	"
		Salobo	789 Mt @ 0.96% Cu, 0.52 g/t Au	"
		Sossego	355 Mt @ 1.1% Cu, 0.28 g/t Au	"
Kiruna (Sweden and Finland)	1.90-1.75 Ga	Aitik	600 Mt @ 0.4% Cu, 0.2 g/t Au, (Ba)	Wanhainen *et al.* (2003; 2006)
		Kiirunavaara	2000 Mt Fe @ 60-68% Fe, (P, Cu)	Nystrom anf Henriquez (1994)
		Tjarrojakka-Cu	13.1 Mt @ 0.43% Cu, (Mo)	Edfelt *et al.* (2005)
		Tjarrojakka-Fe	53 Mt @ 52% Fe, (P, Cu)	"
Cloncurry (Northwest Queensland, Australia)	1.85-1.60 Ga	Lightning Creek	>2000 Mt Fe (modeled from geophysics)	Perring *et al.* (2000)
		Starra	6.9 Mt @ 2.1% Cu, 4.6 g/t Au	Rotherham *et al.* (1998)
		Eloise	3.7 Mt @ 4.1% Cu, 1.1 g/t Au, 12 g/t Ag, (Co, Ni)	Baker *et al.* (2001)
		Osborne	15.5 Mt @ 3.0% Cu, 1.0 g/t Au, (Co, Mo)	Fischer and Kendrick (2008)
		Ernest Henry	167 Mt @ 1.1% Cu, 0.54 g/t Au, (Co, As, Mo, Ba)	Mark *et al.* (2006)
Gawler Craton (South Australia)	1.60-1.585 Ga	Olympic Dam	7738 Mt @ 0.87% Cu, 0.29 kg/t U3O8, 0.30 g/t Au, 1.19 g/t Ag	Williams *et al.* (2005)
		Prominent Hill	97 Mt @ 1.5% Cu, 0.5 g/t Au	Belperio *et al.* (2007)

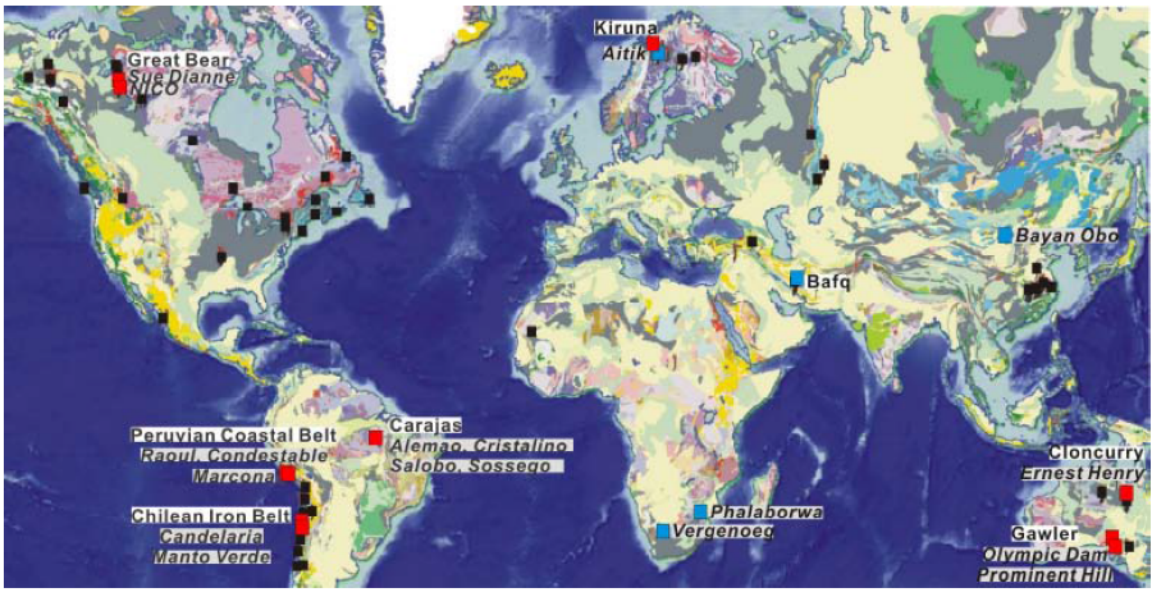

Figure 1.1 – Global distribution of IOCG deposits. Red squares are IOCG deposits, black squares are IOCG occurrences and blue squares are IOCG-like occurrences. Districts are named on a white background (from Corriveau and Mumin, 2009).

With more insight to how these deposits form, geologists have recognized several districts worldwide with large deposits that fall into the IOCG classification. Isolated occurrences do also occur (Figure 1.1); however, these tend to be smaller and lower grade deposits. Table 1.2 lists several of the deposits referenced throughout the present study.

1.3.2 IOCG deposit classification

The broad classification of IOCG can be subdivided into three classes based on the dominant iron oxide present. These subgroups are represented by oxidized and reduced end-members (hematite and magnetite groups, respectively) and an intermediate group (magnetite - hematite group). Further subdivision can be made based on textural and temporal mineral relationships and are defined below (Williams, 2010a).

Hematite group IOCG deposits are thought to be developed in a shallow crustal environment with temperatures ranging from 200-350°C (Williams, 2010a). They are often related to coeval volcanic activity and usually involve a large component of surficially-derived water. Within this class there are two subclasses based on the presence or absence of zoned copper mineralization: zoned deposits and deposits that lack systematic zoning. The Olympic Dam deposit in Australia is the best example of a zoned hematite group IOCG, while the Mantoverde deposit in Chile represents an unzoned deposit.

The next class of IOCG deposit encompasses a wide range of deposits where there are subequal proportions of magnetite and hematite. This class can be subdivided into three subclasses based on the evolution of the mineral association. These are

represented by zoned deposits with coeval precipitation of magnetite and hematite in different zones, telescoped deposits where one oxide replaces the other in a single system, and deposits where hematite forms from replacement of magnetite iron formation (Williams, 2010a). The Sue Dianne deposit in the Northwest Territories, Canada represents an example of the zoned variety of this class, while the telescoped variety can be represented by parts of the Raúl-Condestable deposit in Peru. The Juno deposit in central Australia is thought to have formed by replacement of a magnetite iron formation (Skirrow and Walshe, 2002).

The magnetite group of IOCG deposits form a spectrum of deposits forming in generally deeper crustal environments and higher temperatures (>350°C) than those represented in the hematite class (Williams, 2010a). These are subdivided based on the timing of iron enrichment and on the dominant alteration assemblage where sulphides and magnetite appear to be contemporaneous. One subclass can be explained in a similar manner to the hematized magnetite iron formation class described above. In this class the hematite stability field was not reached and sulphide assemblages commonly include pyrrhotite (e.g. Gecko in Australia; Huston *et al.*, 1993). The other subclasses of magnetite IOCG occur when magnetite and sulphides occur as part of a single system and are based on the dominant silicate alteration assemblage. These are represented by the high temperature potassic iron, calcic iron and skarn, and siliceous types. These are best exemplified by the Sossego deposit in Brazil, the Raúl-Condestable deposit in Peru and the Osborne deposit in Australia, respectively (Williams, 2010a).

Since these classifications are based largely on textural relationships between mineral assemblages, it is not uncommon for a given deposit to fall into more than one

category. Parts of the Raúl-Condestable deposit, for example, fall into both the telescoped magnetite - hematite group and the calcic iron and skarn type of the magnetite group (Williams, 2010a).

1.4 Thesis Structure

This thesis is structured into seven chapters: (1) introduction, (2) methodology, (3) geology of Hamlin Lake, (4) alteration paragenesis, (5) fluid inclusions, (6) stable isotopes and (7) discussion and conclusions. The chapter on methodology discusses the property location as well as the analytical methods and procedures taken to ensure data quality. Chapter three describes the local and regional geology of the Hamlin Lake area, including a synopsis of previous work and mineral exploration. Chapters four, five and six present and begin to discuss the results of the alteration paragenetic study, fluid inclusion study and stable isotope studies respectively. These chapters cover the interpretation of the data from the present study, whereas the final chapter discusses the overall relationships and their significance to a genetic model for the formation of the Hamlin Lake deposit.

Chapter 2 – Methodology

2.1 Property location and access

The study area is located approximately 120 kilometers west of the city of Thunder Bay, Ontario (Figure 2.1). During this study workers were based in Thunder Bay and accessed the property by road, starting with a 110 kilometer drive along Hwy 11 to the community of Kashabowie, followed by a 50 kilometer drive south on the Swamp Road. The property is approximately 6 square kilometers, the interior of which can be easily accessed by foot or all terrain vehicle. Recent logging in the area has left many trails in place allowing for even easier access, while improving the quality and abundance of rock exposure.

The Hamlin Lake area is comprised of ridges and valleys with moderate relief. The highest ridges in the area represent the mafic debris flows while the more intermediate to felsic volcanics are usually low lying. These ridges define an east-northeast morphological trend that can be seen on topographic maps. Vegetation is typical of Canadian Boreal Forest; low lying swampy areas that were originally filled with black spruce stands have been logged. Topographically higher areas are host to a variety of tree species including trembling aspen, white birch, balsam fir, and occasional white and red pine.

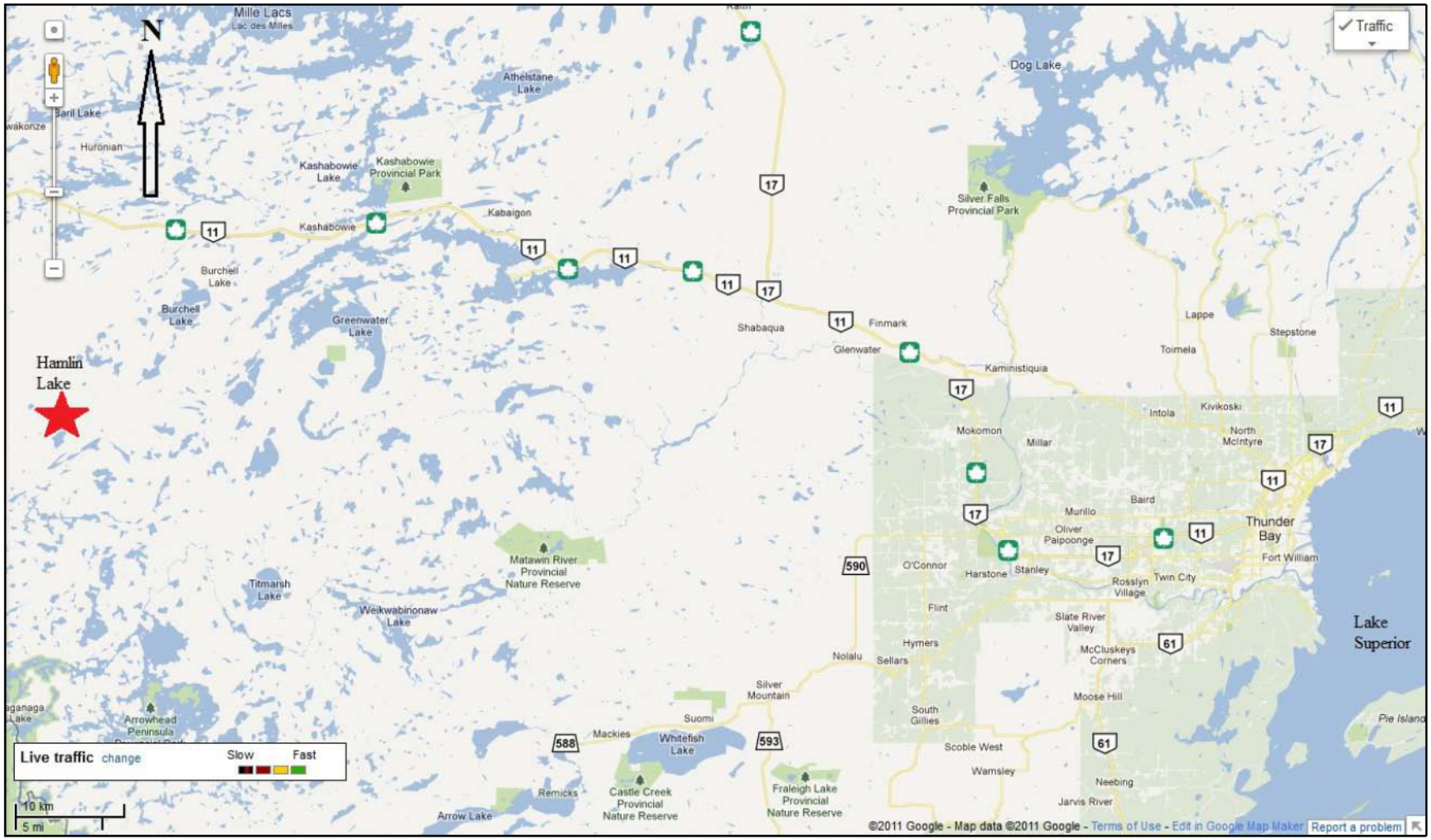

Figure 2.1 – The location of the Hamlin Lake property.

2.2 Core logging and sampling

Over 60 drill holes have been drilled across the deposit and time would not allow for re-logging of every hole. For this reason, only holes proximal to the ore body were examined. A complete list of the drill holes used in this study is provided in Table 2.1 and their locations are shown in Figure 2.2.

Although all the holes have been logged before, they were logged with an emphasis on economic geology. Thus, the old logs give detailed descriptions of mineralization (grade estimates and styles) and lithology (rock type and structure), but give very little detail on the alteration relationships present. Since this study was focused on how fluids were involved in the genesis of the Hamlin Lake deposit, the logs focused on defining spatial and temporal alteration relationships in the form of mineral associations and assemblages. Each hole was divided into 10 meter intervals, and the intensities of common alteration minerals were estimated visually.

Samples were taken for polished thin section wherever visual observations alone were not conclusive; for example, to aid in the identification of an unknown mineral phase, defining complex timing relationships or determination of lithology of altered rock. Some polished thin sections were taken of alteration quartz with the intention of finding fluid inclusions, but this will be discussed in greater detail below. Because of the significance of iron oxides in these deposits, several samples of magnetite were selected and cut into 100μm thick polished thin sections for analysis of trace elements. To attain the detection limits required for this study, the use of laser ablation inductively coupled

Table 2.1 – List of drill hole collars. Easting and northing coordinates are in NAD83, UTM Zone 15.

DDH	Easting	Northing	Azimuth	Dip	Length	Elevation
HAM-05-29B	663040	5372281	140	-45	150	446
HAM-05-30	663040	5372281	140	-60	181	420
HAM-05-31	663244	5372542	140	-45	306	457
HAM-05-32	663614	5372613	320	-45	307	420
HAM-05-33	663456	5372469	320	-45	298	439
HAM-05-36	663010	5372324	140	-55	197	440
HAM-06-39	663386	5372458	320	-60	308	434
HAM-06-40	663247	5372332	320	-45	124	441
HAM-06-41	663044	5372412	140	-45	252	452
HAM-06-43	663376	5372462	320	-50	249	420
HAM-06-53	663473	5372501	140	-60	267	439
HAM-06-54	663473	5372501	140	-45	96	420
HAM-06-55	663630	5372848	140	-45	192	420
HAM-06-56	663079	5372357	140	-45	204	440
HAM-06-57	663473	5372501	320	-62	279	420
HAM-08-58	663588	5372651	120	-47	417	432
HAM-08-59	663423	5372501	138	-44	342	434
HAM-08-60	662752	5372503	145	-46	399	431
HAM-09-61	663656	5372978	140	-44	300	426
HAM-09-62	663374	5372752	140	-45	432	431
HAM-10-63	663247	5372628	140	-68	386	456
HAM-10-64	663155	5372519	177	-65	363	462
HAM-10-65	663040	5372433	150	-67	387	452
HAM-10-66	663020	5372318	124	-79	327	439

plasma mass spectrometry (LA-ICP-MS) was used and the procedure is outlined below in section 2.5.

2.3 Fluid Inclusion Microthermometry

Fluid inclusions in quartz from one double polished section are analyzed using an Olympus BX51 microscope with attached Linkam TMS94 stage and controller. Inclusions are supercooled to -60°C with liquid nitrogen where the entire inclusion is frozen and slowly heated at a rate of 1°C per minute until the eutectic temperature (T_E) is

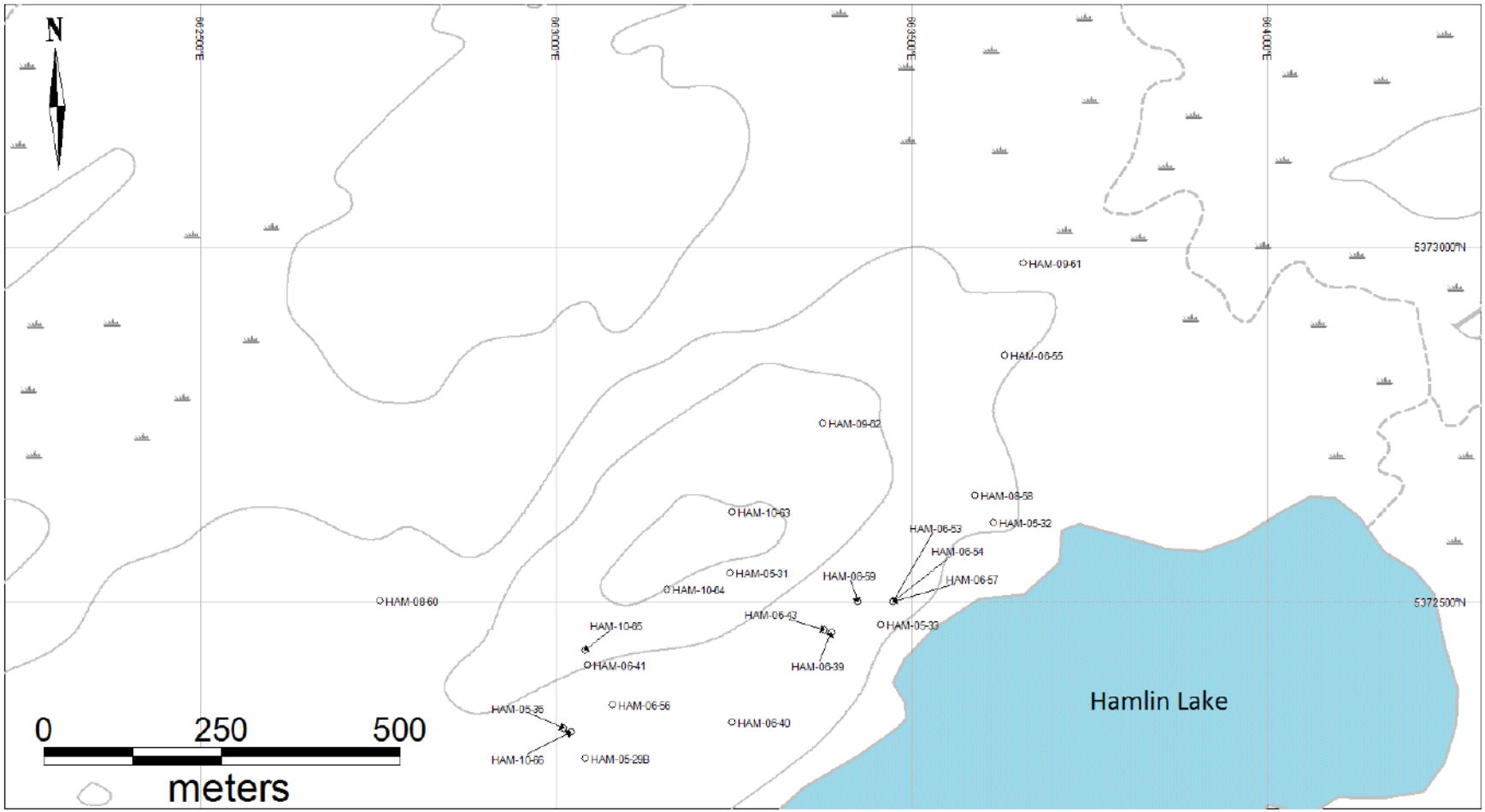

Figure 2.2 – Drill collar location map, see Table 2.1 for hole orientations.

reached. Heating is continued at the same rate until the melting temperature (T_M) is reached. Inclusions are then quickly heated to just under the homogenization temperature (T_H) and slowly (1°C per minute) brought past T_H.

2.4 Isotope Analysis

Samples selected for mineral isotope analysis were subject to rigorous preparation in order to ensure a pure sample. After a sample was selected, it was crushed and subjected to multiple stages of magnetic and density based separation until a sample with >99% of the mineral in question was attained. The mineral separates are then bottled and shipped to the Queen's Facility for Isotope Research (QFIR) in Kingston, Ontario, to be analyzed.

2.4.1 Mineral separation

The first step in the mineral separation was to crush the sample down to a usable size. This was done by repeated cycles of crushing and sieving until a suitable sized sample was obtained. Crushing was first done by hand with a tungsten-carbide mortar and pestle until grains were <2 mm in size. The pulp was then run through a mechanical mortar and pestle for 30 seconds before it was sieved. Usable sample was required to pass through a 100 mesh (150 µm) sieve and be caught by a 200 mesh (75 µm) sieve. The coarse material was returned to the mechanical mortar and pestle and the process was repeated until a suitable amount of sample was collected. The amount of sample required

depended on the amount of mineral present, and was usually between 20 and 40 grams. This portion was washed with distilled water and dried in an oven at 85°C.

Once the sample had dried it was ready for the separation. Mineral separation was achieved through a combination of the techniques outlined below. The methods used depended on the nature of the sample and the mineral to be separated. All samples were first treated with a simple handheld magnet to isolate the most magnetic material.

Magnetic separation is a technique used to separate minerals with differing magnetic susceptibilities. Separation was achieved with a Frantz Isodynamic magnetic separator (Figure 2.3). The sample was loaded into an aluminum funnel which fed into a chute oriented at a 15° side slope. Two electromagnets driven by a variable current source controlled the intensity of the magnetic field. The chute was divided midway down so that the magnetic portion of the sample remained up-slope and fell into one collector, while the non-magnetic portion fell into another. The sample was first run with low current to remove any strongly magnetic material, and the current was progressively increased until the mineral in question is removed. This method was used to isolate chlorite from the sample and it came off at a range of currents between 0.4 A and 0.6 A. Chalcopyrite was also separated from pyrite using this method; chalcopyrite is usually removed at a range of currents between 1.0 A and 1.1 A.

Density based separation was also useful for separating minerals with different densities. This method was best applied to the initial separation of heavier minerals to reduce the sample size going through the magnetic separator (e.g., pyrite and chalcopyrite); however, it was also applied to some of the chlorite rich samples with

Figure 2.3 - Frantz Isodynamic magnetic separator.

minor impurities dense impurities, such as epidote. In this method the sample was mixed into a separating flask filled with a heavy liquid. Over time the material with a higher density than the liquid sank and the remainder either floated or remained in suspension. The separated material was filtered, and the sample was washed with either distilled water or acetone, depending on the fluid. Table 2.2 lists the fluids used in this study along with their properties. All samples were refined to a purity of >99% using a combination of this and the magnetic separation described above.

Table 2.2 – Heavy liquid properties.

Fluid name	Nature	Formula	Density
Bromoform	organic	$CHBr_3$	2.87
Lithium metatungstate	tungsten based	$Li_6(H_2W_{12}O_{40})•3H_2O$	2.90 (varies with concentration)
Tetra bromoethane	organic	$C_2H_2Br_4$	2.95
Methylene iodide	organic	CH_3I	3.31

2.4.2 Isotopic ratio mass spectrometry

Samples of chlorite, magnetite, pyrite, chalcopyrite and pyrrhotite were sent to Queens Facility for Isotope Research (QFIR) in Kingston, Ontario, for isotopic analysis. All isotopic ratios were measured in a dual inlet Finnigan MAT 252 isotope ratio mass spectrometer (IRMS). This analyzer used a dual gas inlet where sample and standard were rapidly alternated into the ion source. Ionized gases were shot through the mass spectrometer, which consisted of a variable intensity electromagnetic field. Multiple mass paths were stabilized, depending on the isotope to be analyzed. Ions of each mass were collected in three faraday cups, each of which monitored a different mass. For hydrogen, masses ^{2}H and ^{3}H (herein referred to as deuterium, or D) were monitored, for oxygen masses ^{16}O, ^{17}O and ^{18}O were monitored and for sulphur masses ^{32}S, ^{33}S and ^{34}S were monitored. Samples were converted to gas using the methodology outlined below.

For this study, pairs of sulphides were selected for determination of their sulphur isotope composition. Each pair represented two sulphide species that appeared to be in equilibrium based on reflected light petrography. Sample purity was especially important in the case of the sulphide pairs, since the isotope data was used for geothermometry. Therefore, X-ray diffraction (XRD) analysis was used to ensure a monomineralic sample.

The pure samples were sent to QFIR where they were prepared in a Carlo Erba elemental analyzer model NCS 2500, and converted to SO_2 gas before entering the IRMS. The powdered sample was dropped into a combustion furnace in the presence of an oxidizing agent (CuO). Sulphur in the sample was oxidized and the resulting SO_2 gas was carried into the ion source of the IRMS. The results were reported in per mil relative to the Canyon Diablo Troilite (CDT) as $\delta^{34}S$:

$$\delta^{34}S = \left(\frac{R_{sample} - R_{CDT}}{R_{CDT}} \right) \times 1000 \qquad R = \frac{^{34}S}{^{32}S} \qquad (2.1)$$

Oxygen was extracted from magnetite and converted to a gas using bromine pentafluoride (BrF_5) as outlined by Clayton and Mayeda (1963). Samples were heated to 400°C to remove adsorbed water and air. The reagent (BrF_5) was added to the sample and heated to 600°C for 12 hours. After the reaction the apparatus was cooled to room temperature and O_2 was the only volatile that could be filtered through a cold trap. The O_2 was passed over hot graphite at approximately 550°C and quantitatively converted to CO_2. The CO_2 then entered the IRMS where both carbon and oxygen isotope ratios were measured, but only oxygen was reported relative to Vienna Standard Mean Ocean Water (V-SMOW) as $\delta^{18}O$:

$$\delta^{18}O = \left(\frac{R_{sample} - R_{VSMOW}}{R_{VSMOW}} \right) \times 1000 \qquad R = \frac{^{18}O}{^{16}O} \qquad (2.2)$$

Analyses for chlorite measured both oxygen and hydrogen ratios. Oxygen was converted to CO_2 gas using the same BrF_5 method described above. Hydrogen was extracted through the process outlined in Kyser and O'Neil (1984), which is briefly described here. The sample was placed in a combustion furnace, where it was heated to 150°C for 12 hours to remove surficially derived adsorbed water. The chlorite was then

heated to 1400°C for 20 minutes and the gasses released were collected in a cold trap at -196°C. The trapped gasses were passed over CuO at 500°C to oxidize and remove hydrocarbons. The remaining water represented the total amount of hydrogen and was reacted with zinc at 750°C to produce H_2, which could enter the IRMS. Hydrogen and oxygen analyses were done separately and results were reported relative to V-SMOW in δD and $\delta^{18}O$ respectively, where $\delta^{18}O$ is reported according to equation 2.2, and δD is:

$$\delta D = \left(\frac{R_{sample} - R_{VSMOW}}{R_{VSMOW}} \right) \times 1000 \qquad R = \frac{D}{H} \qquad (2.3)$$

2.5 Laser Ablation Inductively Coupled Plasma Mass Spectrometry

Laser ablation and inductively coupled-plasma mass spectrometry (LA-ICP-MS) was done at Laurentian University in Sudbury, Ontario, to determine trace element composition of iron-oxides and sulphides. Ablation was achieved using a New Wave Nd: YAG 213nm laser in a helium atmosphere. The helium acted as a carrier gas for transporting the sample and had to be mixed with argon before entering a quadrupole Thermo X Series 2 ICP-MS. The argon entered a high frequency time varying magnetic field, and when spark was applied an electric current was produced, breaking the argon gas down into high temperature plasma. Temperatures in the plasma reached 10,000 K, and this lead to the ionization of the sample. The ion beam was passed through a quadrupole mass filter which used a radio frequency quadrupole field to selectively stabilize ionic paths. Only atoms of a specific charge to mass ratio could pass through at a given time, and these struck a detector that recorded their charge. The intensity of the resulting signal was proportional to the number of atoms detected, and as the quadrupole

swept through the range of possible mass to charge ratios, a mass spectrum was produced.

Ten polished thick sections (100µm thickness) were analyzed for magnetite with a 30 µm spot size and a repetition rate of 10Hz, while 40 µm spot size and 5Hz were used for the sulphide analysis. Energy density was kept constant at approximately 6-7J/cm^2 and the beam width was 5ns. Samples were analyzed for 55 seconds, including 30 seconds background acquisition and 25 seconds of ablation. Data quantification followed the approach outlined in Heinrich *et al.* (2003). The NIST 611 synthetic glass standard was used as the external standard and stoichiometric Fe concentrations were used as the internal standard to quantify the data.

2.6 Back Scattered Electron Petrography and Energy Dispersive X-ray Analysis

Fifteen of the 103 polished thin sections were selected for analysis by back scattered electron imagery and analytical X-ray spectrometry at Lakehead University in Thunder Bay, Ontario. Data was obtained with a JEOL 5900, low vacuum scanning electron microscope (SEM) with attached LINK ISIS 300 analytical system with incorporated Super ATW Light Element Detector and energy dispersive X-ray spectrometer (EDS). The polished sections were carbon coated before the analysis.

Elemental compositions were quantified using the EDS, where samples were bombarded with electrons emitted from an electron gun. The electron beam (20kV, 0.475nA) interacted with valence electrons in the sample causing excitement of the valence electrons to higher energy shells. Upon dropping back to valence, a small

amount of energy was released (the photoelectric effect) in the form of a photon in the X-ray region of the electromagnetic spectrum. These X-rays were detected by a lithium-drifted silicon crystal detector after passing through a beryllium window that kept the detector under a vacuum. An unfortunate side effect of this window was that low energy X-rays are partially absorbed and either could not be detected or were detected at inaccurate levels. Light elements whose X-rays fall into this low energy portion of the spectrum could not be accurately measured and include beryllium, boron, lithium and carbon; however, elements through to silicon are affected and suffer from higher detection limits. X-rays that were detected produced an analog voltage signal with voltage proportional to the energy of the X-ray. The analog signal was passed through an operational amplifier that converted the analog pulse a digital one and counted the frequency of each incoming energy signal. This was displayed on screen as a plot of energy versus counts and was depicted as a series of peaks whose amplitude were indicative of elemental proportions.

Calibration of the EDS was highly important for acquiring meaningful data. The locations of the energy peaks were sensitive to temperature, and their location was calibrated every two hours using a nickel standard. In addition each element to be analyzed needed to be standardized to a known concentration from a predetermined standard. The standards used in this study are given in Table 2.3. Once the standardization process was complete, a known mineral was checked to verify the quality of standardization.

Table 2.3 – SEM standards used for quantitative analyses.

Mineral	Elements
Apatite	P
Benitoite	Ba, Ti
Cerium fluoride	Ce
Chalcopyrite	Cu, S
Clausthalite	Se, Pb
Jadeite	Na, Al
Lanthanum fluoride	La
Manganoan hortonolite	Mg, Si, Mn, Fe
Millerite	S
Native bismuth	Bi
Native cadmium	Cd
Native copper	Cu
Native gold	Au
Native molybdenum	Mo
Native selenium	Se
Native silver	Ag
Native tellurium	Te
Native tungsten	W
Orthoclase	K,
Sphalerite	Zn
Wollastonite	Ca, Si

Chapter 3 – Geology of Hamlin Lake

3.1 Regional Geology

3.1.1 The Superior Province

The Superior Province, also referred to as the Canadian Shield, is a well studied Archaean Craton that covers 1,572,000 km^2 (Thurston, 1991). The craton was divided into several sub-parallel belts called subprovinces by Card and Ciesielski (1986). Over the years this model has undergone numerous revisions based on new geologic and geophysical data (Thurston *et al*., 1991; Stone, 2005; Percival *et al*., 2006; Stott *et al*. 2007). The most recent versions exchange the general term "subprovince" with more geologically accurate term of "terrane" which is defined in Stott *et al.* (2010) as "a tectonically bounded region with internal characteristics distinct from those in adjacent regions prior to Neoarchean assembly of the Superior Province". The most recent revisions to the terrane boundaries are presented in Figure 3.1 (Stott *et* al., 2010). Granite-greenstone dominated terranes such as the Wawa-Abitibi, and the Wabigoon are separated by tracts of metasedimentary rocks, migmatites and S-type granites like the Quetico and English River basins (Williams, 1990).

The tectonic formation of the Superior Province has been the subject of much debate over the past couple of decades. Lithologies found in the various terranes range from granites and tonalite-trondhjemite-granodiorite (TTG) suites to komatiites, basalts, rhyolites and iron formations. Geological and isotopic studies of these rocks have led to

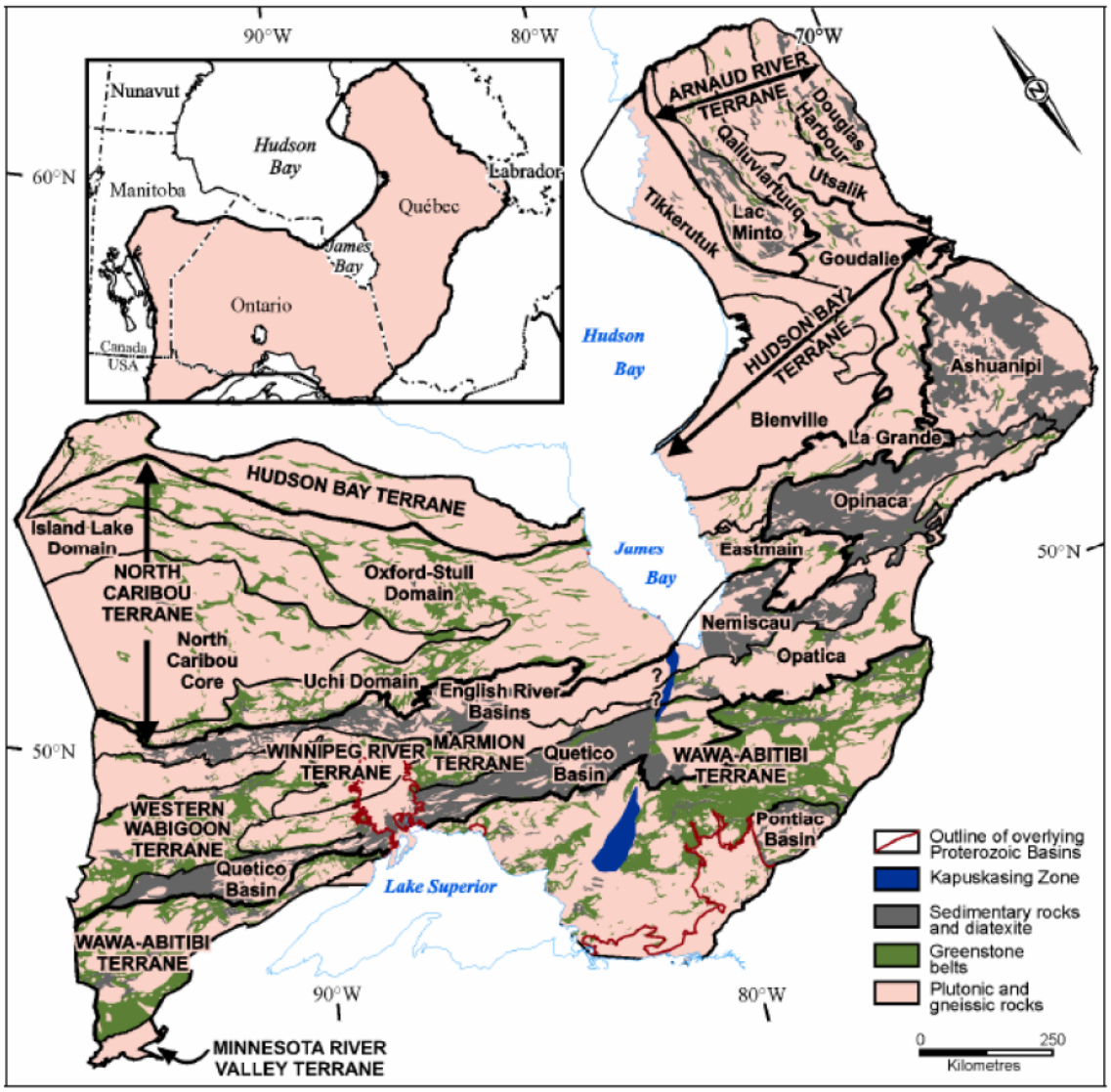

Figure 3.1 – Geological map of the Superior Province subdivided into its various terranes (Stott *et al.*, 2010)

a range of tectonic environments from volcanic arcs, back arcs, plateau basalts and ocean island basalts (Thurston *et al.*, 1991; Hollings *et al.*, 1999; Whalen *et al.*, 2002; Polat and Kerrich, 2001). The greenstone belts young to the south with ages ranging from 3.0 to 2.65 Ga (Thurston *et al.*, 1991). Those in favor of Archean plate tectonics suggest that

the greenstone belts of the Superior Province represent juvenile island arc sequences and that southward amalgamation through subduction-accretion processes ultimately produced the assembly we see today (Stott *et al.*, 2010). This model suggests that the metasedimentary tracts separating the granite-greenstone belts represent accretionary prisms; however, these lack the structural repetition usually seen in accretionary sequences. A model in support of vertical tectonics (Bedard *et al.*, 2003) resolves this issue, but the debate is ongoing.

3.1.2 The western Wawa-Abitibi Terrane

The Wawa Subprovince was initially considered to be separate from the Abitibi Subprovince (Williams *et al.*, 1991). Although the two are physically separated by the Kapuskasing Structural Zone, they are now considered to have originally been a single terrane called the Wawa-Abitibi Terrane (Stott *et al.*, 2010). The western Wawa-Abitibi Terrane is bounded to the north by the Quetico Basin. Most of the southern boundary is largely hidden beneath Lake Superior, and covered by unconformable Proterozoic supracrustal rocks of the Animikie Basin. In the southwest, however, the Great Lakes Tectonic Zone marks the contact between the western Wawa-Abitibi Terrane and the Minnesota River Valley gneiss terrane (Corfu and Stott, 1998; Figure 3.2).

The geology of the western Wawa-Abitibi Terrane consists of Archean greenstone belts dispersed in a sea of granitoid rocks. The greenstone belts themselves are composed of metamorphosed komatiitic to tholeiitic basalt, overlain by iron and

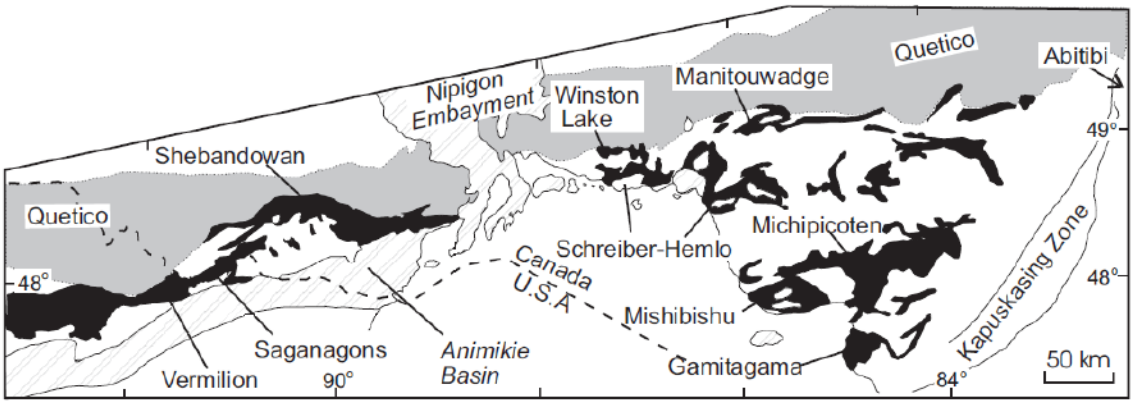

Figure 3.2 – The western Wawa-Abitibi Terrane (white) with its greenstone belts (black). The Quetico Basin (grey) bounds the Wawa-Abitibi to the north, with the Animikie Basin (striped) to the south. The western Wawa-Abitibi Terrane is bounded on the far east of the map by the Kapuskasing Structural Zone, east of which lies the eastern Wawa-Abitibi Terrane (from Corfu and Stott, 1998).

magnesium rich tholeiite and by submarine to subaerial calc-alkalic basalts and felsic to intermediate volcanic rocks (Williams *et al.*, 1991). They can be subdivided into two linear concentrations: one along the northern border with the Quetico Basin includes the present study area within the Shebandowan Greenstone belt and the other in the south-central part of the Subprovince near the municipality of Wawa (Williams *et al.*, 1991).

The emplacement of the greenstone belts has long been debated. Early models (Williams *et al.*, 1991) suggested that the greenstone belts formed separately and became tectonically juxtaposed in place (allochthons). A more recent model proposed by Thurston (2002) suggests that many of the greenstone belts in the Superior Province, including those in the Wawa-Abitibi Terrane, actually formed autochthonously or parautochthonously.

3.1.3 The Shebandowan greenstone belt

The Shebandowan greenstone belt, located on the northern boundary of the western Wawa-Abitibi Terrane, is one of two greenstone belts in the Wawa-Abitibi Terrane to the west of the Nipigon Embayment. The other greenstone belt is the Saganagons greenstone belt and it has been proposed that the two belts were continuous at one time (Williams *et al.*, 1991). The Shebandowan greenstone belt (Figure 3.3) is bounded to the south by the Northern Light-Perching Gull Lakes (NLPG) batholith complex. The arcuate shaped belt extends approximately 170km from east of Thunder Bay to west of the town of Shebandowan.

Three assemblages were originally defined by Williams *et al.* (1991). The older Greenwater and Burchell assemblages are separated by the Knife Lake fault, and the younger Shebandowan assemblage overlaps these. This interpretation was revised by Corfu and Stott (1998) who suggested three new assemblages. The Greenwater and Burchell assemblages were combined due to consistent ages (2720 Ma) and younging directions. They consist of volcanic cycles represented by tholeiitic basalt, and an upper sequence of calc-alkaline intermediate to felsic volcanic rocks. The northern part of the Burchell assemblage was incorporated into the Shebandowan assemblage and termed the Kashabowie assemblage. This assemblage (2695 Ma; Corfu and Stott, 1998) is Timiskaming-type as evident by the association of calc-alkalic to alkalic mafic to felsic volcanic rocks and clastic sedimentary rocks with shallow water to subaerial depositional environments. The third subdivision is termed the Auto Road assemblage and stratigraphically overlies the Kashabowie assemblage in a small sedimentary basin in the

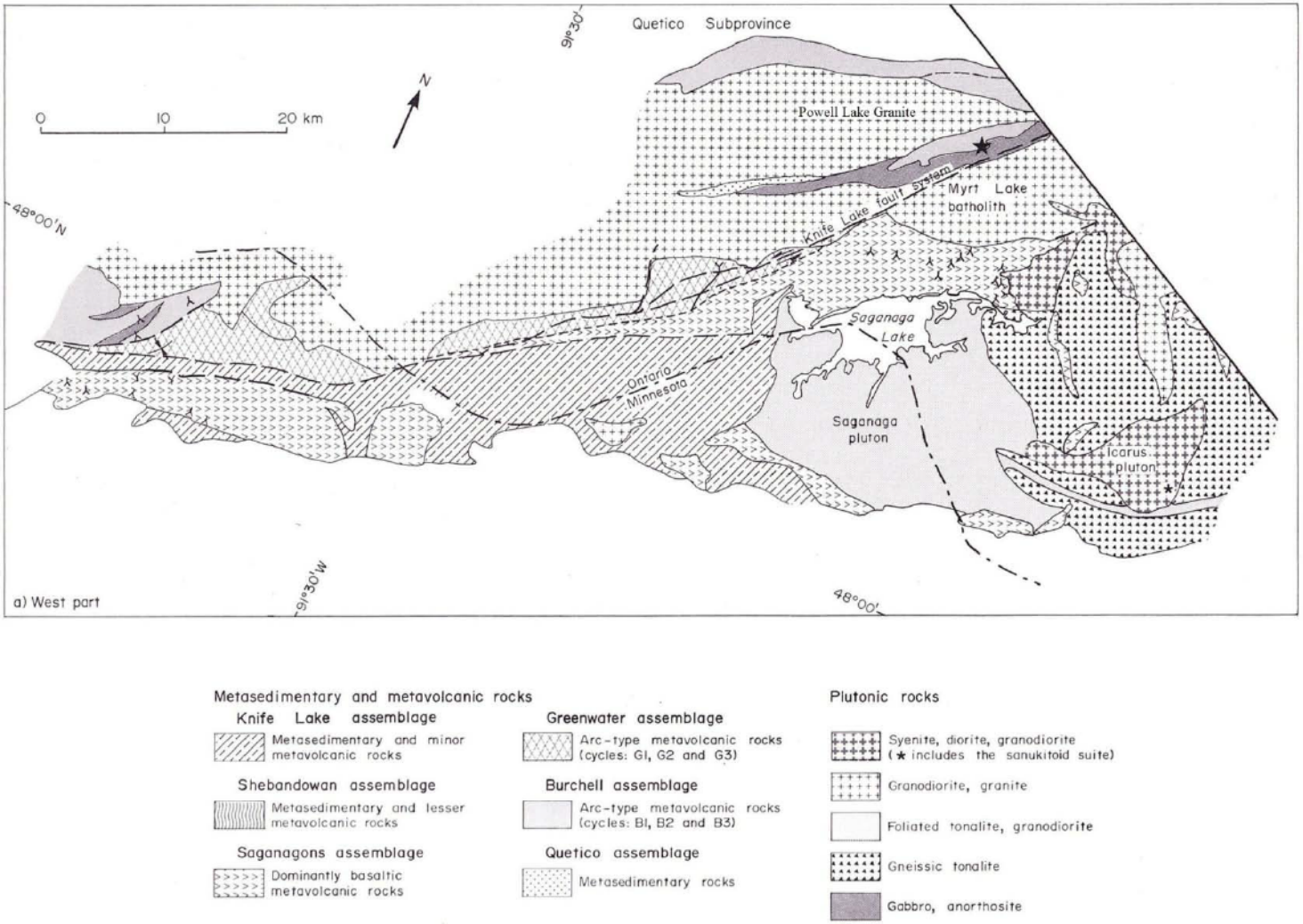

Figure 3.3a – The western portion of the Shebandowan greenstone belt (*modified from* Williams *et al.*, 1991)

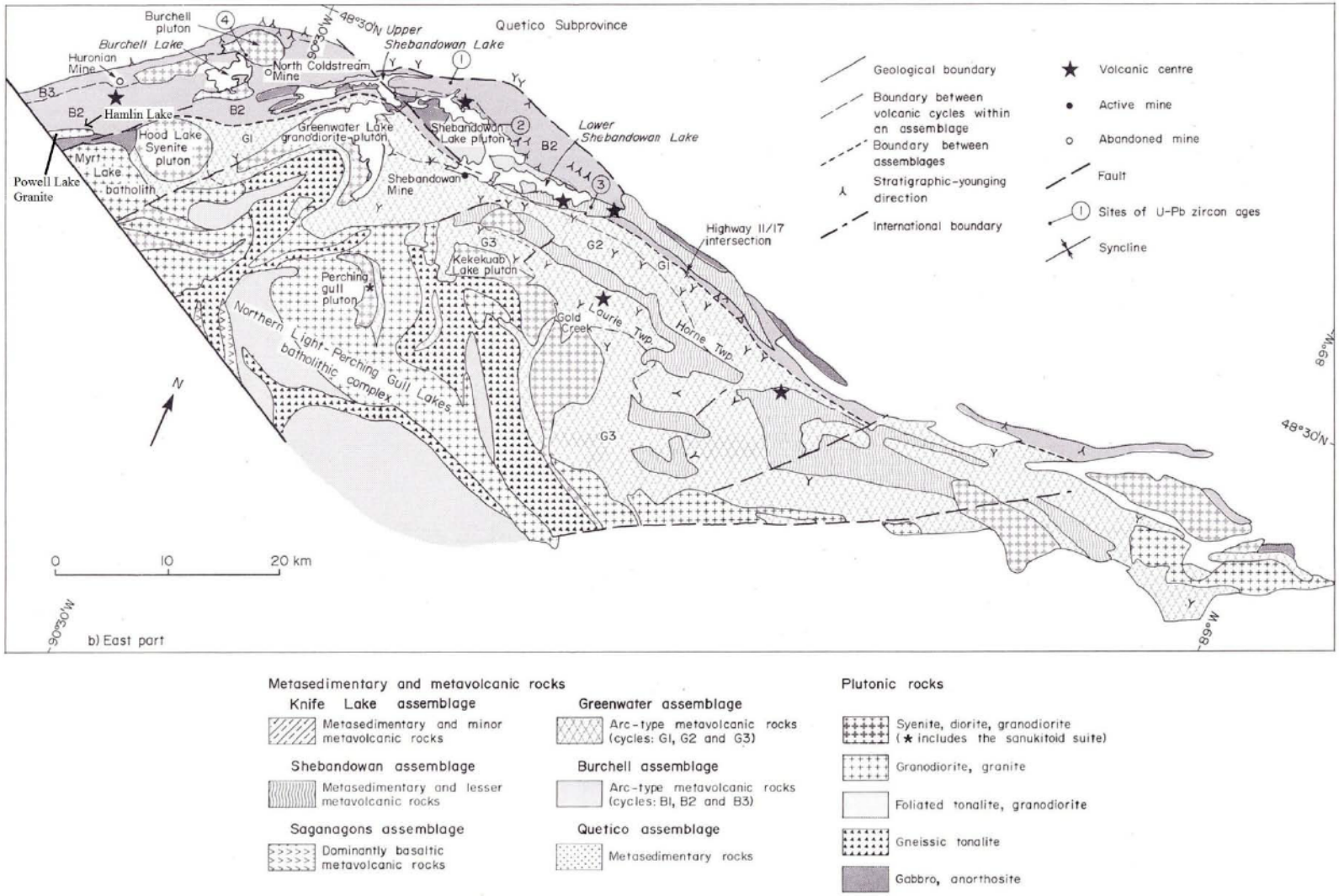

Figure 3.3b – The eastern portion of the Shebandowan greenstone belt (*modified from* Williams *et al.*, 1991)

northeast.

Three episodes of deformation characterize the structural geology of the Shebandowan greenstone belt (Williams *et al.*, 1991). The earliest event (D_1) can be seen across the entire belt, and involved northwest-southeast compression resulting in a sub-vertical to steeply northward dipping schistosity. Minerals and mineral aggregates are lineated consistently to the west, plunging between 40 and 60 degrees. The D_2 event partly overprinted the D_1 event, mostly in the northern regions of the belt. The schistosity produced from D_2 is parallel to that produced by D_1, however mineral lineations from D_2 plunge shallowly to the east. Williams *et al.* (1991) noticed that the Shebandowan assemblage (later termed the Kashabowie assemblage, see above; Corfu and Stott, 1998) remained unaffected by the D_1 event, but was subject to D_2. This has been attributed to the deposition of the Shebandowan assemblage after D1. The D_2 event is also responsible for many brittle-ductile shear zones, several of which host gold mineralization (Stott and Schnieders, 1983). The third deformation event (D_3) resulted in a series of late steeply plunging kink folds near the northern boundary of the belt. It has been suggested that these are the result of west-northwest shortening that produced the D_2 fabrics (Williams *et al.*, 1991).

Numerous faults affect the Shebandowan greenstone belt, and these are generally northeast or northwest striking. The Knife Lake fault (Figure 3.3a) is the closest major fault to the study area and strikes northeast with sinistral displacement. Late stage vertical displacement is also evident from nearly vertical lineations on the fault system (Williams *et al.*, 1991).

Regional metamorphism throughout the belt ranges from greenschist to lower amphibolite (Williams *et al.*, 1991). Greenschist metamorphosed rocks encompass the entire belt, whereas amphibolite grades were only reached in proximity to late, post-tectonic felsic intrusions. The current study area, located near Hamlin Lake, lies entirely in the greenschist facies region.

3.2 Local Geology

The most recent mapping project on the Hamlin Lake area was undertaken by Shute (2009). The mapping study utilized field observations as well as thin section work and whole rock geochemistry. The following descriptions of the local rock units are largely based on that study, as well as a 2009 Ontario Geological Survey's mapping project by Hart and Metsaranta. It is worth noting that all of the units are metamorphosed, and for the purpose of readability the prefix meta- has been omitted from the descriptions below. The area hosts a wide array of rock types ranging from calc-alkalic to shoshonitic felsic to intermediate volcanic rocks with textures ranging from massive to porphyritic, volcaniclastic rocks dominated by tuffaceous rocks, debris flows, iron formation, as well as intrusive rocks ranging from felsic to mafic in composition. The real focus of this study is on the hydrothermal breccia that lies north of Hamlin Lake.

3.2.1 Volcanogenic units

The felsic to intermediate rocks north of Hamlin Lake cover a full spectrum of compositions and textures (units 2 and 4 on Figure 3.4; Hart and Metsaranta, 2009). Units that were mapped by Shute (2009) include massive to porphyritic to tuffaceous rhyolite to dacite and andesite. Several outcrops of felsic debris flow were also mapped. Rhyolites were observed and ranged from massive porphyritic flows, to rhyolitic tuff. On fresh surface the rhyoltic rocks can have a variety of colours ranging from light brown, yellow-white, grey-tan, dark grey and black-green depending on how the rock was altered. Quartz phenocrysts were occasionally observed in the more massive flows and range in colour from bluish to clear grey. These massive flows are often lobe-like and closely associated with highly angular clasts arranged in a jigsaw breccia. This was interpreted as a hyaloclastic breccia (Shute, 2009). Pyroclastic rhyolites contain fragments of chert (Figure 3.5A) that are often difficult to distinguish from quartz filled amygdules observed elsewhere. These amygdules (Figure 3.5B) are generally quite large, usually between 5 mm and 1 cm, however one amygdule was approximately 9.0 cm long.

Outcrops of dacite are rare, and when they are observed they are usually found as ash or lapilli tuff, and are often banded with 1.0 cm to 2.0 cm thick layers of ash (Figure 3.5C). The andesitic units observed are difficult to distinguish from the rhyolite based on field observations alone, and are separated here based on whole rock geochemistry (Shute, 2009). The tuffaceous variety of andesites often have their clasts replaced by chlorite; however, the clast textures are preserved. Porphyritic varieties of andesites were

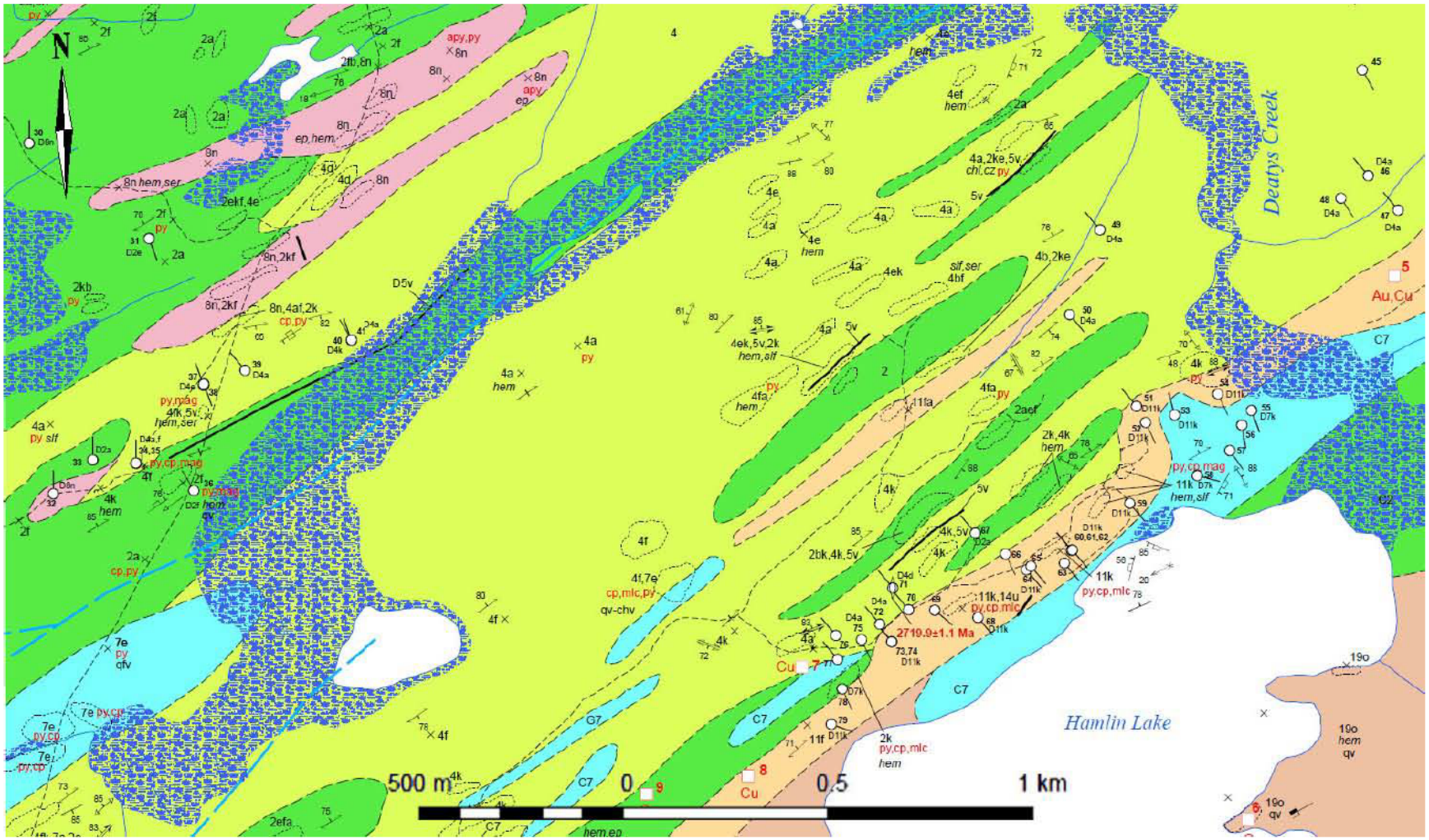

Figure 3.4 – Local geology map of the study area from Hart and Metsaranta (2009). Units are described on the legend on the next page.

LEGEND

PHANEROZOIC

CENOZOIC

QUATERNARY

RECENT
Lake, stream and swamp deposits

PLEISTOCENE
Glacial deposits: sand, gravel, clay and till

UNCONFORMITY

PRECAMBRIAN

PROTEROZOIC

MESOPROTEROZOIC

22 **Diabase Dikes (Mine Centre)**
22e Gabbro / diabase

INTRUSIVE CONTACT

ARCHEAN

NEOARCHEAN

Mafic to Intermediate Alkalic Intrusive Rocks (~2680 Ma)

21 **Gabbro to Syenite**
21e Gabbro
21i Monzonite
21k Syenite

INTRUSIVE CONTACT

Intermediate to Felsic Intrusive Rocks

19 **Hornblende Tonalite to Granite**
19n Granodiorite
19o Granite

INTRUSIVE CONTACT

17 **Biotite Granodiorite to Granite**
17i Monzonite
17n Granodiorite
17o Granite
17t Aplite

INTRUSIVE CONTACT

Mafic Intrusive Rocks

14 **Lamprophyre**
14u Lamprophyre (biotite +/- muscovite)

INTRUSIVE CONTACT

Shebandowan Assemblage (Timiskaming Type)

12 **Calc-Alkalic and Shoshonitic Felsic to Intermediate Intrusive Rocks**
12i Granodiorite
12o Granite

INTRUSIVE CONTACT

11 **Calc-Alkalic and Shoshonitic Felsic to Intermediate Metavolcanic Rocks**
11a Massive flow
11e Tuff
11f Lapilli tuff
11b Breccia, debris flow
11s Quartz-feldspar schist

RELATIONS UNKNOWN

10 **Clastic Metasedimentary Rocks**
10b Mudstone
10c Siltstone
10d Muddy siltstone
10e Sandy siltstone
10f Sandstone

RELATIONS UNKNOWN

8 **Synvolcanic to Syntectonic Intermediate to Felsic Intrusive Rocks**
8n Granodiorite
8o Granite

INTRUSIVE CONTACT

Greenwater Assemblage Mafic Intrusive Rocks

7 **Synvolcanic to Syntectonic Mafic to Ultramafic Intrusive Rocks**

7b Peridotite

7c Very coarse feldspar porphyritic gabbro
7e Gabbro

7f Feldspar porphyritic gabbro

7g Leucogabbro
7k Diorite
7m Amphibolite
7s Serpentine-talc-chlorite schist

INTRUSIVE CONTACT

6 **Clastic Metasedimentary Rocks**
6b Mudstone
6c Siltstone
6e Sandstone

5 **Chemical Metasedimentary Rocks**
5p Chert
5w Oxide facies iron formation
5w Sulphide facies iron formation

4 **Felsic to Intermediate Metavolcanic Rocks**
4a Massive flow
4b Quartz-porphyritic massive flow
4d Tuff
4e Quartz-porphyritic tuff
4f Lapilli tuff
4k Debris flow
4s Quartz-feldspar schist

2 **Mafic to Intermediate Metavolcanic Rocks**
2a Massive flow
2b Pillowed flow
2e Tuff
2f Lapilli tuff
2k Debris flow
2s Chlorite schist

ABBREVIATIONS

chl - chlorite
chv - chlorite veining
cp - chalcopyrite
cz - carbonatization
ep - epidote
hem - hematite
mag - magnetite
mlc - malachite
py - pyrite
ser - sericite
slf - silicification
qv - quartz veining

SYMBOLS

Geologic contact

Limit of mapping

Area of outcrop

Small bedrock outcrop

Fault

Brittle fault, unknown horizontal displacement (inclined, trend only)

Brittle-ductile fault, unknown horizontal displacement (inclined)

Shear, unknown horizontal displacement (inclined)

Bedding, facing direction unknown (inclined, trend only, dip not measurable)

Cleavage (inclined, vertical)

Mineral foliation (inclined, trend only, vertical)

Primary igneous foliation (inclined, vertical)

Schistosity (inclined)

Dike (trend only, vertical, magnitude of dip uncertain)

Fracture, unknown horizontal displacement (inclined, trend only)

Fracture, unknown horizontal displacement (vertical, magnitude of dip unknown)

Fracture- or fault-hosted vein (inclined, trend only)

Mineral lineation

Intersection lineation

Location of diamond-drill hole (keyed to table 2)

Location of geochronology sample, with age in Ma

Trail

Swamp

not observed. Felsic debris flows were also occasionally observed on the property, and are comprised of chert fragments in a matrix of felsic volcanic ash. The fragments in these units are usually sub-rounded and tectonically flattened. A more "mafic" variety of debris flow was also mapped (Figure 3.5D), and these consist of chert fragments in a more melanocratic matrix. Although they have been termed "mafic" debris flows, it is proposed that the dark coloured flows are identical to the felsic flows except that they contained muddy sediment in the matrix in addition to the volcanic ash (Shute, 2009). Oxide facies iron formations are found sporadically across the property, and are generally not traceable in the field. These units are dominated by alternating beds of chert and magnetite; the chert layers are often up to several centimeters in thickness, while magnetite rarely exceeds several millimeters and often occurs as wispy bands.

The descriptions of the various lithologies by Shute (2009) led to interpretation of the environment as a shallow water environment influenced by multiple volcanic centers. Evidence for a shallow subaqueous environment includes: (1) the presence of thick lobe shaped massive flows with possible hyaloclastite. The lobe-like nature of the flows is indicative of shallow water because in a deeper eruption the fluid pressure would cause a thinner, more widespread flow, (2) the presence of banded iron formation, and (3) the presence of large amygdules also suggests the low fluid pressure of a shallow environment. Evidence for multiple volcanic centers includes: (1) the extreme variation in pyroclastic flows over relatively small areas, and (2) the presence of the dacitic ash layers together with the pyroclastic flows. The eruptions appear to become progressively more explosive over time until the collapse of the volcanic column and the deposition of debris flows commences in response to increase in volcaniclastic debris.

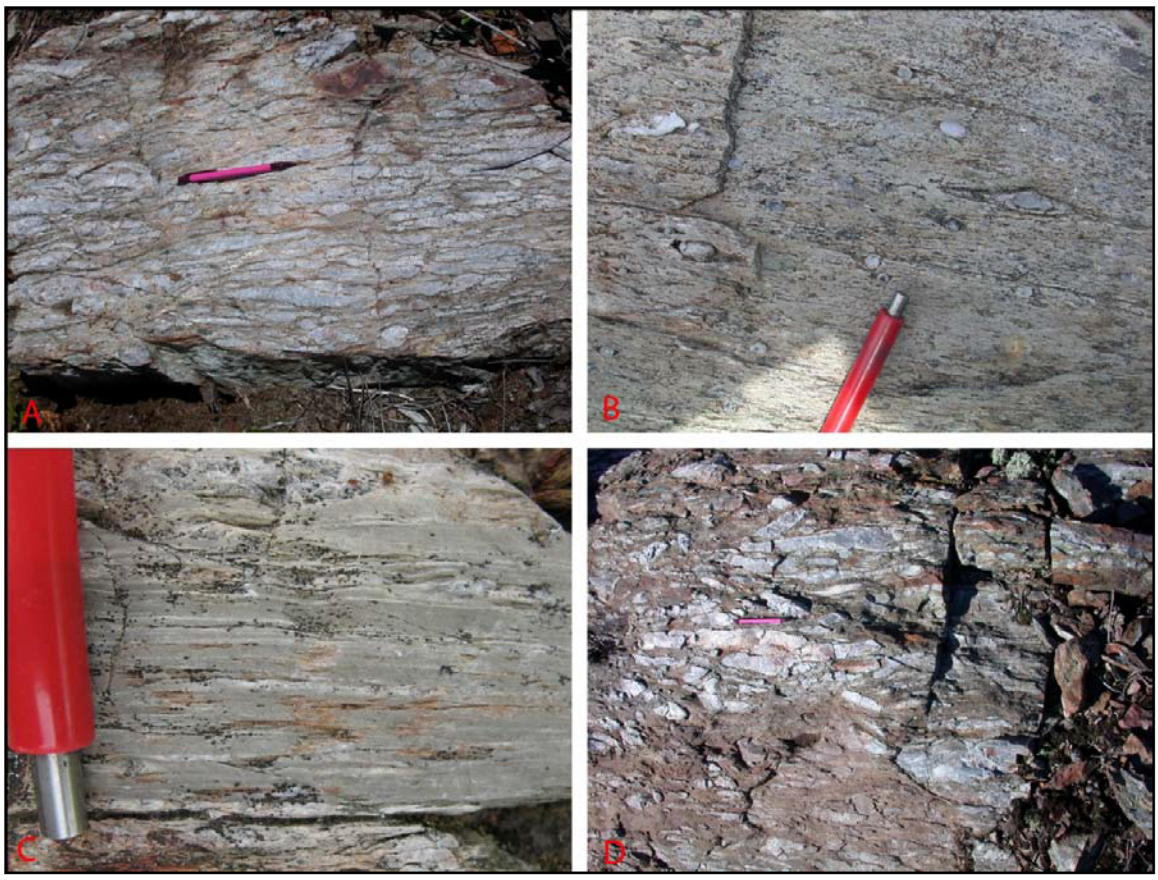

Figure 3.5 – A.) Felsic debris flow with large cherty fragments, B.) Amygdaloidal rhyolite with chert filled vesicles, C.) Dacitic ash layers, and D.) "Mafic" debris flow with cherty clasts (*photos from* Shute, 2009).

A later episode of volcanic activity is evident with the shoshonitic volcanic rocks on the north shore of Hamlin Lake (unit 11 on Figure 3.4; Hart and Metsaranta, 2009). The compositions of these rocks are felsic to intermediate with textures ranging from massive to porphyritic to tuffaceous. These rocks are largely brecciated and make up the breccia described below. Intensive alteration and brecciation makes an interpretation of this unit difficult.

3.2.2 Intrusive units

Figure 3.6 – A.) Outcrop of the Powell Lake granite on the western shore of Hamlin Lake, and B.) Fine grained "gabbro" intersected in hole HAM09-59, the mafic minerals are largely altered to chlorite and biotite.

Very little detailed work has been done on the intrusive rocks near Hamlin Lake. The intrusive rocks present include localized outcrops of the Powell Lake granite on the shores of Hamlin Lake (Figure 3.6A), as well as several smaller outcrops of altered gabbro that have been traced from the east side of Deaty's Creek to the north shore of Hamlin Lake. The granite has been described by Shute (2009) as being pink in colour with equigranular grains of plagioclase and quartz. Grain size varies from 0.5 mm up to 2.0 mm in length. The gabbro (Figure 3.6B) consists of medium to coarse grained

plagioclase and pyroxene. Intense alteration has converted the mafic minerals almost entirely to chlorite-biotite-magnetite, and the plagioclases are often highly epidotized. This intense alteration often masks the true lithology of the rock. Neither the granite nor the gabbro have been directly age dated, but appear to predate or be contemporaneous with brecciation.

3.2.3 IOCG breccia

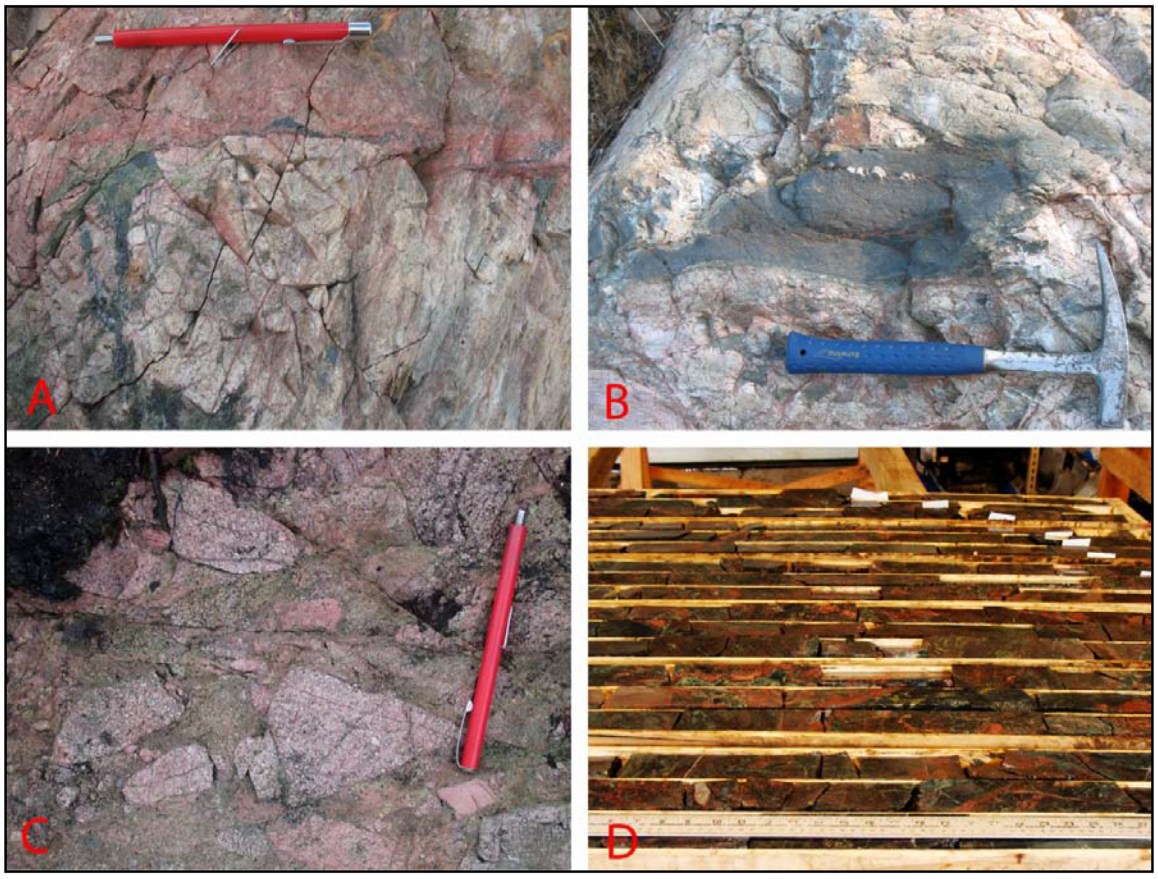

Figure 3.7 – Rocks brecciated during IOCG mineralization. A.) Multiple stages of overprinting brecciation outcropping at surface, B.) Magnetite forming the matrix to brecciated volcanic rocks, C.) Brecciated diorite, D.) Mineralized breccia at depth in drill core.

The breccia (Figure 3.7) encompasses a large area on the north shore of Hamlin Lake. It has been traced approximately 1.2km in length striking to the northeast. The brecciated body is up to 200 meters wide and has been traced to approximately 350 m vertical depth. The contacts with the surrounding volcanic rocks and intrusions are gradual and only detectable in drill core. Extensive drilling by East West Resource Corporation (now Rainy Mountain Royalty Corporation) and more recently by Xstrata Copper has defined the shape and orientation of the brecciated body. The breccia is sub-vertical or steeply dipping to the north, with no apparent plunge.

Jébrak (2010) developed a technique for effectively describing a hydrothermal breccia, and this method has been adopted to describe the breccias observed here. Three types of data need to be noted: (1) composition of the breccia clasts and matrix; (2) shape of the fragments themselves; and (3) the spatial organization of the fragments. Composition of clasts and matrix is described based on the clast lithology and matrix textures and mineralogy. It is also important to note whether the breccia is monomictic or polymictic. The shapes of the clasts can be described in terms of roundness, aspect ratio and boundary fractal dimensions (BFD). The spatial organization of clasts can be described based on clast size distribution, presence of a dominant fabric and the dilation ratio of the clasts. These are demonstrated in Figure 3.8 (Jébrak, 2010).

The compositions of the clasts in the Hamlin Lake breccia are dominantly shoshonitic (Hart and Metsaranta, 2009) felsic to intermediate volcanic rocks with textures similar to those described above. Occasionally cherty clasts are present in the breccia, but they are rarely the dominant clast type. Several drill holes intersected brecciated varieties of gabbro and diorite, near the bottom of the holes. The lower

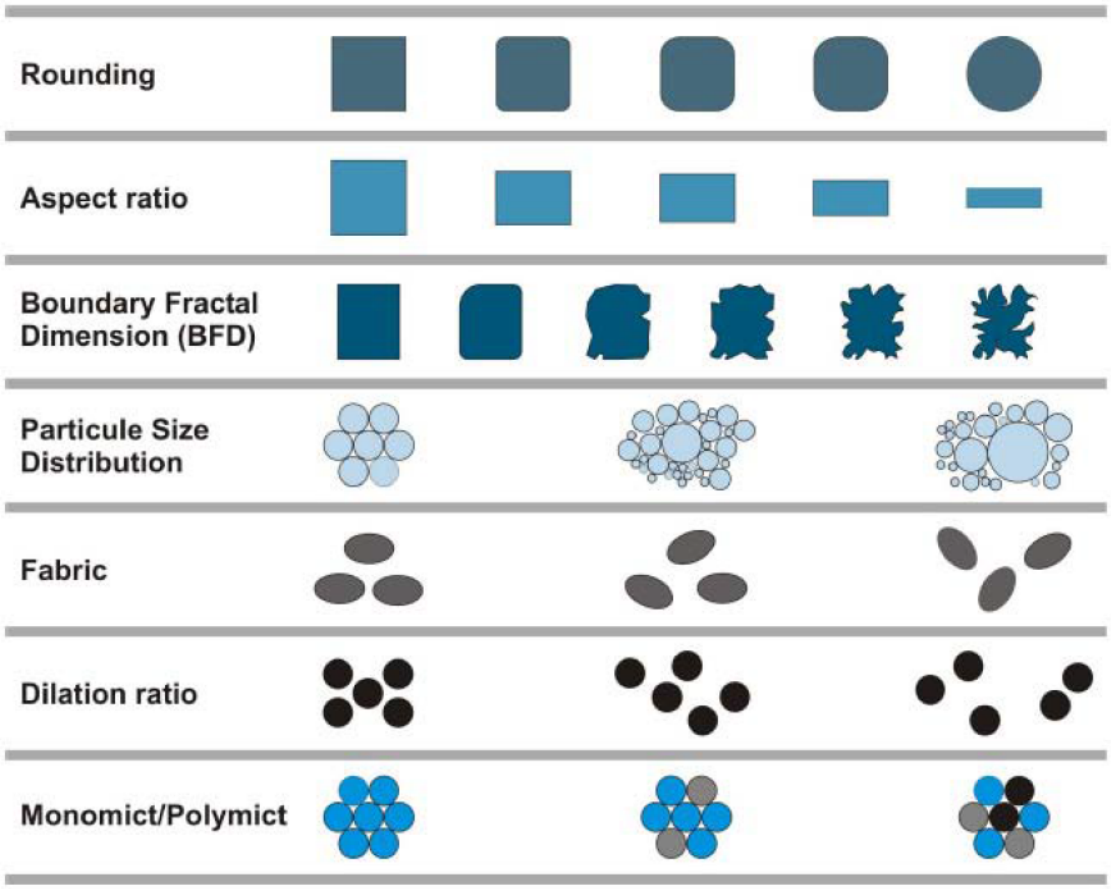

Figure 3.8 – The seven characteristics needed for an effective characterization of a breccia (Jébrak, 2010)

contact of the breccia grades into the Powell Lake Granite, incorporating large pink granitic fragments into the breccia (Figure 3.7C). Where fragments of intrusive rock are present, the breccia is often polymictic with the intrusive clasts making up anywhere from 30% to 80% of the rock, whereas the remainder is smaller clasts of volcanic rocks and chert. The matrix of the breccia is a mixture of small (<0.5 cm) fragments of host rock and variable amounts of chlorite, epidote, biotite, calcite, quartz, potassium feldspar, magnetite, pyrite, pyrrhotite and chalcopyrite. This matrix is probably of mixed crushed-hydrothermal origin.

The shapes of the clasts are varied and can range from rounded to angular and range in size from less than 0.5 cm to greater than 1.0 m. Using the method proposed by Bérubé and Jébrak (1999) for Euclidian distance mapping to estimate BFD, 16 breccia clasts were analyzed using the publicly available NIH-ImageJ software available from the US National Institute of Heath website. Calculated BFD's range from 1.12 to 1.31 with an average of about 1.19 (See Appendix A). Clast aspect ratios are also highly variable and range from 1.0 to 6.0.

In most of the Hamlin Lake breccia the brecciation style is usually chaotic (greater than 20° clast rotation); however, as the margins of the breccia are approached the style becomes more of a mosaic breccia (10-20° rotation) or crackle breccia (less than 10° rotation). Usually the clasts do not exhibit a preferred orientation to define a fabric, but in some places a slight foliation can be detected. The orientation of this foliation measured in degrees to the core axis (DTCA) varies depending on the orientation of the drill hole, and since the core was not oriented an absolute orientation can only be inferred based on multiple holes. Drill holes oriented at a steep inclination (~60°) usually exhibit foliation at lower angles to the core axis (30-40 DTCA), whereas holes with a more gradual incline (~45°) have foliation at higher angles (40-60 DTCA). This would suggest that the overall orientation of the foliation is close to vertical. Particle size distributions are usually within 1 order of magnitude, but occasionally more variable clast sizes can be seen with small fragments making up a matrix supporting larger (up to 1m) clasts. The dilation (or matrix to clast ratio) of the breccia is generally fairly low, usually ranging from 0.1 to 0.5.

In 2006, East West Resource Corporation obtained a Re-Os date on a molybdenite mineral separate from the matrix of the breccia. The analyses were done using negative thermal ion mass spectrometry on purified Re and Os separates. The results yielded an age of 2692 ±12 Ma; this is the only age constraint on brecciation available. No age dates are available on rocks mapped as shoshonitic volcanic rocks (unit 11 on Figure 3.4); however, the volcanic rocks just north of these (units 2 and 4 on Figure 3.4) have been dated at 2719.9 ±1.1 Ma (Hart and Metsaranta, 2009).

3.3 Previous Work and Mineral Exploration

The Shebandowan area has a rich history of mineral exploration beginning in 1871 with the first discovery of gold in northwestern Ontario near Moss Lake (Hodgekinson, 1968). Since this discovery, numerous prospects and occurrences have been explored for a variety of base and precious metals, including three deposits that made it to the production stage (Table 3.1). Despite the interest in the area, poor access kept prospectors from exploring the Hamlin Lake area until the mid 1950s.

Table 3.1 – Past mining operations in the Shebandowan area.

Mine	Resources	Operation	References
INCO Shebandowan Mine	Cu-Ni-PGE, 8.7M tonnes @ 2.07% Ni, 1.00% Cu and 3.0 g/tonne PGM+Au	1972-1998	Lavigne *et al*, 1990, Osmani, 1997
Huronian Mine	29,948 ounces gold, 172,376 ounces silver	1884-1885, 1932-1936 and 1942	Hodgkinson, 1968, Harris, 1970
North Coldstream Mine	VMS, 1,968,356 lbs copper, 6,224 ounces gold, 139,505 ounces of silver	1903, 1906, 1916-1917, 1957-1958 and 1960-1964	Hodgkinson, 1968, Giblin, 1964

In the summer of 1956, prospector Ray Smith and his partner Red Sanderson discovered copper mineralization near the northwest shore of Hamlin Lake. Later that year Noranda Mines and Prospector Airways optioned 31 claims, and spurred a half century of exploration into motion (Harris, 1970). For 20 years following this initial discovery several companies have since optioned the Hamlin Lake claims and advanced exploration through several stages of geophysics, geochemistry and diamond drilling. By the 1980s several new geological maps of the area had been published and more powerful geophysical methods were available. Kennco Explorations and later, Grand Portage Resources put these to use to target new areas and further develop the existing occurrences, but still nothing was found to warrant a mine.

Renewed interest in the property in 2004 was prompted with the recognition of similarities between Hamlin Lake mineralization and some of the global IOCG deposits. This most recent exploration was undertaken by Rainy Mountain Royalty Corporation who later formed a joint venture agreement with Xstrata Copper. Since 2004, 67 drill holes were completed with a strong emphasis on defining mineralization in the pink breccia. No NI-43-101 deposit has yet been defined, but the IOCG model provides a good foundation for further exploration.

Chapter 4 – Alteration Paragenesis

4.1 Introduction

Fluids in any hydrothermal or magmatic-hydrothermal deposit are driven by pressure and temperature gradients. As these fluids progress they interact with the rock, altering the chemistry of the rock in a manner that is indicative of the fluids' characteristics. Where magmatic fluids are dominant (e.g., porphyry and skarn deposits), a systematic spatial zoning of alteration styles can sometimes be mapped and used to understand fluid movement and evolution. IOCG deposits can also be zoned in this way, although it may be difficult to appreciate due to extensive textural overprinting and recrystallization (Corriveau *et al.*, 2010). Zoning becomes more apparent on a regional to deposit scale, where early high temperature sodic to calcic-ferroan alteration dominates regionally grading to lower temperature potassic-ferroan and associated breccia system that characterizes many of the larger classic IOCG deposits around the world (Corriveau *et al.*, 2010).

Observations from the field and in drill core suggest that alteration at Hamlin Lake took place before, during and after brecciation. Hydrothermal mineral assemblages make up the matrix to the breccia, forming masses of mineral precipitate and veins. Wall rock and breccia clasts are pervasively altered with occasional vein style alteration. Several key stages of alteration can be mapped through time using mineral relationships and textural evidence (e.g., cross-cutting relationships and replacement). These stages

have distinct characteristics and are indicative of the fluid conditions at the time of alteration.

4.2 Spatial Zoning

Often in an environment that has been altered by magmatic fluids spatial zoning is apparent. This can be seen in skarn (Meinert *et al.*, 2005) and porphyry (Seedorff *et al.*, 2005) systems with an outward zoning of alteration styles centered on a magmatic heat source. As mentioned above, it is not uncommon for IOCG deposits to lack this spatial zoning at the scale of an ore deposit. Regionally, however, there can often be a large scale calcic to sodic signature that can extend for 10s of kilometers (Oliver *et al.*, 2004).

The drill holes examined for the purposes of this study are concentrated on the brecciated rocks most proximal to the ore. In order to define zones of similar alteration, a systematic approach to logging the alteration was needed. Drill holes were divided into 10 meter intervals over which the intensities of common alteration minerals or mineral assemblages were ranked semi-quantitatively on a scale from 0 to 3, with 0 being absent, 1 being weak, 2 being moderate and 3 being intense. Other attributes that could be measured quantitatively included the magnetic susceptibility of the rocks and the assay values for Cu, Ag, Au and Mo. Where available, these data were averaged over the same 10 meter intervals. These logs are presented in Appendix B.

4.2.1 Regional sodic alteration

Regional scale sodic alteration at the Hamlin Lake occurrence is dominated by pervasive albitisation. This alteration has been noted in outcrops, and reportedly extends laterally at least 10 kilometers from the deposit, following the regional northeast-southwest trend (M. Keogh, pers. comm.). Despite its extensive signature along strike, albitisation diminishes rapidly along a northwest traverse, and becomes weak and patchy within a few hundred meters of its highest intensity. The timing and significance of albitisation will be discussed below.

4.2.2 Proximal alteration

The IOCG breccia is host to a variety of alteration styles with textural evidence for multiple fluids or generations of fluids. Any attempt to define zonation within the alteration on a deposit scale quickly proved to be problematic. The nature of the problem can be broken down into three issues: (1) minerals that commonly define zones of alteration are very similar in hand specimen, (2) some minerals overlap between alteration styles, and (3) the possibility that no spatial zonation exists.

The first issue involves the simple fact that fine-grained mineral assemblages of fundamentally different chemistries may appear similar in hand specimen. Fine grained hematite staining of quartz is easily confused with fine grained potassium feldspar alteration or pink albitisation. These three different mineralogies represent iron enrichment, potassium enrichment, and sodium enrichment, respectively, but all three

appear pale pinkish-red in hand specimen. The issue can be further complicated by the fact that potassium feldspar alteration is often accompanied by hematization, producing a full spectrum of pink shades that need to be calibrated to the eye. Other authors have resolved this issue using a staining technique that highlights potassium feldspars (Landry, 2006; Corriveau *et al.*, 2010).

Staining rock slabs or thin sections with sodium cobaltinitrite is a common method in petrology used to distinguish potassium feldspars from plagioclase. The method of Hutchison (1974) was used in the current study on six polished slabs with varying shades of pink alteration, with the aim of calibrating the various shades of pink. In the method potassium feldspars react with the sodium cobaltinitrite and form an insoluble yellow precipitate that stains the potassium feldspars yellow. Of the six slabs that were stained (Figure 4.1), two showed significant potassium feldspar. A quick comparison between the unstained slabs and the stained slabs indicates that the potassium feldspars are a similar shade of pink to the hematization, and are often masked by the hematization.

The second issue involves overlapping of alteration stages in space. Iron-bearing minerals are so common to IOCG alteration that minerals such as magnetite, hematite, chlorite and biotite are accessory minerals in multiple stages of alteration, and it is not uncommon for these minerals to overprint one another over time. In some IOCG districts, where high temperature assemblages of magnetite and apatite dominate the ore (iron-oxide apatite deposits), proximal iron enrichment is considered to be the discharge site for iron leached during regional albitisation (Oliver *et al.*, 2004; Edfelt *et al.*, 2005). This process is likely to be the cause of iron enrichment in the lower temperature settings

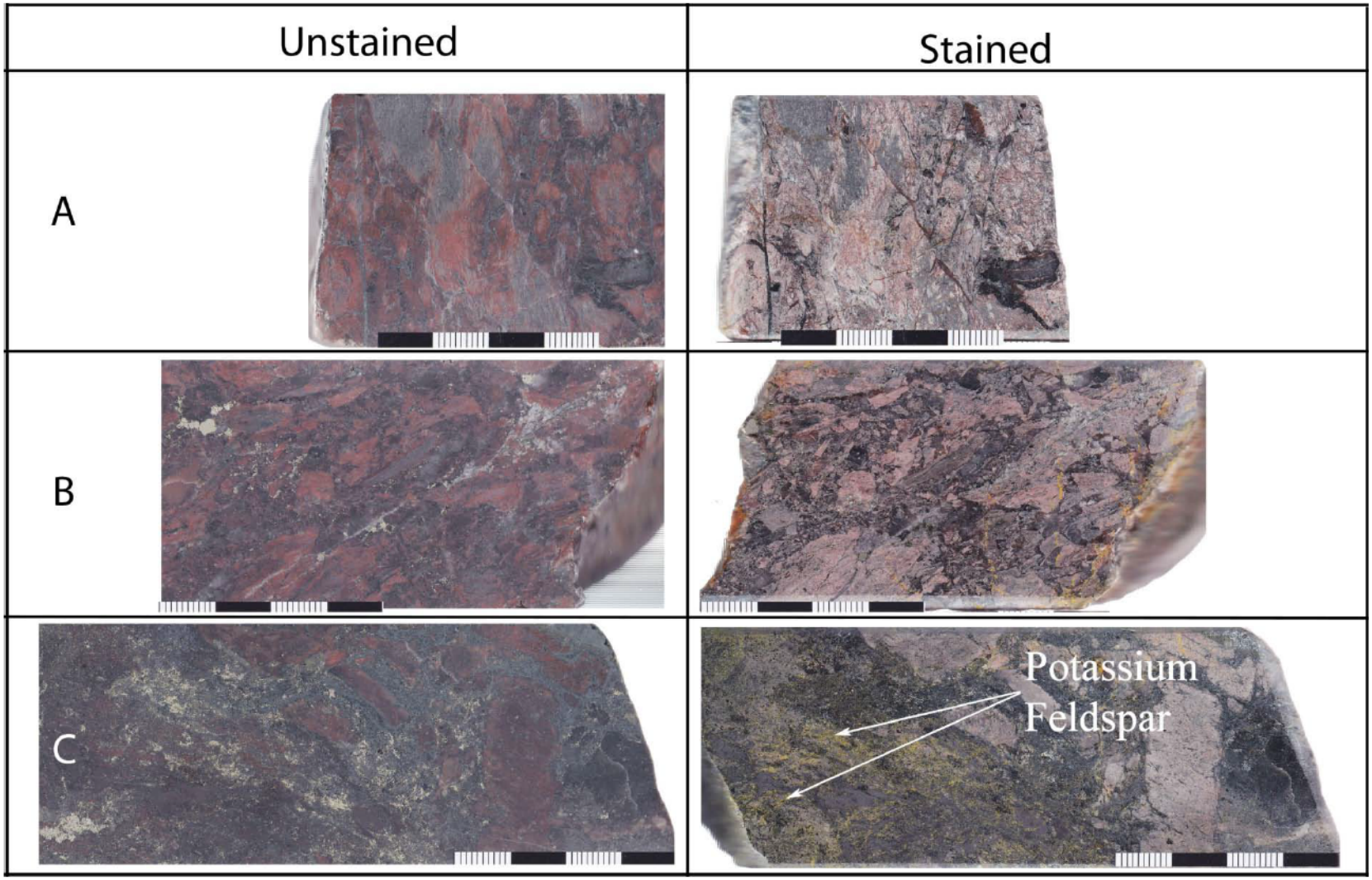

Figure 4.1a – Six polished slabs with varying shades of pink alteration stained with sodium cobaltinitrite. A.) HAM-63-11, B.) HAM-63-12, C.) HAM-63-13.

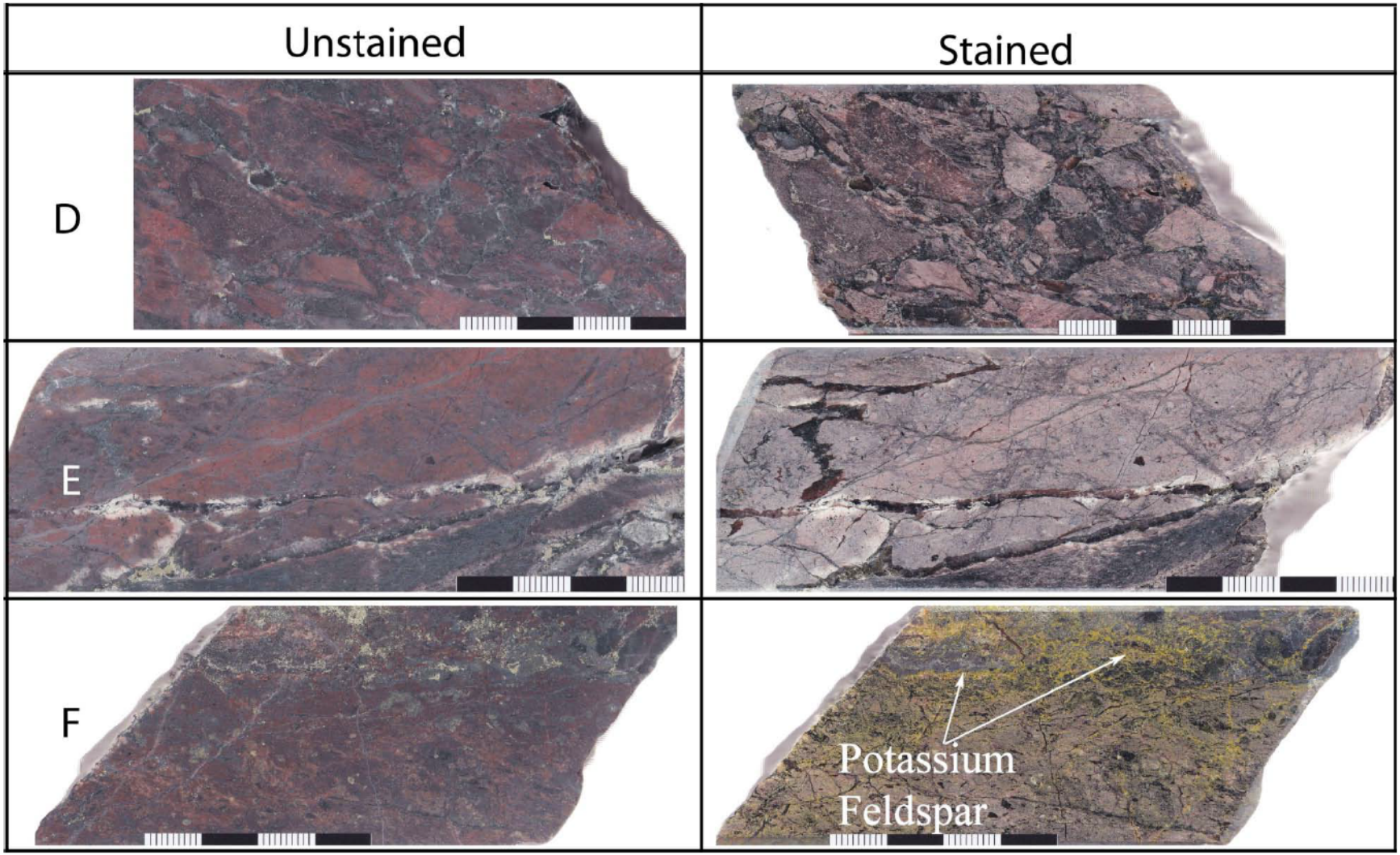

Figure 4.1a – Six polished slabs with varying shades of pink alteration stained with sodium cobaltinitrite. D.) HAM-64-05, E.) HAM-64-06, F.) HAM-64-07.

well, but iron can be remobilized during later stages of alteration. At Hamlin Lake, iron bearing minerals are easy to identify and map, but multiple stages of alteration redistribute these minerals through time. Textural evidence in thin section suggests that magnetite is a product of multiple stages of alteration, ranging from early breccia formation to ore deposition. The modern configuration of iron minerals is sporadic and defines no apparent zoning, except as regional scale iron enrichment proximal to ore.

The third issue involves the possibility that the Hamlin Lake occurrence is an unzoned deposit. Such deposits have no zoned chemical traits aside from the regional sodic or calcic alteration and proximal iron enrichment. To test this, the mineral epidote was used because it is easily identified in drill core and defines a single event of strong calcic enrichment. The intensity was mapped at a 10 meter resolution in each of the 22 holes across the deposit. The resulting model (one section is shown in Figure 4.2, see Appendix B for additional sections and plan map) indicates that calcic enrichment is distributed at irregular intervals throughout the breccia and is not a continuous zone.

There is still a possibility that the distribution of the drill holes themselves is too sparse, and the resolution of mineral mapping is too high, but mapping minerals on a resolution larger than 10 meters results in too much loss of detail. Attempts to define a model for spatial zoning on a deposit scale were abandoned. It should be noted that very little attention was paid to the vuggy quartz alteration during this study, and mapping out the distribution of this unit may prove worthwhile. This unit will be discussed in more detail below.

4.3 Paragenesis

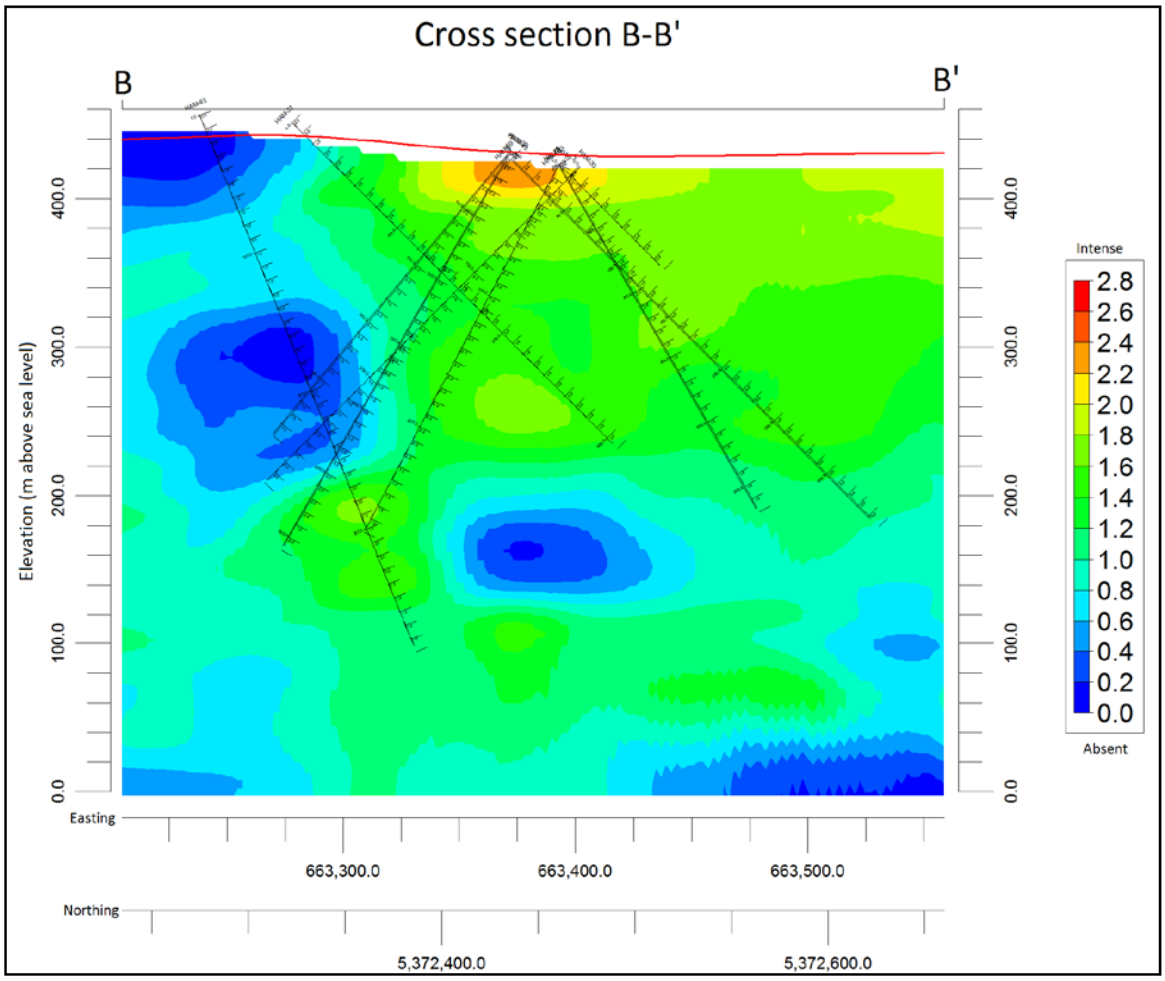

Figure 4.2 – Cross section showing the intensity of epidote alteration across the central part of the mineralized zone.

Producing a model for spatial zoning in the Hamlin Lake IOCG occurrence proved to be problematic. One of the reasons for this is the overprinting of proximal alteration styles through time. By this reasoning, a study of the textural relationships between alteration styles could yield a much more meaningful model for the proximal alteration. Gangue and ore minerals were examined in hand specimen and thin section, and textures were documented photographically. Scanning electron microscope (SEM)

and laser ablation inductively coupled plasma mass spectroscopy (LA-ICP-MS) are used to determine mineral formulae and chemistries. Six distinct styles of alteration are noted in this paragenetic study; however, due to the complexity of the system, more may be present. The six discussed here are: (1) early regional sodic, (2) early proximal potassic-iron, (3) calcic, (4) late mineralizing potassic, (5) carbonate, and (6) silicic.

4.3.1 Early sodic alteration

Early sodic alteration at Hamlin Lake is a regional style of alteration that occurred before the brecciation. The best preserved examples of the regional sodic alteration are distal to the mineralization; however, it is often preserved within volcanic clasts of the breccia (Figure 4.3A). Defining the regional extent of this alteration is beyond the scope of the mapping project; however, second hand descriptions of regional alteration (M. Keogh, pers. comm.) report that sodic alteration extends laterally up to 10km from the occurrence. In hand specimen regional sodic alteration is described as having a pale pink hue on weathered surface (Figure 4.3B).

The pristine examples of sodic alteration are found far from the proximal alteration; however, this is not to say that sodic alteration cannot be seen in the proximal breccia. Polished thin sections of clasts from within the breccia were examined and appear to consist of fine grained (~10μm) anhedral feldspars. SEM-EDS analyses of these areas show that feldspars are albitic with the end member composition $NaAlSi_3O_8$, with undetectable potassium and calcium. The presence of quartz phenocrysts in some of these volcanic clasts suggests a dacitic or rhyolitic composition, and alkalic feldspars

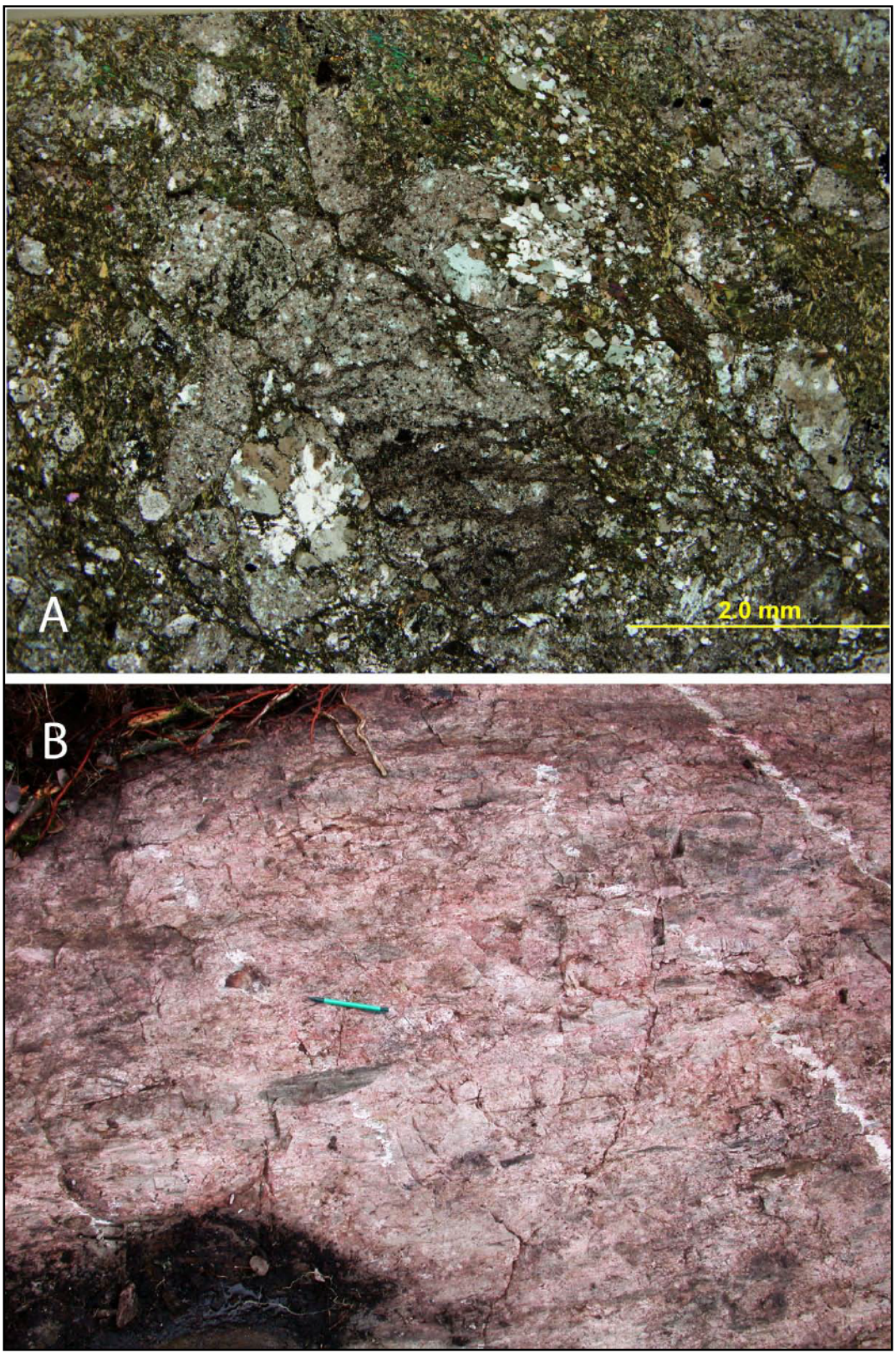

Figure 4.3 – A.) Photomicrograph of an albitized clast of volcanics in a matrix of biotite, B.) Pink weathering in an outcrop caused by albitisation.

could be either primary or secondary. The purity of the albite tends to suggest a hydrothermal origin, since plagioclase of volcanic origin is typically a solid solution between albite and anorthite and is rarely pure albite. Albite grains appear as a pale pink in hand specimen; however, this colour may be due to iron staining from later styles of alteration. Some of the albitized clasts display only a pink envelope on the edges of the clasts where it is in contact with hydrothermal matrix. Quartz is less abundant in the albitized groundmass of felsic volcanic rocks than one might expect in a rhyolite or dacite.

Albite is also an abundant constituent in the altered gabbros and diorites intersected sporadically in drill holes. No thin sections of these rocks were analyzed with the SEM, but the crystals are euhedral and twinned, so the Michel-Lévy method can be applied. Plagioclase compositions determined using this method range from An5 to An8. Primary albite is a common constituent of dioritic intrusions; however, one would expect the composition of a primary plagioclase in gabbro to have a calcic composition (Streckeisen, 1974). It is likely that the albite in the gabbro is a product of the early sodic alteration, converting primary calcic plagioclase to sodic. The relict pyroxenes in the gabbro are sparse, and were likely altered to the assemblage biotite + magnetite, which are the dominant mafic minerals. Albites were often subject to later epidotization, possibly related to subsequent calcic alteration.

4.3.2 Early potassic-iron alteration

Potassic-iron alteration occurs at Hamlin Lake as assemblages of biotite and chlorite with minor magnetite. The early nature of this alteration makes it difficult to find pristine examples; however, the patchiness of the overprinting alteration resulted in small intervals (up to several meters) where this early alteration is largely preserved (Figure 4.4). Textures most commonly observed include infilling or replacement of breccia matrix and pervasive replacement.

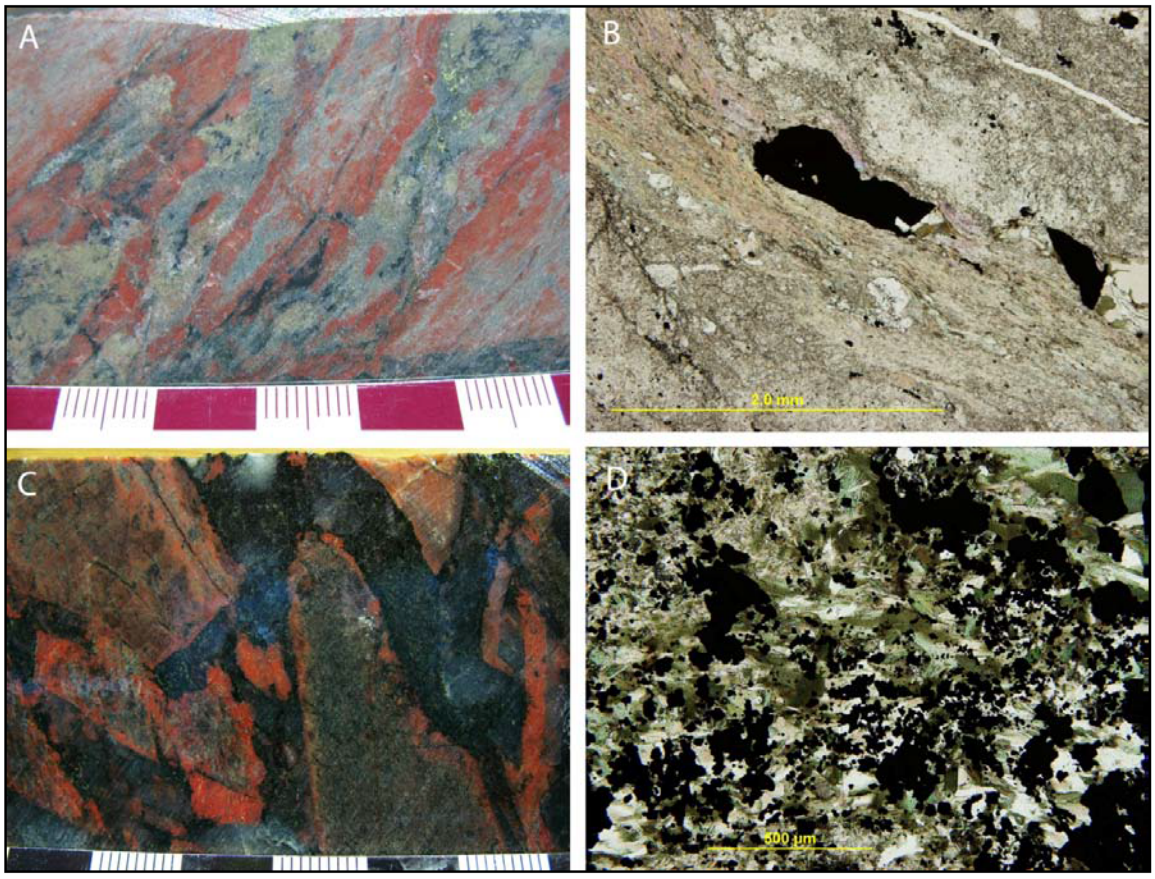

Figure 4.4 – A.) and B.) show sericite in hand specimen and thin section respectively, sericitization may be a result of breakdown of early biotite during late alteration, C.) shows the assemblage biotite + chlorite + magnetite as the matrix to the breccia. The red rims on the clasts are due to iron staining, and D.) shows biotite + chlorite with disseminated magnetite and pyrite; the pyrite may accompany the late chloritization. Scale bars in A.) and C.) have 1 cm intervals.

The alteration style affects the whole spectrum of rocks in the deposit. Massive rhyolites and their tuffaceous equivalents are altered pervasively with various assemblages commonly including sericite and hematite staining (Figure 4.4A and B). Assemblages that include sericite are difficult to time, since relationships with other styles of potassic alteration are absent. Sericitic alteration is a common feature of late alteration styles associated with chloritization and the pervasive sericite described here may be a late product of the breakdown of the early biotite. Breccias with clasts of fairly low BFD are frequently supported in a mixed rock flour-hydrothermal infill matrix of biotite + chlorite ± magnetite (Figure 4.4C and D). Clast angularity can be used to estimate the role of physical erosion of the clasts, with more angular clasts representing a lower portion of rock flour in the matrix. Examples of breccias with clasts of moderate to high BFD suggest that dissolution processes played a larger role in breccia formation, and these tend to have a replacive matrix of sericite.

The mineralogy of the potassic-iron alteration was identified with the help of the SEM. The analyses of a number of dark micas suggest a composition $K(Mg,Fe^{2+},Al)_3(Si,Al)_4O_{10}(OH)_2$ that is consistent with Bailey's (1984) classification of biotite. Fe/(Fe+Mg) ratios range from 0.35 to 0.44, and while aluminum is not usually a large component of the octahedral sites it can occupy between 0.32 and 0.48 atoms per formula unit (APFU). The A site is almost entirely potassium, but up to 0.07 APFU may be vacant or filled with Na or Ca that fall below detection limits in the analyses. Sericite was also analyzed and yields the composition of muscovite, $K(Al,Fe^{3+},Mg)_2(Si,Al)_4O_{10}(OH)_2$. Potassium feldspars were not identified as part of this

stage of alteration; they were detected with neither SEM-EDS nor with sodium cobaltinitrite staining.

4.3.3 Calcic(-iron) alteration

The calcic(-iron) alteration stage is comprised of epidote, chlorite, sphene, apatite, magnetite and minor hornblende confined within the matrix of the breccia. The alteration style encompasses the entire breccia body, cross-cutting and often replacing the earlier potassic-iron assemblages.

Epidote alteration is by far the most extensive example of calcic alteration (Figure 4.5A-H). Where this alteration is most intense it can make up 10% to 15% of the total rock by volume. Epidote forms clumpy aggregates that partially replace earlier calcic minerals (usually calcite). Epidote is usually characteristic enough to identify in hand specimen by its pistachio green colour (Figure 4.5A, B), but several polished thin sections were made to verify it optically and with SEM (Figure 4.5C-F). SEM analysis revealed that epidote is of the end-member composition $Ca_2Al_2Fe^{3+}(SiO_4)(Si_2O_7)O(OH)$. Optical examination of epidote usually revealed an aggregate texture (Figure 4.5C, D and F); however, some subhedral to euhedral crystals were observed as well. The anhedral aggregates and subhedral crystals have nearly identical compositions, despite slightly different interference colors under crossed polarized light. Figure 4.5E shows both euhedral and anhedral epidote in association with chlorite and sphene replacing earlier calcite. Chlorite is also abundant in rocks

subject to the calcic(-iron) stage of alteration; however, it may be again due to a later stage of metasomatism as discussed below.

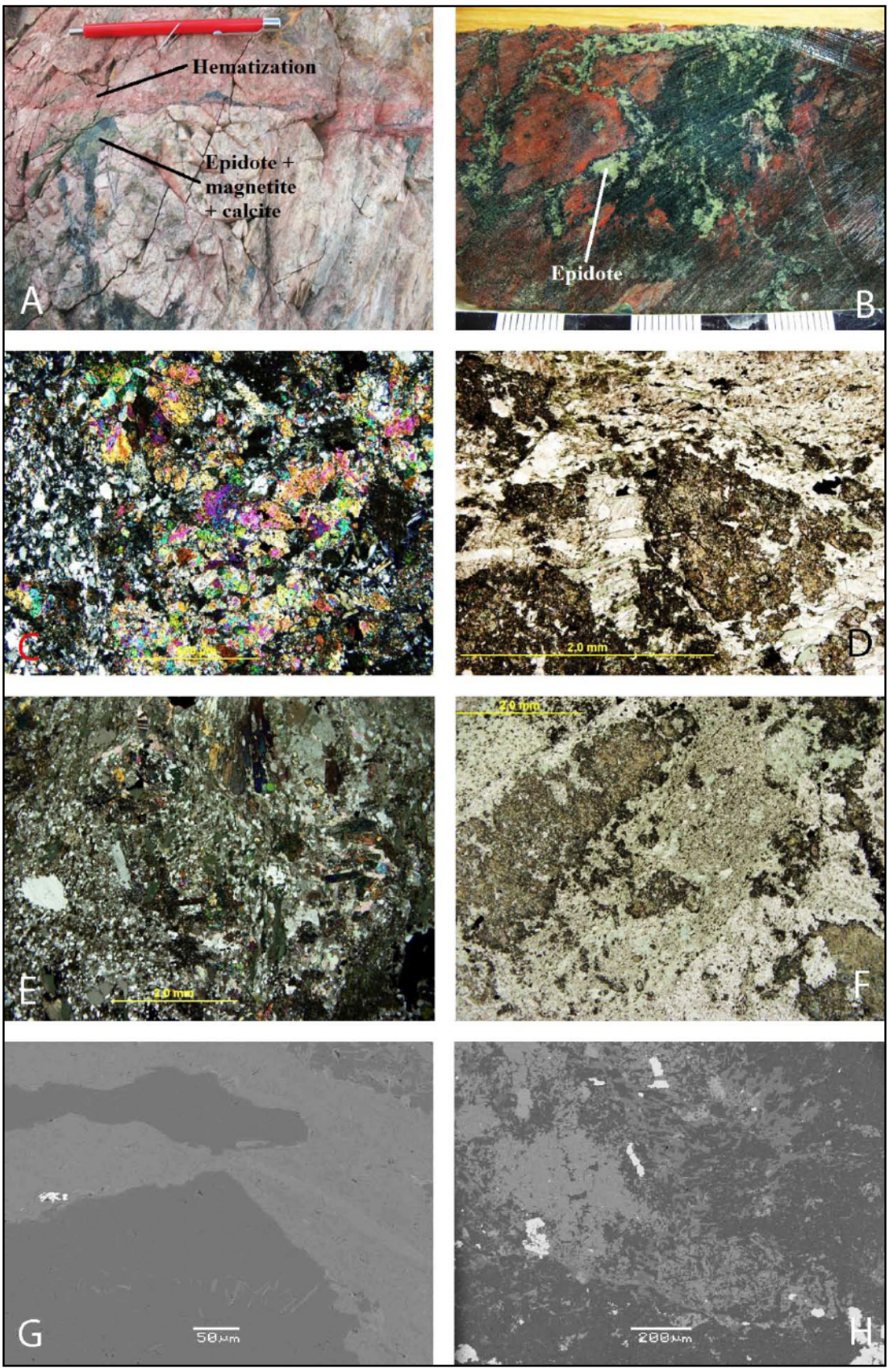
Hematization
Epidote +
magnetite
+ calcite
A
Epidote
B
C
2,0 mm
D
2,0 mm
E
2,0 mm
F
50µm
G
200µm
H

Figure 4.5 – (*previous page*) Varieties of calcic alteration A.) Epidote in an outcrop, B.) Epidote overprinting biotite in drill core, C.) Aggregate of epidote in thin section, D.) Aggregate of epidote and sphene overprinting calcite in thin section, E.) Aggregates of epidote with euhedral crystals of epidote in thin section, F.) Aggregate of epidote and sphene in thin section, G.) BSE image of monazite-Ce (light grey) in epidote (medium grey), H.) BSE image of epidote (medium grey) and sphene (light grey).

Sulphide mineralization is largely absent from this stage of alteration; however, there are several minerals of economic interest. Phosphates of calcium (apatite, $Ca_5(PO_4)_3(OH, F, Cl)$ and light-rare earth elements (monazite, $(Ce,La)PO_4$, Figure 4.5G) were detected in trace amounts with SEM analyses. One occurrence of the epidote group mineral allanite with Ce and La was also analyzed $(Ce, La)_2(Al, Fe^{3+})_3(SiO_4)_3(OH)$.

4.3.4 Late potassic alteration and IOCG mineralization

Late potassic alteration was responsible for the main stage IOCG style mineralization. Ore mineralogy observed in this stage is dominated by magnetite-chalcopyrite(-pyrite) with trace amounts of silver and bismuth tellurides (hessite and tellurobismuthite), sulphides (argentite and bismuthinite) and, more rarely, selenides (naumannite and guanajuatite). Silver, bismuth and copper in their native forms were also detected; however, they appear to postdate this stage of mineralization. Mineralization in this stage is characterized by a variety of styles ranging from veins to disseminations to replacement. Ore deposition is accompanied by potassium silicate gangue assemblages dominated by potassium feldspar.

Chalcopyrite and magnetite (Figure 4.6A-G) are the most abundant ore minerals present in the rocks subject to IOCG style potassic alteration. Although ore stage magnetite does not always appear to be assembled with chalcopyrite in hand specimen,

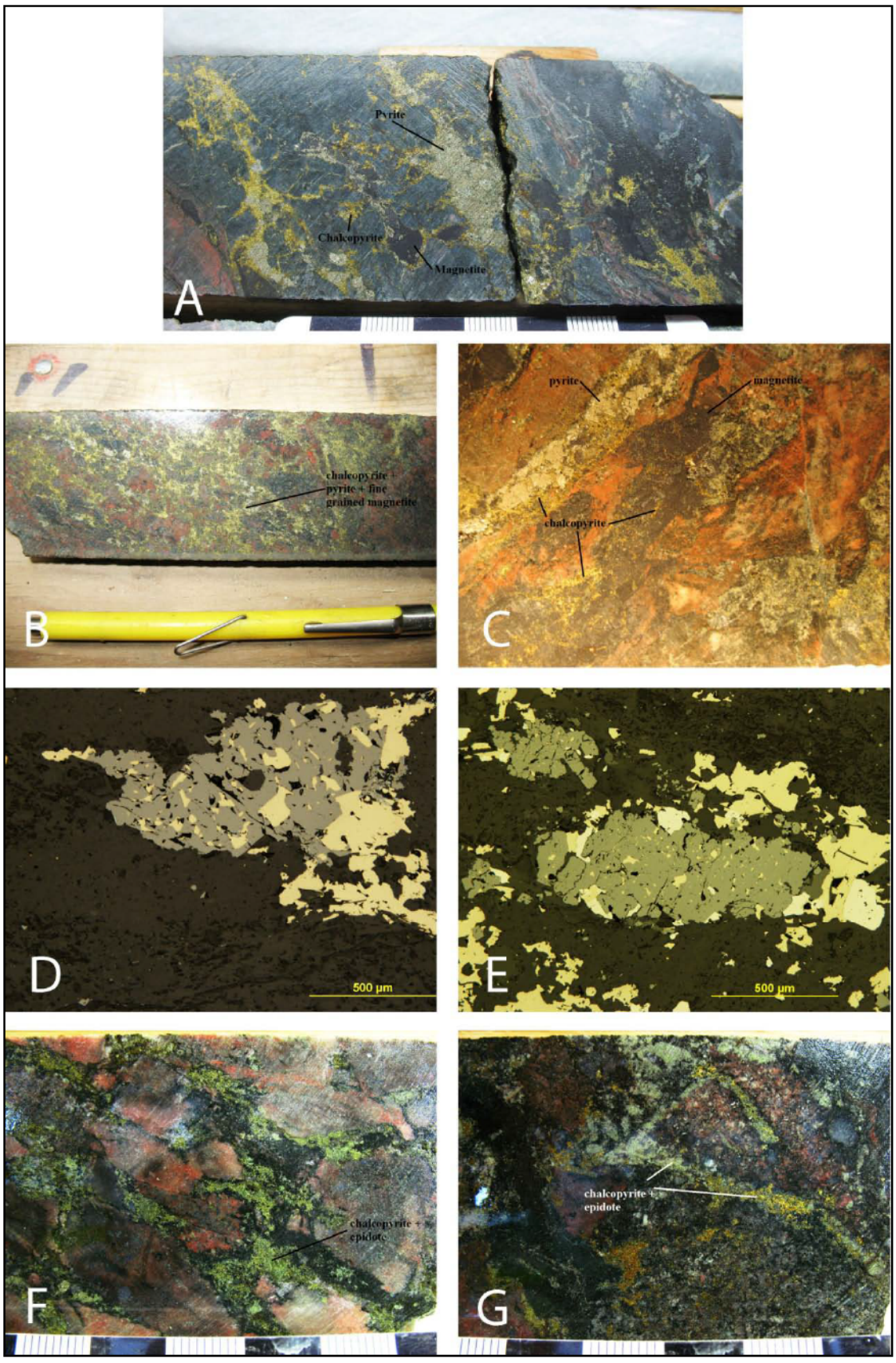
Pyrite
Chalcopyrite
Magnetite
A
chalcopyrite + pyrite + fine grained magnetite
B
pyrite
magnetite
chalcopyrite
C
500 µm
D
500 µm
E
chalcopyrite + epidote
F
chalcopyrite + epidote
G

Figure 4.6 – (*previous page*) A., B. and C.) Typical IOCG style mineralization with pyrite and chalcopyrite assembled with magnetite, D. and E.) Small inclusions of chalcopyrite within masses of magnetite from the IOCG mineralizing event, F. and G.) Chalcopyrite replacing epidote from earlier calcic alteration.

polished section analyses usually show small micrometer sized chalcopyrite inclusions within the magnetite (Figure 4.6D and E). In many of the highest grade chalcopyrite occurrences magnetite appears to be thermodynamically isolated from the chalcopyrite, although magnetite is never far off. These examples may be the result of a later mineralizing event, which will be discussed below. Pyrite is often present within the IOCG mineralization as subhedral to euhedral crystals assembled with chalcopyrite or magnetite. Modal abundance of sulphides is generally around 1 to 5% of the total rock volume; however, it can reach as high as 40% over small intervals (Figure 4.6A). Magnetite normally comprises 3 to 10% of the rock and can reach 30% locally.

Chalcopyrite is the most common ore of copper across the deposit, and it occurs during several of the later stages of alteration. Generations of chalcopyrite are differentiated based on mineral assemblages, and in the potassic stage chalcopyrite commonly occurs in equilibrium with magnetite and potassium silicates such as biotite and potassium feldspar. Aggregates of epidote-chlorite from the calcic(-iron) stage of alteration are often partially replaced by assemblages of chalcopyrite and magnetite (Figure 4.6F and G), and accompanied by slightly later carbonate alteration. This relationship introduces itself in hand specimen and a closer inspection through thin

Table 4.1 – A) Laser ablation data from sulphides, B) Laser ablation data from magnetite. All values are in ppm unless otherwise indicated.

A) **Sulphides**

Mineral	Sample	27Al	29Si	45Sc	52Cr	55Mn	59Co	60Ni	64Zn	65Cu	75As	82Se	107Ag	111Cd	115In	118Sn	121Sb	182W	197Au	205Tl	206Pb	209Bi	232Th	238U
cpy	65-01	24.34	246.72	0.48	2.17	2.64	0.93	1.27	38.82	32.93%	1.18	215.21	69.86	5.31	3.79	0.34	0.07	0.01	0.00	0.05	2.91	4.85	0.02	0.02
cpy	63-05	26.26	474.72	0.25	1.63	0.24	0.15	0.11	13.51	34.29%	0.57	265.37	23.90	2.53	0.31	0.11	0.02	0.00	0.00	0.10	1.13	2.86	0.02	0.50
cpy	64-03	1.67	255.19	0.28	0.90	0.27	0.23	0.06	54.75	29.66%	0.63	176.24	44.19	5.98	3.42	0.08	0.00	0.00	0.00	0.01	0.94	1.76	0.00	0.00
cpy	63-02	41.81	400.03	0.21	1.15	2.00	0.39	2.46	33.08	27.22%	0.85	70.02	18.50	0.81	1.55	0.04	0.11	0.03	0.00	0.14	6.25	28.39	0.00	0.07
cpy	63-04	0.00	409.75	0.25	1.22	0.24	0.97	1.40	25.84	28.65%	0.30	77.27	22.22	3.51	1.76	0.04	0.01	0.00	0.00	0.01	0.57	3.76	0.00	0.00
cpy	64-01	6.98	477.80	0.00	0.41	2.40	0.56	50.83	125.09	24.87%	0.00	105.64	104.40	6.96	0.29	0.13	0.34	0.00	0.02	0.22	9.88	21.57	0.01	0.11
cpy	NG07-01	24.30	273.13	0.22	0.75	9.17	0.43	7.52	74.85	32.32%	0.64	36.58	225.38	6.67	0.90	0.53	0.01	0.00	0.00	0.08	1.73	3.62	0.00	0.10
py	63-02	149.95	438.27	0.19	1.89	3.14	3124.16	430.21	23.27	3247.13	47.76	103.61	5.02	0.54	0.05	0.20	0.02	0.72	0.37	0.03	3.89	26.03	0.01	0.37
py	63-01	84.34	220.64	0.26	0.52	79.43	8.13	199.46	9.59	0.00	0.34	8.34	0.40	0.08	0.00	1.18	0.03	0.17	0.00	0.03	5.99	1.02	0.02	0.06
py	63-04	4.79	153.65	0.07	0.65	0.27	1907.97	549.80	18.63	29.38	16.88	43.20	0.20	0.04	0.00	0.01	0.00	0.00	0.00	0.00	0.44	2.64	0.01	0.20
py	64-01	2.31	82.27	0.05	0.53	0.31	470.87	65.63	11.50	57.85	130.40	52.91	0.11	0.02	0.00	0.00	0.02	0.00	0.00	0.00	0.52	2.71	0.00	0.11
py	NG07-01	83.01	111.80	0.02	0.23	1.69	3350.20	750.38	25.55	11.84	39.90	13.59	46.10	0.08	0.00	0.00	0.00	0.00	0.94	0.05	0.69	3.90	0.00	0.02

B) **Magnetite**

Mineral	Sample	24Mg	27Al	29Si	39K	45Sc	47Ti	51V	52Cr	55Mn	59Co	60Ni	64Zn	65Cu	75As	89Y	90Zr	93Nb	107Ag	121Sb	137Ba	208Pb	209Bi	232Th	238U
mt	HAM63-2	1296	3383	6120	1905	1.2	215.1	422.8	24.51	120.9	14.51	328.7	22.89	10.12	3.92	1.05	1.07	0.13	<dl	1.7	11.2	8.31	2.19	0.48	1.87
mt	HAM63-3	1642	2011	5216	1666	1.91	347.1	638.1	31.55	111.9	18.79	248.5	14.61	164.01	7.9	1.56	2.02	0.33	0.13	4.54	5.65	24.02	9.16	0.79	6.73
mt	HAM63-4	826.4	1167	3556	1098	0.6	151.6	611.2	8.83	151.6	8.93	180.9	10.35	59.86	3.07	0.32	0.53	1.46	0.03	1.3	4.39	6.33	2.78	0.18	2.4
mt	HAM63-5	2251	2704	6615	2047	0.6	221.4	919.4	3.7	169.15	34.39	124.1	11.23	1060	4.65	0.1	0.68	0.12	0.54	1.06	25.19	5.74	3.16	0.3	0.49
mt	HAM64-2	2002	2335	9162	706.4	8.52	336.8	336.2	106.8	152.4	38.16	226.5	18.62	4.6	1.68	1.76	0.13	0.08	0.01	1.14	5.95	0.81	0.35	0.02	0.13
mt	HAM64-3	850.7	971.1	4569	249	1.17	158.2	844.7	5.31	176.8	37.59	152.4	12.9	27.23	1.15	0.7	0.09	<dl	<dl	0.2	1.38	0.59	0.26	0.11	0.05
mt	HAM65-1	3099	3278	5735	1481	1.1	193.7	1081	17.86	170.6	36.2	198.5	18.3	158.7	2.97	0.15	0.47	1.55	0.06	2.82	6.66	8.15	3.43	0.09	3.48
mt	NG07-01	765.5	1301	2839	905.5	<dl	173	488.7	3.23	135.3	5.17	641.6	40.67	165.8	2.53	0.04	0.07	0.47	0.08	0.53	9.18	1.98	0.75	0.03	0.36

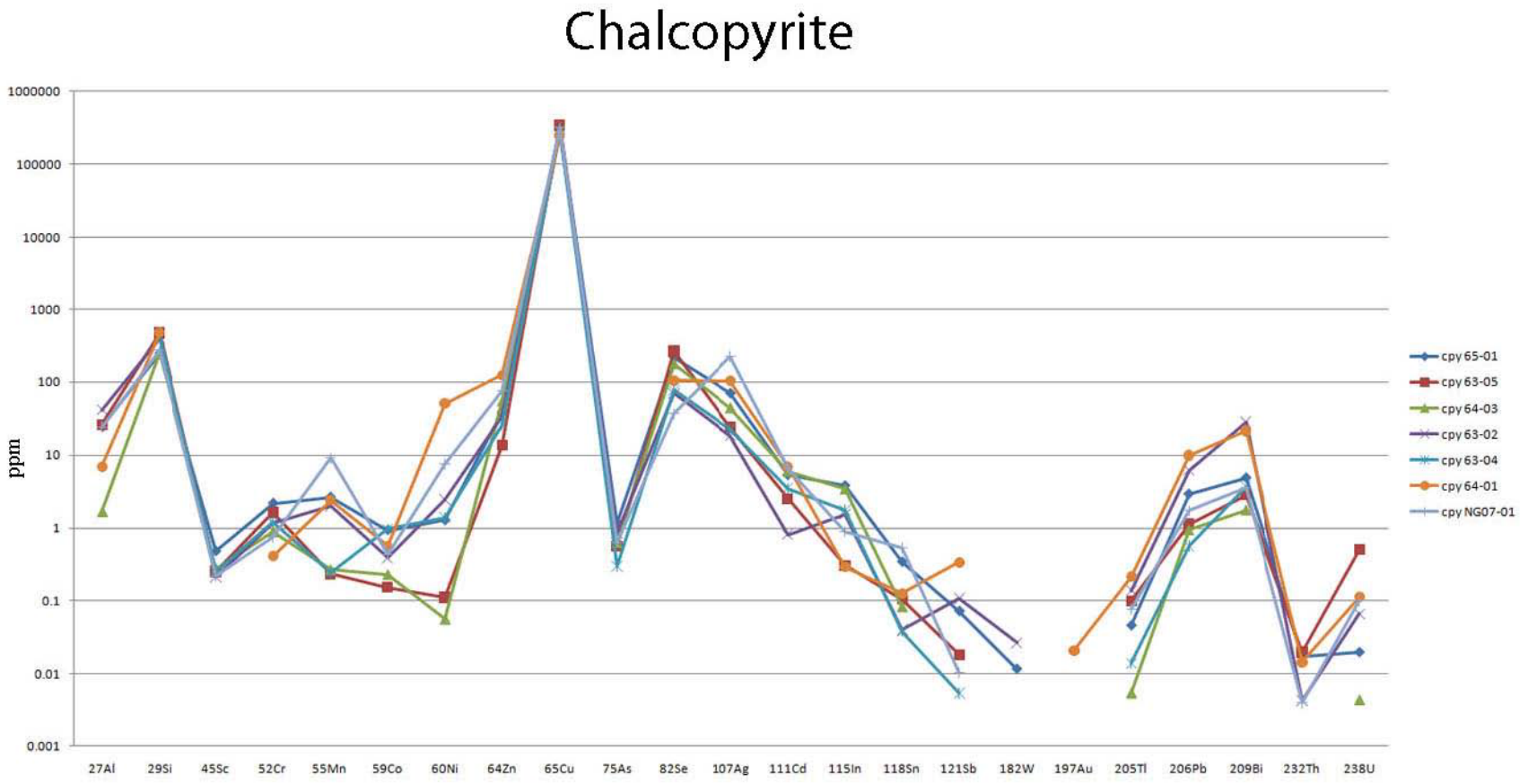

Figure 4.7a – Spider diagram for chalcopyrite from LA-ICP-MS data in Table 4.1.

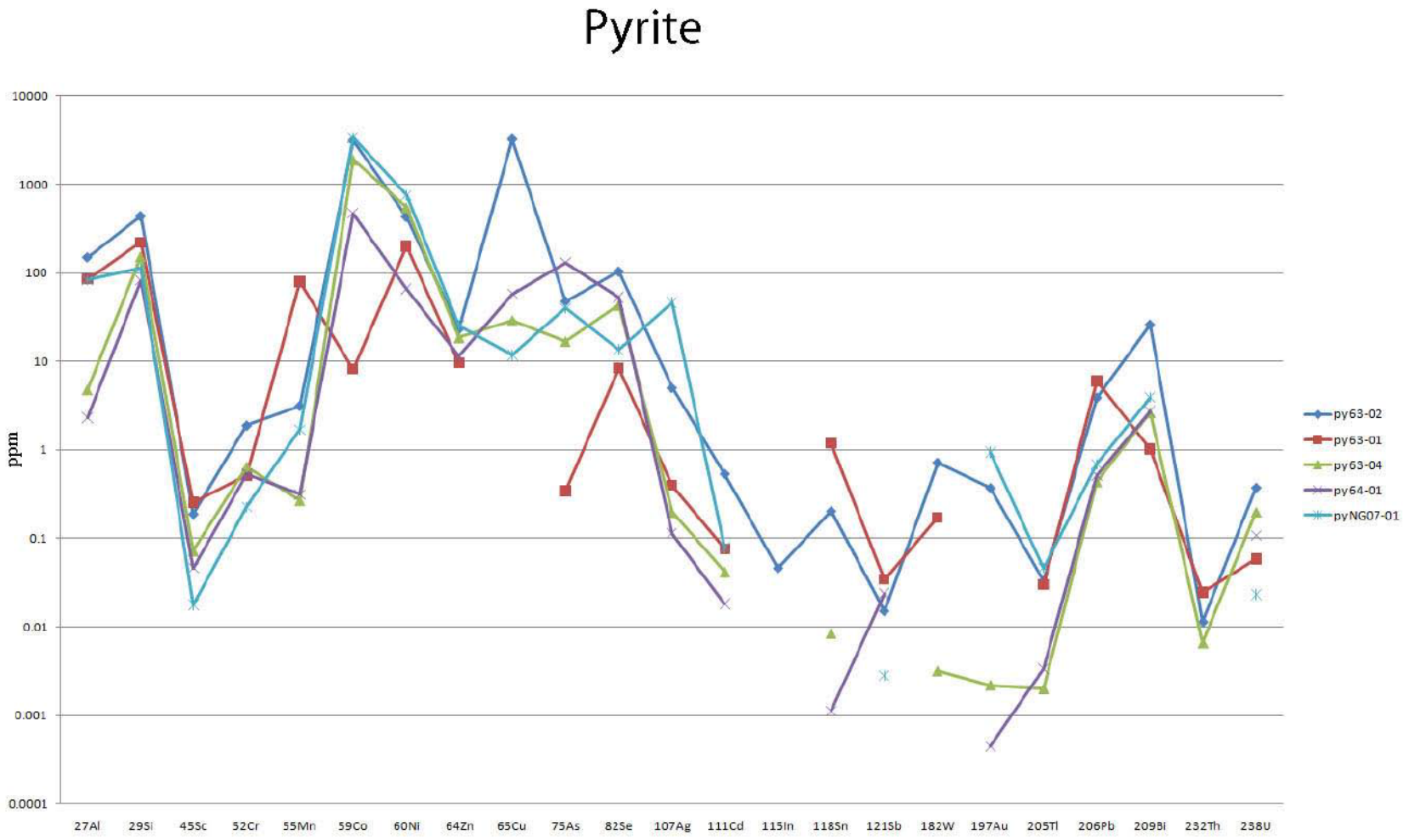

Figure 4.7b – Spider diagram for pyrite from LA-ICP-MS data in Table 4.1.

section petrography reveals that there are subhedral epidote crystals that are untouched by mineralization, whereas anhedral masses are replaced. These subhedral crystals are likely metamorphic and paragenetically later than the copper mineralization. LA-ICP-MS analyses of sulphides are summarized in Table 4.1, and spider diagrams of chalcopyrite and pyrite are presented in Figure 4.7. Se, Ag, Pb, and Bi are characteristically elevated in chalcopyrite, while pyrite has a more erratic trace element pattern with somewhat elevated Co, Ni, Pb, and Bi. Spikes in Si, Al, and Mn are likely related to small silicate inclusions, and are not indicative of enrichments in the crystal lattice of the sulphides.

Polished thin sections of the magnetite were analyzed and carefully documented, given the significance of iron oxides in IOCG deposits. Magnetite appears in reflected light as grey aggregates of subhedral to euhedral grains as well as anhedral masses. Occasionally magnetite displays an atypical texture where it forms as bent tabular aggregates (Figure 4.8A), which may be pseudomorphs of hematite called mushketovite (Williams, 2010b); however, the earlier hematite is never observed, so this relationship is

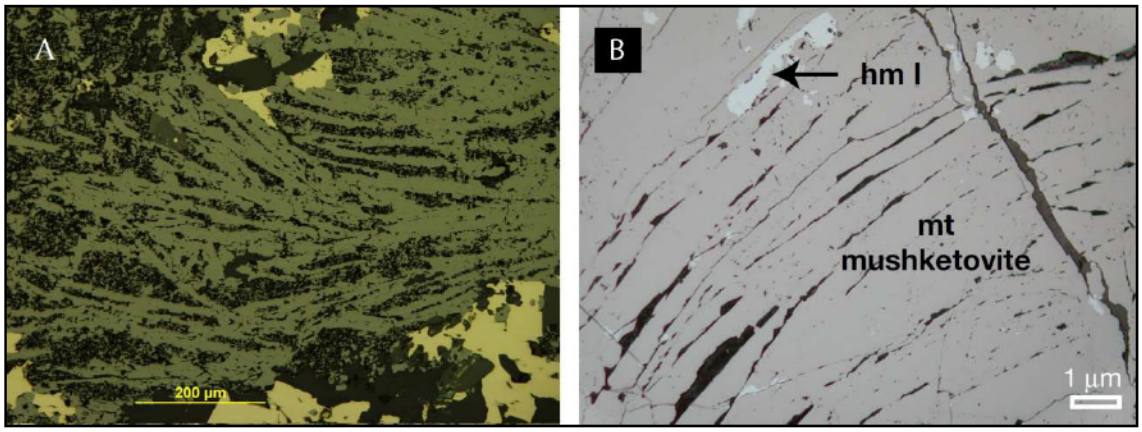

Figure 4.8 – A.) Possible mushketovite texture observed in IOCG stage magnetite from Hamlin Lake, and B.) Mushketovite from the Candelaria Mine (from Marschik and Fontbote, 2001).

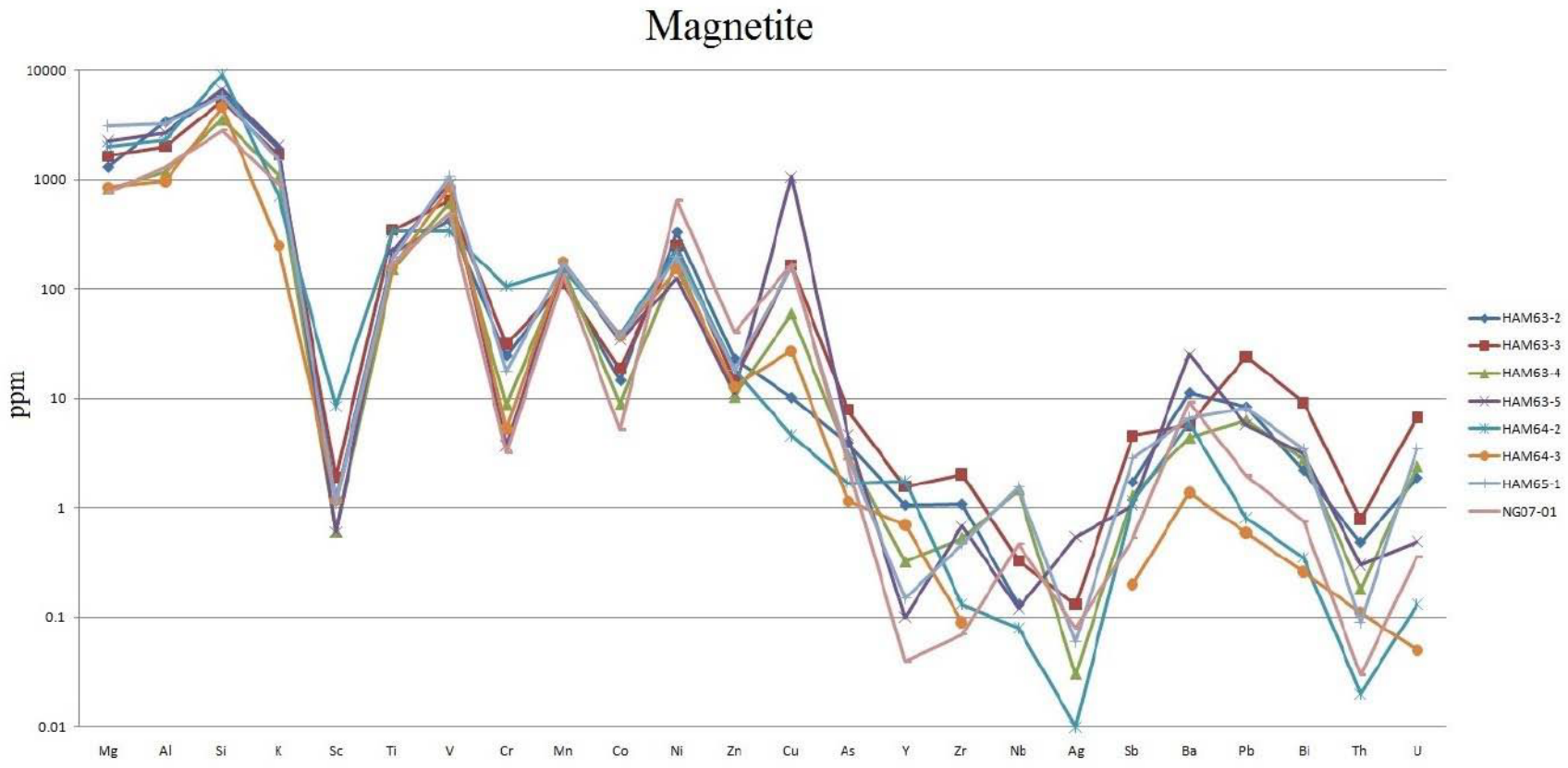

Figure 4.9 – Magnetite spider diagram from the data in Table 4.1.

difficult to prove. Larger masses of magnetite have trapped inclusions of chlorite, epidote and quartz from earlier stages of alteration. Masses of magnetite can be up to several centimeters in diameter, and often contain rounded intergrowths of chalcopyrite. LA-ICP-MS analyses of eight magnetite grains related to the mineralization across the deposit have detectable levels of Mg, Al, Si, K, Sc, Ti, V, Cr, Mn, Co, Ni, Zn, Cu, As, Y, Zr, Nb, Ag, Sb, Ba, Pb, Bi, Th and U. Of these elements Mg through to Zn display a consistent pattern that can be seen in a spider diagram (Figure 4.9). The other elements have highly variable abundances. The analyses are summarized in Table 4.1.

Two magnetite occurrences assembled with pyrrhotite and chlorite were also analyzed with LA-ICP-MS. These two occurrences (blue dots) plot well outside the grouping of IOCG related magnetite (red dots) on a discrimination diagram showing Ni/(Cr + Mn) versus Ti + V (Beaudoin and Dupuis, 2010; Figure 4.10A). The spider plots for these two samples also do not match the pattern observed for the magnetite seen with pyrite and chalcopyrite, and pyrrhotite mineralization is therefore taken to be unrelated to the IOCG mineralization. Wispy textures and banding seen in pyrrhotite (Figure 4.10B) bearing rocks suggest a possible sedimentary or volcanogenic origin, and the rocks are not discussed further here.

Silver and bismuth tellurides, sulphides and selenides are common accessory minerals and often occur as inclusions or intergrowths within chalcopyrite and pyrite (Figure 4.11A). These minerals appear as highly reflectant white or grey intergrowths in

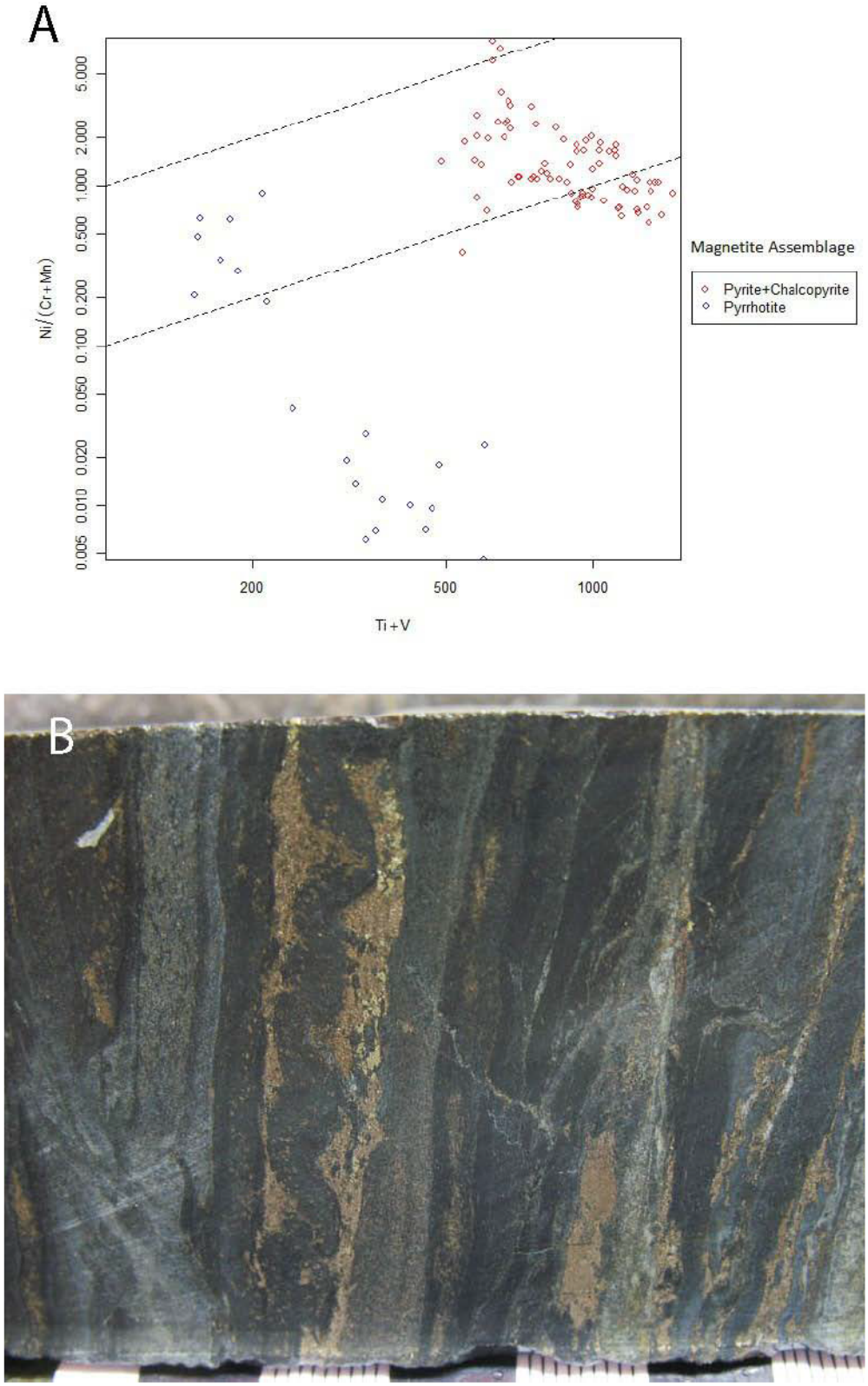

Figure 4.10 – A.) Magnetite discrimination diagram based off Beaudoin and Dupuis, 2010, B.) Wispy banded pyrrhotite from drill core, dark bands are magnetite and wispy brown mineral is pyrrhotite.

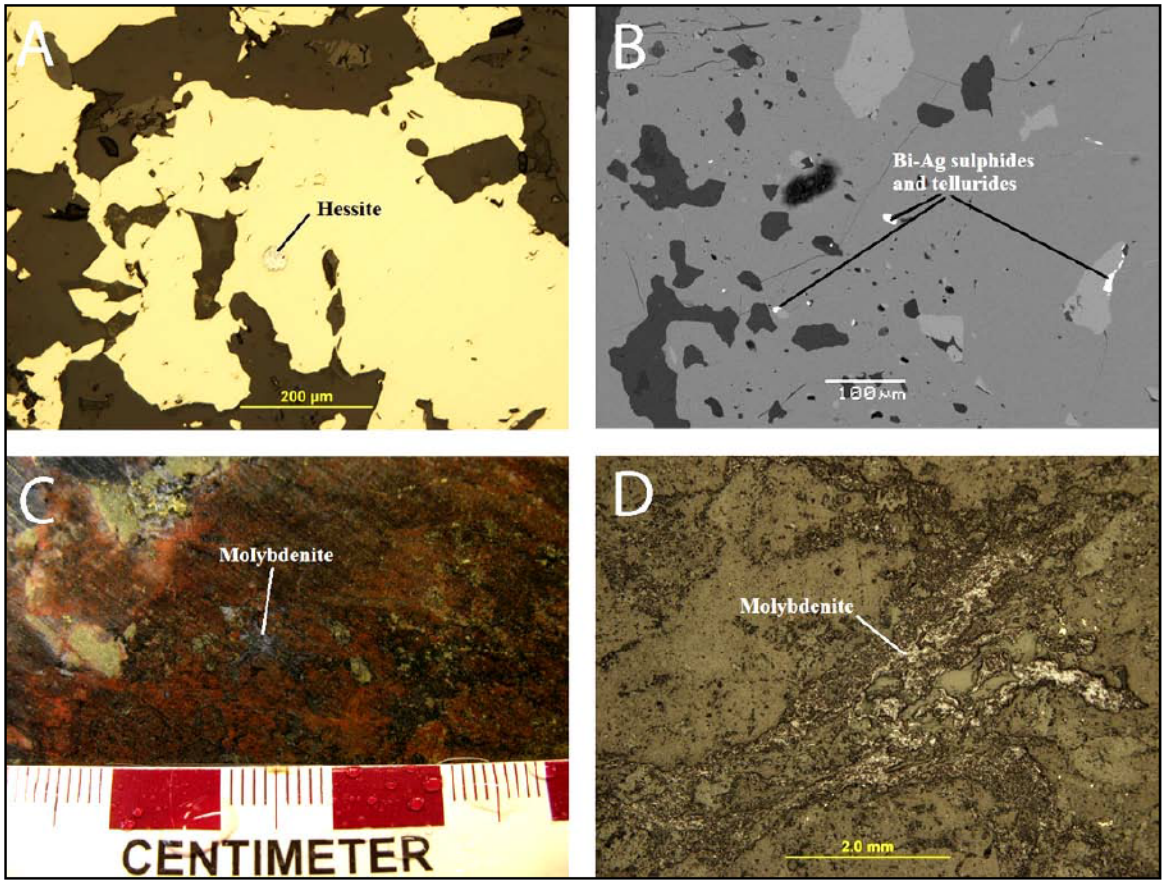

Figure 4.11 – A.) A round inclusion of hessite (Ag_2Te) in chalcopyrite, B.) High density solid solutions of Bi-Ag sulphides and tellurides in pyrite and chalcopyrite, C.) Silvery-blue molybdenite with biotite seen in drill core, and D.) Reflected light photomicrograph of molybdenite from C.

chalcopyrite and pyrite under reflected light; however, SEM-EDS analyses are required to differentiate between species. Back-scattered electron (BSE) images display grayscale images with varying shades of grey proportional to mineral density, and the dense silver and bismuth minerals are easily recognized (Figure 4.11B).

Molybdenite (Figure 4.11C) is another common ore mineral, and it is the primary source of molybdenum at Hamlin Lake. It is formed as small (up to 50µm) grey blades of moderate to high reflectance (Figure 4.11D). Molybdenite may occur with or without chalcopyrite, but usually appears with other potassic minerals that link it to the

mineralizing potassic alteration. Scheelite is occasionally present as an accessory phase with molybdenite; it was detected with the SEM as a calcium-tungstate; however, quantitative analyses are not included in Appendix C due to poor totals. SEM-EDS analyses of molybdenite were impossible to gather due to the nearly perfect overlap between the visible sulphur and molybdenum peaks.

Gangue mineralogy related to the mineralizing potassic alteration is typically dominated by biotite, muscovite and potassium feldspar. Identification of these minerals was aided by the use of thin sections and SEM-EDS, as well as sodium cobaltinitrite staining to emphasize potassium feldspars. Biotite and muscovite are fine- to medium-grained and exhibit vein and replacement textures throughout the matrix of the breccia. Potassium feldspar was difficult to differentiate from quartz in optical petrography due to its fine grain-size. BSE images were useful for differentiating fine-grained potassium feldspars from quartz based on the slightly higher mean atomic number of potassium feldspar. Veinlets that cut across earlier styles of alteration (e.g. epidote, Figure 4.12C) were commonly identified in this manner. Hand specimens with significant mineralization were also stained with sodium cobaltinitrite in order to establish a relationship between potassium feldspars and mineralization on a macroscopic scale. This study revealed a strong correlation between stable chalcopyrite + magnetite mineralization and potassium feldspar veining (Figure 4.12 A and B). Samples stained where magnetite and chalcopyrite occur separately (i.e. not part of the same assemblage) have very little to no potassium feldspar veining, and mineralization is linked to a later stage of mineralization, discussed below.

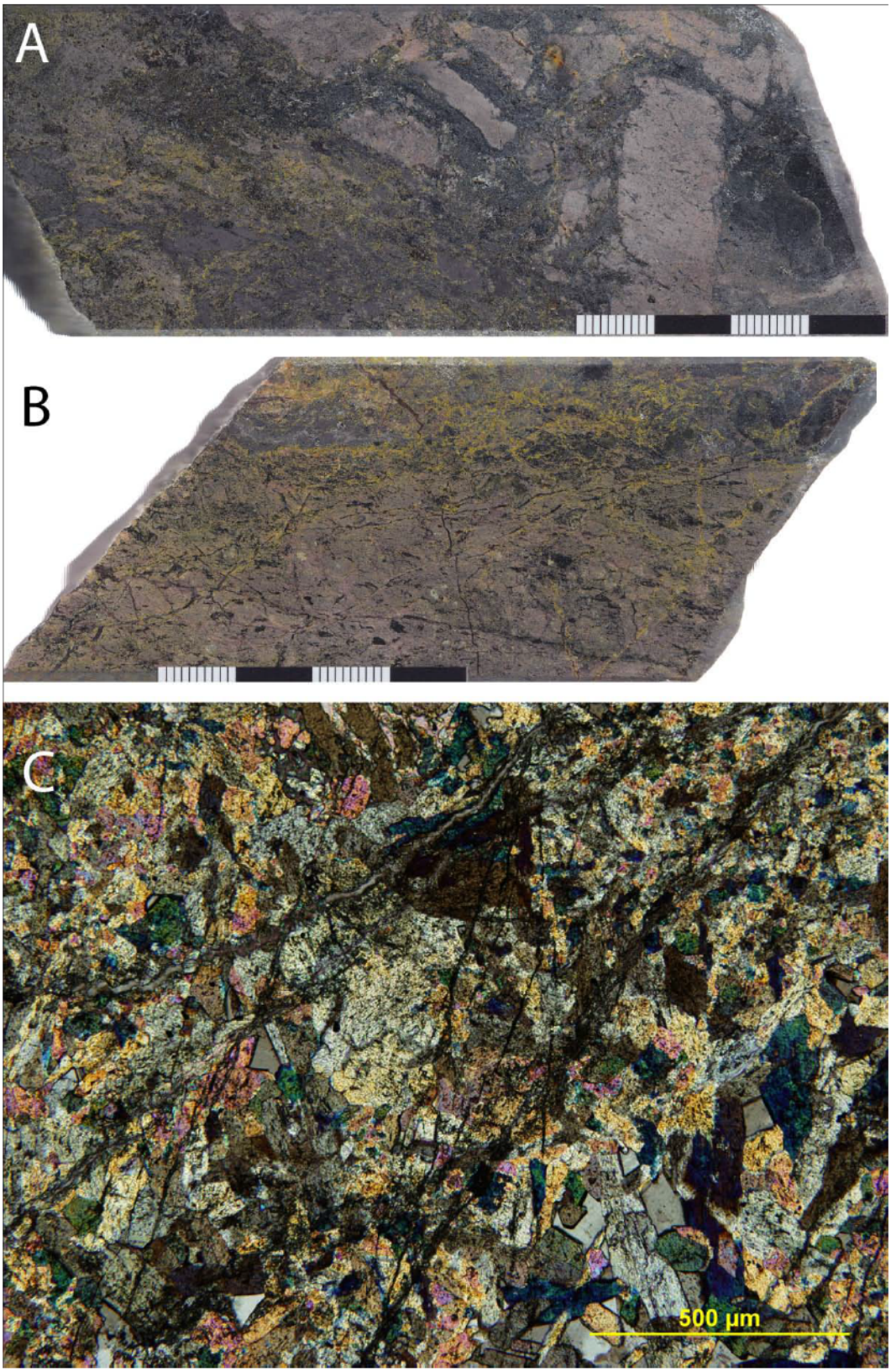

Figure 4.12 – A. and B.) Chalcopyrite-magnetite mineralization stained with sodium cobaltinitrite showing yellow potassium feldspar, C.) Potassium feldspar veining cross-cutting epidote.

4.3.5 Carbonate alteration

Carbonate alteration overlaps the main stage IOCG mineralization and consists largely of calcite veinlets occurring with or shortly after IOCG copper mineralization. Veins of calcite and chlorite accompany chalcopyrite mineralization from the late potassic alteration; however, cross-cutting relationships suggest that some veinlets are emplaced slightly post mineralization. Although this may not warrant its own stage of alteration, it is important since it signifies the transition away from IOCG conditions to shallow, lower temperature epithermal conditions. This will be discussed in more detail in the discussion section of this chapter.

While veinlets of calcite are easily detected in hand specimen, it can also form aggregates dispersed throughout the matrix and in this form it is more difficult to see. Modal abundances of calcite can range anywhere from 1% to 5% in the most altered samples. Veinlets of calcite often cross-cut earlier assemblages of epidote and biotite, and have envelopes of fine grained hematite (Figure 4.13A). Aggregates of alteration can be easily detected in hand specimen by use of hydrochloric acid, which causes the rock to effervesce if calcite is present. Calcite veins are occasionally mineralized with chalcopyrite and are seldom seen with pyrite (Figure 4.13D and E). SEM-EDS analysis of calcite indicates that it is dominantly $CaCO_3$, sometimes having trace amounts of Mg. Veinlets of calcite infrequently have tourmaline along their walls (Figure 4.13B), or as euhedral 1 to 2 mm hard black crystals (Figure 4.13C). Thin sections of tourmaline have a deep green colour in plane polarized light and are often zoned, especially in sections of euhedral crystals. SEM-EDS analysis of these zoned crystals indicate that the deep green

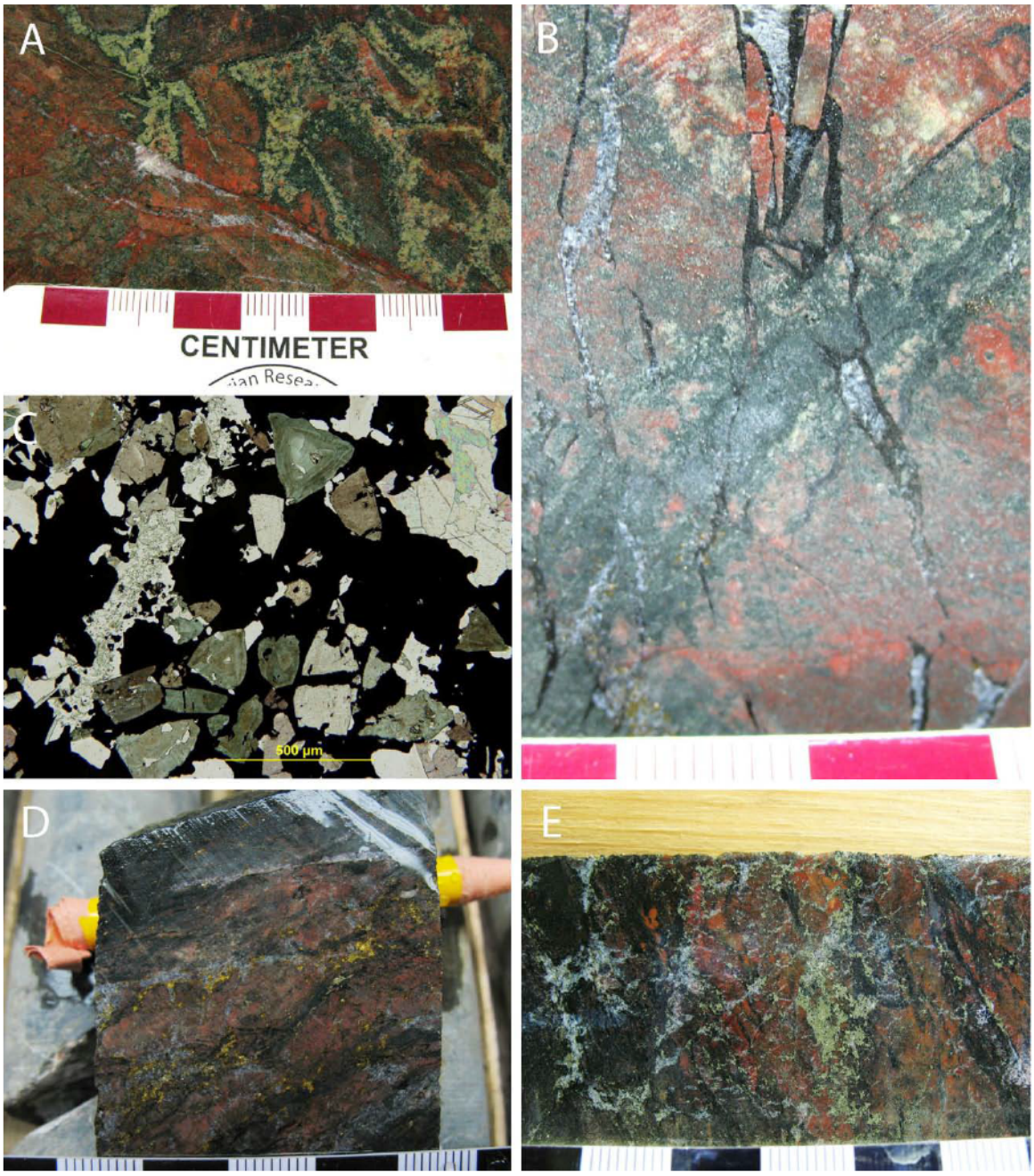

Figure 4.13 – A) Carbonate veins cutting earlier styles of alteration (epidote and biotite from the calcic-iron stage), B.) Carbonate and tourmaline cross-cutting earlier styles of alteration, C.) Tourmaline in thin section, D. and E.) Mineralized carbonate alteration cutting earlier styles of alteration.

areas are rich in iron, brown-green areas are more magnesium rich and pale yellow-green areas are rich in aluminum and depleted in iron (Figure 4.13C). Fully quantitative

formulae calculations of tourmaline are impossible with only SEM-EDS analysis, so only the raw data for tourmaline in oxide weight percentages are shown in Appendix C. H, B and F are too all to light to be detected, and these elements can substitute into multiple sites in the complex tourmaline structure (represented by the general formula: $XY_3Z_6(T_6O_{18})(BO_3)_3V_3W$, where X can be Ca, Na, K or □, Y can be Li, Mg, Fe^{2+}, Mn^{2+}, Zn, Al, Cr^{3+}, V^{3+}, Fe^{3+}, Ti^{4+} or □, Z can be Mg, Al, Fe^{3+}, Cr^{3+} or V^{3+}, T can be Si, Al or B, V can be O or OH and W can be OH, F or O (Deer *et al.*, 1992)).

4.3.6 Silicic alteration

Many locations intersected in the drill core exhibit intense silicic alteration in the form of a quartz-calcite(-dolomite)-gypsum breccia that is mineralized with pyrite-chalcopyrite. In addition to utilizing previously existing breccia matrix as a fluid pathway, the most intense silicic alteration appears to form a secondary breccia with textural evidence for shallow emplacement. Preexisting alteration styles can be observed within the clasts of this secondary breccia.

Quartz is only present as a very minor phase in all of the alteration styles leading up to IOCG mineralization. The presence of quartz as a major product of alteration is evident only in the very latest stages of ore formation, where quartz as veins and breccia matrix can comprise up to 40% of the rock. Silicic veining is the less intense version of silicic alteration and typically forms in the matrix of preexisting breccias as vuggy quartz veins with varying degrees of mineralization. Where the alteration is most developed, mature quartz breccias can fully encompass clasts of previously altered rock (Figure

4.14A and B). Altered envelopes around silicic stockworks and breccias are often represented by assemblages including sericite (Figure 4.14C). Where biotite is present in the protolith from earlier potassic styles of alteration, it is commonly broken down into chlorite and sericite. Individual grains of biotite that are not completely converted to chlorite can exhibit chloritic rims (Figure 4.14D).

The mineralogy of the silicic alteration is dominated by quartz, calcite and gypsum with minor chlorite and dolomite. Quartz usually makes up more than 90% of the veins, often exhibiting a vuggy texture with well developed crystal faces exposed within the vugs. Quartz is clear to milky in hand specimen, and thin sections of milky quartz have abundant fluid inclusions which will be discussed in Chapter 5. The remainder of the mineralogy is dominated by calcite, gypsum, dolomite, chlorite and muscovite in general order of abundance. These minerals are usually intergrown with quartz, but calcite and gypsum are occasionally precipitated in open spaces such as the walls of vugs. Gypsum appears in hand specimen as either pinkish orange aggregates, or as well developed transparent crystals (selenite) as seen in Figure 4.14E. In thin section gypsum can ether appear as anhedral masses with first order grey interference or as crystals with first order yellow birefringence and excellent cleavage (Figure 4.14F). Calcite and dolomite generally appear as anhedral masses intergrown within quartz, except in rare cases where they form well developed rhombs on the walls of vugs. The two are differentiated in hand specimen by their reactivity with hydrochloric acid, but several thin sections of the non-reactive species are analyzed to verify composition. In thin section, both species display high order birefringence and are commonly twinned; however, the twins in dolomite are curved.

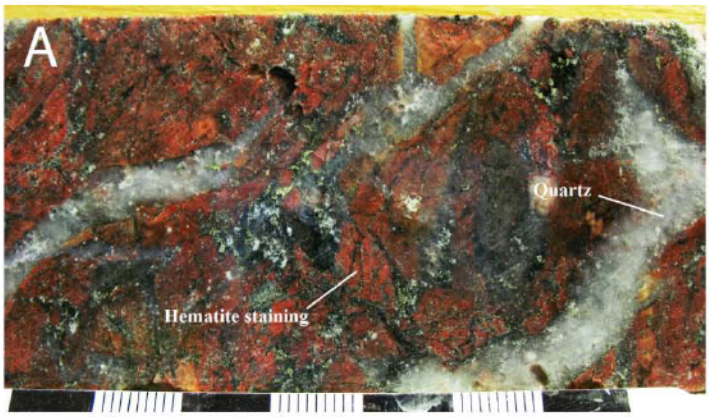
A
Quartz
Hematite staining


B
pyrite +
chalcopyrite
quartz +
calcite

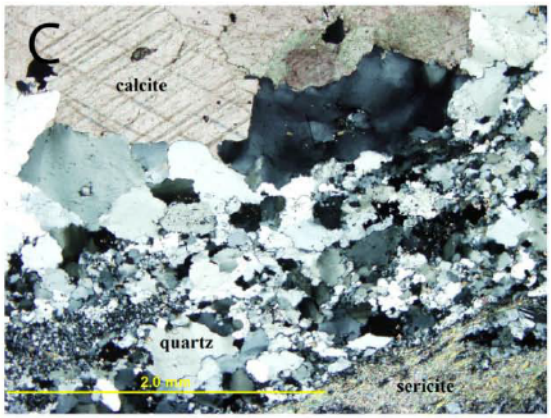
C
calcite
quartz
2.0 mm
sericite

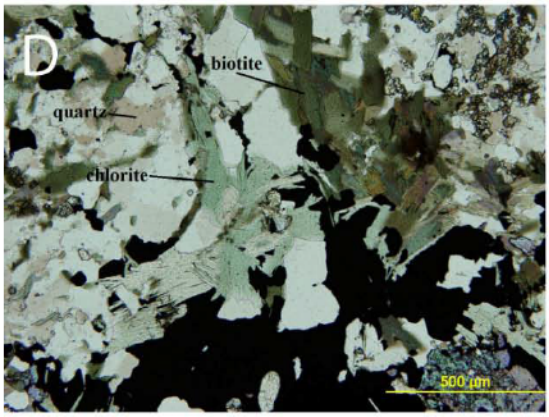
D
biotite
quartz
chlorite
500 µm


E

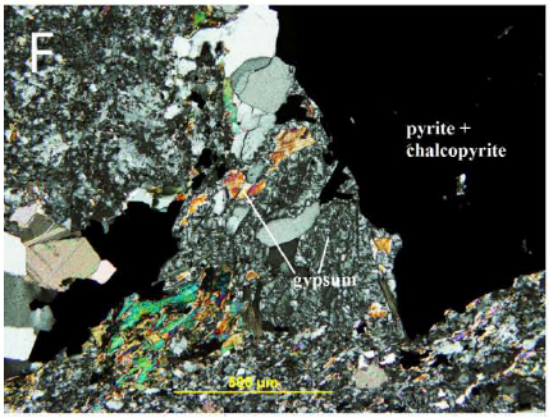
F
pyrite +
chalcopyrite
gypsum
500 µm

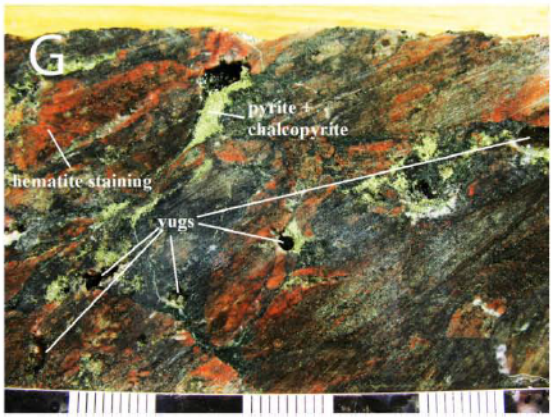
G
pyrite +
chalcopyrite
hematite staining
vugs

Figure 4.14 – (*previous page*) A. and B.) Fully developed quartz breccias overprinting earlier styles of alteration, C.) Sericitic alteration (lower right) in the wall rock of a late quartz breccia, D.) Breakdown of biotite to chlorite associated with mineralizing silicic alteration, E.) A well developed crystal of selenite from a silicic altered rock, F.) Gypsum in a mineralized quartz stockwork with pyrite and chalcopyrite. The large mass of grey mineral and the crystaline yellow-orange mineral are both gypsum, G.) Late mineralization without a fully developed quartz breccia. Note that vugs are still abundant.

Chlorite that is often associated with earlier alteration assemblages may be paragenetically linked to the silicic stage of alteration. While only making up a minor constituent of the silicic veins themselves, the host rocks to the silicic veins, with mineral assemblages including iron-silicates from earlier stages of alteration, appear to be pervasively chloritized. Chlorite grains are subhedral to anhedral and usually fine- to medium-grained (up to 2mm in length). In plane polarized light chlorite is pleochroic, and colour varies on stage rotation from green to yellow-green. Under crossed polars, chlorite has low order interference colours, displaying first order grey and yellow that is usually masked by the green colour of the mineral. Chlorites often grade to biotite within the same crystal, suggesting a paragenetic link between the two, but establishing relative timing between the two is often difficult. SEM analyses of chlorites have the compositions following the general formula $(Mg,Fe^{3+},Al)_6(Si,Al)_4O_{10}(OH)_8$ with the composition of the octahedral site shown in Figure 4.15. SEM analyses of chlorites that grade to biotite show the incorporation minor Ti and K into the chlorite structure.

Mineralization in the silicic alteration is dominated by stringers of anhedral pyrite and chalcopyrite in subequal proportions. Mineralization is hosted in the quartz dominated assemblages described above, usually assembled with calcite and gypsum. The assemblages of pyrite + chalcopyrite from this stage lack the magnetite that characterized the IOCG mineralization; however, relict magnetite is still occasionally

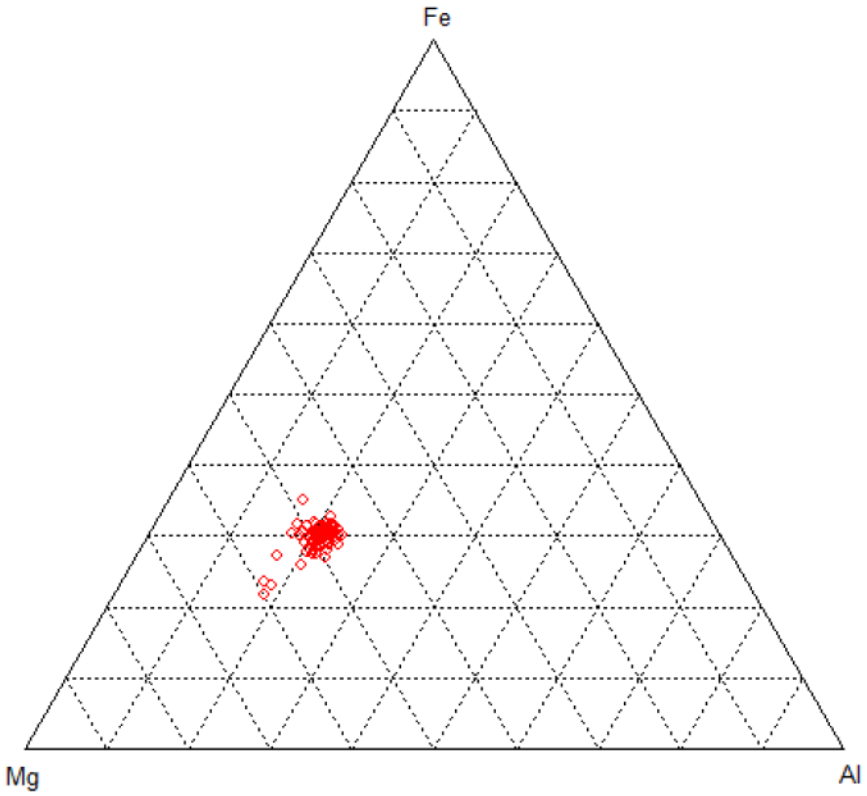

Figure 4.15 – Ternary diagram showing the compositions of the octahedral site in chlorites, calculations are based on stoichiometry; see Appendix C for details.

present in the wall rock and clasts. Caution must, therefore, be exercised when examining the relationship between iron oxides and copper mineralization. Thin section work was usually required to determine the timing of iron oxides relative to mineralization, especially where silicic alteration is underdeveloped and utilized the same fluid pathways as IOCG alteration. Trace amounts of sphalerite-greenockite solid solution were detected with the SEM as inclusions in chalcopyrite.

Most occurrences of silicic alteration are not in the form of a fully developed quartz breccia and utilized the pre-existing matrix as a fluid pathway. In these examples it is less obvious that silicic alteration is dominant, but thin sections and polished slabs show a strong correlation between mineralization and alteration quartz. Magnetite is still present, but only as a relict phase, and it is not part of the mineralizing assemblage. Sodium cobaltinitrite staining of these rocks indicates that potassium feldspar that was associated with the earlier magnetite + chalcopyrite assemblages was destroyed during this stage, as no yellow staining is observed in samples with the quartz + chalcopyrite assemblage (Figure 4.1 B, D and E). Vuggy textures can still be observed even when the alteration is not fully developed (Figure 4.14G); this is an excellent clue that silicic alteration is present.

4.3.7 Supergene alteration

Several samples from shallow and surface levels exhibit evidence for low-temperature supergene weathering of copper, silver and bismuth bearing minerals. Native copper (Figure 4.16A), silver and bismuth are detected with SEM-EDS as massive to dendritic crystals. Figure 4.16B shows a BSE image of dendritic crystals of silver growing around a chalcopyrite crystal from the main stages of ore deposition. The chalcopyrite itself can sometimes be tarnished blue in reflected light where it is replaced along cleavage planes, and SEM analyses of the blue areas indicate that trace amounts of silver are present (Figure 4.16C). Native bismuth is occasionally present by itself or with

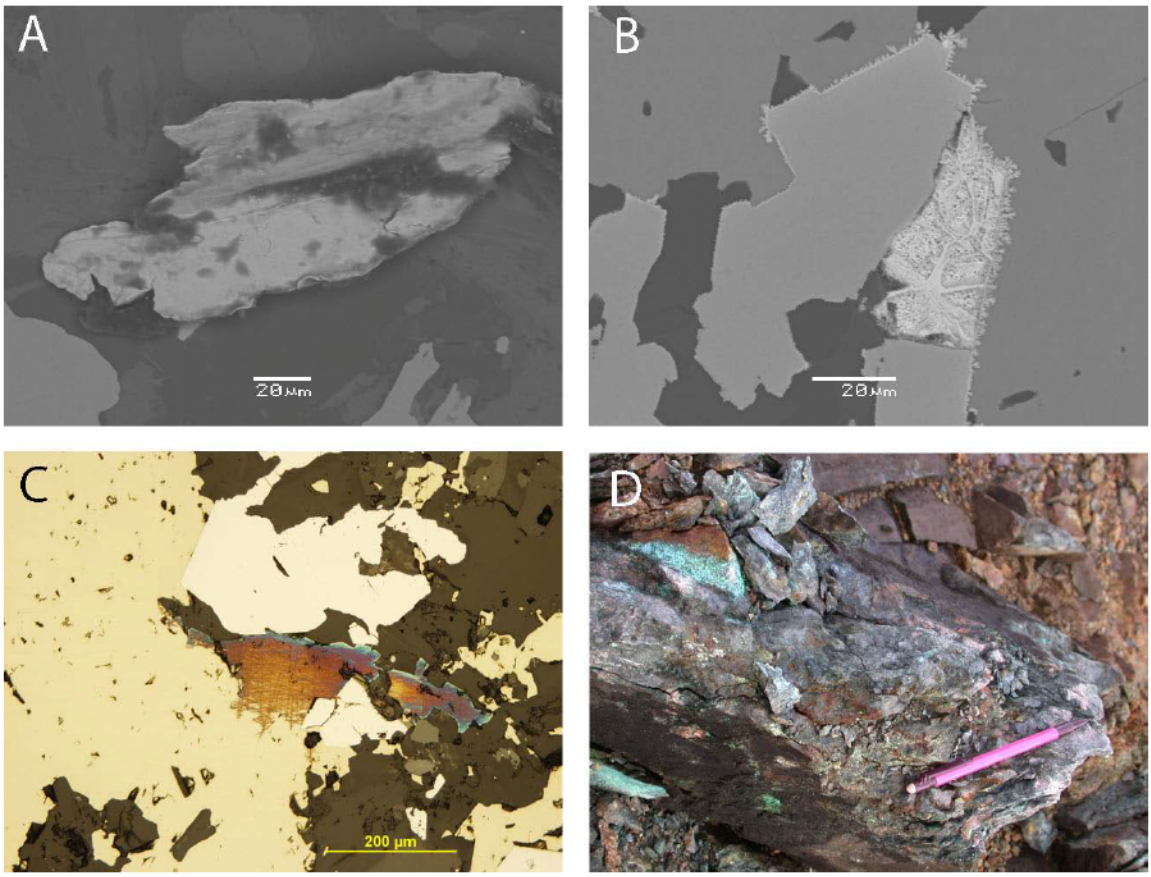

Figure 4.16 – A.) BSE image of native copper, B.) BSE image of dendritic native silver that nucleated along the grain boundary of a chalcopyrite crystal, C.) Reflected light image of chalcopyrite with trace silver causing tarnishing, D.) Malachite staining is very abundant where copper mineralization crops out at surface.

bismuth tellurides and sulphides. On the surface, supergene weathering can be seen in the form of blue-green malachite staining on copper bearing rocks (Figure 4.16D).

4.4 Discussion

A complex history of alteration is present at the Hamlin Lake occurrence, but a good understanding of how the alteration develops in these systems can greatly aid in the formation of a fluid model. IOCG deposits across the globe exhibit a wide variety of

alteration models with many key similarities and differences (Williams *et al.*, 2005). The following discussion will briefly describe the differing alteration styles observed in other magnetite group IOCG deposits in the world, followed by a comparative analysis to what is seen at Hamlin Lake.

4.4.1 Typical IOCG styles of alteration

Since the inaugural use of the term IOCG in the early 1990s geologists have been collectively describing the range of alteration styles observed at these deposits around the globe (e.g, Hitzman *et al.*, 1992; Corriveau *et al.*, 2010). Although no one alteration model fits every IOCG occurrence, several common features have frequently been noted, and these are closely analogous to what is observed at Hamlin Lake. The typical progression for a magnetite group (Cloncurry type) IOCG deposit grades from an early, high-temperature sodic(-calcic) stage, through a high-temperature calcic-iron stage, to a moderate-temperature potassic-iron stage(Corriveau *et al.*, 2010). As these high-temperature ore forming fluids cool, low-temperature potassic-iron assemblages begin to dominate and can be observed in many hematite group (Olympic Dam type) IOCG deposits (Corriveau *et al.*, 2010).

Perhaps the best documented style of alteration at IOCG deposits is the vast regional scale sodic(-calcic) alteration, which can be observed at many of the world class deposits, such as Sossego (Monteiro *et al.*, 2008), Lightning Creek (Perring *et al.*, 2000) and Port Radium, Northwest Territories, Canada (Mumin *et al.*, 2007, Mumin *et al.*,

2010). Although well documented, the origin of the sodic(-calcic) alteration and its role in the formation of IOCG deposits are often debated.

Sodic(-calcic) alteration is most commonly observed as a regional scale alteration that develops in areas most proximal to a heat source. The style is often attributed to high temperature fluids of magmatic origin (e.g., Cloncurry district, Mark *et al.*, 2004), and is generally a very early stage of alteration. Altered rocks are dominated by pervasive to replacement albitisation at the expense of orthoclase, but may also contain epidote, scapolite or amphiboles. Typically, albite dominates felsic volcanic precursor rocks, whereas variants with amphiboles such as actinolite tend to form in mafic precursor rocks (e.g. Tjårrojåkka, Kiruna district; Edfelt *et al.*, 2005).

Geochemical studies using whole rock and fluid inclusion geochemistry have been undertaken to understand element mobility during the sodic(-calcic) stage of alteration (Oliver *et al.*, 2004). While their magmatic origins are generally agreed upon, there is slight variation in the interpretations of the genetic role of these fluids. Sodium is ubiquitously enriched as the name implies, and potassium and iron are depleted. This is as far as the commonalities can be taken as other elements, both major and trace, must be considered deposit by deposit. Calcium, for example, can be either enriched or depleted depending on the abundance of calcium in the precursor rocks (Oliver *et al.*, 2004). The most debated point regarding the fluid chemistry of the early fluids is its role as a source for economic metals, most notably copper, that are discharged during later stages of alteration. Perring *et al.* (2000) utilize proton induced X-ray emission (PIXE) analyses of fluid inclusions from early generations of quartz from the Lightning Creek deposit to show enriched concentrations of copper up to 1.9 wt%, and suggested that copper was

recharged by the same fluids that caused sodic enrichment. Conversely, Oliver *et al.* (2004) use mass change plots to show that copper in many of the other Australian deposits, is not leached during albitisation, and they infer a magmatic origin. This is to say that element mobility needs to be considered on a case by case basis.

The sodic(-calcic) stage of alteration can locally grade into a calcic-iron style of alteration. Where the sodic(-calcic) alteration is largely a pervasive and replacement style of alteration, calcic-iron alteration commonly exhibits veins and breccia infill textures (Corriveau *et al.*, 2010). This style can be readily observed in the wallrocks of many of the Chilean and Peruvian IOCG deposits, but is also responsible for the main stage magnetite mineralization in the iron oxide-apatite (IOA) deposits of the Kiruna district (Edfelt *et al.*, 2005; Corriveau *et al.*, 2010; Chen *et al.*, 2010). Mineralogy of this style of alteration is typically dominated by iron oxides and iron silicates (magnetite, hematite and chlorite), calcium-iron silicates (actinolite, hornblende and epidote) and is often accompanied by apatite. Variations on this style are dependent on the activity of other elements in solution, and again must be considered separately for each deposit. Biotite is often present where potassium is enriched (e.g., Marcona; Chen *et al.*, 2010), and albite can remain present where sodium is enriched or at least stable.

In IOA deposits the evolution of the system is believed to have halted during or shortly after the sodic(-calcic) stage, and polymetallic sulphide mineralization is scarce (Corriveau *et al.*, 2010). These systems host vast quantities of iron ore in the form of magnetite and occasionally hematite (e.g., Kiruna, 2000 Mt ore @ 60-68% Fe; Nystrom and Henriquez, 1994). Deposits where the alteration evolves to a potassic-iron style tend to host the polymetallic deposits with economic quantities of Cu, Au, Ag, Bi, Mo, Co,

etc. This moderate- to high-temperature potassic alteration often consists of biotite and potassium feldspars with magnetite and sulphide mineralization and is observed at many, but not all, magnetite group polymetallic IOCG deposits, such as Sossego, Salobo (Monteiro *et al.*, 2008), Ernest Henry (Mark *et al.*, 2006) and Aitik (Wanhainen *et al.*, 2003,2005). Potassic-iron alteration can take on a variety of forms, from replacement and pervasive, as seen in the NICO deposit (Gandhi *et al.*, 1996), to breccias or stockworks with biotite matrix and potassium feldspar altered clasts, such as those seen at the Birchtree showing in the Great Bear Magmatic zone, Northwest Territories (Corriveau *et al.*, 2010).

Late carbonate and calc-silicate assemblages are present at some deposits such as Candelaria (Marschik and Fontbote, 2001), Sossego (Monteiro *et al.*, 2008) and Raul-Condestable (de Haller *et al.*, 2006). This low-temperature carbonate alteration is often shortly preceded by the formation of mushketovite; a unique style of magnetite that is pseudomorphed after hematite. Mushketovite has been described at several IOCG deposits (e.g. Candelaria; Marschik and Fontbote, 2001; North Portua, P. Williams, pers. comm.; Raul-Condestable, de Haller *et al.*, 2006), and is always closely related to carbonate alteration. Williams (2009b) suggests a mechanism for mushketovite formation:

$$Fe_2O_3 + Fe^{2+} + HCO_3^- \Leftrightarrow Fe_3O_4 + CO_2 + H^+$$

Such a process explains the presence of carbonates, and the formation of carbonate results in a buffering effect on pH; this reduces sulphide solubility and provides a link to sulphide deposition.

The classic hematite breccia observed at Olympic Dam is described by Skirrow (2009) as an example of low-temperature ferric iron-potassic alteration. This alteration style can be seen at many of the hematite group deposits such as Prominent Hill (Belperio *et al.*, 2007) and Mantoverde (Rieger, 2010) represented by mineral assemblages often including hematite, sericite, chlorite and carbonate, with oxidized ore consisting largely of chalcopyrite-bornite. It is this style of alteration that often hosts the uranium mineralization associated with IOCG deposits. Isotopic evidence combined with the low temperature and oxidizing nature of this style of alteration suggests that fluid mixing at shallow crustal levels is important to its formation (Skirrow, 2010).

The Great Bear Magmatic Zone in the Northwest Territories has been studied on a regional scale in an attempt to genetically link the wide array of deposit styles found there. Alteration styles with aspects of porphyry and epithermal systems are detected with close spatial relations to deposits displaying the IOCG-like elements described above. Mumin *et al.* (2009) attributed this to a ternary continuum of deposit styles that genetically link IOCG deposits in the area to porphyry and epithermal systems. They concluded that given the complex nature of hydrothermal systems associated with felsic to intermediate volcano-plutonic complexes this fundamental genetic relationship should be expected and needs to be considered in any thorough investigation of a potential IOCG district. The Andean hydrothermal systems along the coasts of Chile and Peru are a more

modern example of how this continuum may have operated (cf. Naslund *et al.*, 2002; Sillitoe, 2003).

All of the previously described styles of alteration are generally devoid of quartz; however, many IOCG systems exhibit late- and/or distal stage quartz veining or silicification events (Mumin *et al.*, 2010). This late quartz brecciation and veining is considered to mark a transition from a relatively deep, high-temperature environment to epithermal conditions. As discussed above, the best examples of the late epithermal styles of alteration are seen in the Great Bear Magmatic Zone at deposits such as Eldorado and Echo Bay (Mumin *et al.*, 2010). The alteration style is dominated by quartz ± carbonate ± hematite, and may be associated with minor potassic alteration. Iron oxides are less abundant than they are in the higher temperature assemblages, but where present are often represented by fine-grained hematite. This reflects a more oxidizing and lower temperature environment, while vuggy textures imply a shallow environment. The examples at the Sloan and Mariner deposits exhibit high-grade copper mineralization with chalcopyrite and bornite, but this style is usually unmineralized, as it forms in a distal setting to deposits such as NICO and Sue-Dianne (Goad *et al.*, 2000; Byron *et al.*, 2006).

4.4.2 Discussion on Hamlin Lake paragenesis

The descriptions of mineral assemblages, associations and their textural relationships lead to a paragenetic model for of the evolution of the alteration at Hamlin Lake. The interpretations are summarized in Figure 4.17.

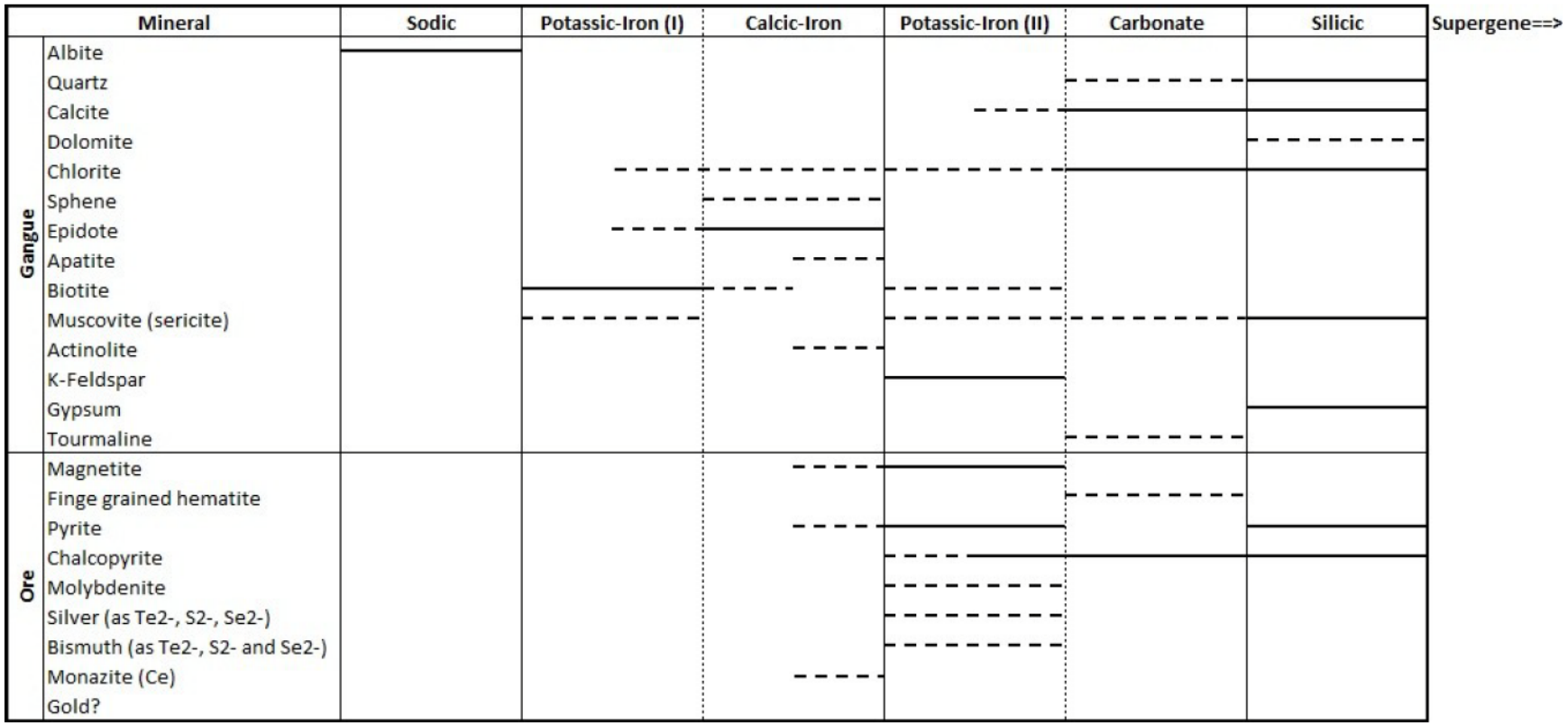

Figure 4.17 – Summarized paragenesis broken down into six distinct styles of alteration, plus supergene weathering. Solid lines are major associations while dashed are minor.

The albitic alteration observed regionally at Hamlin Lake fits the typical descriptions of sodic alteration and can be considered analogous to sodic alteration observed elsewhere. In fact, it is possible that the local "younger" volcanic rocks mapped as shoshonites by Hart and Metsaranta (2009) actually represent the extent of regional sodic alteration. These rocks are classified geochemically, and such a classification would not distinguish between true shoshonites and sodic altered felsic volcanic rocks. SEM analyses described above indicate that albite is pure with no calcium; such minerals are likely of a hydrothermal origin (Engvik *et al.*, 2008). However, the albites that were analyzed only span the area proximal to the ore and are only representative of volcanic clasts in the breccia; a more vigorous geochemical and mineralogical study should be undertaken to verify the nature of the sodic alteration on a regional scale.

Pre-ore alteration at Hamlin Lake is dominated by the biotite + chlorite + epidote ± calcite ± magnetite assemblage in the matrix of the hydrothermal breccia described above. Epidote texturally appears to post-date the earlier biotite alteration, as evident in cross-cutting relationships (Figure 4.5B). Such a relationship, where an early, barren potassic enrichment is succeeded by a barren calcic enrichment, can also be observed at the Ernest Henry deposit where these textural relationships are attributed to multiple cycles of fluid (Mark *et al.*, 2006). It is possible that a similar phenomenon occurred at the Hamlin Lake occurrence, where an early fluid pulse evolved from sodic through to potassic; this coincides with the initial brecciation of the rocks and causes the precipitation of the potassic mineral biotite along with an early stage of magnetite. Thin sections often exhibit epidote that appears to have replaced an earlier stage of carbonate, so it is possible that the early potassic alteration was followed by an early stage of

carbonate alteration; however, these carbonates have been largely destroyed during epidotization. The lack of any sulphide phases during these early stages of alteration suggests that sulphides were not stabilized at this stage of alteration.

The calcic(-iron) stage of alteration marks the early stages of alteration during the second fluid pulse. The evolution of this second fluid pulse is recorded in the rocks by the progression towards a second stage of potassic alteration. Where the early potassic alteration is dominated by a breccia matrix of biotite, the second pulse of fluid results in veinlets of potassium feldspar that cross-cut epidote and are associated with magnetite and chalcopyrite that replace the epidote. The production of copper sulphides suggests an external source of sulphur that was not present during the initial fluid cycle, and this will be discussed in further detail in Chapter 6. Magnetite from this stage occasionally exhibits the classic mushketovite texture where it forms as laths that appear to pseudomorph over hematite (Figure 4.8). It is possible that during the earlier pulse of fluids hematite was formed and was only converted to magnetite through the mushketovite conversion, although this is difficult to prove since relict euhedral hematite is not observed. A possible alternate explanation for this texture as it is observed at Hamlin Lake could be the replacement of iron phylosilicates (biotite or chlorite).

The transition away from potassic alteration is recorded by the introduction of late carbonates to the mineralizing assemblage. These carbonates (dominantly calcite) form veinlets that cross-cut the early breccia, occasionally infiltrating into and throughout the older matrix. Such an alteration is fairly typical during the late stages of IOCG alteration and is attributed to a retrograde phase of fluid evolution (Corriveau *et al.*, 2010). In many hematite-dominated or mixed magnetite-hematite IOCG deposits, the carbonate

alteration is often accompanied by hematization of the magnetite (also known as martite). This is evidence of an increase in oxidation state, often attributed to the influx of an oxidizing meteoric fluid. Coarse grained martite is absent at Hamlin Lake; however, stable isotope data must be considered to determine the true role of meteoric fluids. This will be discussed in more detail in later chapters.

The carbonate alteration at Hamlin Lake trends to a late-stage silicification event accompanied by high-grade copper mineralization and sulphates. Quartz, which is largely absent from the earlier stages of alteration, is now the dominant species and forms a silicic matrix that percolates through the magnetite-chalcopyrite matrix of the earlier mineralization. The vuggy nature observed in this style of alteration is evidence of a shallow environment, and combined with the high sulphidation (sulphates and sulphides are stable) this style seems typical of an epithermal base-metal deposit (Simmons *et al*., 2005). The drop in the solubility of quartz marks a significant change in thermodynamic conditions, possibly a drop in temperature due to the influx of a cooler, sulphur-bearing fluid. Altered envelopes of chlorite + sericite formed from the breakdown of biotite are common with the quartz breccia. Such assemblages are common in the late stages of IOCG formation, but are often accompanied by the formation of euhedral hematite and signify a drop in pH. Hematite, other than fine grained, is absent at Hamlin Lake, and the implications of this are discussed further in Chapter 7. As discussed above, the environments in which IOCG deposits form can easily transition into lower temperature epithermal conditions, and that seems to be the case during the late mineralization at Hamlin Lake.

Chlorite is a common mineral in several paragenetic stages of alteration at Hamlin Lake, but its origin is often difficult to unravel based on petrographic analyses alone. Early examples of chlorite may be hydrothermally precipitated, but these are difficult to differentiate from chlorite formed due to later metamorphic processes. Because of its broad timing, the isotopic characteristics of chlorite may record changes in hydrothermal conditions and could provide an invaluable clue towards how fluids at Hamlin Lake evolved ultimately leading to ore deposition. This is discussed further in Chapter 6.

Chapter 5 – Fluid Inclusions

5.1 Introduction

A thorough fluid inclusion study can often be the best way to examine the chemistry and thermodynamic properties of ore forming fluids through direct measurements. Several methods for analyzing fluid inclusions are available; however, only optical petrography and microthermometry were used here. Optical petrographic methods required no special preparation, and could be performed on all thin sections providing that the inclusions were large enough to be visible under high magnification. Microthermometry requires special preparation of doubly polished sections, and only one such specimen was prepared for this study.

5.2 Results

Fluid inclusion studies have been carried out on other IOCG deposits to help in characterizing the types of fluids involved (Perring *et al.*, 2000; Pollard, 2001; Kendrick *et al.*, 2008; Fisher and Kendrick, 2008; Dreher *et al.*, 2008); however, direct analysis of fluid composition was not carried out in this study. Quartz is the most common mineral analyzed for inclusions due to its transparency and its high tolerance for withstanding the pressures exerted by fluids on heating and cooling; however, calcite, fluorite and sphalerite can be used as well. The inclusions recognized in this study were found in quartz.

Three main types of fluid inclusions were recognized using transmitted light petrography at room temperature (Figure 5.1). Type 1 inclusions have a well developed negative crystaline shape and are isolated from sub-grain boundaries within the quartz. These range in size from 1 to 10 µm and can be divided into two subtypes. Type 1A inclusions are aqueous two-phase liquid-vapour inclusions, while type 1B are 3 phase liquid H_2O-liquid CO_2-vapour inclusions (nicknamed "double-bubble" inclusions because of the appearance of the CO_2 vapour bubble within the CO_2 liquid bubble). The CO_2 bubbles in these inclusions can represent up to 40% of the inclusion volume. The "double bubble" characteristic is more easily seen in real time since the inner bubble undergoes Brownian motion within the outer bubble. Type 2 inclusions are far more abundant and occur in strings of small, (usually less than 1 µm to 5 µm) amorphously

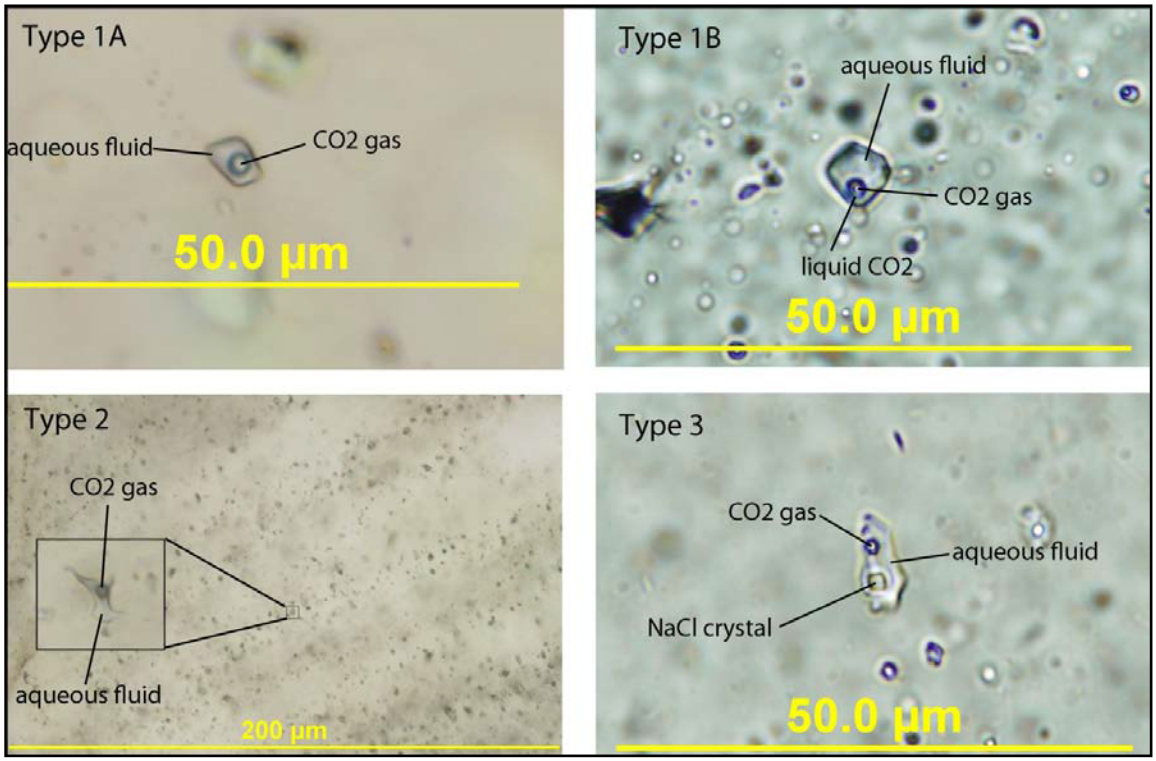

Figure 5.1 – Types of fluid inclusions observed at Hamlin Lake.

shaped, two-phase liquid-vapour inclusions. Vapour bubbles in type 2 inclusions are generally smaller and typically represent only 10-15% of the inclusion's total volume. Type 3 inclusions have similar shape and size as in type 1 inclusions, typically ranging from 1 to 10 μm in size with a well-developed negative crystal shape. These inclusions are three or more phase inclusions with a liquid phase, vapour phase and at least one daughter crystal phase.

Due to time constraints, only one doubly polished section was prepared for a microthermometry study (sample HAM-63-08). This sample contained type 1 and 2 inclusions within a late-stage quartz breccia from the silicic stage of alteration discussed in Chapter 4. Type 3 inclusions were not observed in this sample, and their salinities, trapping temperatures or system could not be established.

5.2.1 Fluid inclusions in HAM-63-08

Sample HAM-63-08 was selected for a quantitative microthermometry study since it represents a style of quartz that is clearly hydrothermal in origin, and can be linked to a single alteration stage. The sample (Figure 5.2) is comprised of a well developed quartz breccia with minor calcite, dolomite and gypsum (silicic alteration), and is taken from a highly mineralized section of drill core. Ore minerals in the sample are pyrite + chalcopyrite. Fragments in the breccia were subject to the earlier styles of alteration, and this sample can be considered as a pristine example of the late silicic alteration.

Figure 5.2 – Sample HAM-63-08, which was cut into a doubly polished section for microthermometry analysis. Sample exhibits silicic alteration forming a quartz + calcite matrix to clasts with fine grained hematite alteration.

Type 1 and 2 inclusions were recognized in this sample, with type 2 being far more abundant. Type 1 inclusions were represented mostly by subtype 1A; only one 1B inclusion was noted in the sample. Upon heating, all frozen inclusions began to melt and form "ice cubes" at -21.2°C, indicating that all inclusions in the sample represent the H_2O-NaCl system. Salinities for this system were calculated from melting temperature after Bodnar (1993). Type 1 inclusions were fully melted between temperatures of -7.3°C and -8.6°C, suggesting fairly low salinities ranging from 10.9 to 12.4 wt% NaCl. Melting of type 2 inclusions followed closely between -4.5°C and -7.1°C, again suggesting low salinities ranging from 7.2 to 10.6 wt% NaCl. Upon heating, strings of

type 2 inclusions were the first to homogenize by dissolution of the vapour bubble into the liquid at a range of temperatures between 92°C and 109°C. Type 1A inclusions homogenize by dissolution of the vapour bubble over a large range from 180°C to 271°C, with mode in the range of 200°C to 220°C. The one type 1B inclusion analyzed homogenized at 337°C, first by boiling of the liquid CO_2 to form a single vapour bubble, followed by dissolution of this vapour bubble into the liquid. A summary of analyses is included in Table 5.1. Fluid inclusions in the calcite and dolomite were also analyzed. These were decrepitated upon heating, which voids any meaningful data. Fluid inclusions in quartz did not leak or decrepitate upon either cooling or heating.

5.3 Discussion

Of the three types of fluid inclusions observed in the rocks at Hamlin Lake, type 1 inclusions seem to be the most useful for understanding the fluids involved in the formation of ore. The good negative crystaline shape of these inclusions is a sign that they are primary in nature and formed cogenetically with the quartz. Type 2 inclusions are often found along subgrains in quartz and even more commonly formed in planar strings of inclusions. These textures, combined with the amorphous shaped often observed indicate an origin of secondary nature. Type 2 inclusions are taken to have formed after the primary quartz and do not represent the ore forming fluids. Type 3 inclusions, not observed in the sample HAM-63-08, also have the distinct negative crystal

Table 5.1 - Full list of fluid inclusions analyzed with microthermometry.

Inclusion type	T(E) (°C)	T(M) (°C)	T(H) (°C)	System	Salinity (wt%)
1A	-21.2	-7.3	202	H2O-NaCl-CO2	10.9
1A	-21.2	-7.5	205	H2O-NaCl-CO2	11.1
1A	-21.2	-7.8	207	H2O-NaCl-CO2	11.5
1A	-21.2	-7.4	271	H2O-NaCl-CO2	11.0
1A	-21.2	-8.3	215	H2O-NaCl-CO2	12.0
1B	-21.2	-8.3	337	H2O-NaCl-CO2	12.0
1A	-21.2	-8.3	238	H2O-NaCl-CO2	12.0
1A	-21.2	-8.6	180	H2O-NaCl-CO2	12.4
1A	-21.2	-8.2	198	H2O-NaCl-CO2	11.9
2	-21.2	-6.2	97	H2O-NaCl-CO2	9.5
2	-21.2	-7.1	102	H2O-NaCl-CO2	10.6
2	-21.2	-5.3	92	H2O-NaCl-CO2	8.3
2	-21.2	-5.2	97	H2O-NaCl-CO2	8.1
2	-21.2	-6.9	105	H2O-NaCl-CO2	10.4
2	-21.2	-5	103	H2O-NaCl-CO2	7.9
2	-21.2	-6.5	101	H2O-NaCl-CO2	9.9
2	-21.2	-4.5	94	H2O-NaCl-CO2	7.2
2	-21.2	-7	96	H2O-NaCl-CO2	10.5
2	-21.2	-5.6	96	H2O-NaCl-CO2	8.7
2	-21.2	-6.5	99	H2O-NaCl-CO2	9.9
2	-21.2	-5.2	100	H2O-NaCl-CO2	8.1
2	-21.2	-4.9	109	H2O-NaCl-CO2	7.7

shape and are probably of a primary nature to the quartz in which they formed. This will be discussed in more detail below.

Data acquired during the microthermometry studies on sample HAM-63-08 for nine type 1 fluid inclusions indicate that late ore forming fluids were of a fairly low salinity. Although only one "double bubble" inclusion was analyzed with microthermometry, other similar inclusions were often seen in similar styles of quartz in other thin sections. These types of inclusions are reported in other IOCG deposits (Fisher and Kendrick, 2008; Dreher *et al.*, 2008) and suggest that fluids are rich in CO_2;

however, these inclusions are often accompanied by daughter crystals and are of much higher salinity than the inclusions described here. The low salinity of the inclusions associated with copper mineralization is typical of distal silicic alteration in other IOCG systems.

Homogenization temperatures in type 1A inclusions range from approximately 200°C to 250°C, with the one type 1B inclusion suggesting a slightly higher trapping temperature (~350°C). These temperatures correspond to an epithermal environment (Simmons *et al.*, 2005), consistent with the textural observations in the silicic alteration discussed in Chapter 4. However, due to the relatively small data set, these data should be treated with caution and are best compared with other means of geothermometry (See Chapter 6).

The more saline fluid inclusions observed in earlier generations of quartz (type 3 inclusions) are also evidently of primary nature. These inclusions were not analyzed quantitatively, but the presence of daughter crystals at room temperature implies salinity greater than 26.4 wt%, or the NaCl saturation at room temperature (Bodnar *et al.*, 1985). Although the negative crystal shape observed in these inclusions suggests that they are primary, the quartz in which they were found is not hydrothermal. These types of inclusions were observed in what appear to be relict quartz phenocrysts from the volcanic fragments (Figure 5.3).

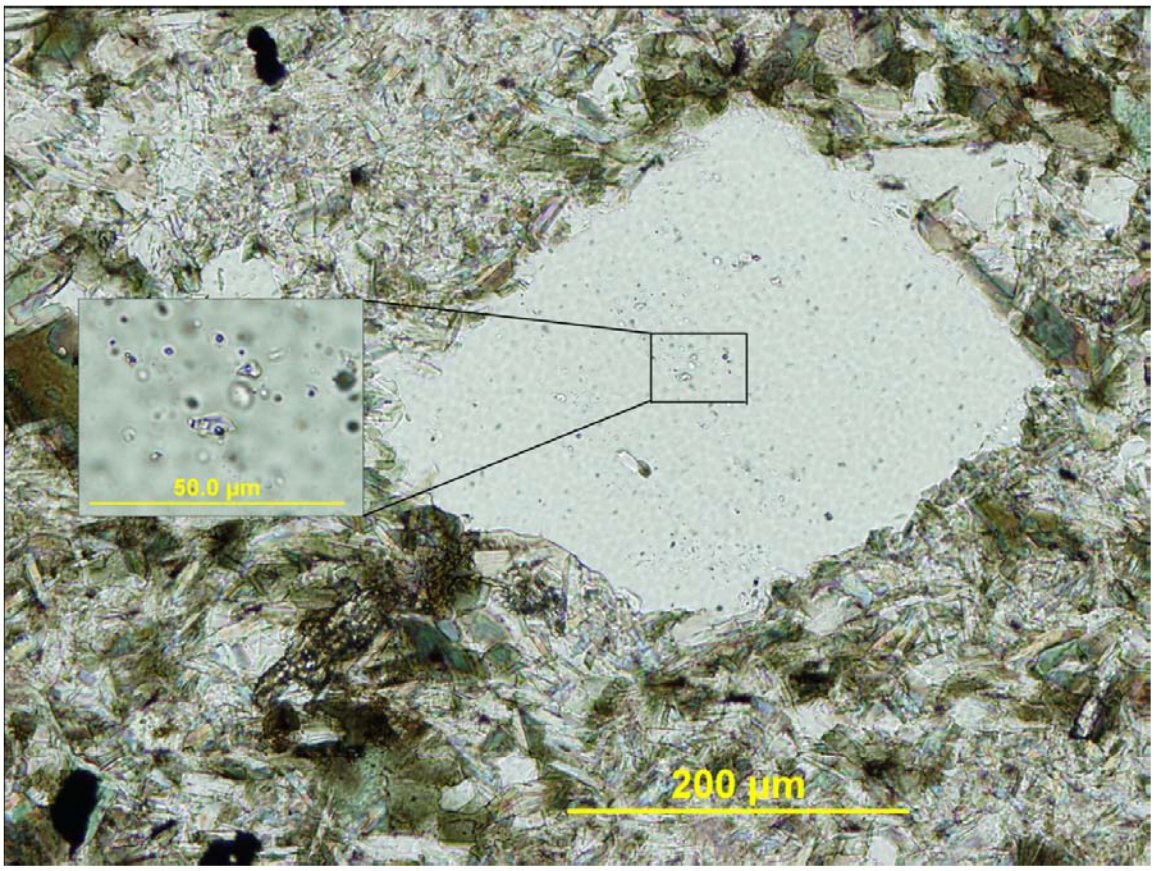

Figure 5.3 – Quartz phenocryst with type 3 inclusions.

Chapter 6 – Stable Isotopes

6.1 Introduction

Stable isotope measurements were undertaken on mineral separates of chlorite (oxygen and deuterium), magnetite (oxygen) and sulphides (sulphur). The analytical procedures are outlined in Chapter 2. Isotope studies are undertaken to get a sense of the derivation of the constituents of the ore forming fluid. Oxygen and deuterium analyses from oxygen and hydrogen in the hydroxyl site of hydrous minerals can indicate the nature of the water taken in during the minerals formation. Oxygen alone from oxides, silicates or carbonates can be used in a similar manner. Sulphur isotopes will allude to the origin of the sulphur required for metal sulphide precipitation.

Isotopic analyses yielded results measured from the mineral itself. These data are reported in terms of δ values, which show the measured value compared to a standard (see discussion in Chapter 2). δ values from mineral analyses (δ_{sample}) need to be corrected for the fractionation of light elements from the natural water to the mineral at low temperatures. This fractionation is accounted for by using a fractionation factor (α) that is determined experimentally for the fractionation system in question. δ values for the water (δ_{water}) are calculated using the formula:

$$\delta_{water} = \left[\left(\frac{1 + (\delta_{sample}/1000)}{\alpha} \right) - 1 \right] \times 1000 \qquad (6.1)$$

where α is calculated by:

$$1000\ln\alpha = A\frac{10^{18}}{T^6} + B\frac{10^{15}}{T^5} + C\frac{10^{12}}{T^4} + D\frac{10^{9}}{T^3} + E\frac{10^{6}}{T^2} + F\frac{10^{3}}{T} + G \qquad (6.2)$$

Table 6.1 – Data used for fractionation factor calculations.

System	Fractionation	A	B	C	D	E	F	G	Temperature	1000 ln(α)	Reference
H	water - chlorite	0.000	0.000	0.000	0.000	-3.700	0.000	-24.000	268°-274°C	-36.6 to -36.4	Graham et al. (1984)
O	water - chlorite	0.000	0.000	0.028	-0.312	2.500	3.720	-12.620	268°-274°C	0.94 to 1.15	Savin and Lee (1988)
O	water - magnetite	-0.426	0.000	3.302	0.000	-8.984	0.000	0.000	400°-550°C	-8.32 to -7.44	Cole et al. (2004)

where T is the temperature of the fluid in Kelvin and the values A through G are constants determined experimentally or theoretically, and the values used for this study are presented in Table 6.1.

When two minerals equilibrate isotopically from the same fluid of an unknown temperature, these equations can be applied using the assumption that δ_{water} is the same for each mineral. With two mutually independent equations and two unknowns (δ_{water} and T), temperature can be calculated. In this study, such calculations were attempted for oxygen isotopes in chlorite-magnetite pairs and for sulphur isotopes in sulphide pairs. For the case of sulphide pairs, the equations are quite simple and can be solved algebraically. The term $\Delta_{A\text{-}B}$ must be known and represents the difference in δ values between the two sulphide phases:

$$\Delta_{A\text{-}B} = \delta^{34}S_A - \delta^{34}S_B \qquad (6.3)$$

6.2 Oxygen and Hydrogen Isotopes

Oxygen from chlorite and magnetite, and hydrogen from chlorite were analyzed in an effort to characterize the hydrothermal fluids from which they precipitated. Magnetite exhibits a variety of textures and styles that appear to range in timing from

early barren stages of alteration to the mineralizing events. Chlorite samples were taken from rocks subject to the late stages of alteration, ranging from the carbonate stage to the late silicic stage discussed in Chapter 4. The samples of chlorite that were taken consist of fine- to medium-grained chlorite in the matrix of the breccia. Chlorite ranges in colour from blue-green to dark green and is often associated with biotite, epidote and magnetite. In six of the samples selected for chlorite analysis, magnetite was also separated; however, thin section observations suggest that the two are not cogenetic. Magnetite forms fine- grained aggregates, where individual grains of magnetite range in form from anhedral to euhedral. Two additional samples of magnetite were taken from samples selected for sulphide separation. Full descriptions of the samples are presented in Appendix D.

Geothermometry based on pairs of chlorite and magnetite cannot be done, because the two are not cogenetic; other means of determining the temperature of formation are required. Cathelineau and Nivea (1985) have proposed a geothermometer based on the Al-content of the tetrahedral sites of the chlorite structure. Application of this geothermometer based on data acquired from 82 SEM analysis of chlorites from late stages of alteration have a range from 192° to 303°C with a mean of 271±3°C (Appendix C). This temperature is slightly higher than those measured in the type 1 fluid inclusions (generally 200° to 250°C); however, due to the small fluid inclusion data set, the chlorite temperature is preferred. Estimating temperatures for water-magnetite fractionation is more difficult. Stable isotope studies on IOCG deposits use data from fluid inclusions to estimate early fluid temperatures; however, since early generations of quartz are rarely

Table 6.2 – Chlorite isotope data from oxygen and hydrogen.

Sample	$\delta^{18}O_{chl}$	$\delta^{18}O_{H2O}$		δD_{chl}	δD_{H2O}	
29B-08-chl	7.0	5.90	±0.11	-53	-17.76	±0.14
33-07-chl	4.3	3.22	±0.11	-54	-18.43	±0.14
41-06-chl	2.1	1.10	±0.11	-55	-19.53	±0.14
43-05-chl	3.0	1.94	±0.11	-52	-17.02	±0.14
55-02-chl	5.8	4.73	±0.11	-53	-18.01	±0.14
57-06-chl	4.1	3.07	±0.11	-53	-17.86	±0.14
61-03-chl	4.2	3.14	±0.11	-54	-18.39	±0.14
62-07-chl	1.5	0.42	±0.11	-60	-25.36	±0.13

identified at Hamlin, this method cannot be directly applied. Studies at other deposits suggest early fluid temperatures in the 400° to 550°C range (Dreher *et al.*, 2008; Monteiro *et al.*, 2008; Williams, 2010b), so this range was used to calculate water-magnetite fractionation. The resulting data still only have a small error, since water-magnetite fractionation does not vary much over this temperature range (1000 lnα ranges from -8.32 to -7.44) (Cole *et al.*, 2004).

The results of the chlorite study are presented in Table 6.2. $\delta^{18}O_{water}$ values from chlorite range from 0.4‰ to 5.9‰, while δD_{water} values range from -17.0‰ to -25.4‰. Plotting these values on a diagram of δD versus $\delta^{18}O$ (Figure 6.1) shows that the data lies in the region between the meteoric water line and the metamorphic water region (Sheppard, 1986). The data have an atypical flat-lying slope that is difficult to explain. One possibility is inherent due to the structure of the chlorite itself. Oxygen occurs in chlorite in two structural sites, within the framework of the mineral itself and as hydroxyl groups in the brucite layer. Hydrogen occurs exclusively in the hydroxyl site. The BrF_5 method used to analyze oxygen will not distinguish between the two sites, so the oxygen data reported are actually a hybrid of the oxygen from two structural sites. If the isotopes

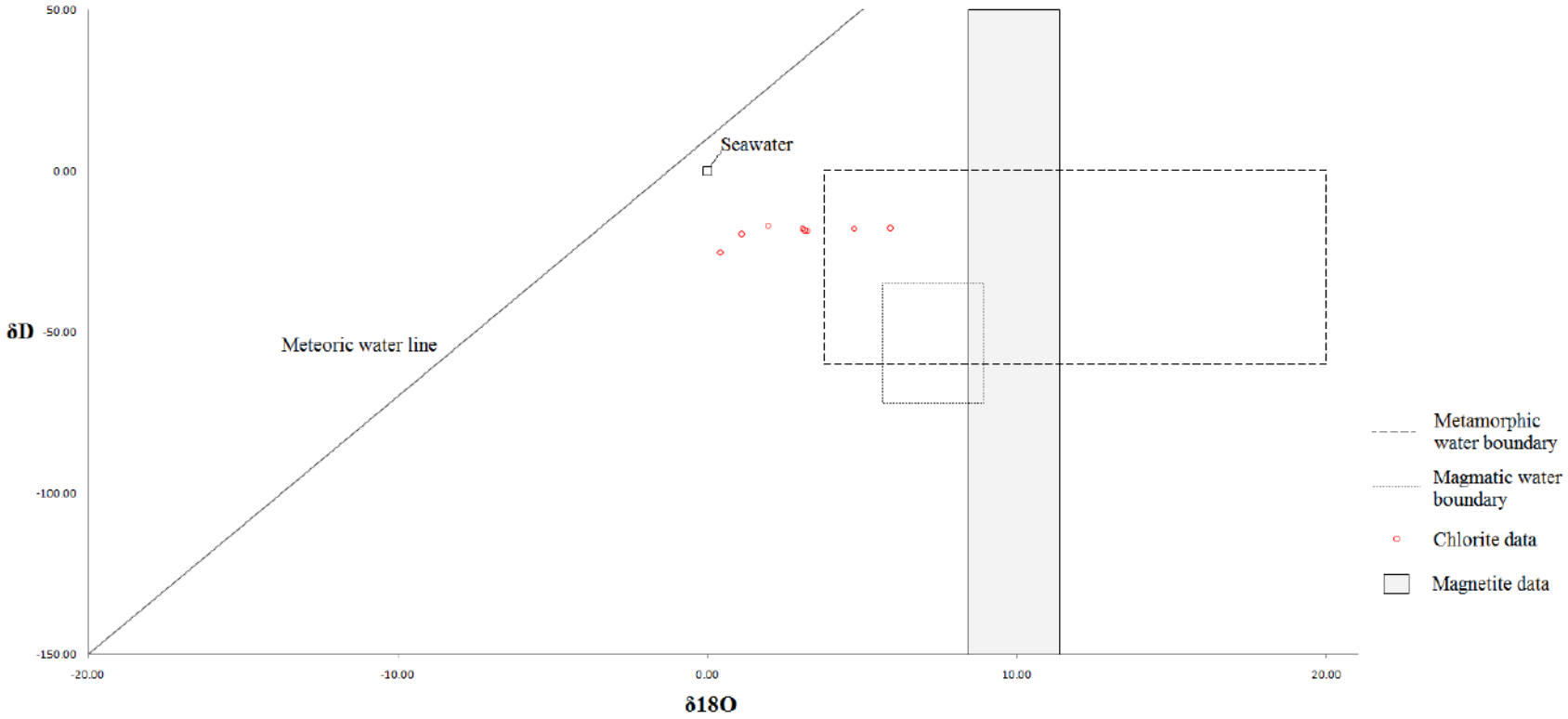

Figure 6.1 – Chlorite and magnetite data from Hamlin Lake plotted on the diagram of Sheppard, 1986. Error bars for chlorite data are approximately the size of the circles.

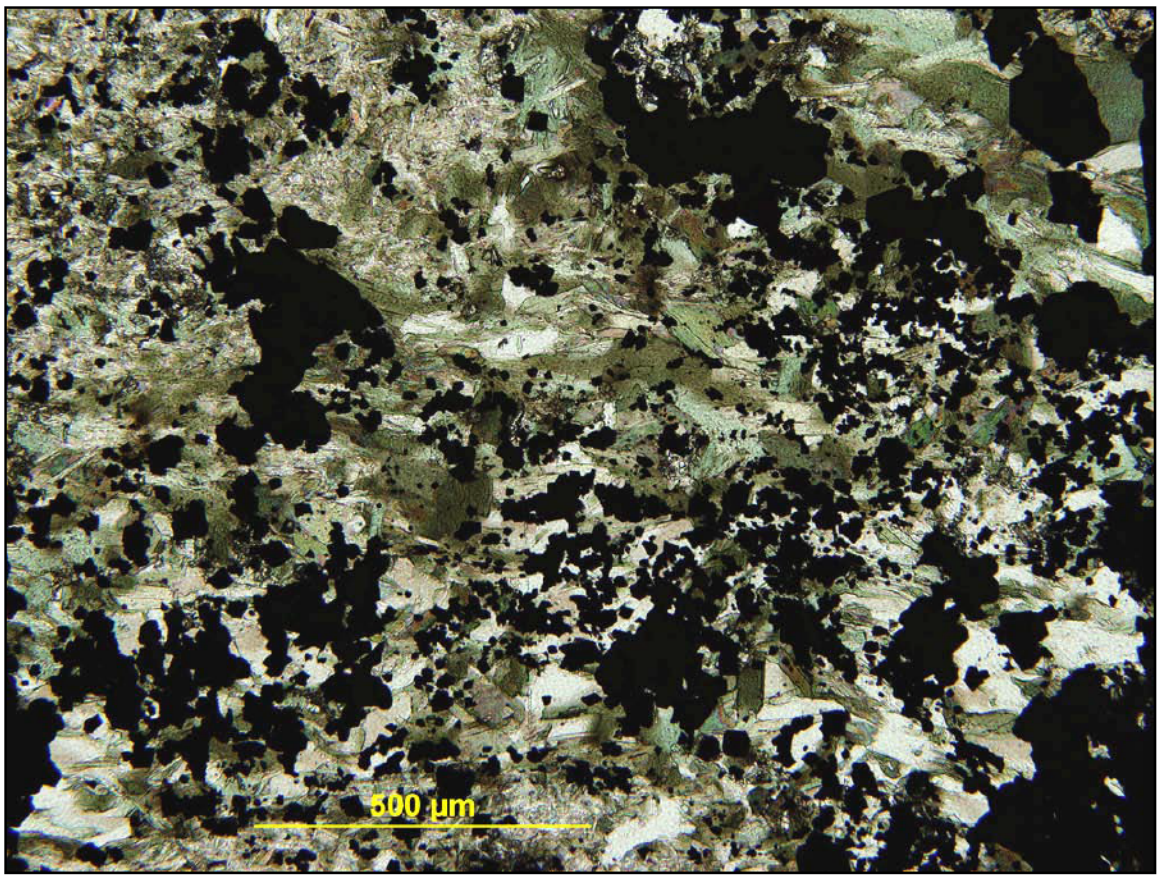

Figure 6.2 – Photomicrograph of chlorite after biotite alteration in mineralized rock.

in the hydroxyl group were re-equilibrated by some later fluid, then the hydrogen data would reflect that later fluid. Oxygen will still reflect the signature from the isotopes in the framework sites, even if slightly modified. The spread in the oxygen isotope values can still represent mixing of some early fluid with a meteoric fluid, despite the lack of a slope. This suggests that the fluids responsible for chlorite formation are likely of crustal origin, possibly a modified meteoric water. Petrographic analysis of chlorite often reveals evidence for a metamorphic origin, where the conversion of biotite to chlorite is incomplete (Figure 6.2). These samples were not used for isotopic analysis; however, the pure samples of chlorite that were analyzed may still be of a metamorphic origin, rather

than hydrothermally precipitated. Since the formation of chlorite from biotite requires the addition of water to an already hydrous mineral, the oxygen and hydrogen measured in this study might represent a mixture of the early hydrothermal fluids that formed biotite with a secondary fluid involved in the later conversion of biotite to chlorite.

Magnetite may be a better representation of the isotopic composition of the oxygen from early waters. Results of the magnetite analysis are presented in Table 6.3. $\delta^{18}O_{water}$ values from magnetite range from 8.9‰ to 10.9‰. In the absence of hydrogen isotope data these values plot on the diagram of Sheppard (1986) as a vertical column (Figure 6.1), and these values agree well with a water of metamorphic or magmatic origin. Contrary to what is observed in the oxygen isotope values of chlorite, the data set for magnetite has a low spread of values. This supports the earlier statement that the chlorite isotopes may have been modified by a later metasomatic event.

Table 6.3 – Magnetite oxygen isotope data.

Sample	$\delta^{18}O_{mt}$	$\delta^{18}O_{H2O}$	
31-06-mt	1.0	8.90	±0.45
32-06-mt	2.3	10.23	±0.45
33-07-mt	2.5	10.41	±0.45
41-06-mt	2.3	10.22	±0.45
43-05-mt	1.0	8.91	±0.45
55-02-mt	3.0	10.92	±0.45
57-06-mt	3.0	10.94	±0.45
61-03-mt	2.5	10.42	±0.45

6.3 Sulphur Isotopes

Sulphides from a variety of mineralized rocks were analyzed for sulphur isotope content in cogenetic pairs. Eight pairs of sulfides were selected; six pairs of pyrite-

chalcopyrite from high grade mineralized zones and two of pyrite-pyrrhotite from the wispy textured pyrite + pyrrhotite + magnetite assemblage. The pyrite-pyrrhotite samples are only weakly mineralized with trace chalcopyrite. Detailed sample descriptions are presented in Appendix D. The purpose of taking cogenetic sulphide pairs is to calculate the temperature of their formation based on light isotope fractionation between species. In addition to geothermometry, sulphur isotopes can be taken independently to determine the source of the sulphur.

Sulphur isotopes from pyrite and chalcopyrite in the mineralized zones have a range of $\delta^{34}S$ values from -6.9‰ to 1.8‰. Chalcopyrite generally has lower $\delta^{34}S$ values than pyrite, which is attributed to fractionation from H_2S to the sulfide. The large range of negative values observed in IOCG deposits has often been interpreted to represent an exotic source of sulphur (Benavides *et al,* 2007; de Haller and Fonteboté, 2009).

Sulphur isotope values from the pyrite-pyrrhotite pairs are generally higher than those from the pyrite-chalcopyrite pairs; however, it is difficult to define a definite pattern based on such a small data set. One pyrite-pyrrhotite pair gave $\delta^{34}S$ values of 0.0‰ and 0.2‰ respectively, while the other pair yielded 4.7‰ and 4.0‰. While the values close to zero might suggest a magmatic origin for sulphur, the higher values contradict this. No conclusions regarding the source of sulphur are made here. With only two samples it is impossible to tell whether there is a continuous range of values between the two or if it is truly a bimodal data set.

Geothermometry was attempted on these sulphide pairs in an effort to confine fluid temperatures. The two pairs of pyrite-pyrrhotite suggest fairly high temperatures for formation. Sample HAM-31-05 has the close to 0‰ values and a temperature of

Table 6.4 – Sulphur isotope data from samples of pyrite, chalcopyrite and pyrrhotite at Hamlin Lake. The sample highlighted in red is suspected to represent a bad analysis, given the high %S reported. Temperatures are calculated based on the equations of Ohmoto and Rye, 1979.

Sample	Stage	Chalcopyrite		Pyrite		Temperature (°C)	
		% S	δ34S (‰)	% S	δ34S (‰)		
29B-08	I	38.9	-1.4	56.2	0.0	304	±34
31-06	I	37.6	0.3	52.2	1.8	283	±33
33-06	II	89.8	-1.3	62.9	-2.4	Infinite	
39-08	II	39.3	-4.5	59.9	-1.1	94	±22
63-14	II	36.3	-6.9	55.7	-4.0	119	±23
65-02	II	38.9	-4.0	56.6	-3.0	399	±40

Sample	Stage	Pyrite		Pyrrhotite		Temperature (°C)	
		% S	δ34S (‰)	% S	δ34S (‰)		
31-05	early?	59.7	4.7	46.1	4.0	391	±48
63-15	early?	62.6	0.0	43.5	0.2	Infinite	

391 ±48°C. The error in this sample is introduced by uncertainty in the constant terms of equation (6.2) above, and does not account for error in the analysis itself. Given the low degree of fractionation between pyrite and pyrrhotite ($\Delta_{po\text{-}py} \approx 0‰$), error in the $\delta^{34}S$ analyses may account for a large portion of error in the temperatures. In sample HAM-63-15 the fractionation between pyrite and pyrrhotite is reverse of what is expected, and gives a slightly negative value for $\Delta_{po\text{-}py}$. This yields an infinite temperature of formation, and can again be accounted for by error in the $\delta^{34}S$ values. Despite the problems with error, it seems consistent that pyrite-pyrrhotite pairs are forming in equilibrium at high temperatures, since Δ tends to 0 with increasing temperature. This suggests that the pyrite-pyrrhotite observed in the upper volcanic sequences at Hamlin Lake may itself be volcanogenic, not hydrothermal. Textures in rocks with pyrite-pyrrhotite also support a volcanogenic origin (e.g., exhalative layering seen in Figure 4.10).

Pyrite-chalcopyrite pairs are confined within the matrix to a hydrothermally formed breccia and appear to be of a hydrothermal origin. Temperatures calculated from these pairs are presented in Table 6.4. Stage I mineralization seems to suggest equilibration from temperatures around 300°C, while those from stage II mineralization are more varied. Given the small sample set and large amount of error in these temperatures, caution must be used when interpreting these data.

6.4 Discussion

A comparison between the present study and other isotopic studies on worldwide IOCG deposits reveals similarities and differences. Table 6.5 summarizes several isotopic studies from other IOCG deposits and shows the great variation in isotopic characteristics. This follows from the lack of a genetic model and is the basis for much of the debate regarding the roles of magmatic fluids versus non-magmatic fluids in a given IOCG district. It is fairly obvious that no one genetic model will fit every IOCG deposit on a global scale, but there is still much debate over unified models on a district scale. A good example of this debate is the role of magmatic sulphur (Marschik and Fontboté, 2001) versus non-magmatic sulphur (Barton and Johnson, 1996) in the mineralization of some of the Peru-Chilean IOCG deposits. Since the Hamlin Lake occurrence is currently a standalone IOCG discovery, there are no other isotopic data for comparison.

Understanding the isotopic composition of the fluids and host rocks can lead to a dynamic model for fluid evolution over time. While these are very common studies in all

Table 6.5 – Summary of selected isotope studies from other IOCG districts showing the great variation in isotopic characteristics. Abreviations are: bn = bornite, chl = chlorite, cpy = chalcopyrite, mt = magnetite, py = pyrite, qtz = quartz, ser = sericite, sid = siderite.

Deposit	δ34S	δ13C	δD	δ18O	Reference
Igarape Bahia	cpy: -1.1 to 5.6 (outlier at -10.8)	carbonate: -6.7 to -13.4	N/A	mt, qtz, sid: 5 to 16.5	Dreher et al., 2008
Salobo	bn, cpy: 0.2 to 1.6	N/A	N/A	mt: 6.6 to 12.1 (mode at 7)	Requia and Fontbote, 2001
Raul-Condestable	main stage: 1 to 26.3 (median at 6.6)	N/A	N/A	N/A	de Haller and Fontbote, 2009
	deep vein: 1 to 6.3 (average of 3.5)	N/A	N/A	N/A	
	shallow: 2.7 to 26.3 (median at 7.5)	N/A	N/A	N/A	
	late stage: -32.7 to -22.9	N/A	N/A	N/A	
Gawler Craton	from sub-economic prospects: -5 to 2 and 5 to 10 (bimodal)	N/A	mt assemblages: -21 to -15	mt assemblages: 7.7 to 12.8	Skirrow et al., 2006
	Olympic Dam: -5 to -10	N/A	chl-ser: -9	chl-ser: 4.7 to 9.8	
Rakkurijarvi	N/A	carbonate: -11.7 to 4.5	N/A	carbonate: 9.4 to 19.9	Smith et al., 2007
Mont-de-L'Aigle	py, cpy: -1.5 to 4.8	N/A	N/A	qtz: -0.4 to 2.7	Simard et al., 2006
Mantoverde	Stage I py: -0.6 to 2	N/A	N/A	Stage I iron oxide: 7.3 to 9.9	Benavides et al., 2007
	Stage II py: -1.2 to 9.1	N/A	N/A	Stage II iron oxide: 3.0 to 8.0	
	Stage III py, cpy: -11.2 to 1.4	N/A	N/A	Stage III iron oxide: -2 to 1.7	
Sossego	N/A	N/A	Inclonclusive	calcic-sodic assemblages: ~6.9 +/- 0.9	Monteiro et al., 2008
				mineralizing: -1.8 to 3.4	

types of rocks, the interpretation of the data is more difficult in such ancient rocks. At Hamlin, where the host rocks and mineralization are Archean in age and subject to such a complex history of alteration, it is difficult to determine with certainty the isotopic characteristics and evolutionary path of each cycle of fluids. With textural evidence for low temperature supergene weathering it is important to know that the isotope data do in fact represent hypogene alteration, especially when dealing with clay minerals. Taylor (1974) showed that the mineral chlorite has an isotopic signature that is not easily reset by low temperature supergene waters. If the ^{18}O and D contents of the chlorite had been modified by the supergene event, the points in Figure 6.1 would slope towards the kaolinite line in the lower right portion of the diagram.

The best examples of isotopic studies involve large data sets from a variety of mineral assemblages that have been precisely age dated. There are no dating techniques available that can date the mineral assemblages in Archean rocks precisely enough to confine ages within the period of active hydrothermal systems. The paragenetic study undertaken in Chapter 4 is the best clue towards relative timing of the mineral assemblages characterized by isotopes here.

Isotopic compositions from assemblages representing various stages of alteration were measured and yield interesting results. Measurements from oxygen in magnetite mineralization and chloritization imply evidence for at least two fluids responsible for the mineralizing system. Magnetite is paragenetically early in comparison with most of the highest grade mineralization, and most textural evidence suggests that its formation spans the early stages of development up to the first stage of mineralization (the IOCG mineralization). The magnetite has an oxygen isotope composition that is consistent with

magmatic or metamorphic fluids. Chloritization appears to occur after stage I mineralization through a process related to metasomatism of earlier iron-silicates. Oxygen and hydrogen in chlorite were analyzed and yield data consistent with mixing between the early fluid and a later crustally derived fluid, possibly meteoric. The chloritization is a more widespread style of alteration than the iron-oxide alteration and is difficult to time with much precision. Thin section analysis does seem to suggest that the majority of chloritization shortly predates or accompanies the late stage epithermal style mineralization (Figure 4.13D).

The range in $\delta^{34}S$ values has several implications when considered with the styles of mineralization they come from. The pyrite-pyrrhotite pairs often have textural relationships with their host rocks that suggest a primary origin. The slightly positive near neutral $\delta^{34}S$ values are consistent with a magmatic sulphur source and when combined with textural observations, supports a volcanogenic origin. Pyrite-chalcopyrite pairs have a wider range of values ranging from -6.9‰ to +1.8‰ that suggests the importance of a non-magmatic sulphur source to the mineralizing events.

Chapter 7 – Discussion and Conclusions

7.1 Introduction

Results from this study are presented in chapters 3, 4, 5 and 6. While preliminary interpretations are made and discussed at the end of each chapter, no overall genetic story is presented. The aim of this final chapter is to put all of the pieces into context and present a genetic model. Mineral assemblages described in Chapter 4 can be combined with temperature estimates from Chapters 5 and 6 to establish other thermodynamic parameters such as oxygen fugacity (f_{O2}) and pH. Stable isotopes discussed in Chapter 6 provide insight to the environment in which the deposit formed.

7.2 Discussion

Chapter 4 discusses the paragenesis of various alteration styles over time. Alteration styles are attributed to two pulses of hot deep-seated fluid, the second of which appears to have mixed with a crustally derived fluid during late stages of mineralization. These fluids left behind clues to their thermodynamic properties in the form of stable mineral assemblages, which form only under certain conditions.

The first fluid pulse is responsible for the regional albitisation and the subsequent brecciation of the host volcanic rocks. Mineral assemblages present in these stages include albite and biotite respectively. These assemblages are rarely preserved, and it is difficult to tell with any certainty what other minerals were stable during early alteration.

Without knowing what mineral assemblages are stable, the thermodynamic properties of these early fluids cannot be inferred.

Harris (1970) attributed ore forming fluids in mineral deposits of the Shebandowan greenstone belt to the emplacement of the Powell Lake Granite. This seems to be the case for Hamlin Lake based on the close proximity of the deposit to the intrusion; however, no definitive magmatic signature was observed in the isotopic data presented here. Early fluids had an isotopic signature typical of metamorphic fluids; however, a magmatic contribution cannot be ruled out, because of the overlap in the magmatic and metamorphic regions of Figure 6.1. These early fluids are therefore referred to as neither magmatic nor metamorphic, but as deep-seated high-temperature fluids.

The early fluid pulse (pulse I) would have began as a high-temperature deep-seated fluid and progressively cooled towards the brittle-ductile pressure temperature regime as evident by the onset of rock brecciation. Temperatures for these early fluids were not calculated in this study, but can be inferred to have cooled from near magmatic temperatures to 400° to 550°C as evident from fluid inclusion studies on similar deposits (Oliver *et al.*, 2004).

Laser ablation of magnetite from the earliest generations indicate elevated copper content (sample HAM63-5 in Figure 4.9 is an example of early magnetite associated with no copper mineralization, but has the highest concentrations of copper) compared to magnetite from mineralizing fluids, suggesting that copper is present in early fluids. These early fluids did not, however, result in any major mineralization; they are likely to have been too hot or lacked the sulphur-content for base metals to precipitate as sulfides.

Had the hydrothermal activity ceased at this stage of formation, then the Hamlin Lake occurrence may have shared many aspects with IOA deposits such as Kiirunavaara in Sweden (Nystrom and Henriquez, 1994).

A second sequence of IOCG style alteration (Corriveau *et al.*, 2010) evolved from calcic alteration through to potassic alteration and IOCG mineralization. Multiple sequences of sodic(-calcic) through potassic styles of alteration have been observed at the Ernest Henry deposit in Australia (Mark *et al.*, 2006). This is attributed to multiple pulses of initially similar early high-temperature fluids, each resulting in a successive sequence of IOCG style alteration. A similar phenomenon seems to be responsible for the Hamlin Lake IOCG mineralization.

The first stage of mineralization (chalcopyrite + magnetite + pyrite) was likely discharged from a fluid of a temperature in the range from 350° to 450°C, given temperatures inferred from similar stages in other IOCG deposits (Williams, 2010b). Considering the Fe-S-O systems at these temperatures, the pH and f_{O2} can be estimated based on the stable assemblage pyrite + magnetite. Figure 7.1 shows phase diagrams in 20°C increments from 300°C to 400°C, the data for which is shown in Appendix E. It is not difficult to see that the pyrite + magnetite assemblage is only stable to a maximum temperature of approximately 380°C, above which pyrite is stable only with hematite. Two possibilities arise from this conjecture: (1) temperatures for this early stage of mineralization had dropped below those typical in other IOCG deposits (to less than 380°C), or (2) the assemblage pyrite + magnetite has been re-equilibrated during later hydrothermal or metamorphic events.

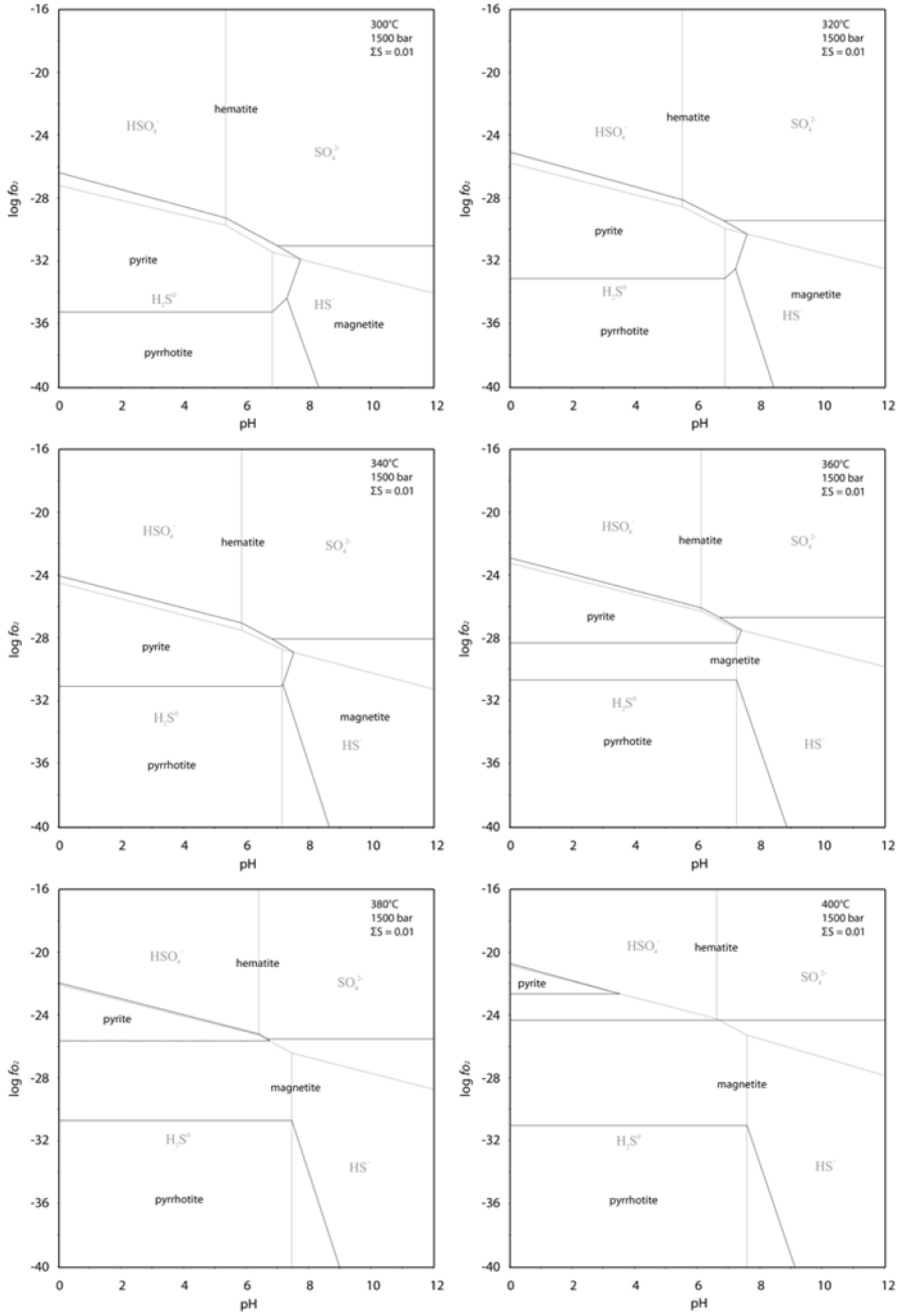
300°C
1500 bar
ΣS = 0.01
320°C
1500 bar
ΣS = 0.01
340°C
1500 bar
ΣS = 0.01
360°C
1500 bar
ΣS = 0.01
380°C
1500 bar
ΣS = 0.01
400°C
1500 bar
ΣS = 0.01
hematite
pyrite
magnetite
pyrrhotite
HSO4-
SO4 2-
H2S0
HS-
log fO2
pH
-16
-20
-24
-28
-32
-36
-40
0
2
4
6
8
10
12

Figure 7.1 – (*previous page*) fo_2 – pH diagrams for the temperature range 300°C to 400°C, showing the "disappearance" of the pyrite-magnetite stability line above 380°C. Black lines and text show mineral reactions, while grey lines and text show the regions of the dominant aqueous sulphur species.

Metal discharge during this stage I mineralization could be the result of either an increase in pH or a drop in fluid temperature, either of which reduce the solubility of copper and cause it to form copper and iron sulphides. The close temporal association between stage I copper mineralization and the onset of carbonate precipitation suggests that mineralization cannot be attributed to a drop in temperature alone. Since the solubility of CO_2 increases with decreasing temperature, a rise in pH in addition to decreasing temperature is an attractive mechanism for discharge of copper mineralization. The mushketovite reaction described in Chapter 4 is a very convenient mechanism for this increase in pH, since the production of CO_2 buffers pH to nearly neutral conditions (Williams, 2010b). The reaction would also provide an alternative metal complexing ligand as bicarbonate. This explains the presence high grade copper mineralization, despite the rather low salinities observed in all late fluid inclusions. The complete lack of relict hematite makes this argument difficult to verify, but regardless of the mechanism for buffering, an increase in pH does appear to be plausible as the primary means of early mineralization.

The transition to carbonate alteration also signifies the end of the classic IOCG style mineralization and the onset of a style of mineralization more typical in epithermal environments. At this level in the system the deep-seated fluids are able to cool, possibly mixing with shallow low temperature fluids of meteoric derivation. Fluid temperatures during this stage of alteration are much cooler, generally in the 250° to 300°C range, as

evident from fluid inclusions and chlorite geothermometry presented in earlier chapters of the present study.

Thermodynamic properties of the late fluids can be inferred using the 250° to 300°C temperature estimates combined with the various assemblages. The quartz breccias typical of this style of alteration are often accompanied by a pervasive assemblage of chlorite + sericite (Figure 4.14C). This assemblage is often observed in the late stages of hematite group IOCG systems (e.g., Candelaria; Marschik and Fontboté, 2001; Olympic Dam, Skirrow, 2010) and reflects a drop in pH. Specular hematite breccias that usually accompany these acidic conditions are absent and may reflect a lower dissolved iron content or a sulfidation state high enough for all iron to form as sulfides. The stability of gypsum and pyrite at these low temperature acidic conditions can be taken to indicate sulfur fugacity. Comparing f_{S2} with f_{O2} relates sulfidation to oxidation potentials and a very high oxidation potential is needed for the formation of hematite in these conditions (Einaudi *et al.*, 2003). Where meteoric waters dominate in the shallow levels of IOCG systems, highly oxidizing assemblages (hematite + bornite) suggest that the meteoric fluids are usually highly oxidizing. This is not the case at Hamlin Lake, and this may be attributed to the anoxic conditions in the Archean atmosphere that could result in a more reducing meteoric fluid (Krupp *et al.*, 1994).

7.3 Future Work and Recommendations

Hamlin Lake is a new IOCG discovery that is in the early stages of exploration. The complex nature of the occurrence requires that studies be undertaken from a variety

of geologic angles. The present study attempts at suggesting a possible means of formation based on characterisation of the fluids through paragenetic, isotopic and fluid inclusion studies. Such a study only touches the surface of the genetic story, and many questions remain to be answered.

Even with the narrow scope of the present study, several aspects could easily be expanded upon. The large variety of analytical techniques attempted in this study should be taken as a foundation for further research. There is merit in expanding the present data set with respect to several methods that demonstrate promise in advancing the understanding of the deposit. Sodium cobaltinitrite staining was only performed on six polished slabs, but the method proved instrumental in distinguishing between iron staining and potassium feldspar alteration associated with ore. This is a relatively cheap and effective method and, if done on a larger sample set, could be a means to vectoring to a large high grade ore body. The isotopic data presented here is also a very small data set that could be expanded upon on both a local and regional scale, again with the aim of vectoring to ore bodies. Carbon isotopes from the various stages of carbonates are a possible means to a better understanding of what is going on during the transitional time between the IOCG mineralization and the epithermal stage.

Fluid inclusions in quartz from late stages of alteration prove to be useful in establishing the role of low temperature fluids in late ore formation, but no early generations of quartz could be easily identified to undertake a similar study on early fluids. It is possible that these early generations are absent given the estimations for early fluid temperatures; however, more reliable means of identifying multiple stages of quartz should be tested. These may include in situ $\delta^{18}O$ isotope analysis of quartz using

secondary ion mass spectrometry (SIMS) or by utilizing cathodoluminescence (CL) imagery. If these early generations of quartz can be identified, quantitative studies of their fluid inclusions would resolve many issues concerning the temperature and properties of the early fluids.

On a more regional scale, detailed studies on the Powell Lake Granite, with respect to its age, petrology and chemistry should be undertaken, since it is a very viable candidate as a heat source or even as a fluid source for many of the deposits along its boundaries. The volcanic rocks mapped as shoshonites in contact with the northern boundary of the Powell Lake Granite may in fact be the regional sodic alteration that is characteristic of an IOCG district. Mapping and geochemistry of this unit needs to be done to verify that this unit is indeed shoshonitic.

Another area of research that needs to be addressed is the structural side of the genetic story, which is hardly touched upon in the present study. IOCG deposits always have a strong structural component, and this closely relates to fluid movement. A full characterization of the breccia at Hamlin Lake is recommended and should be correlated with regional deformation events (discussed in Chapter 3). Relating the structural component of Hamlin Lake to other copper-gold deposits in the region (not only IOCG but the abundant shear-hosted gold deposits as well), could provide much insight and may shed light on the Shebandowan greenstone belt as a district for further IOCG exploration.

7.4 Concluding Remarks

The extreme diversity of the IOCG class of deposits makes these especially difficult deposits to study. At Hamlin Lake, a grassroots IOCG occurrence, the rocks are Archean in age adding yet another level of complexity to the system. For these reasons, the scope of the present study entails a variety of petrographic, stable isotope and geochemical methods in order to provide insight to the formation of these types of deposits in the Shebandowan greenstone belt in Ontario, Canada.

A variety of generic genetic models have been proposed to explain the tectonic settings in which IOCG deposits can form (Williams *et al*., 2005, Mumin, *et al.*, 2009, Williams, 2010b). Many, if not all, of these models include magmatic-hydrothermal systems such as those active in the Superior Province during the Archean period. The role of various proportions of magmatic and non-magmatic fluids in the formation of IOCG deposits is still highly debated, but it seems evident that the deposits can form from fluids of either derivation. Several districts (most notably in the Great Bear Magmatic Zone and along the Peru-Chile coastal belt) where IOCG deposits are prominent often exhibit a continuum of deposit styles between porphyry, IOCG and epithermal. It seems evident that the particular style of IOCG deposit present depends largely on where in this continuum the deposit sits. Figure 7.2 (Williams, 2010b) depicts the various environments where IOCG and related deposits typically form.

There is evidence for both deep-seated fluids and crustal fluids at Hamlin Lake. The mineralization seems to have formed through a complex history involving constantly

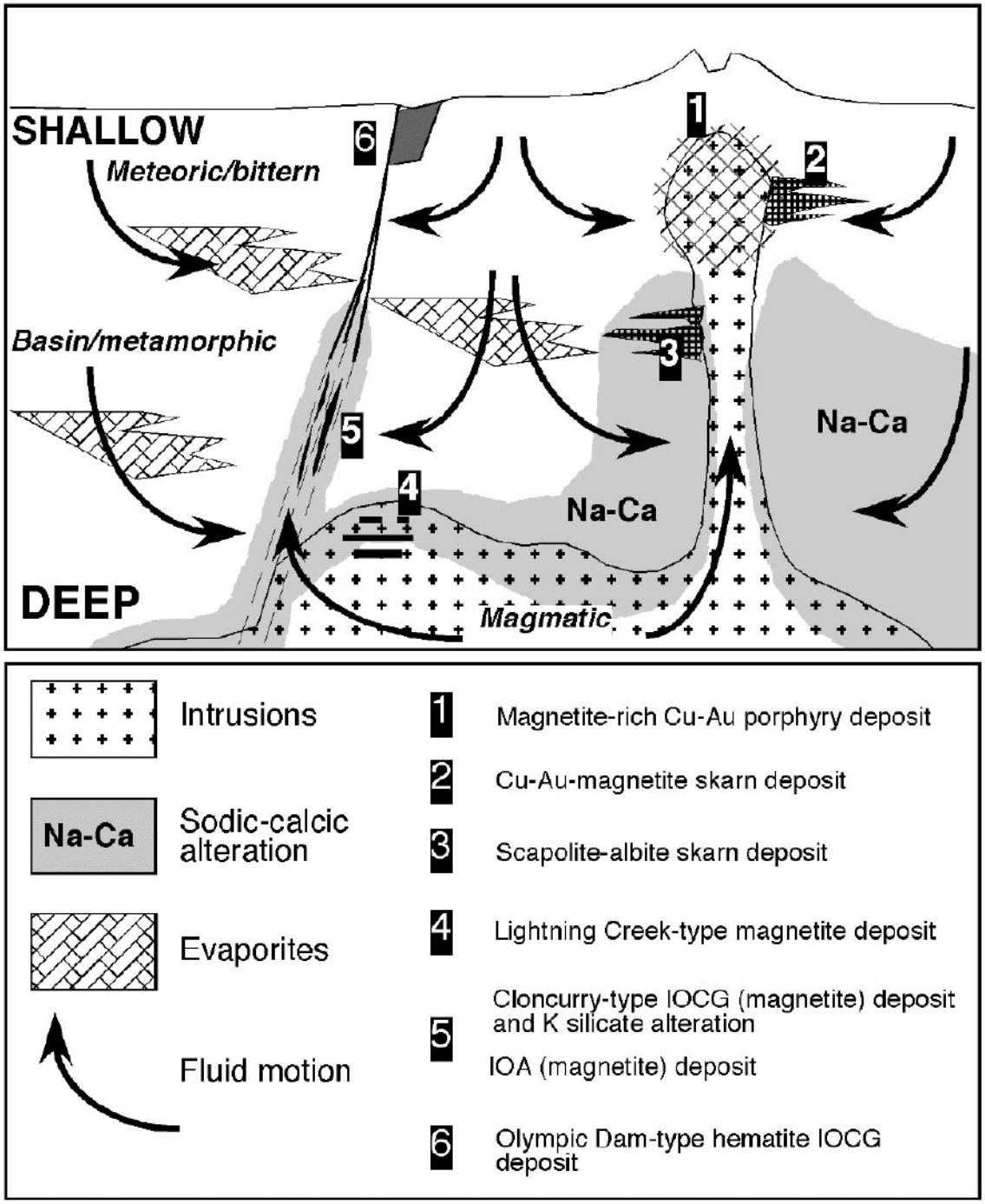

Figure 7.2 – Cartoon from Williams (2010b) depicting the roles of crustal versus magmatic fluids in the formation of IOCG and related deposits. Epithermal deposits are not included on the diagram, but form at depths less than those of areas 1 and 6.

changing structural and geochemical conditions. Where preserved, early copper mineralization and associated potassic alteration appears to be consistent with many Cloncurry type IOCG deposits; however, textural and mineralogical evidence from late (or distal) assemblages suggests that conditions shifted to those of an epithermal environment. This shift in conditions does not require any physical change in the depth of formation. While high temperature conditions are dominant in the region most proximal to the heat source, the system rapidly changes to near surface conditions in distal environments. If the heat source is emplaced at a shallow enough level, then this transition will be over a relatively small distance. In the Sue-Dianne deposit in the Great Bear Magmatic Zone the system transitions from magmatic conditions to near surface conditions in only 300 meters (Mumin *et al.*, 2010). As the system begins to retrograde as a whole, the "epithermal" styles of alteration can collapse and superimpose on the high-temperature alteration styles, and this seems to be the case at Hamlin Lake.

References

Baker, T., Perkins, C., Blake, K.L. and Williams, P.J., 2001. Radiogenic and stable isotopic constraints on the genesis of the Eloise Cu-Au deposit, Cloncurry district, NW Queensland, Australia. Economic Geology, v.96, p.723-742.

Barton, M.D. and Johnson, D.A., 1996. Evaporitic source model for igneous related Fe oxide-(REE-Cu-Au-U) mineralization. Geology, v.24, p.259-262.

Beaudoin, G. and Dupuis, C., 2010. Iron-oxide trace element fingerprinting of mineral deposit types. GAC SCN 20: Exploring for IOCG deposits: Canada and global analogues, p.111-125.

Bédard, J.H., Brouillette, P., Madore, L. and Berclaz, A., 2003. Archaean cratonization and deformation in the northern superior Province, Canada: an evaluation of plate tectonic versus vertical tectonic models. Precambrian Research, v.127, p.61-87.

Belprerio, A.P., Flint, R. and Freeman, H., 2007. Prominent Hill; a hematite-dominated, iron oxide copper-gold system. Economic Geology, v.102, p.1499-1510.

Benavides, J., Kyser, T.K., Clark, A.H., Oates, C.J., Zamora, R., Tarnovschi, R. and Castillo, B., 2007. The Mantoverde iron oxide-copper-gold district, III region Chile: The role of regionally derived, nonmagmatic fluids in chalcopyrite mineralization. Economic Geology, v.102, p.415-440.

Bennett, N.A., 2007. An investigation of the potential IOCG occurrence at Hamlin Lake, Northwestern Ontario. Unpublished bachelor's thesis, Lakehead University, Thunder Bay, Ontario, 25p.

Bérubé, D., and Jébrak, M., 1999. High precision boundary fractal analysis for shape characterization. Computers and Geosciences, v.25, p.1059-1071.

Bodnar, R.J., Burnham, C.W. and Sterner, S.M., 1985. Synthetic fluid inclusions in natural quartz. III. Determination of the phase equilibrium properties in the system H_2O-NaCl to 1000°C and 1500 bars. Geochimica et Cosmochimica Acta, v.49, p.1861-1873.

Bodnar, R.J., 1993. Revised equation and table for determining the freezing point depression of H2O-NaCl solutions. Geochimica et Cosmochimica Acta, v.57, p.683-684.

Byron, S.J., Gleeson, S., Goad, R., Ootes, L. and Jackson, V., 2006. Quartz vein at NICO Great Bear magmatic zone, Northwest Territories (abstract only): 34th Yellowknife Geoscience forum, Yellowknife, NT.

Card, K.D. and Ciesielski, A., 1986. DNAG#1, Subdivisions of the Superior Province of the Canadian Shield. Geoscience Canada, v.13, p.5-13.

Cathelineau, M. and Nieva, D., 1985. A chlorite solid solution geothermometer The Los Azufres (Mexico) geothermal system. Contributions to Mineral Petrology, v.91, p.235-244.

Chen, H., Clark, A.H., Kyser, T.K., Ullrich, T.D., Baxter, R., Chen, Y. and Moody, T.C., 2010. Evolution of the Giant Marcona-Mina Justa iron oxide-copper-gold district, South-Central Peru. Economic Geology, v.105, p.155-185.

Clayton, R.N. and Mayeda, T.K., 1963. The use of bromine pentafluoride in the extraction of oxygen from oxides and silicates for isotopic analysis. Geochimica et Cosmochimica, v.27, p.43-52.

Cole, D.R., Horita, J., Eniamin, V., Polyakov, V.B., Valley J.W., Spicuzza, M.J., Coffey and D.W., 2004. An experimental and theoretical determination of oxygen isotope fractionation in the system magnetite-H_2O from 300° to 800°C. Geochimica et Cosmochimica Acta, v.68, p.3569-3585.

Corfu, F. and Stott, G.M., 1998. Shebandowan Greenstone Belt, western Superior Province: U ages, tectonic implications, and correlations. GSA Bulletin, v.110, p.1467-1484.

Corriveau, L., Williams, P.J. and Mumin, A.H., 2010. Alteration vectors to IOCG mineralization from uncharted terranes to deposits. GAC SCN 20: Exploring for IOCG deposits: Canada and global analogues, p.89-110.

de Haller, A., Corfu, F., Fontboté, L., Frank, M. and Zuniga, A.J., 2006. Geology and U-Pb geochronology of the Raul-Condestable iron oxide-copper-gold deposit, central coast of Peru. Economic Geology, v.101, p.281-310.

de Haller, A. and Fontboté, L., 2009. The Raúl-Condestable iron oxide copper-gold deposit, central coast of Peru: ore and related hydrothermal alteration, fluid inclusions, sulfur isotopes, and thermodynamic constraints. Economic Geology, v.104, pp.365-384.

Deer, W.A., Howie, R.A. and Zussman, J., 1992. An introduction to the rock forming minerals (second edition). Essex: Pearson Education Limited, 696p.

Dreher, A.M., Xavier, R.P., Taylor, B.E. and Martini, S.L., 2008. New geologic, fluid inclusion and stable isotope studies on the controversial Igarapé Bahia Cu-Au deposit, Carajas Province, Brazil. Mineralium Deposita, v.43, p.161-184.

Edfelt, A., Armstrong, R.N., Smith, M. and Martinsson, O., 2005. Alteration paragenesis and mineral chemistry of the Tjårrojåkka apatite-iron and Cu (-Au) occurrences, Kiruna area, Northern Sweden. Mineralium Deposita, v.40, p.409-434.

Einaudi, M.T., Hedenquist, J.W. and Inan, E.E., 2003. Sulfidation states of Fluids in Active and Extinct Hydrothermal Systems: Transitions from Porphry to Epithermal Environments. Society of Economic Geologists, Special Publication 10, p.285-313.

Engvik, A.K., Putnis, A., Fitzgerald, J.D. and Austrheim, H., 2008. Albitization of granitic rocks: the mechanism of replacement of oligoclase by albite. The Canadian Mineralogist, v. 46, p.1401-1415.

Fisher, L.A. and Kendrick, M.A., 2008. Metamorphic fluid origins in the Osborne Fe oxide-Cu-Au deposit, Australia: evidence from noble gasses and halogens. Mineralium Deposita, v.43, p.483-497.

Gandhi, S.S., Prasad, N. and Charbonneau, B.W., 1996. Geological and geophysical signatures of a large polymetallic exploration target at Lou Lake, Southern Great Bear Magmatic Zone, Northwest Territories. Geological Survey of Canada, Current Reasearch paper 1996-E, p.147-158.

Giblin, P.E., 1964. Geology of the Burchell Lake Area, District of Thunder Bay. Ontario Department of Mines, Geological Report 19, 39p.

Graham, C.M., Atkinson, J. and Harmon, R.S., 1984. Hydrogen isotope fractionation in the system chlorite-water. NERC 6th Progress Report of Research 1981-1984, NERC Publication Series D, No. 25, p.139.

Grainger, C.J., Groves, D.I., Tallarico, F.H.B. and Fletche, I.R., 2008. Metallogenesis of the Carajás Mineral Province, Southern Amazon Craton, Brazil: Varying styles of Archean through Paleoproterozoic to Neoproterozoic base- and precious-metal mineralisation. Ore Geology Reviews, v.33, p.451-489.

Goad, R.E., Mumin, A.H., Duke, N.A., Neale, K.L. and Mulligan, D.L., 2000. Geology of the iron oxide-hosted NICO cobalt-gold-bismuth, and Sue Dianne copper-silver deposits, southern Great Bear Magmatic Zone, Northwest Territories, Canada. *in* Porter, T.M. (Ed.), Hydrothermal Iron Oxide-Copper-Gold and Related Deposits: A Global perspective: Australian Mineral Foundation, v.1, p.249-267.

Harris, F.R., 1970. Geology of the Moss Lake Area, District of Thunder Bay. Ontario Department of Mines and Northern Affairs, Geological Report 85, 61p.

Hart, T.R. and Metsaranta, D.-A. 2009. Precambrian geology of the Wye and Hamlin lakes area. Ontario Geological Survey, Preliminary Map P.2511, scale 1:20 000.

Heinrich, C. A., Pettke, T., Halter, W. E., Aigner-Torres, M., Audétat, A., Günther, D., Hattendorf, B., Bleiner, D., Guillong, M. and Horn, I., 2003. Quantitative multi-element analysis of minerals, fluid and melt inclusions by laser-ablation inductively-coupled-plasma mass-spectrometry. Geochim. et Cosmochim, Acta, v.67, p.3473-3497.

Hitzman, M.W., Oreskes, N. and Einaudi, M.T., 1992. Geological characteristics and tectonic setting of iron oxide (Cu-U-Au-LREE) deposits. Precambrian Research, v.58, p.241-287.

Hodgkinson, J.M., 1968. Geology of the Kashabowie area, District of Thunder Bay. Ontario Department of Mines, Geological Report 53, 35p.

Hollings, P., Wyman, D. and Kerrich, R., 1999. Komatiite-basalt-rhyolite volcanic associations in Northern Superior Province Greenstone Belts: significance of plume-arc interaction in the generation of the proto continental Superior Province. Lithos, v.46, p.137-161.

Huston, D.L., Bolger, C., and Cozens, G., 1993. A comparison of mineral deposits at the Gecko and White Devil deposits: implications for ore genesis in the Tennant Creek District, Northern Territory, Australia. Economic Geology, v.88, p.1198-1225.

Hutchison, C.S., 1974. Laboratory handbook of petrographic techniques. New York: Wiley, 527p.

Jébrak, M., 2010. Use of breccias in IOCG(U) exploration. GAC SCN 20: Exploring for IOCG deposits: Canada and global analogues, p.79-87.

Kendrick, M.A., Honda, M., Gillen, D., Baker, T and Phillips, D., 2008. New constraints on regional brecciation in the Wernecke Mountains, Canada, from He, Ne, Ar, Kr, Xe, Br and I in fluid inclusions. Chemical Geology, v.255, p.33-46.

Krupp, R., Oberthur, T. and Hirdes, W., 1994. The early Precambrian atmosphere and hydrosphere: thermodynamic constraints from mineral deposits. Economic Geology, v.89, p.1581-1598.

Kyser, T.K. and O'Neil, J.R., 1984. Hydrogen isotope systematics of submarine basalts. Geochimica et Cosmochimica, vol.48, p.2123-2133.

Landry, J.-Y., 2006. Detailed relationships of iron oxide-copper-gold type alteration zones at DeVries Lake, southern Great Bear magmatic zone, NWT. Unpublished bachelors thesis, University of Ottawa, Ottawa, Ontario, 73p.

Lavigne, M.J., Aubut, A.J. and Scott, J.F., 1990. Base metal mineralization in the Shebandowan Greenstone Belt. In Field Trip Guidebook, 36th Annual Meeting, Institute on Lake Superior Geology, vol.36, pt.2, p.67-97.

Li, Y.B. and Liu, J.M., 2006. Calculation of sulfur isotope fractionation in sulfides. Geochimica et Cosmochimica Acta, v.70, p.1789-1795.

Mark, G., Foster, D.R.W., Pollard, P.J., Williams, P.J., Tolman, J., Darvall, M. and Blake, K.L., 2004. Stable isotope evidence for magmatic fluid input during large-scale Na-Ca alteration in the Cloncurry Fe oxide Cu-Au district, NW Queensland, Australia. Terra Nova, v.16, p.54-61.

Mark, G., Oliver, N.H.S. and Williams, P.J., 2006. Mineralogical and chemical evolution of the Ernest Henry Fe oxide-Cu-Au ore system, Cloncurry district, northwest Queensland. Mineralium Deposita, v.40, p.769-801.

Marschik, R., and Fontboté, L., 2001. The Candelaria-Punta del Cobre iron oxide-Cu-Au (-Zn-Ag) deposits, Chile. Economic Geology, v.96, p.1799-1826.

Meinert, L.M., Dipple, G.M. and Nicoolescu, S., 2005. World skarn deposits. Economic Geology 100th Anniversary Volume, p.299-336.

Monteiro, L.V.S., Xavier, R.P., de Carvalho, E.R., Hitzman, M.W., Johnson, C.A., de Souza Filho, C.R. and Torresi, I., 2008. Spatial and temporal zoning of hydrothermal alteration and mineralization in the Sossego iron oxide-copper-gold deposit, Carajás Mineral Province, Brazil: paragenesis and stable isotope constraints. Miner Deposita, v.43, p.129-159.

Mumin, A.H., Corriveau, L., Somarin, A.K. and Ootes, L., 2007. Iron oxide copper-gold type polymetallic mineralization in the Contact Lake Belt, Great Bear Magmatic Zone, Northwest Territories, Canada. Exploration and Mining Geology, v.16, p.187-208.

Mumin, A.H., Somarin, A.K., Jones, B., Corriveau, L., Ootes, L. and Camier, J., 2010. The IOCG-porphyry-epithermal continuum of deposit types in the Great Bear Magmatic Zone, Northwest Territories, Canada. GAC SCN 20: Exploring for IOCG deposits: Canada and global analogues, p.39-57.

Naslund, H.R., Henriquez, F., Nystrom, J.O., Vivallo, W. and Dobbs, F.M., 2002. Magmatic iron ores and associated mineralisation: examples from the Chilean

High Andes and Coastal Cordillera. in Porter, T.M. (Ed.), Hydrothermal iron oxide-copper-gold and related deposits: A Global perspective: Australian Mineral Foundation, v.2, p.207-226.

Nystrom, J.O., and Henriquez, F., 1994. Magmatic features of iron ores of the Kiruna-type in Chile and Sweden: ore textures and magnetite geochemistry. Economic Geology, v.89, p.820-839.

Ohmoto, H. and Rye, R.O., 1979. Isotopes of sulfur and carbon, *in* Barnes, H.L. Ed., Geochemestry of Hydrothermal deposits, John Wiley & Sons, p.509-567.

Oliver, N.H.S., Cleverly, J.S., Geordie, M., Pollard, P.J., Fu, B., Marshall, L.J., Rubenach, M.J., Williams, P.J. and Baker, T., 2004. Modeling the role of sodic alteration in the genesis of iron oxide-copper-gold deposits, Eastern Mount Isa Block, Australia. Economic Geology, v.99, p.1145-1176.

Osmani, I.A., 1997. Geology and mineral potential: Greenwater Lakes area, West-Central Shebandowan Greenstone Belt. Ontario Geological Survey, Report 296, 135p.

Percival, J.A., Sanborn-Barrie, M., Skulski, T., Stott, G.M., Helmstaedt, H. and White, D.J. 2006. Tectonic evolution of the western Superior Province from NATMAP and Lithoprobe studies. Canadian Journal of Earth Sciences, v.43, p.1085-1117.

Perring, C.S., Pollard, P.J., Dong, G, Nunn, A.J. and Blake, K.L., 2000. The Lightning Creek Sill Complex, Cloncurry District, Northwest Queensland: A source of fluids for Fe oxide Cu-Au mineralization and sodic-calcic alteration. Economic Geology, v.95, p.1067-1089.

Polat, A. and Kerrich, R., 2001. Magnesian andesites, Nb-enriched basalt andesites, and adakites from late-Archean 2.7 GA Wawa Greenstone Belts, Superior Province Canada: implications for late Archean subduction zone petrogenetic processes. Contributions to Mineral Petrology, v.141, p.36-52.

Pollard, P.J., 2001. Sodic(-calcic) alteration in Fe-oxide-Cu-Au districts: an origin via unmixing of magmatic H_2O-CO_2-NaCl +/- $CaCl_2$-KCl fluids. Mineralium Deposita, v.36, p.93-100.

Requia, K. and Fontboté, L., 2001. The Salobo iron oxide copper-gold system, Carajás mineral province, Brazil (abstract only). Geological Society of America, 2001 annual meeting, v.33, p.2.

Rieger, A., 2010. The hypogene iron oxide copper-gold mineralization in the Mantoverde District, northern Chile. Economic Geology, v.105, p.1271-1299.

Rotherham, J.F., Blake, K.L., Cartwright, I. and Williams, P.J., 1998. Stable isotope evidence for the origin of the Mesoproterozoic Starra Au-Cu deposit, Cloncurry district, northwest Queensland. Economic Geology, v.93, p.1435-1449.

Savin, S.M. and Lee, M., 1988. Isotopic studies of phyllosilicates, in Bailey, S.W., ed., Hydrous phyllosilicates, Reviews in Mineralogy, v.19, p.189-223.

Seedorff, E., Dilles, J.H., Proffett, J.M., Einaudi, M.T., Zurcher, L., Stavast, W.J.A., Johnstone, D.A. and Barton, M.D, 2005. Porphyry deposits: Characteristics and origin of hypogene features. Economic Geology 100th Anniversary Volume, p.251-298.

Shute, A.L., 2009. Geology and alteration associated with the Hamlin Lake VMS system, Shebandowan Greenstone belt, Northwestern Ontario, Canada. Unpublished M.Sc thesis, Lakehead University, Thunder Bay, Ontario 213p.

Sillitoe, R.H., 2003. Iron oxide-copper-gold deposits: an Andean view. Mineralium Deposita, v.38, p.787-812.

Simard, M., Beaudoin, G. and Hupé, A. 2006. Metallogeny of the Mont-de-l'Aigle IOCG deposit, Gaspé Peninsula, Quebec, Canada. Mineralium Deposita, v.41, p.607-636.

Simmons, S.F., White N.C. and John, D.A., 2005. Geological characteristics of epithermal precious and base metal deposits. Economic Geology 100th anniversary edition, p.485-522.

Sheppard, S.M.F., 1986. Characterization and isotopic variations in natural waters. *In* Stable isotopes in high temperature geological processes, J.W. Valley, H.P. Taylor Jr., and J.R. O'Neil, eds. Mineralogical Society of America, Washington, D.C., p.165-183.

Skirrow, R.G., and Walshe, J.L., 2002. Reduced and oxidized Au-Cu-Bi-iron oxide deposits of the Tennant Creek Inlier, Australia: an integrated geologic and chemical model. Economic Geology, v.97, p.1167-1202.

Skirrow, R.G., Bastrakov, E.N. and Barovich, K., 2006. Metals and fluids in IOCG systems of the Gawler Craton: Constraints from Nd, O, H, and S isotopes. Geochimicha et Cosmochimica Acta, v.70, p.A595.

Skirrow, R., 2010. "Hematite-Group" IOCG +/- U Ore systems: tectonic settings, hydrothermal characteristics, and Cu-Au and U mineralizing processes. GAC SCN 20: Exploring for IOCG deposits: Canada and global analogues, p.39-57.

Smith, M., Coppard, J., Herrington, R. and Stein H., 2007. The geology of the Rakkurijarvi Cu-(Au) prospect, Norrbotten: A new iron oxide-copper-gold deposit in Northern Sweden. Economic Geology, v.102, p.393-414.

Stone, D., 2005. Geology of the northern Superior area, Ontario. Ontario Geological Survey, Open File Report 6140, 94p.

Stott, G.M. and Schnieders, B.R., 1983. Gold mineralization in the Shebandowan Belt and its relation to regional deformation patterns. Geology of Gold in Ontario, Ontario Geological Survey, Miscellaneous paper 110, p.181-193.

Stott, G.M., Corkery, T., Leclair, A., Boily, M. and Percival, J., 2007. A revised terrane map for the Superior Province as interpreted from aeromagnetic data (abstract only). Institute on Lake Superior Geology Proceedings, 53rd annual meeting, Lutsen, MN, v53, pt.1, p.74-75.

Stott, G.M., Corkery, M.T., Percival, J.A., Simard, M. and Goutier, J., 2010. Project Units 98-006 and 98-007. A revised terrane subdivision of the Superior Province. Ontario Geological Survey, Open File Report 6260, p.20.1-20.10.

Streckeisen, A.L., 1974. Classification and Nomenclature of Plutonic Rocks. Recommendations of the IUGS Subcommission on the Systematics of Igneous Rocks. Internationale Zeitschrift für Geologie, v.63, p.773-785.

Taylor, H.P., 1974. The application of oxygen and hydrogen isotope studies to problems of hydrothermal alteration and ore deposition. Economic Geology, v.69, p.843-883.

Thurston, P.C., 1991. Archean Geology of Ontario: Introduction. Geology of Ontario, Ontario Geological Survey Special vol. 4, pt.1, p.73-78.

Thurston, P.C., Osmani, I.A. and Stone, D., 1991. Northwestern Superior Province: review and terrane analysis. Geology of Ontario, Ontario Geological Survey Special vol.4, pt.1, p.81-141.

Thurston, P.C., 2002. Autochthonous development of Superior Province greenstone belts? Precambrian Research, v.115, p.11-36.

Wanhainen, C., Broman, C. and Martinsson, O., 2003. The Aitik Cu-Au-Ag deposit in northern Sweden: a product of high salinity fluids. Mineralium Deposita, v.38, p.715-726.

Wanhainen, C., Billstrom, K., Martinsson, O., Stein, H. and Nordin, R., 2005. 160 Ma of magmatic/hydrothermal and metamorphic activity in the Gallivare area: Re-Os

dating of molybdenite and U-Pb dating of titanite from the Aitik Cu-Au-Ag deposit, northern Sweden. Mineralium Deposita, v.40, p.435-447.

Whalen, J.B., Percival, J.A., McNicoll, V.J. and Longstaffe, F.J., 2002. A Mainly Crustal Origin for Tonalitic Granitoid Rocks, Superior Province, Canada: Implications for Late Archean Techtonomagmatic processes. Journal of Petrology, v.43, p.1551-1570.

Williams, H.R., 1990. Subprovince accretion tectonics in the south-central Superior Province. Canadian Journal of Earth Science, v.27, p.570-571.

Williams, H.R., Stott, G.M., Heather, K.B., Muir, T.L. and Sage, R.P., 1991. Wawa Subprovince. In Geology of Ontario, Ontario Geological Survey Special vol.4, pt.1, p.485-539.

Williams, P.J., Barton, M.D., Jonson, D.A., Fontboté, L., de Haller, A., Mark, G., Oliver, N.H.S. and Marschik, R., 2005. Iron-oxide copper-gold deposits: geology, space-time distribution, and possible modes of origin. Economic Geology 100th anniversary volume, p.371-405

Williams, P.J., 2010a. Classifying IOCG Deposits. GAC SCN 20: Exploring for IOCG deposits: Canada and global analogues, p.13-21.

Williams, P.J., 2010b. "Magnetite-Group" IOCGs with Special Reference to Cloncurry (NW Queensland) and Northern Sweden: Settings, Alteration, Deposit Characteristics, Fluid Sources, and Their Relationship to Apatite-Rich Iron Ores. GAC SCN 20: Exploring for IOCG deposits: Canada and global analogues, p.23-38.

Wood, S.A., 2003. Calculation of Activity-Activity and Log fo_2-pH Diagrams. *In* J. Richards and P. Larson, eds., Techniques in Hydrothermal Ore Deposits. Reviews in Economic Geology, v.10, p.81-96.

Appendix A

Boundary Fractal Dimensions

Boundary fractal dimensions (BFD) are a quantitative measurement of how jagged the edge of a shape is. There are several methods for approximating BFD and these include: structured walk, box counting, dilation and Euclidean distance mapping methods. These are summarized in Berube and Jebrak (1999). For complex shapes such as the shape of a rock fragment, the Euclidian distance mapping method is shown to be the closest approximation to the ideal value.

The Euclidean distance mapping method for approximating BFD utilizes an image processing algorithm which produces a grayscale image. The algorithm assigns a brightness level from 0 to 255 (in a 256bit colour system) proportional to the distance from each pixel to its nearest border. This results in a dark image that brightens towards the shape's outline. Thresholding the image at various levels of grey will produce isotropic ribbons that encompass the outline. Plotting the log of the enclosed area of each ribbon versus the log of the number of grey levels will produce a straight line. The slope of the line is directly related to the BFD by:

$$BFD = 2 - s$$

where s is the slope. An example data set and plot for clast "d" in the present study is presented below (Table A1 and Figure A1).

Table A1 – Tabulated Data from clast "d" analysis.

Width	Area	log(Width)	log(Area)	Width	Area	log(Width)	log(Area)
4	27171	0.60206	4.43411	52	227550	1.71600	5.35708
6	36054	0.77815	4.55695	56	241492	1.74819	5.38290
8	47913	0.90309	4.68045	62	261753	1.79239	5.41789
10	56496	1.00000	4.75202	68	281454	1.83251	5.44941
12	66234	1.07918	4.82108	74	300596	1.86923	5.47798
14	74573	1.14613	4.87258	82	325523	1.91381	5.51258
16	83744	1.20412	4.92295	90	349760	1.95424	5.54377
18	93695	1.25527	4.97172	100	379302	2.00000	5.57899
20	101558	1.30103	5.00671	110	407861	2.04139	5.61051
22	110445	1.34242	5.04315	120	434412	2.07918	5.63790
24	118074	1.38021	5.07215	132	464463	2.12057	5.66695
26	127211	1.41497	5.10452	146	496716	2.16435	5.69611
28	135151	1.44716	5.13082	160	526736	2.20412	5.72159
32	151423	1.50515	5.18019	176	558911	2.24551	5.74734
34	159686	1.53148	5.20327	194	592558	2.28780	5.77273
38	175041	1.57978	5.24314	214	627100	2.33041	5.79734
42	190508	1.62325	5.27991	234	659267	2.36922	5.81906
46	205650	1.66276	5.31313				

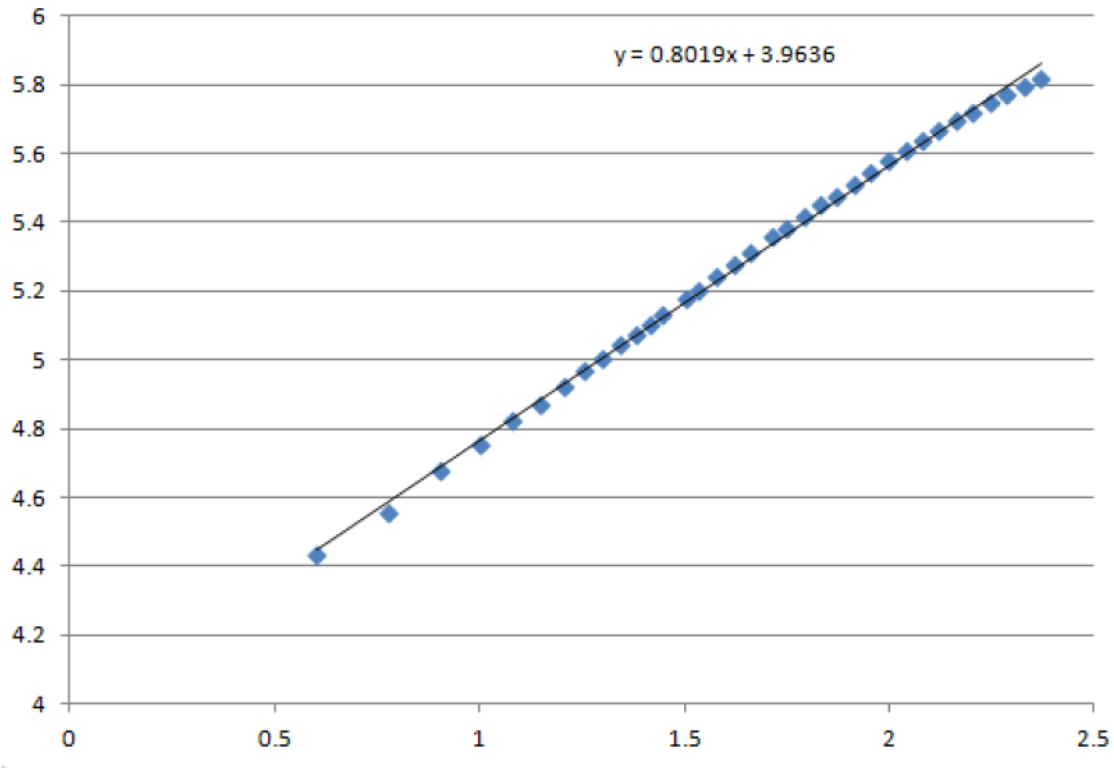

Figure A1 – Plot of the data from Table A1 with the calculated line of best fit.

Table A2 – BFD's for clasts in Figure A2

Clast	BFD
a	1.1661
b	1.144
c	1.2098
d	1.1981
e	1.2498
f	1.1241
g	1.1827
h	1.2043
i	1.2244
j	1.1585
k	1.1869
l	1.2081
m	1.166
n	1.3172
o	1.1697
p	1.129

Figure A2 – Clast outlines of the clasts used in BFD analysis.

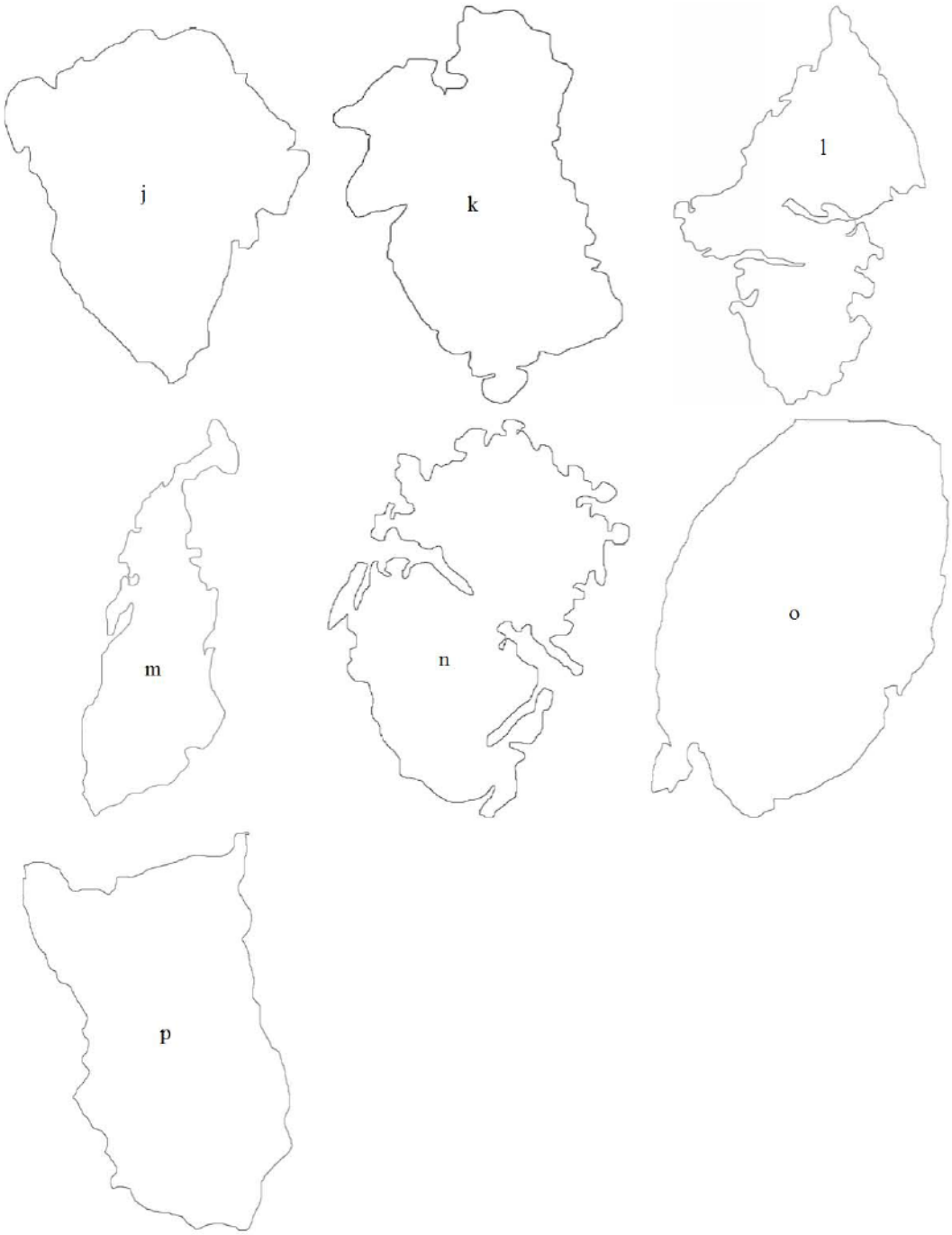

Figure A2 – (*Continued from previous page*) Clast outlines of the clasts used in BFD analysis.

Appendix B

Drill Logs and Cross Sections

Epidote Alteration Cross Sections

Brief note on method:

The following cross sections and long section are compiled using the epidote alteration data from the drill logs to follow. These sections are not "true" cross sections, in that they do not represent a truly two dimensional section. All drill holes are compiled into RockWorks and a three dimensional solid model is produced using an anisotropic inverse distance algorithm. The following sections actually represent three dimensional volumes with a 20m swath, and are projected onto a two dimensional plane centered along the sections shown on the plan map below.

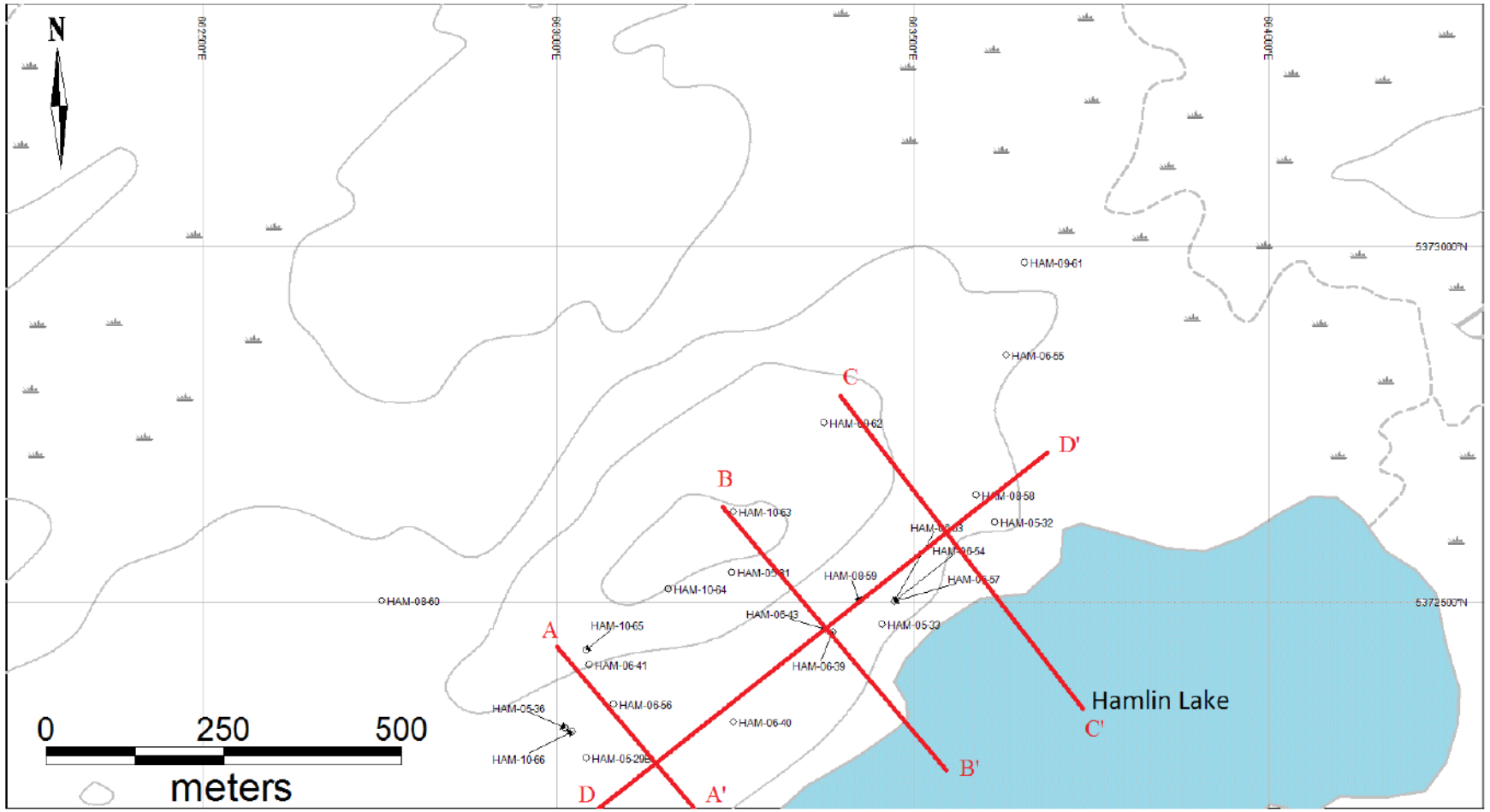
N
0
250
500
meters
A
A'
B
B'
C
C'
D
D'
Hamlin Lake
HAM-09-61
HAM-06-55
HAM-09-62
HAM-10-63
HAM-08-58
HAM-05-32
HAM-08-54
HAM-08-59
HAM-05-57
HAM-10-64
HAM-08-60
HAM-06-43
HAM-05-33
HAM-10-65
HAM-06-41
HAM-06-39
HAM-06-56
HAM-05-36
HAM-06-40
HAM-10-66
HAM-05-29
5373000mN
5372500mN

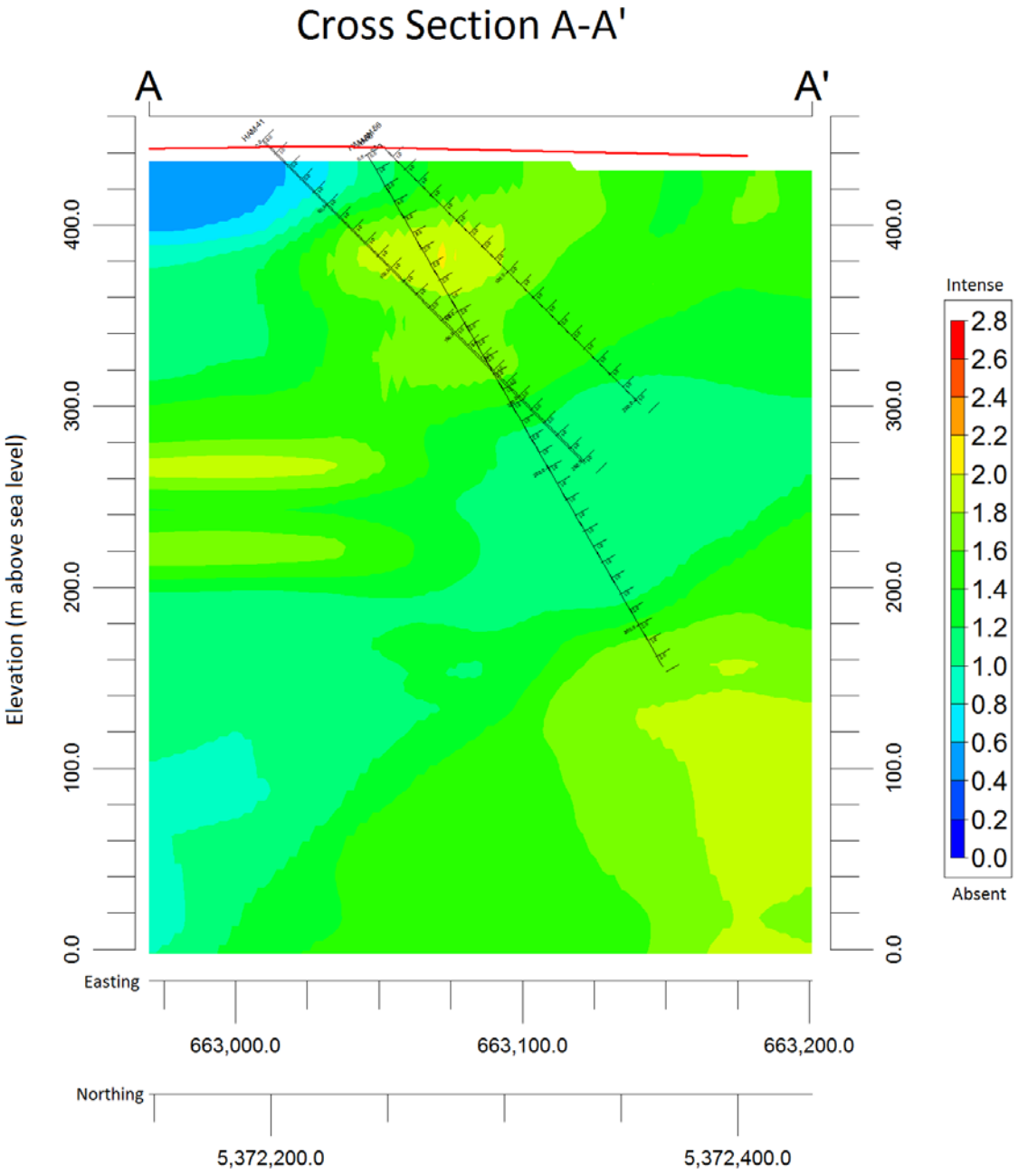
Cross Section A-A'
A
A'
Elevation (m above sea level)
400.0
300.0
200.0
100.0
0.0
Intense
2.8
2.6
2.4
2.2
2.0
1.8
1.6
1.4
1.2
1.0
0.8
0.6
0.4
0.2
0.0
Absent
Easting
663,000.0
663,100.0
663,200.0
Northing
5,372,200.0
5,372,400.0

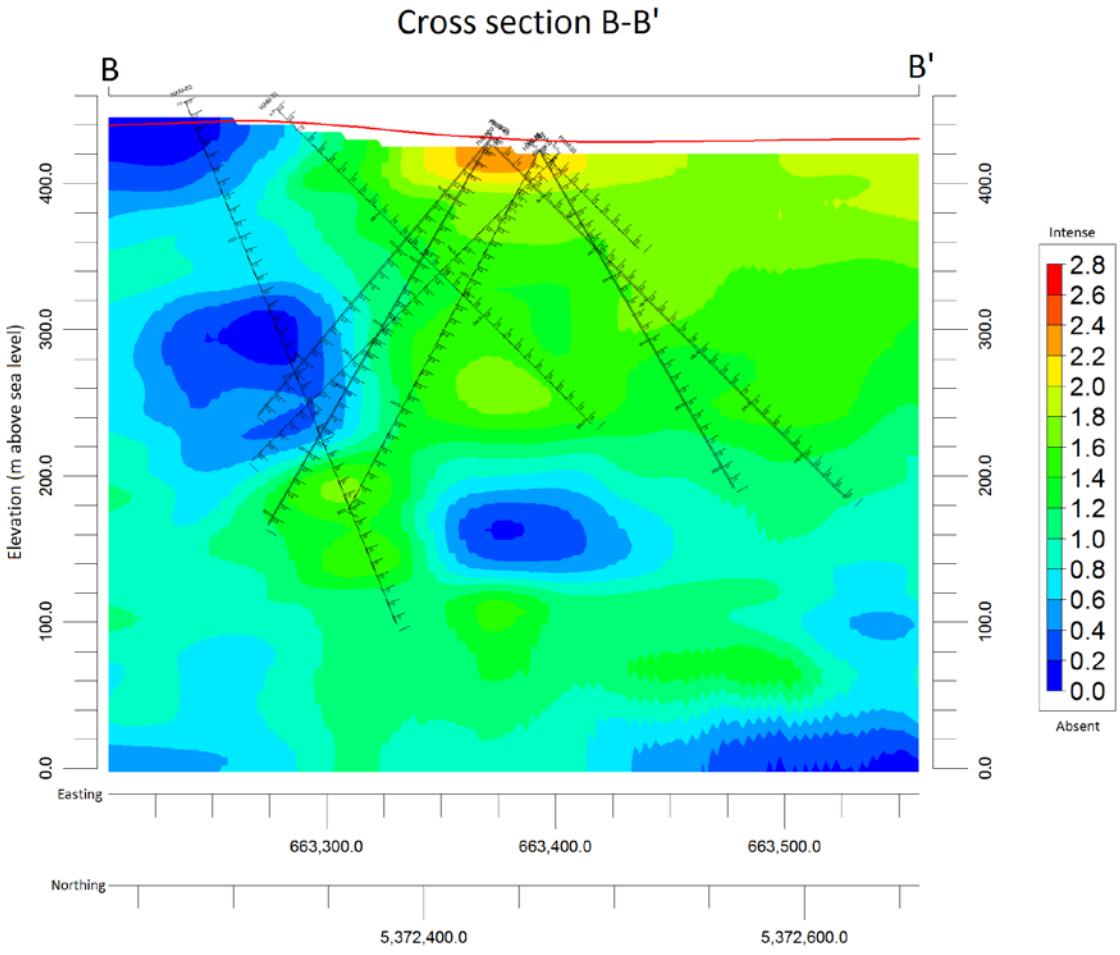
Cross section B-B'
B
B'
Elevation (m above sea level)
0.0
100.0
200.0
300.0
400.0
Easting
663,300.0
663,400.0
663,500.0
Northing
5,372,400.0
5,372,600.0
Intense
2.8
2.6
2.4
2.2
2.0
1.8
1.6
1.4
1.2
1.0
0.8
0.6
0.4
0.2
0.0
Absent

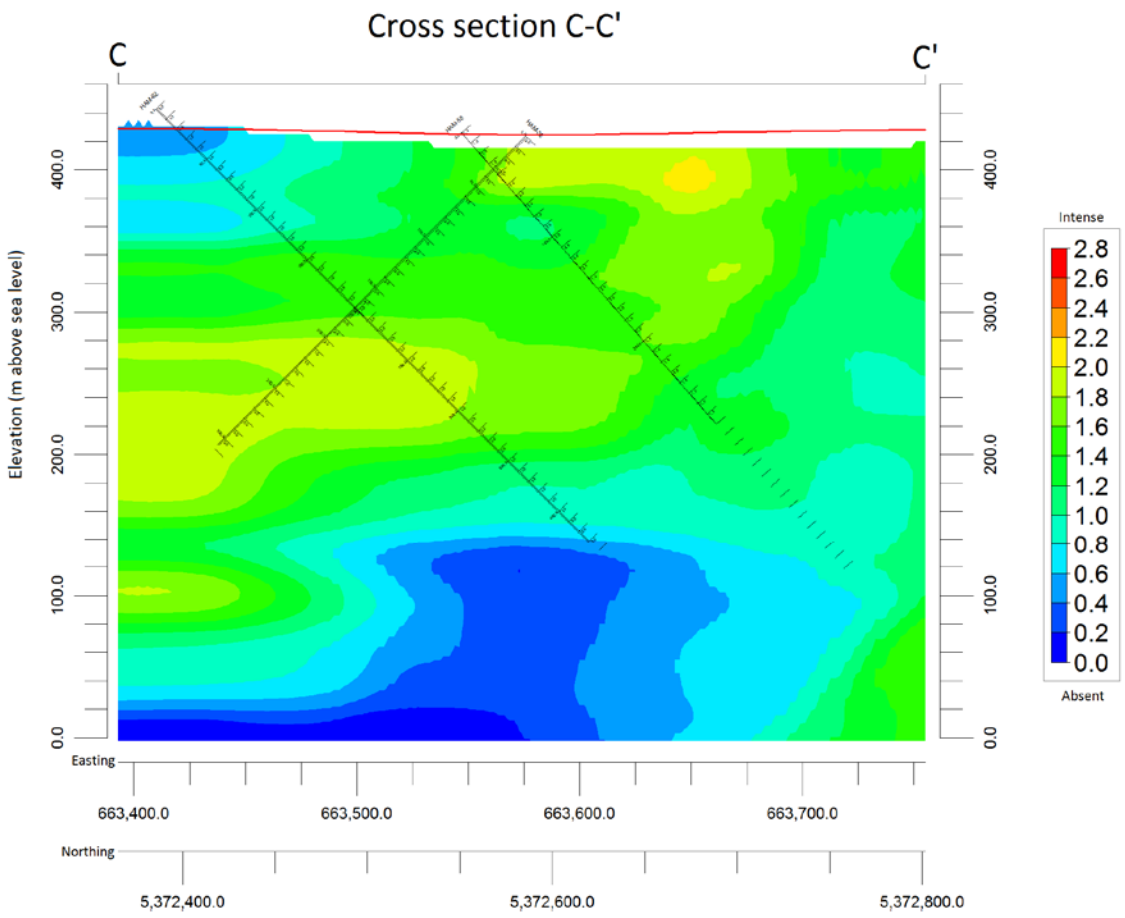
Cross section C-C'
C
C'
Elevation (m above sea level)
400.0
300.0
200.0
100.0
0.0
Intense
2.8
2.6
2.4
2.2
2.0
1.8
1.6
1.4
1.2
1.0
0.8
0.6
0.4
0.2
0.0
Absent
Easting
663,400.0
663,500.0
663,600.0
663,700.0
Northing
5,372,400.0
5,372,600.0
5,372,800.0

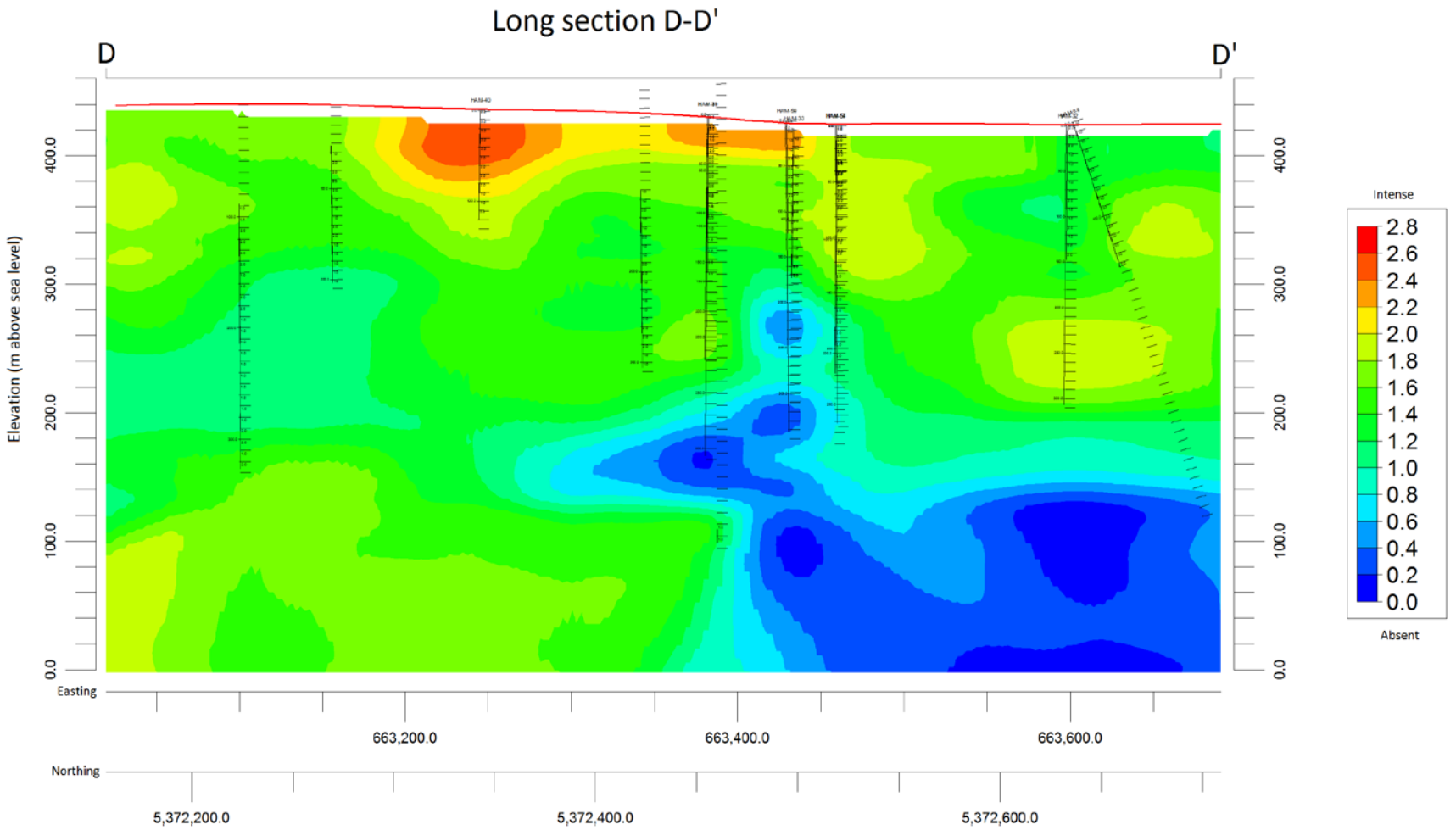
Long section D-D'
D
D'
Elevation (m above sea level)
400.0
300.0
200.0
100.0
0.0
Easting
663,200.0
663,400.0
663,600.0
Northing
5,372,200.0
5,372,400.0
5,372,600.0
Intense
2.8
2.6
2.4
2.2
2.0
1.8
1.6
1.4
1.2
1.0
0.8
0.6
0.4
0.2
0.0
Absent

Drill Logs

Hole:	HAM-29B
Azimuth:	140
Dip:	-45
Easting:	663040
Northing:	5372281
Date:	27-Apr

From: (m)	To: (m)	Description:
0	5.4	Overburden
5.4	17.3	Large fragments of mafic to intermediate volcanics with small intervals of more intensely brecciated volcanics, some areas display a more vein style brecciation.
17.3	93	Brecciated felsic volcanics, quartz eyes in volcanic clasts. Clasts range from <1mm to 10cm. Clasts are generally angular, some clasts show evidence of multiple brecciation events.
93	101.7	Heterolithic breccia with clasts of both felsic volcanics, and clasts of diorite. Clasts range from 1cm-20cm.
101.7	113.4	Brecciated diorite. Clasts range from 2 to 40cm.
113.4	152.4	Heterolithic breccia with clasts of diorite (1-20cm) and volcanics (2mm-5cm).
EOH		

Hole: HAM-030
Azimuth: 140
Dip: -60
Easting: 663040
Northing: 5372281
Date: 29-Apr

From: (m)	To: (m)	Description:
0	2	Overburden
2	16.8	Stockworked mafic to intermediate volcanics, minor brecciation in places.
16.8	120.6	Brecciated felsic to intermediate volcanics, various clast to matrix ratios which seem to affect alteration.
120.6	138.9	Brecciated diorite, diorite represents ~90% of clasts, other clasts are felsic to intermediate volcanics.
138.9	180.1	Heterolithic breccia with clasts of diorite and felsic volcanics, dominantly felsic volcanics.
EOH		

Hole:	HAM-31	a=absent	chl = chlorite	bi = biotite
Azimuth:	140	w=weak	mt = magnetite	cc = calcite
Dip:	-45	m=moderate	ep = epidote	py = pyrite
Easting:	663241	i=intense	qtz = quartz	cpy = chalcopyrite
Northing:	5372542		hem = hematite staining	po = pyrrhotite
Date:	25-May			

		Minerals									
From: (m)	**To: (m)**	**chl**	**mt**	**ep**	**qtz (blue)**	**hem**	**bi**	**cc**	**py**	**cpy**	**po**
0	10	i	i	a	a	a	a	w	m	w	w
10	20	i	i	a	a	a	a	w	m	w	w
20	30	w	w	w	w	a	a	m	w	w	a
30	40	w	a	m	a	a	a	m	w	w	a
40	50	m	a	m	a	a	a	w	w	a	a
50	60	m	a	m	a	a	a	w	w	w	a
60	70	m	a	w	a	a	m	w	m	m	i
70	80	w	w	w	w	a	w	w	m	m	i
80	90	m	w	w	w	a	a	w	w	m	m
90	100	w	w	m	a	w	a	m	w	w	w
100	110	m	a	w	w	a	a	w	m	m	m
110	120	w	m	w	a	w	a	w	m	w	w
120	130	w	w	w	w	m	w	w	w	w	a
130	140	w	m	m	w	i	m	m	w	w	a
140	150	w	w	w	w	m	a	w	m	w	w
150	160	m	m	w	w	m	a	w	m	m	a
160	170	m	w	m	m	m	w	a	w	m	a
170	180	m	w	w	m	m	a	w	w	w	a
180	190	w	m	w	m	w	a	w	a	a	a
190	200	w	m	m	i	w	a	w	w	w	a
200	210	w	m	m	m	w	a	w	w	w	a
210	220	m	m	w	w	m	a	w	w	m	a
220	230	m	w	w	m	w	w	w	w	w	a
230	240	m	a	w	m	w	w	w	w	w	a
240	250	m	w	w	w	m	w	m	w	w	a

Hole:	HAM-31	a=absent	chl = chlorite	bi = biotite
Azimuth:	140	w=weak	mt = magnetite	cc = calcite
Dip:	-45	m=moderate	ep = epidote	py = pyrite
Easting:	663241	i=intense	qtz = quartz	cpy = chalcopyrite
Northing:	5372542		hem = hematite staining	po = pyrrhotite
Date:	25-May			

		Minerals									
From: (m)	**To: (m)**	**chl**	**mt**	**ep**	**qtz (blue)**	**hem**	**bi**	**cc**	**py**	**cpy**	**po**
250	260	m	w	m	w	w	w	w	w	w	a
260	270	w	a	m	m	w	w	m	w	w	a
270	280	w	a	m	w	w	a	m	w	w	a
280	290	w	a	m	w	w	w	m	a	a	a
290	300	m	a	w	w	m	w	m	w	m	a
300	310	w	w	w	w	m	w	w	w	w	a

Hole: HAM-31
Azimuth: 140
Dip: -45
Easting: 663241
Northing: 5372542
Date: 25-May

From: (m)	To: (m)	Description:
0	3.2	Overburden
3.2	22.7	Mafic volcanic fragmental. Felsic (or cherty?) volcanics in an extremely chloritized (mafic) matrix.
22.7	66.5	Brecciated felsic volcanics, fragments are angular and fairly undeformed, no quartz-eyes, possibly intermediate in composition.
66.5	74.6	Siliceous brecciated metasediments, shows evidence of soft sediment deformation.
74.6	108.6	Brecciated felsic to intermediate volcanics. Fragments are sub-angular. Small bands or siliceous sedaments (cherty?).
108.6	117.1	Brecciated siliceous metaseds with minor felsic to intermediate volcanics.
117.1	188.5	Intensely brecciated volcanics with minor cherty clasts.
188.5	276	Heterolithic breccia with clasts as follows: 188.5-213.1 Mostly gabbroic clasts, minor volcanic and cherty clasts. 213.1-231.1, mixed breccia with subequal proportions of volcanosedimentary and dioritic clasts. 231.1-276.0, dominantly dioritic clasts with smaller amounts of volcanosedimentary rock.
276	296.1	Fairly massive diorite, only minor brecciation in the form of pink volcanic clasts.
296.1	305.7	Heterolithic breccia with subequal proportions of diorite and felsic volcanics.
EOH		

Hole:	HAM-32	a=absent	chl = chlorite	bi = biotite
Azimuth:	320	w=weak	mt = magnetite	cc = calcite
Dip:	-45	m=moderate	ep = epidote	py = pyrite
Easting:	663614	i=intense	qtz = quartz	cpy = chalcopyrite
Northing:	5372613		hem = hematite staining	po = pyrrhotite
Date:	21-Jul			

		Minerals									
From: (m)	**To: (m)**	**chl**	**mt**	**ep**	**qtz (blue)**	**hem**	**bi**	**cc**	**py**	**cpy**	**po**
0	10	m	a	m	m	m	m	w	w	m	a
10	20	m	w	i	w	m	m	w	w	m	a
20	30	m	w	m	w	m	m	w	w	m	a
30	40	m	m	w	w	m	m	w	w	w	a
40	50	w	m	w	w	i	w	w	w	w	a
50	60	w	w	w	w	m	w	m	w	w	a
60	70	m	m	w	w	m	m	m	w	w	a
70	80	w	w	w	m	w	w	w	w	a	a
80	90	m	w	m	w	w	m	m	w	a	a
90	100	i	w	w	w	w	i	w	w	a	a
100	110	m	w	w	m	m	m	m	w	w	a
110	120	m	m	m	w	w	m	i	w	w	a
120	130	w	m	w	w	w	w	i	w	w	a
130	140	m	m	m	w	w	m	m	w	w	a
140	150	m	m	m	a	w	m	m	w	w	a
150	160	w	w	m	w	m	w	m	m	m	a
160	170	m	w	m	a	m	m	w	w	m	a
170	180	i	w	m	w	m	i	w	w	m	a
180	190	m	w	m	m	w	m	w	w	m	a
190	200	m	w	m	m	m	m	m	w	m	a
200	210	m	w	m	m	m	m	w	w	m	a
210	220	i	m	w	m	m	i	w	w	m	a
220	230	m	w	w	m	m	m	m	m	i	a
230	240	m	w	w	m	m	m	m	w	w	a
240	250	w	m	w	w	i	w	i	w	w	a

Hole:	HAM-32	a=absent	chl = chlorite	bi = biotite
Azimuth:	320	w=weak	mt = magnetite	cc = calcite
Dip:	-45	m=moderate	ep = epidote	py = pyrite
Easting:	663614	i=intense	qtz = quartz	cpy = chalcopyrite
Northing:	5372613		hem = hematite staining	po = pyrrhotite
Date:	21-Jul			

		Minerals									
From: (m)	**To: (m)**	**chl**	**mt**	**ep**	**qtz (blue)**	**hem**	**bi**	**cc**	**py**	**cpy**	**po**
250	260	w	w	w	w	m	w	i	w	w	a
260	270	m	m	w	m	m	m	i	w	a	a
270	280	w	w	a	m	m	w	i	w	a	a
280	290	w	m	a	i	w	w	m	w	w	a
290	300	w	w	a	w	m	w	w	w	a	a
300	310	w	a	a	w	m	w	w	w	w	a

Hole:	HAM-32
Azimuth:	320
Dip:	-45
Easting:	663614
Northing:	5372613
Date:	21-Jul

From: (m)	To: (m)	Description:
0	3.4	Overburden
3.4	34.4	Brecciation of felsic to intermediat volcanic. Sporadic clasts of chert. Clasts are sub-angular. Matrix is chl-bi-ep.
34.4	40.5	Brecciated and altered debris flow. Rounded clasts of diorite, volcanics and minor chert.
40.5	139.3	Brecciated volcanics, mafic to felsic, minor gabbroic clasts. Clasts are varying shades of pink and vary in angularity from angular to sub-rounded. Size of clasts range from sub-angular to sub rounded.
139.3	144	Lightly brecciated gabbro. Altered to mt-bi-chl-through a stockwork of veins. Texture of gabbro is mostly conserved.
144	306.9	Brecciated volcanics, possibly debris flow. Clasts are small (<1cm to 4cm and subangular to rounded. Composition of volcanics range from mafic to felsic. Short sample was taken from 156.8 to156.9 for whole rock? Check B639372. Short interval of more siliceous rock from 223.0 to 223.9 (of which a sample was taken for PTS).
	EOH	

Hole:	HAM-33	a=absent	chl = chlorite	bi = biotite
Azimuth:	320	w=weak	mt = magnetite	cc = calcite
Dip:	-45	m=moderate	ep = epidote	py = pyrite
Easting:	663456	i=intense	qtz = quartz	cpy = chalcopyrite
Northing:	5372469		hem = hematite staining	po = pyrrhotite
Date:	2-Jun			

		Minerals									
From: (m)	**To: (m)**	**chl**	**mt**	**ep**	**qtz (blue)**	**hem**	**bi**	**cc**	**py**	**cpy**	**po**
0	10										
10	20	m	a	w	a	w	a	w	w	m	a
20	30	m	w	i	a	w	a	w	w	w	a
30	40	m	w	m	w	m	a	w	w	w	a
40	50	w	m	w	m	i	w	w	w	w	a
50	60	m	w	w	w	i	w	m	w	w	a
60	70	m	w	w	w	m	m	w	w	w	a
70	80	m	m	i	m	m	m	w	w	m	a
80	90	m	i	m	w	m	m	w	w	w	a
90	100	m	m	m	w	m	m	w	w	m	a
100	110	m	m	m	w	w	w	w	w	w	a
110	120	m	w	w	w	m	w	m	w	w	a
120	130	m	w	w	w	m	w	m	w	w	a
130	140	m	m	w	w	i	w	m	w	w	a
140	150	w	i	w	a	w	w	w	w	w	a
150	160	m	m	m	w	i	w	m	w	w	a
160	170	m	m	m	w	m	w	w	w	w	a
170	180	m	m	m	w	m	w	w	a	a	a
180	190	m	m	m	a	i	w	w	w	w	a
190	200	m	m	m	a	m	w	w	w	w	a
200	210	m	i	w	m	w	w	w	i	i	w
210	220	m	i	a	i	i	w	w	m	m	a
220	230	m	i	a	m	m	w	m	w	m	a
230	240	w	i	w	m	w	w	w	i	i	a
240	250	m	i	w	w	m	w	i	w	w	a

Hole:	HAM-33	a=absent	chl = chlorite	bi = biotite
Azimuth:	320	w=weak	mt = magnetite	cc = calcite
Dip:	-45	m=moderate	ep = epidote	py = pyrite
Easting:	663456	i=intense	qtz = quartz	cpy = chalcopyrite
Northing:	5372469		hem = hematite staining	po = pyrrhotite
Date:	2-Jun			

		Minerals									
From: (m)	**To: (m)**	**chl**	**mt**	**ep**	**qtz (blue)**	**hem**	**bi**	**cc**	**py**	**cpy**	**po**
250	260	m	m	w	m	m	w	i	w	w	a
260	270	m	i	w	i	m	w	i	w	w	a
270	280	w	i	w	m	m	w	m	i	i	a
280	290	w	m	a	i	m	m	w	i	i	a
290	300	w	m	a	m	i	m	w	i	i	a

Hole: HAM-33
Azimuth: 320
Dip: -45
Easting: 663456
Northing: 5372469
Date: 2-Jun

From: (m)	To: (m)	Description:
0	12	Overburden
12	39.3	Heterolithic breccia consisting of clasts of volcanics along with diorite.
39.3	138.1	Brecciated felsic to intermediate volcanics ("pink breccia"), with the odd fragment of gabbro.
138.1	154.1	Massive to fractured gabbro, lower contact gets more fractured, but not really brecciated in the sence that there are distinct fragments of rock.
154.1	297.8	Brecciated felsic volcanics mixed volcanics and cherty clasts, but mostly (>95%) volcanics.
EOH		

Hole:	HAM-36
Azimuth:	140
Dip:	-55
Easting:	663011
Northing:	5372323
Date:	28-Apr

From: (m)	To: (m)	Description:
0	4.5	Overburden
4.5	21	Stockworked to brecciated felsic volcanics, minor cherty clasts.
21	135.4	Brecciated felsic volcanics, intervals of less brecciated rock (e.g. 116.3-135.4) where stocwork and vein structures dominate more mafic rock.
135.4	197.2	Heterolithic breccia with mixed clasts of felsic volcanics and intrusive clasts ranging from 1mm to 30cm in size, mostly angular.
EOH		

Hole:	HAM-39	a=absent	chl = chlorite	bi = biotite
Azimuth:	320	w=weak	mt = magnetite	cc = calcite
Dip:	-60	m=moderate	ep = epidote	py = pyrite
Easting:	663376	i=intense	qtz = quartz	cpy = chalcopyrite
Northing:	5372462		hem = hematite staining	po = pyrrhotite
Date:	17-Jun			

		Minerals									
From: (m)	**To: (m)**	**chl**	**mt**	**ep**	**qtz (blue)**	**hem**	**bi**	**cc**	**py**	**cpy**	**po**
0	10	m	w	i	a	m	a	w	w	m	a
10	20	i	w	i	a	m	w	w	w	w	a
20	30	m	w	w	a	i	w	w	w	m	a
30	40	m	m	m	a	i	w	w	w	w	a
40	50	m	w	m	a	m	a	w	w	m	a
50	60	m	w	w	w	w	w	i	m	i	a
60	70	w	m	w	w	w	a	w	w	w	a
70	80	m	m	m	w	w	a	m	a	w	a
80	90	w	w	w	w	w	a	m	m	m	a
90	100	m	w	m	w	w	a	m	w	w	a
100	110	m	w	w	a	w	a	w	w	w	a
110	120	m	m	w	a	m	w	m	w	w	a
120	130	m	w	m	w	m	a	m	m	w	a
130	140	m	m	m	w	m	a	m	w	m	a
140	150	i	m	m	w	m	a	w	w	w	a
150	160	i	m	m	w	m	a	w	w	w	a
160	170	m	m	m	a	m	a	m	w	w	a
170	180	i	m	m	a	w	a	w	w	w	a
180	190	m	i	w	a	m	w	m	w	w	a
190	200	w	m	w	w	w	w	m	w	m	a
200	210	w	m	w	a	m	w	i	w	m	a
210	220	m	m	w	m	m	w	w	w	i	a
220	230	w	m	w	i	m	w	w	m	i	a
230	240	m	m	a	i	i	i	w	i	i	a
240	250	m	m	a	i	m	m	m	i	i	a

Hole:	HAM-39	a=absent	chl = chlorite	bi = biotite
Azimuth:	320	w=weak	mt = magnetite	cc = calcite
Dip:	-60	m=moderate	ep = epidote	py = pyrite
Easting:	663376	i=intense	qtz = quartz	cpy = chalcopyrite
Northing:	5372462		hem = hematite staining	po = pyrrhotite
Date:	17-Jun			

		Minerals									
From: (m)	**To: (m)**	**chl**	**mt**	**ep**	**qtz (blue)**	**hem**	**bi**	**cc**	**py**	**cpy**	**po**
250	260	m	w	a	i	m	m	w	i	i	a
260	270	m	w	a	w	m	w	i	w	m	a
270	280	i	w	a	w	m	m	i	w	a	a
280	290	i	w	a	a	w	w	m	a	a	a
290	300	m	a	w	a	w	w	i	a	a	a
300	310	m	w	m	a	a	a	m	a	a	a

Hole: HAM-39
Azimuth: 320
Dip: -60
Easting: 663376
Northing: 5372462
Date: 17-Jun

From: (m)	To: (m)	Description:
0	2.3	Overburden
2.3	26.7	Brecciated felsic to intermediate volcanics, minor cherty clasts. Clast size ranges from <1mm to >20cm.
26.7	28.8	Diorite, very altered, slightly brecciated.
28.8	81.7	Brecciated felsic to intermediate volcanics, minor cherty clasts. Clast size ranges from <1mm to >20cm.
81.7	95.4	Unit of brecciated more mafic (darker: sedimentary?) rock, still minor felsic volcanic fragments.
95.4	262.3	Brecciated felsic to intermediate volcanics, minor cherty clasts and minor more mafic looking clasts.
262.3	307	Coarser grained, felsic looking rock. Possibly diorite altered to pink colour. Brecciation is less intense than previous unit, more in the form of a stockwork of 1mm to 1cm veinlets. Coarse grained nature could be a result of alteration since rock looks more like volcanics at end of hole.

Hole:	HAM-40	a=absent	chl = chlorite	bi = biotite
Azimuth:	320	w=weak	mt = magnetite	cc = calcite
Dip:	-45	m=moderate	ep = epidote	py = pyrite
Easting:	663248	i=intense	qtz = quartz	cpy = chalcopyrite
Northing:	5372338		hem = hematite staining	po = pyrrhotite
Date:	20-Aug			

		Minerals									
From: (m)	**To: (m)**	**chl**	**mt**	**ep**	**qtz (blue)**	**hem**	**bi**	**cc**	**py**	**cpy**	**po**
0	10	m	a	m	w	m	m	w	a	a	a
10	20	m	w	i	w	m	m	w	w	w	a
20	30	i	w	i	w	m	i	w	w	m	a
30	40	m	w	i	w	w	m	w	w	w	a
40	50	m	a	m	w	w	m	w	w	w	a
50	60	m	w	m	w	w	m	m	w	w	a
60	70	m	m	i	w	w	m	w	w	m	a
70	80	m	m	m	w	m	m	m	w	w	a
80	90	m	i	m	w	m	m	m	w	i	a
90	100	m	m	w	w	w	m	i	w	m	a
100	110	m	m	w	w	m	m	i	w	w	a
110	120	m	m	m	w	w	m	m	w	m	a
120	130	m	m	m	w	m	m	m	w	w	a

Hole:	HAM-40
Azimuth:	320
Dip:	-45
Easting:	663248
Northing:	5372338
Date:	20-Aug

From: (m)	To: (m)	Description:
0	9.5	Overburden
9.5	124.3	Brecciated felsic to intermediate volcanics. Not intensely pink altered, only patchy pink areas that have the typical pink breccia appearance. Alteration is dominantly albite epidote, with chl-bi. Clasts are difficult to make out, but are generally sub rounded and have irregular edges. Clasts are <10cm in size, and the composition may be more mafic (darker colour?).
	EOH	

Hole:	HAM-41	a=absent	chl = chlorite	bi = biotite
Azimuth:	140	w=weak	mt = magnetite	cc = calcite
Dip:	-45	m=moderate	ep = epidote	py = pyrite
Easting:	663042	i=intense	qtz = quartz	cpy = chalcopyrite
Northing:	5372410		hem = hematite staining	po = pyrrhotite
Date:	16-Aug			

		Minerals									
From: (m)	**To: (m)**	**chl**	**mt**	**ep**	**qtz (blue)**	**hem**	**bi**	**cc**	**py**	**cpy**	**po**
0	10	w	a	a	w	a	w	w	w	w	m
10	20	w	a	w	w	a	w	w	w	w	m
20	30	w	a	a	w	a	w	w	m	m	i
30	40	w	m	a	w	a	w	w	w	w	m
40	50	w	m	w	w	a	w	w	m	w	m
50	60	w	a	w	w	a	w	w	w	a	a
60	70	w	w	w	w	w	w	w	w	a	a
70	80	w	w	w	w	w	w	w	a	a	a
80	90	w	m	w	w	w	w	w	w	w	a
90	100	w	w	w	w	a	w	m	w	a	a
100	110	m	w	w	w	w	m	m	w	a	a
110	120	m	m	w	w	w	m	m	m	w	a
120	130	m	m	w	w	m	m	w	w	m	a
130	140	m	m	m	w	m	m	m	m	m	a
140	150	m	m	w	w	i	m	m	m	i	a
150	160	m	m	w	w	i	m	m	m	m	a
160	170	m	m	i	w	m	m	m	m	w	a
170	180	w	m	m	w	m	w	i	w	m	a
180	190	m	w	w	w	w	m	m	m	w	a
190	200	m	m	w	i	w	m	m	m	m	a
200	210	m	w	m	w	m	m	w	w	w	a
210	220	m	a	m	w	m	m	m	w	w	a
220	230	w	a	m	w	w	w	m	w	a	a
230	240	m	a	w	w	m	m	m	w	a	a
240	250	m	a	w	w	w	m	w	w	a	a

Hole:	HAM-41	a=absent	chl = chlorite	bi = biotite
Azimuth:	140	w=weak	mt = magnetite	cc = calcite
Dip:	-45	m=moderate	ep = epidote	py = pyrite
Easting:	663042	i=intense	qtz = quartz	cpy = chalcopyrite
Northing:	5372410		hem = hematite staining	po = pyrrhotite
Date:	16-Aug			

		Minerals									
From: (m)	**To: (m)**	**chl**	**mt**	**ep**	**qtz (blue)**	**hem**	**bi**	**cc**	**py**	**cpy**	**po**
250	260	m	a	w	w	m	m	w	w	a	a

Hole: HAM-41
Azimuth: 140
Dip: -45
Easting: 663042
Northing: 5372410
Date: 16-Aug

From: (m)	To: (m)	Description:
0	3.4	Overburden
3.4	19.2	Felsic to intermediate volcanics. Lightly brecciated in places, but mostly massive. Some chert present.
19.2	24	Banded metasedimentary rock, intensely brecciated in places, only mildly brecciated in others. Crackle brecciated with angular clasts.
24	35.1	Felsic to intermediate volcaniclastics, lightly brecciated. Mostly dark clasts, in a pale matrix. Paleness of matrix appears to be due to alteration (silicification) whereas darker clasts are more chloritized. Alteration looks more VMS related.
35.1	42.5	Metasediments, clastic to cherty, lightly brecciated, mt rich.
42.5	83.3	Massive to lightly brecciated felsic to intermediate volcanics. Quartzeye rich areas form distinct layers. Pale banding caused by silicification (related to earlier VMS?) as evident by presence of quarts eyes in both pale and dark material.
83.3	112.7	Lightly brecciated felsic to intermediate volcanics. Matrix is dominantly chl, bi does not appear to be present. Epidote appears to be later than chl. Pale enveloping on clasts similar to pale alteration in previous interval. Fragments are usually too large to distingish size and angularity but smaller clasts are also present (1-5cm)
112.7	216.9	Intensely brecciated pink altered felsic to intermediate volcanics. Matrix alteration appears to have ovvured in the sequence (earliest->latest): chl-mt-bi-ep-(py+cpy)-cc.
216.9	233.2	Brecciated diorite. Heterolithic with dominantly clasts of diorite, minor pink felsic volcanic clasts. Diorite clasts are less pink (less albite?). Clasts range from 1-30cm.
233.2	237.6	Brecciated felsic to intermediate volcanics, clasts are almost entirely volcanics or chert. Clasts are pink and range in size from 2mm to 5cm. Matrix is typical chl-bi-ep-(cc?).

Hole: HAM-41
Azimuth: 140
Dip: -45
Easting: 663042
Northing: 5372410
Date: 16-Aug

From: (m)	To: (m)	Description:
237.6	241.2	Brecciated granite? Very rounded pink intrusive clasts. Matrix is chl-bi and minor volcanic clasts supported in the matrix (1-2mm).
241.2	251.9	Brecciated felsic to intermediate volcanics. Heterolithic clasts, about 60% felsic volcanics, 40% grey diorite. Volcanic clasts are pink and angular, diorite clasts are greenish grey and angular. Matrix is chl-bi-ep.

Hole:	HAM-43	a=absent	chl = chlorite	bi = biotite
Azimuth:	320	w=weak	mt = magnetite	cc = calcite
Dip:	-50	m=moderate	ep = epidote	py = pyrite
Easting:	663376	i=intense	qtz = quartz	cpy = chalcopyrite
Northing:	5372462		hem = hematite staining	po = pyrrhotite
Date:	30-Aug			

		Minerals									
From: (m)	**To: (m)**	**chl**	**mt**	**ep**	**qtz (blue)**	**hem**	**bi**	**cc**	**py**	**cpy**	**po**
0	10	m	a	m	w	m	m	m	w	w	a
10	20	m	w	i	w	m	m	w	w	w	a
20	30	m	w	w	w	i	m	w	w	w	a
30	40	m	m	m	w	m	m	m	w	w	a
40	50	w	w	m	w	m	w	w	w	w	a
50	60	w	m	m	m	m	w	m	m	w	a
60	70	w	m	m	w	m	w	m	m	m	a
70	80	w	w	m	w	w	w	w	w	w	a
80	90	w	w	w	m	w	w	w	m	w	a
90	100	m	w	w	w	w	m	w	m	w	a
100	110	m	w	m	w	m	m	w	w	w	a
110	120	m	w	m	w	m	m	m	w	w	a
120	130	i	m	w	w	m	i	m	w	w	a
130	140	i	w	w	w	m	i	m	w	w	a
140	150	i	m	m	w	m	i	m	w	w	a
150	160	m	m	m	w	w	m	m	m	w	a
160	170	m	m	m	w	m	m	w	w	w	a
170	180	m	m	m	w	m	m	m	m	w	a
180	190	m	m	m	w	m	m	m	m	w	a
190	200	w	m	m	w	m	w	m	m	w	a
200	210	w	m	w	w	m	w	m	w	w	a
210	220	m	m	w	w	m	m	m	w	w	a
220	230	m	m	w	w	m	m	m	w	w	a
230	240	m	m	w	m	m	m	m	w	w	a
240	250	m	m	a	w	m	m	m	w	a	a

Hole: HAM-43
Azimuth: 320
Dip: -50
Easting: 663376
Northing: 5372462
Date: 30-Aug

From: (m)	To: (m)	Description:
0	2	Overburden
2	249	Brecciated felsic to intermediate volcanics. Clasts are 95% felsic to intermediate volcanics with minor cherty clasts and other metaseds. Clasts are subangular and usually altered pink. Size of clasts varies from 1mm to 15cm. Matrix is composed of chl-bi-ep-mt-cc-sulfides. Minor foliation is detectable by a weak alignment of some clasts and varies from 60 to 90 DTCA. Style of brecciation is chaotic (>30 degree clast rotation), though a second crackle brecciation event overprints the first in some places.
	EOH	

Hole:	HAM-53	a=absent	chl = chlorite	bi = biotite
Azimuth:	140	w=weak	mt = magnetite	cc = calcite
Dip:	-60	m=moderate	ep = epidote	py = pyrite
Easting:	663473	i=intense	qtz = quartz	cpy = chalcopyrite
Northing:	5372501		hem = hematite staining	po = pyrrhotite
Date:	25-Aug			

		Minerals									
From: (m)	**To: (m)**	**chl**	**mt**	**ep**	**qtz (blue)**	**hem**	**bi**	**cc**	**py**	**cpy**	**po**
0	10	m	a	w	w	m	m	w	w	w	a
10	20	m	w	m	w	m	m	w	w	w	a
20	30	m	w	m	w	m	m	w	w	w	a
30	40	m	a	w	w	m	m	w	m	m	a
40	50	m	w	m	w	m	m	w	m	m	a
50	60	m	a	m	w	m	m	w	w	w	a
60	70	m	a	w	w	i	m	w	m	m	a
70	80	m	w	m	w	m	m	w	w	m	a
80	90	m	a	m	m	m	m	w	m	m	a
90	100	m	w	m	m	w	m	w	w	w	a
100	110	m	a	m	m	w	m	w	w	a	a
110	120	m	a	m	m	w	m	w	w	w	a
120	130	w	w	w	w	w	w	m	w	w	a
130	140	w	w	w	w	m	w	m	m	w	a
140	150	m	a	w	w	w	m	m	w	a	a
150	160	m	a	w	w	w	m	m	m	m	a
160	170	m	w	w	a	w	m	m	w	w	a
170	180	m	m	w	a	w	m	m	w	w	a
180	190	m	w	w	a	w	m	m	w	w	a
190	200	m	a	w	a	w	m	m	w	a	a
200	210	m	w	w	a	w	m	m	a	a	a
210	220	m	w	w	a	w	m	i	a	a	a
220	230	m	a	w	a	a	m	i	a	a	a
230	240	m	a	w	a	a	m	i	w	a	a
240	250	m	a	w	a	a	m	i	w	a	a

Hole:	HAM-53	a=absent	chl = chlorite	bi = biotite
Azimuth:	140	w=weak	mt = magnetite	cc = calcite
Dip:	-60	m=moderate	ep = epidote	py = pyrite
Easting:	663473	i=intense	qtz = quartz	cpy = chalcopyrite
Northing:	5372501		hem = hematite staining	po = pyrrhotite
Date:	25-Aug			

		Minerals									
From: (m)	**To: (m)**	**chl**	**mt**	**ep**	**qtz (blue)**	**hem**	**bi**	**cc**	**py**	**cpy**	**po**
250	260	m	w	w	a	w	m	i	w	a	a
260	270	i	a	w	a	w	i	i	w	a	a

Hole: HAM-53
Azimuth: 140
Dip: -60
Easting: 663473
Northing: 5372501
Date: 25-Aug

From: (m)	To: (m)	Description:
0	6	Overburden
6	88.1	Pink breccia, clasts are dominantly felsic to intermediate volcanics. Clasts are subangular and 1 to 10cm in size. Matrix is dominantly, chl-bi-cc-mt-ep.
88.1	199.7	Heterolithic breccia, dominantly gabroic to dioritic clasts as described below. 20% pink volcanic clasts are subangular and 1-5cm in size. Matrix is dominantly chl-bi, minor cc-mt.
199.7	267	Gabro (diorite?) Lightly brecciated by quartz-calcite veins. Highly chloritized in places, chl exhibits strong foliation between 0 an 45 DTCA. Gabbro is light in color (leucogabro) and grains are almost 50-50 plag and px. Check B760014 (altered) and B760015 (unaltered) for whole rock comparison (from 200.7 and 203.1 respectively). This gabbro is not as magnetic as the other gabbros in the deposit.
EOH		

Hole:	HAM-54	a=absent	chl = chlorite	bi = biotite
Azimuth:	140	w=weak	mt = magnetite	cc = calcite
Dip:	-45	m=moderate	ep = epidote	py = pyrite
Easting:	663473	i=intense	qtz = quartz	cpy = chalcopyrite
Northing:	5372501		hem = hematite staining	po = pyrrhotite
Date:	24-Aug			

		Minerals									
From: (m)	**To: (m)**	**chl**	**mt**	**ep**	**qtz (blue)**	**hem**	**bi**	**cc**	**py**	**cpy**	**po**
0	10	m	a	w	w	m	m	w	w	w	a
10	20	m	a	m	w	m	m	w	w	w	a
20	30	m	w	m	w	m	m	m	m	m	a
30	40	m	w	m	w	m	m	m	m	m	a
40	50	m	w	m	m	m	m	m	m	m	a
50	60	m	w	m	w	m	m	w	w	w	a
60	70	m	w	m	w	w	m	w	w	w	a
70	80	w	a	m	w	w	w	w	a	a	a
80	90	m	a	m	w	w	m	w	w	a	a
90	100	m	a	m	w	w	m	m	w	w	a

Hole: HAM-54
Azimuth: 140
Dip: -45
Easting: 663473
Northing: 5372501
Date: 24-Aug

From: (m)	To: (m)	Description:
0	7.6	Overburden
7.6	65.5	Brecciated felsic to intermediate volcanics. Chaotic breccia with 95% volcanic clasts 5% cherty clasts. Lower few meters has some dioritic clasts. Clasts are 2mm to 10cm and slightly elongated at 50DTCA. Slightly rounded (subrounded to subangular). Clast edges are fractalized. Matrix is chl-ep-cc(-mt) and clasts are pink.
65.5	96	Lightly brecciated diorite. Large (>1m) diorite fragments with minor small (2mm-10cm) volcanic fragments in between large diorite fragments. Diorite is alb-bi-chl grains with little quartz. Grains are 1-2mm. Matrix is mostly chl-bi-ep-cc. Volcanic clasts are pink.
	EOH	

Hole:	HAM-56	a=absent	chl = chlorite	bi = biotite
Azimuth:	140	w=weak	mt = magnetite	cc = calcite
Dip:	-45	m=moderate	ep = epidote	py = pyrite
Easting:	663080	i=intense	qtz = quartz	cpy = chalcopyrite
Northing:	5372358		hem = hematite staining	po = pyrrhotite
Date:	17-Aug			

		Minerals									
From: (m)	**To: (m)**	**chl**	**mt**	**ep**	**qtz (blue)**	**hem**	**bi**	**cc**	**py**	**cpy**	**po**
0	10										
10	20	w	w	w	a	a	w	w	w	a	a
20	30	w	a	w	a	w	w	w	w	a	a
30	40	m	m	w	w	w	m	w	w	w	a
40	50	m	w	w	w	w	m	m	m	w	a
50	60	m	m	w	w	m	m	m	w	m	a
60	70	w	m	w	w	m	w	m	m	m	a
70	80	w	m	m	w	m	w	m	w	w	a
80	90	m	m	m	w	w	m	i	w	w	a
90	100	w	m	m	w	w	w	i	w	w	a
100	110	m	m	m	m	w	m	m	m	m	a
110	120	m	m	w	m	w	m	i	w	m	a
120	130	m	m	w	m	m	m	m	w	w	a
130	140	m	a	w	w	m	m	w	w	a	a
140	150	m	a	m	w	m	m	m	w	a	a
150	160	m	a	m	w	m	m	w	w	w	a
160	170	m	a	w	w	m	m	m	w	w	a
170	180	m	w	w	w	m	m	w	w	a	a
180	190	m	w	w	w	w	m	m	w	a	a
190	200	m	a	w	w	m	m	w	a	w	a
200	210	m	a	w	w	m	m	w	a	a	a

Hole: HAM-56
Azimuth: 140
Dip: -45
Easting: 663080
Northing: 5372358
Date: 17-Aug

From: (m)	To: (m)	Description:
0	10.2	Overburden
10.2	46.1	Lightly brecciated felsic to intermediate volcanics. Rock is a crackle breccia. Clasts have undergone <10 degree rotation. Matrix is mostly chl-(mt), clasts have bleached (albitic?) rim. Calcite veining postdates chl veining.
46.1	95.2	Pink brecciated felsic volcanics clasts appear to be mixed volcanics (felsic to mafic) but dominantly felsic. Brecciation is more chaotic than last interval, also higher marix to clast ratio. Minor gabroic clasts are present.
95.2	106.9	Brecciated gabbro. Dominant clast is gabbroic, but still a lot of volcanic clasts. Clasts are angular to subangular.
106.9	204	Felsic to intermediate brecciated volcanics as from 46.1 to 95.2. Some smaller clasts are more lensoid in shape. Section from 145.5 to 164.6 where diorite clasts make up about 40% of clasts. From here, diorite clasts continue at ~10% to bottom of hole
	EOH	

Hole:	HAM-57	a=absent	chl = chlorite	bi = biotite
Azimuth:	320	w=weak	mt = magnetite	cc = calcite
Dip:	-62	m=moderate	ep = epidote	py = pyrite
Easting:	663473	i=intense	qtz = quartz	cpy = chalcopyrite
Northing:	5372501		hem = hematite staining	po = pyrrhotite
Date:	23-Aug			

		Minerals									
From: (m)	**To: (m)**	**chl**	**mt**	**ep**	**qtz (blue)**	**hem**	**bi**	**cc**	**py**	**cpy**	**po**
0	10	m	m	w	w	m	m	w	w	w	a
10	20	m	w	m	m	m	m	w	w	a	a
20	30	m	w	m	w	m	m	w	w	a	a
30	40	m	w	m	w	m	m	m	w	w	a
40	50	m	m	m	w	i	m	w	w	a	a
50	60	m	w	m	w	i	m	w	w	w	a
60	70	m	m	m	w	m	m	w		m	a
70	80	m	w	m	w	m	m	m	m	m	a
80	90	m	m	m	w	m	m	w	w	w	a
90	100	m	m	i	m	m	m	m	w	w	a
100	110	w	m	w	m	m	w	m	w	w	a
110	120	m	w	m	m	w	m	m	w	w	a
120	130	m	m	m	m	m	m	m	w	w	a
130	140	m	m	m	w	m	m	m	w	w	a
140	150	m	m	m	w	m	m	i	w	w	a
150	160	w	w	m	w	w	w	m	w	w	a
160	170	m	m	m	w	m	m	w	w	w	a
170	180	m	w	m	w	i	m	w	w	w	a
180	190	m	w	m	w	m	m	m	w	w	a
190	200	w	m	m	m	m	w	m	w	m	a
200	210	w	m	m	w	m	w	m	w	w	a
210	220	m	m	m	w	m	m	i	w	w	a
220	230	w	i	m	w	m	w	w	w	m	a
230	240	m	m	w	w	m	m	m	w	w	a
240	250	m	m	w	w	m	m	w	w	w	a

Hole:	HAM-57	a=absent	chl = chlorite	bi = biotite
Azimuth:	320	w=weak	mt = magnetite	cc = calcite
Dip:	-62	m=moderate	ep = epidote	py = pyrite
Easting:	663473	i=intense	qtz = quartz	cpy = chalcopyrite
Northing:	5372501		hem = hematite staining	po = pyrrhotite
Date:	23-Aug			

		Minerals									
From: (m)	**To: (m)**	**chl**	**mt**	**ep**	**qtz (blue)**	**hem**	**bi**	**cc**	**py**	**cpy**	**po**
250	260	m	m	w	w	m	m	w	w	w	a
260	270	m	i	w	w	m	m	w	w	w	a
270	280	m	m	w	w	i	m	w	w	a	a

Hole:	HAM-57
Azimuth:	320
Dip:	-62
Easting:	663473
Northing:	5372501
Date:	23-Aug

From: (m)	To: (m)	Description:
0	4.1	Overburden
4.1	279	Brecciated felsic to intermediate volcanics, clasts are dominantly pink volcanics, minor dioritic clasts, gabbroic clasts and cherty clasts. Clasts range in size from 2mm to >20cm. Clast shapes are generally subangular with mildly fractalated edges. Brecciation is chaotic and there is no dominant clast orientation. From 260m to EOH there are significantly more cherty clasts, that make up ~30% of clasts.
	EOH	

Hole:	HAM-58	a=absent	chl = chlorite	bi = biotite
Azimuth:		w=weak	mt = magnetite	cc = calcite
Dip:		m=moderate	ep = epidote	py = pyrite
Easting:		i=intense	qtz = quartz	cpy = chalcopyrite
Northing:			hem = hematite staining	po = pyrrhotite
Date:	15-Jul			

		Minerals									
From: (m)	**To: (m)**	**chl**	**mt**	**ep**	**qtz (blue)**	**hem**	**bi**	**cc**	**py**	**cpy**	**po**
0	10	m	w	w	w	i	m	w	w	m	a
10	20	m	m	w	w	i	m	m	w	w	a
20	30	w	w	w	w	m	w	w	w	w	a
30	40	m	w	w	w	m	m	w	w	w	a
40	50	m	w	w	w	m	m	a	w	w	a
50	60	m	w	m	w	w	m	w	w	a	a
60	70	i	m	m	w	m	i	w	w	w	a
70	80	i	w	m	m	m	i	w	w	w	a
80	90	i	w	w	m	m	i	m	w	a	a
90	100	i	a	m	w	m	i	m	w	w	a
100	110	m	w	m	w	w	m	w	w	w	a
110	120	m	w	i	w	w	m	w	a	a	a
120	130	w	w	m	w	w	w	w	a	a	a
130	140	m	w	m	w	w	m	w	w	a	a
140	150	i	w	w	w	m	i	w	w	w	a
150	160	m	w	m	w	w	m	w	w	w	a
160	170	m	m	m	w	w	m	w	m	w	a
170	180	m	i	m	w	w	m	w	w	w	a
180	190	m	i	w	a	w	m	w	w	w	a
190	200	i	m	w	m	w	i	w	w	w	a
200	210	m	m	w	w	a	m	w	a	a	a
210	220	w	w	w	a	w	w	w	a	w	a
220	230	w	w	w	a	w	w	w	w	a	a
230	240	w	w	a	a	m	w	w	w	a	a
240	250	w	m	w	a	m	w	m	a	a	a

Hole:	HAM-58	a=absent	chl = chlorite	bi = biotite
Azimuth:		w=weak	mt = magnetite	cc = calcite
Dip:		m=moderate	ep = epidote	py = pyrite
Easting:		i=intense	qtz = quartz	cpy = chalcopyrite
Northing:			hem = hematite staining	po = pyrrhotite
Date:	15-Jul			

		Minerals									
From: (m)	**To: (m)**	**chl**	**mt**	**ep**	**qtz (blue)**	**hem**	**bi**	**cc**	**py**	**cpy**	**po**
250	260	m	m	w	a	w	m	w	a	a	a
260	270	m	m	w	a	w	m	m	a	w	a
270	280	w	i	w	a	w	w	w	w	w	a
280	290	m	i	w	a	a	m	m	w	a	a
290	300	m	i	w	a	w	m	m	a	a	a
300	310	m	m	w	a	m	m	m	w	w	a
310	320	w	m	w	a	m	w	w	w	a	a
320	330	w	i	w	a	w	w	m	a	a	a
330	340	w	i	w	a	w	w	m	a	a	a
340	350	w	i	w	a	w	w	m	a	a	a
350	360	w	i	w	a	w	w	m	a	a	a
360	370	w	i	w	a	w	w	m	a	a	a
370	380	w	m	w	a	w	w	m	a	a	a
380	390	w	m	m	a	w	w	m	a	a	a
390	400	w	i	w	a	a	w	m	a	a	a
400	410	w	i	w	a	m	w	m	a	a	a
410	420	w	w	m	a	w	w	m	w	a	a

Hole: HAM-58
Azimuth:
Dip:
Easting:
Northing:
Date: 15-Jul

From: (m)	To: (m)	Description:
0	6.1	Overburden
6.1	91.2	Brecciated volcanics, composition ranges from mafic (darker rock) to felsic (pale rock with quartz eyes. Clasts range from angular to subangular and range in size from <1cm to 15cm. Lower contact is very dark rock with not much pink alteration, may be metaseds.
91.2	164.5	Heterolithic breccia. Clasts are mixed lithology from felsic to mafic volcanics, to chert, diorite and gabbro. Clasts range in size from <1cm to several meters. Clasts are usually angular to subangular.
164.5	226.9	Massive to lightly brecciated gabbro, 2-3mm grains of plagioclase and pyroxene now partially altered to magnetite-chlorite. Very broken up rock.
226.9	247.5	Debris flow. Rounded clasts of diorite and chert in a matrix of volcaniclastic material (ash). Upper contact marks contact where rock becomes more consolidated than previous unit.
247.5	295.6	Lightly brecciated gabbro. Slightly more brecciated version of 318.6 to 417. Epidotized plagioclase with mt that appears to have replaced pyroxene, along with chl. Qtz cc veining is prominent.
295.6	318.6	Volcanic fragmental. Fragments of gabbro and diorite in a matrix of ash/lapili tuff. Fragments range from <2mm (lapilli) to >30 cm clasts of gabbro.
318.6	417	Massive to lightly brecciated gabbro/diorite. Relict plagioclase crystals with px altered to chlorite-mt. Plag is slightly epidotized. Main structure is a stockwork of qtz cc veins from 2mm to 2cm in width.

Hole:	HAM-59	a=absent	chl = chlorite	bi = biotite
Azimuth:	138	w=weak	mt = magnetite	cc = calcite
Dip:	-44	m=moderate	ep = epidote	py = pyrite
Easting:	663423	i=intense	qtz = quartz	cpy = chalcopyrite
Northing:	5372501		hem = hematite staining	po = pyrrhotite
Date:	22-Jun			

		Minerals									
From: (m)	**To: (m)**	**chl**	**mt**	**ep**	**qtz (blue)**	**hem**	**bi**	**cc**	**py**	**cpy**	**po**
0	10	m	a	i	w	w	a	a	w	a	a
10	20	i	a	i	w	w	a	w	a	w	a
20	30	m	w	w	w	m	a	w	w	w	a
30	40	m	w	w	a	m	a	w	w	w	a
40	50	m	w	m	w	w	w	w	w	w	a
50	60	m	w	m	w	w	a	w	w	w	a
60	70	w	a	m	w	w	a	w	w	w	a
70	80	m	w	w	w	w	m	w	w	w	a
80	90	w	w	m	w	w	a	w	w	a	a
90	100	m	w	w	w	w	a	m	a	a	a
100	110	m	w	w	m	w	a	m	a	a	a
110	120	w	w	w	w	w	a	m	a	a	a
120	130	m	w	w	w	w	a	w	w	w	a
130	140	w	w	a	w	w	a	w	w	w	a
140	150	w	a	a	w	a	a	w	w	w	a
150	160	a	w	a	a	a	a	a	a	a	a
160	170	a	w	a	w	a	a	w	a	a	a
170	180	a	w	w	a	a	a	w	w	a	a
180	190	w	w	w	a	a	a	w	w	a	a
190	200	a	a	w	a	a	a	w	a	a	a
200	210	w	a	a	a	a	a	w	a	a	a
210	220	w	a	a	a	a	a	w	a	a	a
220	230	w	a	a	a	a	a	a	a	a	a
230	240	w	a	a	a	a	a	a	w	a	a
240	250	w	a	w	a	a	a	a	a	a	a

Hole:	HAM-59	a=absent	chl = chlorite	bi = biotite
Azimuth:	138	w=weak	mt = magnetite	cc = calcite
Dip:	-44	m=moderate	ep = epidote	py = pyrite
Easting:	663423	i=intense	qtz = quartz	cpy = chalcopyrite
Northing:	5372501		hem = hematite staining	po = pyrrhotite
Date:	22-Jun			

		Minerals									
From: (m)	**To: (m)**	**chl**	**mt**	**ep**	**qtz (blue)**	**hem**	**bi**	**cc**	**py**	**cpy**	**po**
250	260	w	a	w	a	a	a	a	w	a	a
260	270	a	a	a	a	a	a	w	w	a	a
270	280	a	a	a	a	a	a	a	a	a	a
280	290	a	a	w	a	a	a	w	a	a	a
290	300	i	w	a	a	a	a	m	a	a	a
300	310	w	m	a	a	a	a	w	a	a	a
310	320	w	m	a	a	a	a	m	a	a	a
320	330	w	w	a	a	a	a	w	a	a	a
330	340	w	w	a	a	a	a	m	a	a	a
340	350	w	w	a	a	a	a	w	a	a	a

Hole: HAM-59
Azimuth: 138
Dip: -44
Easting: 663423
Northing: 5372501
Date: 22-Jun

From: (m)	To: (m)	Description:
0	4.8	Overburden
4.8	39.7	Brecciated felsic volcanics (Clasts ~95%) and minor cherty clasts (<5%). Rock looks very "dirty", possibly result of alteration or possible debris flow. Clasts range from 1cm to 10cm in size and are typically subangular.
39.7	140.2	Heterolithic breccia with alternating zones of diorite rich breccia and volcanic rich breccia. Zones of volcanics characterized by smaller pink subangular clasts ranging from 3mm to 15cm. Diorite rich zones tend to have larger clasts where angularity is difficult to interpret and clast size is generally >5cm and up to several meters. Areas of unit are affected by main brecciating event and other areas by a stockwork of quartz veinlets with associated pink alteration.
140.2	290	Massive to brecciated intermediate intrusive. Composition ranges from intermediate to more mafic (diorite to gabbro) Brecciation intensity varries from fairly massive to lightly brecciated. The consistant structure is represented by a stockwork of pink-quartz veinlets (see HAM-59-01). Long zone of intensely broken core from 151-197.7
290	342	Massive to stockworked gabbro where feldspars may be partially epidotized and pyroxenes are altered to magnetite. Upper contact is highly chloritized.

Hole:	HAM-62	a=absent	chl = chlorite	bi = biotite
Azimuth:	140	w=weak	mt = magnetite	cc = calcite
Dip:	-45	m=moderate	ep = epidote	py = pyrite
Easting:	663374	i=intense	qtz = quartz	cpy = chalcopyrite
Northing:	5372752		hem = hematite staining	po = pyrrhotite
Date:	28-Jul			

		Minerals									
From: (m)	**To: (m)**	**chl**	**mt**	**ep**	**qtz (blue)**	**hem**	**bi**	**cc**	**py**	**cpy**	**po**
0	10	w	a	a	a	a	w	w	w	w	a
10	20	w	a	w	a	a	w	m	w	w	a
20	30	w	a	a	a	a	w	w	a	a	a
30	40	w	a	w	a	a	w	w	w	w	a
40	50	w	a	w	a	a	w	w	w	w	a
50	60	w	a	w	w	a	w	w	a	a	a
60	70	w	a	a	w	a	w	m	a	a	m
70	80	w	a	a	w	a	w	w	w	w	m
80	90	w	a	m	w	a	w	w	w	w	a
90	100	m	w	w	a	w	m	w	i	a	a
100	110	i	a	m	a	w	i	w	w	w	a
110	120	i	m	w	w	m	i	m	m	m	a
120	130	m	m	w	w	w	m	m	w	w	w
130	140	w	m	w	w	w	w	w	m	m	m
140	150	m	m	m	w	w	m	w	w	w	w
150	160	m	i	m	w	w	m	w	m	m	w
160	170	w	i	m	w	m	w	w	m	m	w
170	180	m	m	w	w	w	m	m	m	m	m
180	190	m	m	m	w	w	m	m	w	w	m
190	200	i	w	m	w	m	i	w	w	w	a
200	210	i	m	m	m	m	i	m	w	w	a
210	220	i	m	m	m	m	i	m	w	w	a
220	230	m	m	m	w	w	m	m	w	w	a
230	240	m	i	m	w	w	m	m	w	w	a
240	250	w	m	m	w	m	w	m	w	w	a

Hole:	HAM-62	a=absent	chl = chlorite	bi = biotite
Azimuth:	140	w=weak	mt = magnetite	cc = calcite
Dip:	-45	m=moderate	ep = epidote	py = pyrite
Easting:	663374	i=intense	qtz = quartz	cpy = chalcopyrite
Northing:	5372752		hem = hematite staining	po = pyrrhotite
Date:	28-Jul			

		Minerals									
From: (m)	**To: (m)**	**chl**	**mt**	**ep**	**qtz (blue)**	**hem**	**bi**	**cc**	**py**	**cpy**	**po**
250	260	w	m	m	w	m	w	w	w	w	a
260	270	m	i	m	w	w	m	w	w	w	a
270	280	m	i	m	w	w	m	m	w	w	a
280	290	m	i	w	w	w	m	m	w	w	a
290	300	m	m	w	w	w	m	i	w	w	a
300	310	m	w	w	w	m	m	m	w	w	a
310	320	m	w	m	m	m	m	i	w	w	a
320	330	m	m	m	m	m	m	m	w	m	a
330	340	m	m	m	m	w	m	w	w	w	a
340	350	m	w	m	m	w	m	w	w	w	a
350	360	m	w	w	m	m	m	w	w	m	a
360	370	m	w	w	w	m	m	w	w	m	a
370	380	m	a	w	w	i	m	w	w	w	a
380	390	w	a	w	m	m	w	m	w	a	a
390	400	w	a	w	w	w	w	w	w	a	a
400	410	w	a	w	m	w	w	w	w	w	a
410	420	m	a	a	m	w	m	m	w	m	a
420	430	w	a	a	w	w	w	w	w	a	a
430	440	w	a	a	w	w	w	w	w	a	a

Hole:	HAM-62
Azimuth:	140
Dip:	-45
Easting:	663374
Northing:	5372752
Date:	28-Jul

From: (m)	To: (m)	Description:
0	4.3	Overburden
4.3	65.1	Fairly massive felsic to intermediate volcanics. Only structure is system of cc veins at random DTCA. Also chl veins present.
65.1	81.4	Massive banded sedimentary rock. Evidence of soft sediment deformation. Bands alternate between cherty, darker (biotite rich) and occasionally pyrhottite bands.
81.4	182.5	Brecciated felsic volcanics with zones of brecciated sedimentary rock.
182.5	226.9	Pink brecciated felsic volcanics. Clasts are 1-5cm in size, generally altered pink and subangular.
226.9	242.8	Brecciated gabbro, grains are 1-2mm and composed of feldspars and chl-mt-bi.
242.8	300.5	Heterolithic breccia with clasts of gabbro and volcanics. Gabbro is slightly magnetite altered, while volcanics are altered pink. Volcanics are mostly felsic, no cherty clasts.
300.5	343.9	Heterolithic breccia with subequal proportions of volcanics and clastic sedimentary clasts. Minor cherty fragments. Clasts range from <1cm to >20cm. Shorth unit with gabbroic clasts from 327.4 to 339.5.
343.9	377.3	Heterolithic breccia with clasts of felsic volcanics, diorite and chert. Clasts range from <1cm to >1m. Generally larger clasts are diorite. Lower contact is intensly pink altered volcanics.
377.3	432	Stockworked to lightly brecciated pinkish diorite. Stockwork of pinkish veinlets at bottom similar to that seen deep in other holes.

Hole:	HAM-63	a=absent	chl = chlorite	bi = biotite
Azimuth:	140	w=weak	mt = magnetite	cc = calcite
Dip:	-68	m=moderate	ep = epidote	py = pyrite
Easting:	663247	i=intense	qtz = quartz	cpy = chalcopyrite
Northing:	5372628		hem = hematite staining	po = pyrrhotite
Date:	3-Sep			

		Minerals									
From: (m)	**To: (m)**	**chl**	**mt**	**ep**	**qtz (blue)**	**hem**	**bi**	**cc**	**py**	**cpy**	**po**
0	10	w	a	a	a	a	w	w	w	a	a
10	20	m	a	a	a	a	m	w	w	a	a
20	30	m	a	a	a	a	m	w	w	a	a
30	40	m	a	a	a	a	m	w	w	a	a
40	50	w	a	w	a	a	w	w	w	a	w
50	60	w	a	a	a	a	w	w	w	a	a
60	70	w	a	w	a	a	w	m	w	a	w
70	80	m	w	w	a	a	m	m	w	w	m
80	90	i	m	w	a	a	i	m	m	w	i
90	100	i	m	a	a	a	i	w	m	w	i
100	110	i	m	w	a	a	i	m	m	w	m
110	120	i	m	w	a	a	i	m	m	w	m
120	130	m	m	w	w	w	m	m	m	a	w
130	140	m	w	a	w	a	m	w	w	a	a
140	150	m	w	a	a	w	m	m	w	a	a
150	160	m	w	a	a	w	m	i	w	a	a
160	170	i	m	a	a	i	i	m	w	w	a
170	180	i	m	a	a	m	i	m	w	w	a
180	190	m	m	a	a	m	m	i	m	w	a
190	200	m	m	a	a	m	m	i	w	w	a
200	210	i	m	w	a	m	i	i	w	m	a
210	220	i	m	a	a	m	i	m	m	m	a
220	230	w	w	a	a	i	w	i	w	i	a
230	240	w	m	a	a	i	w	i	m	i	a
240	250	m	m	a	a	i	m	i	m	i	a

Hole:	HAM-63	a=absent	chl = chlorite	bi = biotite
Azimuth:	140	w=weak	mt = magnetite	cc = calcite
Dip:	-68	m=moderate	ep = epidote	py = pyrite
Easting:	663247	i=intense	qtz = quartz	cpy = chalcopyrite
Northing:	5372628		hem = hematite staining	po = pyrrhotite
Date:	3-Sep			

		Minerals									
From: (m)	**To: (m)**	**chl**	**mt**	**ep**	**qtz (blue)**	**hem**	**bi**	**cc**	**py**	**cpy**	**po**
250	260	m	m	w	a	i	m	m	w	m	a
260	270	m	m	m	a	m	m	m	w	w	a
270	280	m	m	m	a	m	m	m	m	w	a
280	290	m	w	m	w	m	m	m	m	w	a
290	300	m	w	w	a	m	m	w	w	m	a
300	310	w	m	w	w	m	w	w	m	w	a
310	320	m	m	m	w	m	m	w	w	w	a
320	330	i	m	m	a	m	i	w	w	w	a
330	340	i	m	m	w	w	i	m	w	w	a
340	350	m	w	w	a	w	m	m	w	w	a
350	360	m	m	w	w	w	m	w	w	m	a
360	370	m	m	w	w	m	m	w	w	m	a
370	380	w	m	w	w	w	w	m	w	w	a
380	390	w	m	w	w	w	w	w	w	w	a

Hole: HAM-63
Azimuth: 140
Dip: -68
Easting: 663247
Northing: 5372628
Date: 3-Sep

From: (m)	To: (m)	Description:
0	6	Overburden
6	79.2	Altered felsic to intermediate volcanics. Sodic alteration dominates with albite? And chlorite. Chlorite veinlets usually have bleached albitic? Envelope.
79.2	112.4	Brecciated cherty sedimentary rock. Subrounded to rounded cherty clasts in a highly chloritic matrix. Clasts range from 1cm to 20cm. Matrix is chl-bi-gnt-mt, and later cc-py-po-cpy.
112.4	159.9	Lightly brecciated volcanics. Composition ranges from mafic (darker) to felsic (lighter albitized with quartz eyes) Brecciation is crackle style, veinlets of chl-bi overprinted by cc-qtz.
159.9	384	Pink altered felsic-mafic volcanic breccia. Clasts are 1mm to 20cm and subangular. A very slight alignment of clasts defines a foliation at 20 to 40 DTCA. Matrix is chl-bi-mt-(ep) with later qtz-cc-(feld) veins. Cpy is assembled with later qtz cc veins. Qtz veining becomes dominant at ~218m, but two distinct brecciation events are still apparent. Quartz alteration is verry vuggy from 217. Darker fragments are also present, possibly more mafic fragments. Gabbro clasts are present from 345.8 to 352.7. Volcanic clasts are darker (more mafic?) from 352.7 down.
	EOH	

Hole:	HAM-66	a=absent	chl = chlorite	bi = biotite
Azimuth:	124	w=weak	mt = magnetite	cc = calcite
Dip:	-79	m=moderate	ep = epidote	py = pyrite
Easting:	663020	i=intense	qtz = quartz	cpy = chalcopyrite
Northing:	5372318		hem = hematite staining	po = pyrrhotite
Date:	13-May			

		Minerals									
From: (m)	**To: (m)**	**chl**	**mt**	**ep**	**qtz (blue)**	**hem**	**bi**	**cc**	**py**	**cpy**	**po**
0	10	m	a	a	a	i	m	w	w	a	a
10	20	i	a	w	m	m	i	w	w	a	a
20	30	m	w	m	a	i	m	m	w	a	a
30	40	m	m	i	w	i	m	m	w	m	a
40	50	m	i	i	a	i	m	w	w	m	a
50	60	i	m	i	m	m	i	i	w	m	a
60	70	m	i	m	m	m	m	i	w	m	a
70	80	m	m	m	w	w	m	w	w	w	a
80	90	m	w	m	m	i	m	m	m	m	a
90	100	m	i	w	m	i	m	m	m	m	a
100	110	w	i	m	w	m	w	m	w	m	a
110	120	m	i	m	w	m	m	m	m	i	a
120	130	m	m	m	i	m	m	m	m	i	a
130	140	m	m	m	w	i	m	w	i	i	a
140	150	m	m	m	w	i	m	w	m	m	a
150	160	m	w	w	w	m	m	w	w	w	a
160	170	w	w	w	m	w	w	w	a	a	a
170	180	w	m	w	w	m	w	m	w	w	a
180	190	m	w	m	m	m	m	w	w	w	a
190	200	m	m	w	m	m	m	m	m	w	a
200	210	m	m	w	w	m	m	m	w	m	a
210	220	m	w	w	w	w	m	m	m	m	a
220	230	i	m	w	w	m	i	a	w	w	a
230	240	m	m	w	m	i	m	w	w	m	a
240	250	m	m	w	i	m	m	w	m	i	a

Hole:	HAM-66	a=absent	chl = chlorite	bi = biotite
Azimuth:	124	w=weak	mt = magnetite	cc = calcite
Dip:	-79	m=moderate	ep = epidote	py = pyrite
Easting:	663020	i=intense	qtz = quartz	cpy = chalcopyrite
Northing:	5372318		hem = hematite staining	po = pyrrhotite
Date:	13-May			

		Minerals									
From: (m)	**To: (m)**	**chl**	**mt**	**ep**	**qtz (blue)**	**hem**	**bi**	**cc**	**py**	**cpy**	**po**
250	260	m	m	w	i	m	m	w	m	i	a
260	270	m	i	w	m	m	m	w	w	m	a
270	280	i	m	w	w	m	i	m	m	i	a
280	290	m	m	w	m	m	m	w	w	i	a
290	300	i	m	m	w	w	i	w	w	m	a
300	310	i	w	m	m	m	i	m	w	w	a
310	320	m	m	w	i	w	m	m	m	m	a
320	330	m	w	m	m	w	m	i	w	w	a

Hole: HAM-66
Azimuth: 124
Dip: -79
Easting: 663020
Northing: 5372318
Date: 13-May

From: (m)	To: (m)	Description:
0	5.8	Overburden
5.8	157.3	Brecciated volcanics, clasts are sub rounded to angular, dominantly angular. Quartz-eyes in some fragments suggest a rhyo-dacitic composition.
157.3	170.2	Less intense brecciation of mafic to intermediate volcanics. Most structure is in the form of a stockwork of veins, however technically still a breccia. Clasts are distinctly larger (up to 1m), lower contact is gradual.
170.2	327	Brecciated volcanic to volcaniclastics, possibly a brecciated debris flow. Volcanic clasts dominate, but minor cherty and gabbroic clasts are present. From 217.7 to 254.9 is an intensely broken zone with ~50% useful recovery. Still appears to be the same lithology. Unit grades to a heterolithic breccia with clasts of gabbro, volcanics and chert near bottom of hole.

EOH

Appendix C

SEM-EDS Mineral Analyses

Biotites

Sample	31-03	31-03	31-03	33-03	33-03	39-03	39-03	39-03
SiO2	36.5	37	38.06	38.86	38.79	38.72	39.36	37.76
TiO2	1.07	1.22	0.66	1.81	2.06	1.75	<dl	1.69
Al2O3	15.48	15.47	16.26	14.14	15.25	15.24	16.45	16.39
Fe2O3	<dl	<dl	<dl	<dl	<dl	<dl	<dl	<dl
FeO	17.12	16.59	16.51	15.84	15.78	15.18	14.88	15.65
MnO	<dl	<dl	<dl	<dl	<dl	<dl	<dl	<dl
MgO	13.32	14.06	14.12	14.32	13.92	15.11	15.17	13.94
CaO	<dl	<dl	<dl	<dl	<dl	<dl	<dl	<dl
Na2O	<dl	<dl	<dl	<dl	<dl	<dl	<dl	<dl
K2O	10.41	10.07	10.18	9.78	9.97	9.98	10.12	10.06
Total	93.9	94.41	95.79	94.75	95.77	95.98	95.98	95.49
Si	2.85	2.85	2.88	2.97	2.94	2.91	2.94	2.87
Ti	0.06	0.07	0.04	0.10	0.12	0.10	0.00	0.10
Al	1.42	1.40	1.45	1.28	1.36	1.35	1.45	1.47
Fe+3	0.00	0.00	0.00	0.00	0.00	0.00	0.00	0.00
Fe+2	1.12	1.07	1.04	1.01	1.00	0.95	0.93	0.99
Mn	0.00	0.00	0.00	0.00	0.00	0.00	0.00	0.00
Mg	1.55	1.61	1.59	1.63	1.57	1.69	1.69	1.58
Ca	0.00	0.00	0.00	0.00	0.00	0.00	0.00	0.00
Na	0.00	0.00	0.00	0.00	0.00	0.00	0.00	0.00
K	1.04	0.99	0.98	0.95	0.97	0.96	0.96	0.97
Si(iv)	2.85	2.85	2.88	2.97	2.94	2.91	2.94	2.87
Ti(iv)	0.06	0.07	0.04	0.10	0.12	0.10	0.00	0.10
Al(iv)	1.09	1.08	1.08	0.92	0.94	0.99	1.06	1.04
Al(vi)	0.33	0.32	0.36	0.35	0.42	0.36	0.38	0.43
Fe+3(vi)	0.00	0.00	0.00	0.00	0.00	0.00	0.00	0.00
Fe+2(vi)	1.12	1.07	1.04	1.01	1.00	0.95	0.93	0.99
Mn(vi)	0.00	0.00	0.00	0.00	0.00	0.00	0.00	0.00
Mg(vi)	1.55	1.61	1.59	1.63	1.57	1.69	1.69	1.58
Ca	0.00	0.00	0.00	0.00	0.00	0.00	0.00	0.00
Na	0.00	0.00	0.00	0.00	0.00	0.00	0.00	0.00
K	1.04	0.99	0.98	0.95	0.97	0.96	0.96	0.97
Fe/(Fe+Mg	0.42	0.40	0.40	0.38	0.39	0.36	0.35	0.39

Sample	39-03	39-03	39-03	39-03	41-01	41-01	41-01	41-01
SiO2	37.5	37.68	37.06	36.39	37.79	38.51	36.7	37.95
TiO2	1.9	<dl	1.9	1.73	1.33	0.98	1.37	1.13
Al2O3	16.16	16.7	16.04	15.84	16.08	15.18	16.45	16.73
Fe2O3	<dl	<dl	<dl	<dl	<dl	<dl	<dl	<dl
FeO	14.58	15.31	15.72	16.14	18.66	17.02	17.12	17.74
MnO	<dl	<dl	<dl	<dl	<dl	<dl	<dl	<dl
MgO	14.71	14.78	13.71	13.16	12.86	15.14	12.3	13.48
CaO	<dl	<dl	<dl	<dl	<dl	<dl	<dl	<dl
Na2O	<dl	<dl	<dl	<dl	<dl	<dl	<dl	<dl
K2O	9.93	10.04	9.97	10.05	9.51	9.47	9.65	9.94
Total	94.78	94.51	94.4	93.31	96.23	96.3	93.59	96.97
Si	2.85	2.86	2.85	2.85	2.86	2.87	2.86	2.84
Ti	0.11	0.00	0.11	0.10	0.08	0.05	0.08	0.06
Al	1.45	1.49	1.45	1.46	1.43	1.33	1.51	1.48
Fe+3	0.00	0.00	0.00	0.00	0.00	0.00	0.00	0.00
Fe+2	0.93	0.97	1.01	1.06	1.18	1.06	1.12	1.11
Mn	0.00	0.00	0.00	0.00	0.00	0.00	0.00	0.00
Mg	1.67	1.67	1.57	1.53	1.45	1.68	1.43	1.51
Ca	0.00	0.00	0.00	0.00	0.00	0.00	0.00	0.00
Na	0.00	0.00	0.00	0.00	0.00	0.00	0.00	0.00
K	0.96	0.97	0.98	1.00	0.92	0.90	0.96	0.95
Si(iv)	2.85	2.86	2.85	2.85	2.86	2.87	2.86	2.84
Ti(iv)	0.11	0.00	0.11	0.10	0.08	0.05	0.08	0.06
Al(iv)	1.04	1.14	1.04	1.05	1.07	1.08	1.06	1.09
Al(vi)	0.41	0.36	0.42	0.41	0.37	0.26	0.45	0.38
Fe+3(vi)	0.00	0.00	0.00	0.00	0.00	0.00	0.00	0.00
Fe+2(vi)	0.93	0.97	1.01	1.06	1.18	1.06	1.12	1.11
Mn(vi)	0.00	0.00	0.00	0.00	0.00	0.00	0.00	0.00
Mg(vi)	1.67	1.67	1.57	1.53	1.45	1.68	1.43	1.51
Ca	0.00	0.00	0.00	0.00	0.00	0.00	0.00	0.00
Na	0.00	0.00	0.00	0.00	0.00	0.00	0.00	0.00
K	0.96	0.97	0.98	1.00	0.92	0.90	0.96	0.95
Fe/(Fe+Mg	0.36	0.37	0.39	0.41	0.45	0.39	0.44	0.42

Sample	58-03	58-04	58-04	58-04	66-04	66-04	66-04	66-04
SiO2	37.95	36.75	36.85	36.76	37.39	37.52	36.85	37.97
TiO2	1.45	1.81	1.44	1.34	1.25	1	1.5	1.53
Al2O3	16.65	16.62	16.26	16.13	16.97	15.51	15.7	16.5
Fe2O3	<dl	<dl	<dl	<dl	<dl	<dl	<dl	<dl
FeO	16.76	17.86	18.1	18.03	16.98	16.99	16.92	17.09
MnO	<dl	<dl	<dl	<dl	<dl	<dl	<dl	<dl
MgO	12.88	13.06	13.27	13.07	13.48	14.04	13.23	13.34
CaO	<dl	<dl	<dl	<dl	<dl	<dl	<dl	<dl
Na2O	<dl	<dl	<dl	<dl	<dl	<dl	<dl	<dl
K2O	9.98	9.56	10.12	10.15	9.81	9.72	9.6	9.85
Total	95.67	95.66	96.04	95.48	95.88	94.78	93.8	96.28
Si	2.89	2.79	2.80	2.82	2.83	2.86	2.85	2.87
Ti	0.08	0.10	0.08	0.08	0.07	0.06	0.09	0.09
Al	1.49	1.49	1.46	1.46	1.51	1.40	1.43	1.47
Fe+3	0.00	0.00	0.00	0.00	0.00	0.00	0.00	0.00
Fe+2	1.07	1.14	1.15	1.16	1.07	1.08	1.10	1.08
Mn	0.00	0.00	0.00	0.00	0.00	0.00	0.00	0.00
Mg	1.46	1.48	1.50	1.49	1.52	1.60	1.53	1.50
Ca	0.00	0.00	0.00	0.00	0.00	0.00	0.00	0.00
Na	0.00	0.00	0.00	0.00	0.00	0.00	0.00	0.00
K	0.97	0.93	0.98	0.99	0.95	0.95	0.95	0.95
Si(iv)	2.89	2.79	2.80	2.82	2.83	2.86	2.85	2.87
Ti(iv)	0.08	0.10	0.08	0.08	0.07	0.06	0.09	0.09
Al(iv)	1.03	1.10	1.11	1.11	1.10	1.08	1.06	1.05
Al(vi)	0.47	0.39	0.34	0.35	0.41	0.32	0.38	0.42
Fe+3(vi)	0.00	0.00	0.00	0.00	0.00	0.00	0.00	0.00
Fe+2(vi)	1.07	1.14	1.15	1.16	1.07	1.08	1.10	1.08
Mn(vi)	0.00	0.00	0.00	0.00	0.00	0.00	0.00	0.00
Mg(vi)	1.46	1.48	1.50	1.49	1.52	1.60	1.53	1.50
Ca	0.00	0.00	0.00	0.00	0.00	0.00	0.00	0.00
Na	0.00	0.00	0.00	0.00	0.00	0.00	0.00	0.00
K	0.97	0.93	0.98	0.99	0.95	0.95	0.95	0.95
Fe/(Fe+Mg	0.42	0.43	0.43	0.44	0.41	0.40	0.42	0.42

Sample	66-04	66-08
SiO2	36.2	37.49
TiO2	1.59	1.54
Al2O3	16.26	16.36
Fe2O3	<dl	<dl
FeO	16.53	17.13
MnO	<dl	<dl
MgO	12.91	12.26
CaO	<dl	<dl
Na2O	<dl	<dl
K2O	9.49	10.17
Total	92.98	94.95
Si	2.83	2.90
Ti	0.09	0.09
Al	1.50	1.49
Fe+3	0.00	0.00
Fe+2	1.08	1.11
Mn	0.00	0.00
Mg	1.50	1.41
Ca	0.00	0.00
Na	0.00	0.00
K	0.95	1.00
Si(iv)	2.83	2.90
Ti(iv)	0.09	0.09
Al(iv)	1.08	1.01
Al(vi)	0.42	0.48
Fe+3(vi)	0.00	0.00
Fe+2(vi)	1.08	1.11
Mn(vi)	0.00	0.00
Mg(vi)	1.50	1.41
Ca	0.00	0.00
Na	0.00	0.00
K	0.95	1.00
Fe/(Fe+Mg	0.42	0.44

Chlorites

(Including geothermometry of Cathelineau and Nieva (1985))

Sample	31-03	31-03	31-03	31-03	31-03	31-03	31-03	31-03
SiO2	25.1	25.51	25.52	26	25.01	26.24	26.03	25.5
TiO2	<dl	<dl	<dl	<dl	<dl	<dl	<dl	<dl
Al2O3	20.62	20.11	20.58	20.16	20.35	20.94	20.23	20.75
FeO	20.31	21.21	20.17	20.82	20.24	21.12	20.47	20.55
Fe2O3	<dl	<dl	<dl	<dl	<dl	<dl	<dl	<dl
MnO	<dl	<dl	<dl	<dl	<dl	<dl	<dl	<dl
MgO	17.49	18.51	17.97	18.53	18	18.28	17.96	18.39
CaO	<dl	<dl	<dl	<dl	<dl	<dl	<dl	<dl
Na2O	<dl	<dl	<dl	<dl	<dl	<dl	<dl	<dl
K2O	<dl	<dl	<dl	<dl	<dl	<dl	<dl	<dl
Total	83.52	85.34	84.24	85.51	83.6	86.58	84.69	85.19
Si	2.71	2.71	2.73	2.74	2.70	2.73	2.77	2.70
Ti	0.00	0.00	0.00	0.00	0.00	0.00	0.00	0.00
Al	2.62	2.52	2.59	2.51	2.59	2.57	2.53	2.59
Fe (as 2+)	1.83	1.88	1.80	1.84	1.83	1.84	1.82	1.82
Fe (as 3+)	0.00	0.00	0.00	0.00	0.00	0.00	0.00	0.00
Mn	0.00	0.00	0.00	0.00	0.00	0.00	0.00	0.00
Mg	2.81	2.93	2.86	2.92	2.90	2.84	2.85	2.90
Ca	0.00	0.00	0.00	0.00	0.00	0.00	0.00	0.00
Na	0.00	0.00	0.00	0.00	0.00	0.00	0.00	0.00
K	0.00	0.00	0.00	0.00	0.00	0.00	0.00	0.00
Total	9.98	10.03	9.98	10.00	10.01	9.98	9.97	10.01
Si(iv)	2.71	2.71	2.73	2.74	2.70	2.73	2.77	2.70
Ti(iv)	0.00	0.00	0.00	0.00	0.00	0.00	0.00	0.00
Al(iv)	1.29	1.29	1.27	1.26	1.30	1.27	1.23	1.30
Al(vi)	1.33	1.22	1.32	1.25	1.29	1.30	1.30	1.29
Fe2+(vi)	1.83	1.88	1.80	1.84	1.83	1.84	1.82	1.82
Fe3+(vi)	0.00	0.00	0.00	0.00	0.00	0.00	0.00	0.00
Mn(vi)	0.00	0.00	0.00	0.00	0.00	0.00	0.00	0.00
Mg(vi)	2.81	2.93	2.86	2.92	2.90	2.84	2.85	2.90
Ca	0.00	0.00	0.00	0.00	0.00	0.00	0.00	0.00
Na	0.00	0.00	0.00	0.00	0.00	0.00	0.00	0.00
K	0.00	0.00	0.00	0.00	0.00	0.00	0.00	0.00
R	5.98	6.03	5.98	6.00	6.01	5.98	5.97	6.01
Fe/R	0.31	0.31	0.30	0.31	0.30	0.31	0.30	0.30
T (°C)	292	292	288	284	294	287	279	294

Sample	31-03	31-03	31-03	31-03	31-03	31-03	31-03	31-03
SiO2	25.88	25.09	25.77	25.6	26.38	25.41	25.47	29.81
TiO2	<dl	<dl	<dl	<dl	<dl	<dl	<dl	0.3
Al2O3	20.7	19.79	20.33	20.43	21.08	20.34	20.55	18.42
FeO	21.27	20.42	21.11	20.23	21.18	20.69	20.93	18.72
Fe2O3	<dl	<dl	<dl	<dl	<dl	<dl	<dl	<dl
MnO	<dl	<dl	<dl	<dl	<dl	<dl	<dl	<dl
MgO	17.62	17.8	18.17	18.72	18.49	18.63	17.97	17.21
CaO	<dl	<dl	<dl	<dl	<dl	<dl	<dl	<dl
Na2O	<dl	<dl	<dl	<dl	<dl	<dl	<dl	<dl
K2O	<dl	<dl	<dl	<dl	<dl	<dl	<dl	2.61
Total	85.47	83.1	85.38	84.98	87.13	85.07	84.92	87.07
Si	2.74	2.73	2.73	2.71	2.73	2.70	2.71	3.08
Ti	0.00	0.00	0.00	0.00	0.00	0.00	0.00	0.02
Al	2.58	2.54	2.54	2.55	2.57	2.55	2.58	2.24
Fe (as 2+)	1.88	1.86	1.87	1.79	1.83	1.84	1.86	1.62
Fe (as 3+)	0.00	0.00	0.00	0.00	0.00	0.00	0.00	0.00
Mn	0.00	0.00	0.00	0.00	0.00	0.00	0.00	0.00
Mg	2.78	2.88	2.87	2.96	2.85	2.95	2.85	2.65
Ca	0.00	0.00	0.00	0.00	0.00	0.00	0.00	0.00
Na	0.00	0.00	0.00	0.00	0.00	0.00	0.00	0.00
K	0.00	0.00	0.00	0.00	0.00	0.00	0.00	0.34
Total	9.97	10.00	10.00	10.01	9.99	10.03	10.00	9.95
Si(iv)	2.74	2.73	2.73	2.71	2.73	2.70	2.71	3.08
Ti(iv)	0.00	0.00	0.00	0.00	0.00	0.00	0.00	0.02
Al(iv)	1.26	1.27	1.27	1.29	1.27	1.30	1.29	0.90
Al(vi)	1.32	1.26	1.27	1.26	1.30	1.24	1.29	1.34
Fe2+(vi)	1.88	1.86	1.87	1.79	1.83	1.84	1.86	1.62
Fe3+(vi)	0.00	0.00	0.00	0.00	0.00	0.00	0.00	0.00
Mn(vi)	0.00	0.00	0.00	0.00	0.00	0.00	0.00	0.00
Mg(vi)	2.78	2.88	2.87	2.96	2.85	2.95	2.85	2.65
Ca	0.00	0.00	0.00	0.00	0.00	0.00	0.00	0.00
Na	0.00	0.00	0.00	0.00	0.00	0.00	0.00	0.00
K	0.00	0.00	0.00	0.00	0.00	0.00	0.00	0.34
R	5.97	6.00	6.00	6.01	5.99	6.03	6.00	5.95
Fe/R	0.31	0.31	0.31	0.30	0.31	0.30	0.31	0.27
T (°C)	286	288	287	291	287	294	291	208

Sample	31-03	31-03	31-03	31-03	31-03	31-03	31-03	31-03
SiO2	26.66	25.9	27.45	26.85	26.16	27.36	27.57	27.06
TiO2	<dl	<dl	<dl	<dl	<dl	0.28	<dl	<dl
Al2O3	19.91	20.27	19.05	20.54	21.07	20.01	19.71	17.46
FeO	21.02	20.41	20.2	21.19	21.61	20.53	20.81	20.2
Fe2O3	<dl	<dl	<dl	<dl	<dl	<dl	<dl	<dl
MnO	<dl	0.27	<dl	<dl	<dl	<dl	<dl	<dl
MgO	17.43	18.7	17.76	19.68	18.12	18.41	19.23	19.3
CaO	<dl	<dl	<dl	<dl	<dl	<dl	<dl	<dl
Na2O	<dl	<dl	<dl	<dl	<dl	<dl	<dl	<dl
K2O	1	<dl	1.04	<dl	<dl	1.05	<dl	0.16
Total	86.02	85.55	85.5	88.26	86.96	87.64	87.32	84.18
Si	2.81	2.73	2.90	2.74	2.72	2.82	2.84	2.90
Ti	0.00	0.00	0.00	0.00	0.00	0.02	0.00	0.00
Al	2.48	2.52	2.37	2.47	2.58	2.43	2.39	2.20
Fe (as 2+)	1.85	1.80	1.78	1.81	1.88	1.77	1.79	1.81
Fe (as 3+)	0.00	0.00	0.00	0.00	0.00	0.00	0.00	0.00
Mn	0.00	0.02	0.00	0.00	0.00	0.00	0.00	0.00
Mg	2.74	2.94	2.80	3.00	2.81	2.83	2.95	3.08
Ca	0.00	0.00	0.00	0.00	0.00	0.00	0.00	0.00
Na	0.00	0.00	0.00	0.00	0.00	0.00	0.00	0.00
K	0.13	0.00	0.14	0.00	0.00	0.14	0.00	0.02
Total	10.02	10.01	9.99	10.02	9.99	10.01	9.97	10.01
Si(iv)	2.81	2.73	2.90	2.74	2.72	2.82	2.84	2.90
Ti(iv)	0.00	0.00	0.00	0.00	0.00	0.02	0.00	0.00
Al(iv)	1.19	1.27	1.10	1.26	1.28	1.16	1.16	1.10
Al(vi)	1.29	1.25	1.27	1.21	1.30	1.27	1.23	1.10
Fe2+(vi)	1.85	1.80	1.78	1.81	1.88	1.77	1.79	1.81
Fe3+(vi)	0.00	0.00	0.00	0.00	0.00	0.00	0.00	0.00
Mn(vi)	0.00	0.02	0.00	0.00	0.00	0.00	0.00	0.00
Mg(vi)	2.74	2.94	2.80	3.00	2.81	2.83	2.95	3.08
Ca	0.00	0.00	0.00	0.00	0.00	0.00	0.00	0.00
Na	0.00	0.00	0.00	0.00	0.00	0.00	0.00	0.00
K	0.13	0.00	0.14	0.00	0.00	0.14	0.00	0.02
R	6.02	6.01	5.99	6.02	5.99	6.01	5.97	6.01
Fe/R	0.31	0.30	0.30	0.30	0.31	0.29	0.30	0.30
T (°C)	270	287	251	285	289	263	264	252

Sample	31-04	31-04	31-04	31-04	31-04	31-04	33-03	33-03
SiO2	28.84	27.24	27.77	27.22	27.11	25.95	26.75	26.58
TiO2	<dl	<dl	<dl	<dl	<dl	<dl	<dl	<dl
Al2O3	17.09	16.13	17.35	17.76	18.77	20.13	21.49	20.48
FeO	21.01	20.7	21.09	20.6	20.7	21.87	19.8	20.16
Fe2O3	<dl	<dl	<dl	<dl	<dl	<dl	<dl	<dl
MnO	0.43	0.37	0.37	0.31	0.3	0.34	<dl	<dl
MgO	20.27	18.63	18.72	19.07	18.65	18.78	20.14	18.75
CaO	0.2	<dl	<dl	<dl	<dl	<dl	<dl	<dl
Na2O	<dl	<dl	<dl	<dl	<dl	<dl	<dl	<dl
K2O	<dl	<dl	<dl	<dl	<dl	<dl	<dl	<dl
Total	87.84	83.07	85.3	84.96	85.53	87.07	88.18	85.97
Si	2.96	2.97	2.94	2.89	2.86	2.71	2.71	2.77
Ti	0.00	0.00	0.00	0.00	0.00	0.00	0.00	0.00
Al	2.07	2.07	2.17	2.22	2.33	2.48	2.57	2.52
Fe (as 2+)	1.81	1.89	1.87	1.83	1.83	1.91	1.68	1.76
Fe (as 3+)	0.00	0.00	0.00	0.00	0.00	0.00	0.00	0.00
Mn	0.04	0.03	0.03	0.03	0.03	0.03	0.00	0.00
Mg	3.10	3.03	2.96	3.02	2.93	2.92	3.04	2.92
Ca	0.02	0.00	0.00	0.00	0.00	0.00	0.00	0.00
Na	0.00	0.00	0.00	0.00	0.00	0.00	0.00	0.00
K	0.00	0.00	0.00	0.00	0.00	0.00	0.00	0.00
Total	10.00	9.99	9.97	10.00	9.98	10.05	10.00	9.97
Si(iv)	2.96	2.97	2.94	2.89	2.86	2.71	2.71	2.77
Ti(iv)	0.00	0.00	0.00	0.00	0.00	0.00	0.00	0.00
Al(iv)	1.04	1.03	1.06	1.11	1.14	1.29	1.29	1.23
Al(vi)	1.03	1.04	1.11	1.12	1.19	1.19	1.28	1.29
Fe2+(vi)	1.81	1.89	1.87	1.83	1.83	1.91	1.68	1.76
Fe3+(vi)	0.00	0.00	0.00	0.00	0.00	0.00	0.00	0.00
Mn(vi)	0.04	0.03	0.03	0.03	0.03	0.03	0.00	0.00
Mg(vi)	3.10	3.03	2.96	3.02	2.93	2.92	3.04	2.92
Ca	0.02	0.00	0.00	0.00	0.00	0.00	0.00	0.00
Na	0.00	0.00	0.00	0.00	0.00	0.00	0.00	0.00
K	0.00	0.00	0.00	0.00	0.00	0.00	0.00	0.00
R	6.00	5.99	5.97	6.00	5.98	6.05	6.00	5.97
Fe/R	0.30	0.31	0.31	0.31	0.31	0.32	0.28	0.29
T (°C)	238	236	242	253	260	291	291	278

Sample	33-03	33-03	33-03	33-03	33-03	33-03	36-05	36-05
SiO2	27.03	26.77	26.75	26.34	26.5	26.49	26.59	26.87
TiO2	<dl	<dl	<dl	<dl	<dl	<dl	<dl	<dl
Al2O3	20.32	20.16	20.2	21.73	20.92	21.16	20.95	19.8
FeO	19.5	19.18	19.6	19.91	19.93	19.04	19.75	21.5
Fe2O3	<dl	<dl	<dl	<dl	<dl	<dl	<dl	<dl
MnO	<dl	<dl	<dl	<dl	<dl	<dl	<dl	<dl
MgO	19.38	19.41	20	18.83	19.52	19.75	18.4	18.05
CaO	<dl	<dl	<dl	<dl	<dl	<dl	<dl	<dl
Na2O	<dl	<dl	<dl	<dl	<dl	<dl	<dl	<dl
K2O	<dl	<dl	<dl	<dl	<dl	<dl	<dl	<dl
Total	86.23	85.52	86.55	86.81	86.87	86.44	85.69	86.22
Si	2.80	2.79	2.77	2.72	2.73	2.73	2.77	2.82
Ti	0.00	0.00	0.00	0.00	0.00	0.00	0.00	0.00
Al	2.48	2.48	2.46	2.64	2.54	2.57	2.58	2.44
Fe (as 2+)	1.69	1.67	1.69	1.72	1.72	1.64	1.72	1.88
Fe (as 3+)	0.00	0.00	0.00	0.00	0.00	0.00	0.00	0.00
Mn	0.00	0.00	0.00	0.00	0.00	0.00	0.00	0.00
Mg	2.99	3.02	3.08	2.89	3.00	3.04	2.86	2.82
Ca	0.00	0.00	0.00	0.00	0.00	0.00	0.00	0.00
Na	0.00	0.00	0.00	0.00	0.00	0.00	0.00	0.00
K	0.00	0.00	0.00	0.00	0.00	0.00	0.00	0.00
Total	9.96	9.97	10.00	9.96	10.00	9.98	9.94	9.96
Si(iv)	2.80	2.79	2.77	2.72	2.73	2.73	2.77	2.82
Ti(iv)	0.00	0.00	0.00	0.00	0.00	0.00	0.00	0.00
Al(iv)	1.20	1.21	1.23	1.28	1.27	1.27	1.23	1.18
Al(vi)	1.28	1.27	1.23	1.36	1.28	1.30	1.35	1.26
Fe2+(vi)	1.69	1.67	1.69	1.72	1.72	1.64	1.72	1.88
Fe3+(vi)	0.00	0.00	0.00	0.00	0.00	0.00	0.00	0.00
Mn(vi)	0.00	0.00	0.00	0.00	0.00	0.00	0.00	0.00
Mg(vi)	2.99	3.02	3.08	2.89	3.00	3.04	2.86	2.82
Ca	0.00	0.00	0.00	0.00	0.00	0.00	0.00	0.00
Na	0.00	0.00	0.00	0.00	0.00	0.00	0.00	0.00
K	0.00	0.00	0.00	0.00	0.00	0.00	0.00	0.00
R	5.96	5.97	6.00	5.96	6.00	5.98	5.94	5.96
Fe/R	0.28	0.28	0.28	0.29	0.29	0.27	0.29	0.32
T (°C)	272	274	280	290	287	287	278	269

Sample	36-05	36-05	36-05	36-05	36-05	36-05	39-01	39-01
SiO2	29.54	28.55	29.19	27.24	27.8	26.8	25.51	26.19
TiO2	<dl	<dl	<dl	<dl	<dl	<dl	<dl	<dl
Al2O3	16.65	18.51	14.81	21.23	21.94	20.32	22.16	21.69
FeO	21.38	21.37	23.35	20.67	19.12	21.78	20.23	21.2
Fe2O3	<dl	<dl	<dl	<dl	<dl	<dl	<dl	<dl
MnO	<dl	<dl	<dl	<dl	<dl	<dl	<dl	<dl
MgO	18.24	18.35	18.1	18.02	19.73	17.94	18.32	18.64
CaO	<dl	<dl	<dl	<dl	<dl	<dl	<dl	<dl
Na2O	<dl	<dl	<dl	<dl	<dl	<dl	<dl	<dl
K2O	0.45	<dl	<dl	<dl	<dl	<dl	<dl	<dl
Total	86.26	86.78	85.45	87.16	88.59	86.84	86.22	87.72
Si	3.09	2.96	3.12	2.80	2.78	2.79	2.66	2.69
Ti	0.00	0.00	0.00	0.00	0.00	0.00	0.00	0.00
Al	2.05	2.26	1.86	2.57	2.59	2.49	2.72	2.63
Fe (as 2+)	1.87	1.85	2.09	1.78	1.60	1.90	1.76	1.82
Fe (as 3+)	0.00	0.00	0.00	0.00	0.00	0.00	0.00	0.00
Mn	0.00	0.00	0.00	0.00	0.00	0.00	0.00	0.00
Mg	2.84	2.84	2.88	2.76	2.95	2.78	2.84	2.86
Ca	0.00	0.00	0.00	0.00	0.00	0.00	0.00	0.00
Na	0.00	0.00	0.00	0.00	0.00	0.00	0.00	0.00
K	0.06	0.00	0.00	0.00	0.00	0.00	0.00	0.00
Total	9.91	9.91	9.95	9.91	9.92	9.96	9.98	10.00
Si(iv)	3.09	2.96	3.12	2.80	2.78	2.79	2.66	2.69
Ti(iv)	0.00	0.00	0.00	0.00	0.00	0.00	0.00	0.00
Al(iv)	0.91	1.04	0.88	1.20	1.22	1.21	1.34	1.31
Al(vi)	1.14	1.22	0.98	1.37	1.37	1.28	1.38	1.32
Fe2+(vi)	1.87	1.85	2.09	1.78	1.60	1.90	1.76	1.82
Fe3+(vi)	0.00	0.00	0.00	0.00	0.00	0.00	0.00	0.00
Mn(vi)	0.00	0.00	0.00	0.00	0.00	0.00	0.00	0.00
Mg(vi)	2.84	2.84	2.88	2.76	2.95	2.78	2.84	2.86
Ca	0.00	0.00	0.00	0.00	0.00	0.00	0.00	0.00
Na	0.00	0.00	0.00	0.00	0.00	0.00	0.00	0.00
K	0.06	0.00	0.00	0.00	0.00	0.00	0.00	0.00
R	5.91	5.91	5.95	5.91	5.92	5.96	5.98	6.00
Fe/R	0.32	0.31	0.35	0.30	0.27	0.32	0.29	0.30
T (°C)	211	238	205	272	276	274	303	295

Sample	39-01	39-01	39-01	39-01	39-01	39-02	39-02	39-02
SiO2	26.08	26.64	26.9	26.18	26.57	26.51	26.44	26.29
TiO2	<dl	<dl	<dl	<dl	<dl	<dl	<dl	<dl
Al2O3	21.38	21.01	20.74	20.05	20.59	21.21	21.06	20.9
FeO	20.74	20.58	20.62	20.34	20.71	21.14	21.13	20.44
Fe2O3	<dl	<dl	<dl	<dl	<dl	<dl	<dl	<dl
MnO	<dl	<dl	<dl	<dl	<dl	<dl	<dl	<dl
MgO	18.86	19.26	18.02	18.05	18.5	20.08	19.57	18.66
CaO	<dl	<dl	<dl	<dl	<dl	<dl	<dl	<dl
Na2O	<dl	<dl	<dl	<dl	<dl	<dl	<dl	<dl
K2O	<dl	<dl	<dl	<dl	<dl	<dl	<dl	<dl
Total	87.06	87.49	86.28	84.62	86.37	88.94	88.2	86.29
Si	2.70	2.74	2.80	2.78	2.77	2.69	2.70	2.74
Ti	0.00	0.00	0.00	0.00	0.00	0.00	0.00	0.00
Al	2.60	2.54	2.54	2.51	2.53	2.53	2.54	2.57
Fe (as 2+)	1.79	1.77	1.79	1.81	1.80	1.79	1.81	1.78
Fe (as 3+)	0.00	0.00	0.00	0.00	0.00	0.00	0.00	0.00
Mn	0.00	0.00	0.00	0.00	0.00	0.00	0.00	0.00
Mg	2.91	2.95	2.79	2.86	2.87	3.03	2.98	2.90
Ca	0.00	0.00	0.00	0.00	0.00	0.00	0.00	0.00
Na	0.00	0.00	0.00	0.00	0.00	0.00	0.00	0.00
K	0.00	0.00	0.00	0.00	0.00	0.00	0.00	0.00
Total	10.00	9.99	9.93	9.96	9.97	10.05	10.03	9.98
Si(iv)	2.70	2.74	2.80	2.78	2.77	2.69	2.70	2.74
Ti(iv)	0.00	0.00	0.00	0.00	0.00	0.00	0.00	0.00
Al(iv)	1.30	1.26	1.20	1.22	1.23	1.31	1.30	1.26
Al(vi)	1.30	1.28	1.34	1.29	1.29	1.22	1.24	1.30
Fe2+(vi)	1.79	1.77	1.79	1.81	1.80	1.79	1.81	1.78
Fe3+(vi)	0.00	0.00	0.00	0.00	0.00	0.00	0.00	0.00
Mn(vi)	0.00	0.00	0.00	0.00	0.00	0.00	0.00	0.00
Mg(vi)	2.91	2.95	2.79	2.86	2.87	3.03	2.98	2.90
Ca	0.00	0.00	0.00	0.00	0.00	0.00	0.00	0.00
Na	0.00	0.00	0.00	0.00	0.00	0.00	0.00	0.00
K	0.00	0.00	0.00	0.00	0.00	0.00	0.00	0.00
R	6.00	5.99	5.93	5.96	5.97	6.05	6.03	5.98
Fe/R	0.30	0.29	0.30	0.30	0.30	0.30	0.30	0.30
T (°C)	294	286	273	276	279	296	293	286

Sample	39-02	39-02	39-02	39-02	39-03	39-03	39-03	39-03
SiO2	27.72	27.17	25.87	27.43	27.37	28.79	26.98	30.85
TiO2	<dl	<dl	<dl	<dl	<dl	<dl	<dl	<dl
Al2O3	18.89	21.56	20.46	18.31	20.34	17.85	19.99	15.87
FeO	20.7	21.53	20.97	20.35	19.05	16.68	17.83	15.57
Fe2O3	<dl	<dl	<dl	<dl	<dl	<dl	<dl	<dl
MnO	<dl	<dl	<dl	<dl	<dl	<dl	<dl	<dl
MgO	18.88	18.07	18.11	17.48	19.94	23.45	20.64	22.23
CaO	<dl	<dl	<dl	<dl	<dl	<dl	<dl	<dl
Na2O	<dl	<dl	<dl	<dl	<dl	<dl	<dl	<dl
K2O	<dl	<dl	<dl	0.45	<dl	<dl	<dl	<dl
Total	86.19	88.33	85.41	84.02	86.7	86.77	85.44	84.52
Si	2.89	2.77	2.73	2.94	2.81	2.92	2.80	3.18
Ti	0.00	0.00	0.00	0.00	0.00	0.00	0.00	0.00
Al	2.32	2.59	2.55	2.31	2.46	2.13	2.44	1.93
Fe (as 2+)	1.80	1.83	1.85	1.82	1.64	1.41	1.55	1.34
Fe (as 3+)	0.00	0.00	0.00	0.00	0.00	0.00	0.00	0.00
Mn	0.00	0.00	0.00	0.00	0.00	0.00	0.00	0.00
Mg	2.93	2.74	2.85	2.79	3.05	3.55	3.19	3.41
Ca	0.00	0.00	0.00	0.00	0.00	0.00	0.00	0.00
Na	0.00	0.00	0.00	0.00	0.00	0.00	0.00	0.00
K	0.00	0.00	0.00	0.06	0.00	0.00	0.00	0.00
Total	9.95	9.94	9.99	9.93	9.96	10.01	9.98	9.86
Si(iv)	2.89	2.77	2.73	2.94	2.81	2.92	2.80	3.18
Ti(iv)	0.00	0.00	0.00	0.00	0.00	0.00	0.00	0.00
Al(iv)	1.11	1.23	1.27	1.06	1.19	1.08	1.20	0.82
Al(vi)	1.21	1.36	1.28	1.25	1.27	1.05	1.24	1.10
Fe2+(vi)	1.80	1.83	1.85	1.82	1.64	1.41	1.55	1.34
Fe3+(vi)	0.00	0.00	0.00	0.00	0.00	0.00	0.00	0.00
Mn(vi)	0.00	0.00	0.00	0.00	0.00	0.00	0.00	0.00
Mg(vi)	2.93	2.74	2.85	2.79	3.05	3.55	3.19	3.41
Ca	0.00	0.00	0.00	0.00	0.00	0.00	0.00	0.00
Na	0.00	0.00	0.00	0.00	0.00	0.00	0.00	0.00
K	0.00	0.00	0.00	0.06	0.00	0.00	0.00	0.00
R	5.95	5.94	5.99	5.93	5.96	6.01	5.98	5.86
Fe/R	0.30	0.31	0.31	0.31	0.27	0.24	0.26	0.23
T (°C)	253	279	286	242	270	247	273	192

Sample	39-03	41-01	41-01	41-01	41-01	41-01	56-03	58-03
SiO2	31.13	27.14	27.93	27.66	28.15	27.38	27.26	26.95
TiO2	<dl	<dl	<dl	<dl	<dl	<dl	<dl	<dl
Al2O3	17.81	19.93	19.67	19.86	21.02	21.05	21.25	20.86
FeO	15.67	22.43	21.92	19.37	20.54	21.06	21.68	21.78
Fe2O3	<dl	<dl	<dl	<dl	<dl	<dl	<dl	<dl
MnO	<dl	<dl	<dl	<dl	<dl	<dl	<dl	<dl
MgO	24.42	17.74	18.73	20.22	19.71	18.96	19.37	19.31
CaO	<dl	<dl	<dl	<dl	<dl	<dl	<dl	<dl
Na2O	<dl	<dl	<dl	<dl	<dl	<dl	<dl	<dl
K2O	<dl	<dl	<dl	<dl	<dl	<dl	<dl	<dl
Total	89.03	87.24	88.25	87.11	89.42	88.45	89.56	88.9
Si	3.04	2.82	2.86	2.83	2.81	2.78	2.74	2.74
Ti	0.00	0.00	0.00	0.00	0.00	0.00	0.00	0.00
Al	2.05	2.44	2.37	2.40	2.48	2.52	2.52	2.50
Fe (as 2+)	1.28	1.95	1.87	1.66	1.72	1.79	1.82	1.85
Fe (as 3+)	0.00	0.00	0.00	0.00	0.00	0.00	0.00	0.00
Mn	0.00	0.00	0.00	0.00	0.00	0.00	0.00	0.00
Mg	3.56	2.75	2.86	3.09	2.94	2.87	2.91	2.93
Ca	0.00	0.00	0.00	0.00	0.00	0.00	0.00	0.00
Na	0.00	0.00	0.00	0.00	0.00	0.00	0.00	0.00
K	0.00	0.00	0.00	0.00	0.00	0.00	0.00	0.00
Total	9.93	9.96	9.96	9.97	9.95	9.96	10.00	10.01
Si(iv)	3.04	2.82	2.86	2.83	2.81	2.78	2.74	2.74
Ti(iv)	0.00	0.00	0.00	0.00	0.00	0.00	0.00	0.00
Al(iv)	0.96	1.18	1.14	1.17	1.19	1.22	1.26	1.26
Al(vi)	1.09	1.26	1.23	1.23	1.29	1.30	1.26	1.24
Fe2+(vi)	1.28	1.95	1.87	1.66	1.72	1.79	1.82	1.85
Fe3+(vi)	0.00	0.00	0.00	0.00	0.00	0.00	0.00	0.00
Mn(vi)	0.00	0.00	0.00	0.00	0.00	0.00	0.00	0.00
Mg(vi)	3.56	2.75	2.86	3.09	2.94	2.87	2.91	2.93
Ca	0.00	0.00	0.00	0.00	0.00	0.00	0.00	0.00
Na	0.00	0.00	0.00	0.00	0.00	0.00	0.00	0.00
K	0.00	0.00	0.00	0.00	0.00	0.00	0.00	0.00
R	5.93	5.96	5.96	5.97	5.95	5.96	6.00	6.01
Fe/R	0.22	0.33	0.31	0.28	0.29	0.30	0.30	0.31
T (°C)	221	268	260	266	269	276	284	285

Sample	58-03	58-04	66-04	66-04	66-04	66-04	66-04	66-08
SiO2	27.18	25.8	27.98	26.75	26.98	29.38	28.31	28.42
TiO2	<dl	<dl	<dl	<dl	<dl	<dl	<dl	<dl
Al2O3	20.85	20.27	21.02	21.41	20.83	17.32	18.35	19.8
FeO	21.01	20.84	19.44	19.93	19.84	19.23	20.07	19.84
Fe2O3	<dl	<dl	<dl	<dl	<dl	<dl	<dl	<dl
MnO	<dl	<dl	<dl	<dl	<dl	<dl	<dl	<dl
MgO	19.37	18.69	19.18	19.42	19.24	22.05	19.75	17.12
CaO	<dl	<dl	<dl	<dl	<dl	<dl	<dl	<dl
Na2O	<dl	<dl	<dl	<dl	<dl	<dl	<dl	<dl
K2O	<dl	<dl	0.3	<dl	<dl	<dl	<dl	1.64
Total	88.41	85.6	87.92	87.51	86.89	87.98	86.48	86.82
Si	2.76	2.72	2.84	2.73	2.78	2.97	2.93	2.95
Ti	0.00	0.00	0.00	0.00	0.00	0.00	0.00	0.00
Al	2.50	2.52	2.51	2.58	2.53	2.07	2.24	2.42
Fe (as 2+)	1.79	1.84	1.65	1.70	1.71	1.63	1.74	1.72
Fe (as 3+)	0.00	0.00	0.00	0.00	0.00	0.00	0.00	0.00
Mn	0.00	0.00	0.00	0.00	0.00	0.00	0.00	0.00
Mg	2.94	2.94	2.90	2.96	2.95	3.33	3.05	2.65
Ca	0.00	0.00	0.00	0.00	0.00	0.00	0.00	0.00
Na	0.00	0.00	0.00	0.00	0.00	0.00	0.00	0.00
K	0.00	0.00	0.04	0.00	0.00	0.00	0.00	0.22
Total	9.99	10.02	9.93	9.98	9.96	9.99	9.95	9.95
Si(iv)	2.76	2.72	2.84	2.73	2.78	2.97	2.93	2.95
Ti(iv)	0.00	0.00	0.00	0.00	0.00	0.00	0.00	0.00
Al(iv)	1.24	1.28	1.16	1.27	1.22	1.03	1.07	1.05
Al(vi)	1.26	1.24	1.35	1.31	1.30	1.04	1.17	1.37
Fe2+(vi)	1.79	1.84	1.65	1.70	1.71	1.63	1.74	1.72
Fe3+(vi)	0.00	0.00	0.00	0.00	0.00	0.00	0.00	0.00
Mn(vi)	0.00	0.00	0.00	0.00	0.00	0.00	0.00	0.00
Mg(vi)	2.94	2.94	2.90	2.96	2.95	3.33	3.05	2.65
Ca	0.00	0.00	0.00	0.00	0.00	0.00	0.00	0.00
Na	0.00	0.00	0.00	0.00	0.00	0.00	0.00	0.00
K	0.00	0.00	0.04	0.00	0.00	0.00	0.00	0.22
R	5.99	6.02	5.93	5.98	5.96	5.99	5.95	5.95
Fe/R	0.30	0.31	0.28	0.29	0.29	0.27	0.29	0.29
T (°C)	280	289	265	286	277	235	245	241

Sample	66-08	66-08
SiO2	27.53	26.31
TiO2	<dl	<dl
Al2O3	18.59	20.71
FeO	19.52	20.09
Fe2O3	<dl	<dl
MnO	<dl	<dl
MgO	19.04	18.17
CaO	<dl	0.2
Na2O	<dl	<dl
K2O	<dl	<dl
Total	84.68	85.48
Si	2.91	2.76
Ti	0.00	0.00
Al	2.31	2.56
Fe (as 2+)	1.72	1.76
Fe (as 3+)	0.00	0.00
Mn	0.00	0.00
Mg	3.00	2.84
Ca	0.00	0.02
Na	0.00	0.00
K	0.00	0.00
Total	9.94	9.96
Si(iv)	2.91	2.76
Ti(iv)	0.00	0.00
Al(iv)	1.09	1.24
Al(vi)	1.22	1.33
Fe2+(vi)	1.72	1.76
Fe3+(vi)	0.00	0.00
Mn(vi)	0.00	0.00
Mg(vi)	3.00	2.84
Ca	0.00	0.02
Na	0.00	0.00
K	0.00	0.00
R	5.94	5.96
Fe/R	0.29	0.30
T (°C)	250	280

Epidotes

Sample	31-03	31-03	31-03	31-03	31-03	31-03	31-03	31-03
SiO2	37.21	37.17	36.20	35.90	35.79	36.63	36.62	38.18
Al2O3	23.93	22.51	21.64	21.19	21.69	23.62	21.88	23.45
Fe2O3*	12.45	15.75	14.21	15.89	15.23	12.64	14.20	13.85
MnO	<dl	<dl	<dl	0.31	<dl	<dl	<dl	<dl
MgO	<dl	<dl	<dl	<dl	0.32	<dl	<dl	0.36
CaO	23.37	23.62	23.06	22.24	22.72	23.34	23.03	23.91
La2O3	<dl	<dl	<dl	<dl	<dl	<dl	<dl	<dl
Ce2O3	<dl	<dl	<dl	<dl	<dl	<dl	<dl	<dl
Total	96.96	99.05	95.11	95.53	95.75	96.23	95.73	99.75
* note: all iron is measured as FeO and converted to Fe2O3 by multiblying by 1.111349275								
Si	2.97	2.95	2.98	2.97	2.94	2.97	3.00	2.98
Al	2.25	2.10	2.10	2.06	2.10	2.26	2.11	2.16
Fe+3	0.75	0.94	0.88	0.99	0.94	0.77	0.88	0.81
Mn	0.00	0.00	0.00	0.02	0.00	0.00	0.00	0.00
Mg	0.00	0.00	0.00	0.00	0.04	0.00	0.00	0.04
Ca	2.00	2.01	2.03	1.97	2.00	2.03	2.02	2.00
La	0.00	0.00	0.00	0.00	0.00	0.00	0.00	0.00
Ce	0.00	0.00	0.00	0.00	0.00	0.00	0.00	0.00
Si(iv)	2.97	2.95	2.98	2.97	2.94	2.97	3.00	2.98
Al(iv)	0.03	0.05	0.02	0.03	0.06	0.03	0.00	0.02
Al	2.23	2.05	2.08	2.03	2.05	2.22	2.11	2.14
Fe3+	0.75	0.94	0.88	0.99	0.94	0.77	0.88	0.81
Mn	0.00	0.00	0.00	0.02	0.00	0.00	0.00	0.00
Mg	0.00	0.00	0.00	0.00	0.04	0.00	0.00	0.04
Ca	2.00	2.01	2.03	1.97	2.00	2.03	2.02	2.00
La	0.00	0.00	0.00	0.00	0.00	0.00	0.00	0.00
Ce	0.00	0.00	0.00	0.00	0.00	0.00	0.00	0.00

Sample	31-04	31-04	31-04	31-04	36-05	36-05	36-05	36-05
SiO2	35.98	31.51	38.63	38.25	37.42	38.29	38.86	38.61
Al2O3	21.61	13.84	24.04	22.49	21.00	23.43	23.48	23.26
Fe2O3*	14.70	19.18	12.42	13.29	16.37	14.53	14.07	15.38
MnO	<dl	<dl	<dl	<dl	<dl	<dl	<dl	<dl
MgO	<dl	0.70	<dl	<dl	<dl	<dl	<dl	<dl
CaO	20.84	11.51	26.29	26.41	23.44	23.94	24.29	24.16
La2O3	<dl	4.98	<dl	<dl	<dl	<dl	<dl	<dl
Ce2O3	<dl	12.66	<dl	<dl	<dl	<dl	<dl	<dl
Total	93.13	94.38	101.38	100.44	98.23	100.19	100.70	101.41
* note: all i								
Si	3.02	2.98	2.98	3.00	3.01	2.99	3.01	2.99
Al	2.14	1.54	2.19	2.08	1.99	2.16	2.15	2.12
Fe+3	0.93	1.36	0.72	0.78	0.99	0.85	0.82	0.90
Mn	0.00	0.00	0.00	0.00	0.00	0.00	0.00	0.00
Mg	0.00	0.10	0.00	0.00	0.00	0.00	0.00	0.00
Ca	1.87	1.17	2.17	2.22	2.02	2.00	2.02	2.00
La	0.00	0.17	0.00	0.00	0.00	0.00	0.00	0.00
Ce	0.00	0.44	0.00	0.00	0.00	0.00	0.00	0.00
Si(iv)	3.02	2.98	2.98	3.00	3.01	2.99	3.01	2.99
Al(iv)	0.00	0.02	0.02	0.00	0.00	0.01	0.00	0.01
Al	2.14	1.52	2.17	2.07	1.99	2.15	2.15	2.11
Fe3+	0.93	1.36	0.72	0.78	0.99	0.85	0.82	0.90
Mn	0.00	0.00	0.00	0.00	0.00	0.00	0.00	0.00
Mg	0.00	0.10	0.00	0.00	0.00	0.00	0.00	0.00
Ca	1.87	1.17	2.17	2.22	2.02	2.00	2.02	2.00
La	0.00	0.17	0.00	0.00	0.00	0.00	0.00	0.00
Ce	0.00	0.44	0.00	0.00	0.00	0.00	0.00	0.00

Sample	39-01	39-03	39-03	41-01	41-01	58-03	58-04	66-04
SiO2	38.23	37.63	37.40	37.74	38.67	38.84	38.57	38.70
Al2O3	24.79	24.15	22.60	23.08	22.94	23.34	24.57	24.93
Fe2O3*	12.44	12.22	14.65	14.14	15.30	15.39	12.66	12.60
MnO	<dl	<dl	<dl	<dl	<dl	<dl	<dl	<dl
MgO	<dl	<dl	<dl	<dl	<dl	<dl	<dl	<dl
CaO	24.01	23.60	23.61	23.55	23.58	23.78	24.32	24.59
La2O3	<dl	<dl	<dl	<dl	<dl	<dl	<dl	<dl
Ce2O3	<dl	<dl	<dl	<dl	<dl	<dl	<dl	<dl
Total	99.47	97.60	98.26	98.51	100.49	101.35	100.12	100.82
* note: all i								
Si	2.99	3.00	2.99	3.00	3.01	3.00	3.00	2.99
Al	2.28	2.27	2.13	2.16	2.11	2.13	2.25	2.27
Fe+3	0.73	0.73	0.88	0.84	0.90	0.89	0.74	0.73
Mn	0.00	0.00	0.00	0.00	0.00	0.00	0.00	0.00
Mg	0.00	0.00	0.00	0.00	0.00	0.00	0.00	0.00
Ca	2.01	2.01	2.02	2.00	1.97	1.97	2.02	2.03
La	0.00	0.00	0.00	0.00	0.00	0.00	0.00	0.00
Ce	0.00	0.00	0.00	0.00	0.00	0.00	0.00	0.00
Si(iv)	2.99	3.00	2.99	3.00	3.01	3.00	3.00	2.99
Al(iv)	0.01	0.00	0.01	0.00	0.00	0.00	0.00	0.01
Al	2.27	2.26	2.11	2.16	2.11	2.13	2.25	2.25
Fe3+	0.73	0.73	0.88	0.84	0.90	0.89	0.74	0.73
Mn	0.00	0.00	0.00	0.00	0.00	0.00	0.00	0.00
Mg	0.00	0.00	0.00	0.00	0.00	0.00	0.00	0.00
Ca	2.01	2.01	2.02	2.00	1.97	1.97	2.02	2.03
La	0.00	0.00	0.00	0.00	0.00	0.00	0.00	0.00
Ce	0.00	0.00	0.00	0.00	0.00	0.00	0.00	0.00

Sample	66-04	66-08	66-08
SiO2	37.72	37.88	37.82
Al2O3	22.34	23.69	21.08
Fe2O3*	15.34	13.35	15.69
MnO	<dl	<dl	<dl
MgO	<dl	<dl	<dl
CaO	23.98	23.19	23.61
La2O3	<dl	<dl	<dl
Ce2O3	<dl	<dl	<dl
Total	99.38	98.11	98.20
* note: all i			
Si	2.99	3.01	3.03
Al	2.08	2.22	1.99
Fe+3	0.91	0.80	0.95
Mn	0.00	0.00	0.00
Mg	0.00	0.00	0.00
Ca	2.03	1.97	2.03
La	0.00	0.00	0.00
Ce	0.00	0.00	0.00
Si(iv)	2.99	3.01	3.03
Al(iv)	0.01	0.00	0.00
Al	2.07	2.22	1.99
Fe3+	0.91	0.80	0.95
Mn	0.00	0.00	0.00
Mg	0.00	0.00	0.00
Ca	2.03	1.97	2.03
La	0.00	0.00	0.00
Ce	0.00	0.00	0.00

Feldspars

Sample	31-03	31-03	31-03	31-03	31-03	31-04	31-04	31-04
Group	Albite	Ortho.	Albite	Ortho.	Ortho.	Ortho.	Ortho.	Ortho.
SiO2	66.91	64.66	67.93	64.71	62.61	64.04	63.08	63.84
Al2O3	20.39	18.75	20.15	18.94	17.71	17.62	17.26	17.49
Feo	<dl	<dl	<dl	<dl	<dl	<dl	<dl	<dl
MgO	<dl	<dl	<dl	<dl	<dl	<dl	<dl	<dl
CaO	0.62	<dl	0.32	<dl	<dl	<dl	<dl	<dl
Na2O	12.32	0.47	12.44	<dl	<dl	0.52	<dl	0.29
K2O	<dl	16.67	<dl	16.69	16.47	15.73	15.83	15.95
Total	100.24	100.55	100.84	100.34	96.79	97.91	96.17	97.57
Si	2.93	2.98	2.96	2.98	3.00	3.02	3.03	3.02
Ti	0.00	0.00	0.00	0.00	0.00	0.00	0.00	0.00
Al	1.05	1.02	1.03	1.03	1.00	0.98	0.98	0.98
Fe2+	0.00	0.00	0.00	0.00	0.00	0.00	0.00	0.00
Mg	0.00	0.00	0.00	0.00	0.00	0.00	0.00	0.00
Ca	0.03	0.00	0.01	0.00	0.00	0.00	0.00	0.00
Na	1.05	0.04	1.05	0.00	0.00	0.05	0.00	0.03
K	0.00	0.98	0.00	0.98	1.01	0.95	0.97	0.96

Sample	31-04	31-04	36-05	36-05	39-02	39-02	41-01	41-01
Group	Ortho.	Ortho.	Ortho.	Ortho.	Ortho.	Ortho.	Ortho.	Albite
SiO2	65.01	64.08	65.21	65.29	64.64	63.43	64.15	69.16
Al2O3	18.59	18.74	18.79	19.02	18.92	18.81	18.70	20.51
Feo	<dl	<dl	<dl	<dl	<dl	<dl	<dl	<dl
MgO	<dl	<dl	<dl	<dl	<dl	<dl	<dl	<dl
CaO	<dl	<dl	<dl	<dl	<dl	<dl	<dl	<dl
Na2O	0.22	<dl	<dl	<dl	<dl	<dl	<dl	11.11
K2O	16.83	17.02	16.66	16.56	16.41	16.14	17.00	<dl
Total	100.65	99.84	100.66	100.87	99.97	98.38	99.85	100.78
Si	2.99	2.98	2.99	2.99	2.99	2.98	2.98	2.99
Ti	0.00	0.00	0.00	0.00	0.00	0.00	0.00	0.00
Al	1.01	1.03	1.02	1.03	1.03	1.04	1.02	1.04
Fe2+	0.00	0.00	0.00	0.00	0.00	0.00	0.00	0.00
Mg	0.00	0.00	0.00	0.00	0.00	0.00	0.00	0.00
Ca	0.00	0.00	0.00	0.00	0.00	0.00	0.00	0.00
Na	0.02	0.00	0.00	0.00	0.00	0.00	0.00	0.93
K	0.99	1.01	0.98	0.97	0.97	0.97	1.01	0.00

Sample	41-01	58-04	58-04	66-04	66-04	66-04	66-04	66-04
Group	Albite	Albite	Ortho.	Albite	Albite	Albite	Ortho.	Albite
SiO2	70.36	66.50	64.02	66.56	67.68	66.81	64.26	66.89
Al2O3	20.64	20.39	18.70	20.36	20.63	21.46	18.17	21.32
Feo	<dl	<dl	0.59	<dl	<dl	<dl	<dl	<dl
MgO	<dl	<dl	0.45	<dl	<dl	<dl	<dl	<dl
CaO	<dl	0.92	<dl	1.01	0.86	2.05	<dl	0.96
Na2O	11.61	11.56	<dl	11.27	11.66	10.66	<dl	11.45
K2O	<dl	<dl	16.53	<dl	<dl	<dl	16.36	<dl
Total	102.61	99.37	100.29	99.20	100.83	100.98	98.79	100.62
Si	2.99	2.94	2.96	2.94	2.94	2.90	3.01	2.91
Ti	0.00	0.00	0.00	0.00	0.00	0.00	0.00	0.00
Al	1.03	1.06	1.02	1.06	1.06	1.10	1.00	1.09
Fe2+	0.00	0.00	0.02	0.00	0.00	0.00	0.00	0.00
Mg	0.00	0.00	0.03	0.00	0.00	0.00	0.00	0.00
Ca	0.00	0.04	0.00	0.05	0.04	0.10	0.00	0.04
Na	0.96	0.99	0.00	0.97	0.98	0.90	0.00	0.97
K	0.00	0.00	0.98	0.00	0.00	0.00	0.98	0.00

Sample	66-04	66-04
Group	Albite	Albite
SiO2	67.40	64.75
Al2O3	19.81	20.79
Feo	<dl	<dl
MgO	<dl	<dl
CaO	<dl	2.02
Na2O	10.03	11.04
K2O	2.32	<dl
Total	99.56	98.60
Si	2.98	2.89
Ti	0.00	0.00
Al	1.03	1.09
Fe2+	0.00	0.00
Mg	0.00	0.00
Ca	0.00	0.10
Na	0.86	0.96
K	0.13	0.00

Muscovites

Sample	39-01	39-01	39-01	39-02	39-03	39-03	39-03	39-03
SiO2	47.15	44.77	46.61	46.21	46.24	46.72	46.14	45.86
TiO2	0.68	0.76	0.55	0.57	0.78	<dl	0.90	0.76
Al2O3	29.04	25.26	30.17	30.68	28.65	31.95	29.56	29.47
Fe2O3	5.28	11.09	4.66	4.67	4.95	5.03	5.40	5.45
MgO	2.11	6.71	1.85	2.09	2.85	1.85	1.46	1.45
K2O	10.68	9.97	10.89	10.41	10.76	10.67	10.49	10.67
Total	94.94	98.56	94.73	94.63	94.23	96.22	93.95	93.66
* note: all iron is measured as FeO and converted to Fe2O3 by multiblying by 1.111349275								
Si	3.19	3.00	3.16	3.13	3.16	3.11	3.16	3.15
Ti	0.03	0.04	0.03	0.03	0.04	0.00	0.05	0.04
Al	2.32	1.99	2.41	2.45	2.31	2.51	2.38	2.39
Fe3+	0.27	0.56	0.24	0.24	0.25	0.25	0.28	0.28
Mg	0.21	0.67	0.19	0.21	0.29	0.18	0.15	0.15
K	0.92	0.85	0.94	0.90	0.94	0.91	0.92	0.94
Si(iv)	3.19	3.00	3.16	3.13	3.16	3.11	3.16	3.15
Ti(iv)	0.03	0.04	0.03	0.03	0.04	0.00	0.05	0.04
Al(iv)	0.78	0.96	0.81	0.84	0.80	0.89	0.80	0.81
Al(vi)	1.54	1.03	1.60	1.60	1.51	1.62	1.58	1.58
Fe3+(vi)	0.27	0.56	0.24	0.24	0.25	0.25	0.28	0.28
Mg(vi)	0.21	0.67	0.19	0.21	0.29	0.18	0.15	0.15
K	0.92	0.85	0.94	0.90	0.94	0.91	0.92	0.94
Avac	0.08	0.15	0.06	0.10	0.06	0.09	0.08	0.06
R(vi)	2.02	2.26	2.02	2.05	2.05	2.06	2.01	2.01

Sample	58-03	66-04	31-04
SiO2	47.35	45.20	50.15
TiO2	<dl	0.54	<dl
Al2O3	31.19	28.25	17.73
Fe2O3	5.10	5.69	10.14
MgO	1.62	2.34	8.75
K2O	10.89	10.22	9.26
Total	96.15	92.24	96.03
* note: all i			
Si	3.16	3.16	3.40
Ti	0.00	0.03	0.00
Al	2.45	2.32	1.42
Fe3+	0.26	0.30	0.52
Mg	0.16	0.24	0.89
K	0.93	0.91	0.80
Si(iv)	3.16	3.16	3.40
Ti(iv)	0.00	0.03	0.00
Al(iv)	0.84	0.82	0.60
Al(vi)	1.61	1.51	0.82
Fe3+(vi)	0.26	0.30	0.52
Mg(vi)	0.16	0.24	0.89
K	0.93	0.91	0.80
Avac	0.07	0.09	0.20
R(vi)	2.03	2.05	2.23

Phosphates

Sample	31-04	31-04	39-03	56-03
Group?	Apatite	Apatite	Monazite	Apatite
TiO2	<dl	<dl	<dl	2.82
Al2O3	<dl	<dl	<dl	1.56
FeO	0.47	0.42	0.8	2.05
CaO	55.77	54.26	1.14	51.84
K2O	<dl	<dl	<dl	<dl
P2O5	40.99	39.57	26.79	38.33
SO3	<dl	<dl	1.8	<dl
La2O3	<dl	<dl	13.6	<dl
Ce2O3	<dl	<dl	30.99	<dl
Total	97.23	94.25	75.12	96.6
Ti	0.00	0.00	0.00	0.18
Al	0.00	0.00	0.00	0.16
Fe	0.03	0.03	0.03	0.15
Ca	5.08	5.11	0.06	4.78
K	0.00	0.00	0.00	0.00
P	2.95	2.94	1.04	2.79
S	0.00	0.00	0.06	0.00
La	0.00	0.00	0.23	0.00
Ce	0.00	0.00	0.52	0.00

Sphene

Sample	31-03	31-04	31-04	31-04	31-04	36-05	36-05	36-05
SiO2	30.31	31.09	31.08	31.14	33.03	31.24	30.93	30.89
TiO2	36.03	37.74	39.26	37.43	38.31	40.11	39.79	39.18
Al2O3	1.36	2.02	1.54	1.99	1.87	<dl	<dl	1.06
FeO	<dl	<dl	<dl	<dl	<dl	<dl	<dl	<dl
Fe2O3*	0.87	1.16	0.84	1.12	1.04	1.73	1.79	1.00
MnO	<dl	<dl	<dl	<dl	<dl	<dl	<dl	<dl
MgO	0.24	<dl	<dl	<dl	<dl	<dl	<dl	<dl
CaO	28.53	28.65	29.26	28.89	30.50	29.69	29.20	28.66
Na2O	<dl	<dl	<dl	<dl	<dl	<dl	<dl	<dl
K2O	<dl	<dl	<dl	<dl	<dl	<dl	<dl	<dl
Total	97.34	100.66	101.98	100.57	104.75	102.77	101.71	100.79
* note: all iron is measured as FeO and converted to Fe2O3 by multiblying by 1.111349275								
Si	1.01	1.01	0.99	1.01	1.03	1.00	1.00	1.00
Ti	0.91	0.92	0.95	0.91	0.90	0.96	0.97	0.95
Al	0.05	0.08	0.06	0.08	0.07	0.00	0.00	0.04
Fe2+	0.00	0.00	0.00	0.00	0.00	0.00	0.00	0.00
Fe3+	0.02	0.03	0.02	0.03	0.02	0.04	0.04	0.02
Mn	0.00	0.00	0.00	0.00	0.00	0.00	0.00	0.00
Mg	0.01	0.00	0.00	0.00	0.00	0.00	0.00	0.00
Ca	1.02	0.99	1.00	1.00	1.02	1.02	1.01	0.99
Na	0.00	0.00	0.00	0.00	0.00	0.00	0.00	0.00
K	0.00	0.00	0.00	0.00	0.00	0.00	0.00	0.00
Si(iv)	1.00	1.00	0.99	1.00	1.00	1.00	1.00	1.00
Si	0.01	0.01	0.00	0.01	0.03	0.00	0.00	0.00
Ti	0.91	0.92	0.95	0.91	0.90	0.96	0.97	0.95
Al	0.05	0.08	0.06	0.08	0.07	0.00	0.00	0.04
Fe3+	0.02	0.03	0.02	0.03	0.02	0.04	0.04	0.02
Mg	0.01	0.00	0.00	0.00	0.00	0.00	0.00	0.00
Ca	1.02	0.99	1.00	1.00	1.02	1.02	1.01	0.99
K	0.00	0.00	0.00	0.00	0.00	0.00	0.00	0.00

Sample	39-01	39-02	39-02	41-01	41-01	41-01	41-01	56-03
SiO2	34.06	31.49	31.04	30.13	30.94	30.63	31.48	30.88
TiO2	34.37	36.13	30.75	36.14	34.32	36.82	34.38	38.25
Al2O3	2.15	1.64	4.22	1.23	1.52	0.92	2.05	1.59
FeO	<dl	<dl	<dl	<dl	<dl	<dl	<dl	<dl
Fe2O3*	1.29	1.44	1.09	1.04	2.76	0.88	1.18	0.68
MnO	<dl	<dl	<dl	<dl	<dl	<dl	<dl	<dl
MgO	<dl	<dl	<dl	<dl	<dl	<dl	<dl	<dl
CaO	27.17	29.26	28.11	27.85	27.83	27.52	26.36	28.86
Na2O	<dl	<dl	<dl	<dl	<dl	<dl	<dl	<dl
K2O	0.45	<dl	<dl	0.33	0.27	<dl	1.08	<dl
Total	99.49	99.96	95.21	96.72	97.64	96.77	96.53	100.26
* note: all i								
Si	1.10	1.03	1.05	1.02	1.04	1.03	1.06	1.00
Ti	0.84	0.89	0.79	0.92	0.86	0.93	0.87	0.94
Al	0.08	0.06	0.17	0.05	0.06	0.04	0.08	0.06
Fe2+	0.00	0.00	0.00	0.00	0.00	0.00	0.00	0.00
Fe3+	0.03	0.04	0.03	0.03	0.07	0.02	0.03	0.02
Mn	0.00	0.00	0.00	0.00	0.00	0.00	0.00	0.00
Mg	0.00	0.00	0.00	0.00	0.00	0.00	0.00	0.00
Ca	0.94	1.02	1.02	1.01	1.00	0.99	0.95	1.01
Na	0.00	0.00	0.00	0.00	0.00	0.00	0.00	0.00
K	0.02	0.00	0.00	0.01	0.01	0.00	0.05	0.00
Si(iv)	1.00	1.00	1.00	1.00	1.00	1.00	1.00	1.00
Si	0.10	0.03	0.05	0.02	0.04	0.03	0.06	0.00
Ti	0.84	0.89	0.79	0.92	0.86	0.93	0.87	0.94
Al	0.08	0.06	0.17	0.05	0.06	0.04	0.08	0.06
Fe3+	0.03	0.04	0.03	0.03	0.07	0.02	0.03	0.02
Mg	0.00	0.00	0.00	0.00	0.00	0.00	0.00	0.00
Ca	0.94	1.02	1.02	1.01	1.00	0.99	0.95	1.01
K	0.02	0.00	0.00	0.01	0.01	0.00	0.05	0.00

Sample	56-03	58-03	58-04	66-04	66-04
SiO2	31.81	31.96	30.53	30.40	29.85
TiO2	39.45	33.92	39.53	37.91	36.14
Al2O3	1.44	2.42	1.17	0.92	1.60
FeO	<dl	<dl	<dl	<dl	<dl
Fe2O3*	1.54	2.68	1.29	0.70	0.98
MnO	<dl	<dl	<dl	<dl	<dl
MgO	<dl	0.98	<dl	<dl	<dl
CaO	29.09	25.69	29.42	29.54	28.19
Na2O	<dl	<dl	<dl	<dl	<dl
K2O	<dl	<dl	<dl	<dl	0.61
Total	103.33	97.65	101.94	99.47	97.37
* note: all i					
Si	1.00	1.06	0.98	1.00	1.00
Ti	0.94	0.84	0.96	0.94	0.91
Al	0.05	0.09	0.04	0.04	0.06
Fe2+	0.00	0.00	0.00	0.00	0.00
Fe3+	0.04	0.07	0.03	0.02	0.02
Mn	0.00	0.00	0.00	0.00	0.00
Mg	0.00	0.05	0.00	0.00	0.00
Ca	0.98	0.91	1.01	1.04	1.02
Na	0.00	0.00	0.00	0.00	0.00
K	0.00	0.00	0.00	0.00	0.03
Si(iv)	1.00	1.00	0.98	1.00	1.00
Si	0.00	0.06	0.00	0.00	0.00
Ti	0.94	0.84	0.96	0.94	0.91
Al	0.05	0.09	0.04	0.04	0.06
Fe3+	0.04	0.07	0.03	0.02	0.02
Mg	0.00	0.05	0.00	0.00	0.00
Ca	0.98	0.91	1.01	1.04	1.02
K	0.00	0.00	0.00	0.00	0.03

Sulphates

Sample	33-03	33-03	33-03	33-03	33-03	33-03	33-03	33-03
Group?	Gypsum	Gypsum	Gypsum	Gypsum	Gypsum	Gypsum	Gypsum	Gypsum
CaO	37.98	37.54	39.12	39.96	40.04	38.65	36.6	42.01
K2O	<dl	<dl	<dl	<dl	<dl	<dl	0.19	<dl
SO3	50.57	51.61	52.09	54.14	53.75	51.11	48.39	55.47
BaO	<dl	<dl	<dl	<dl	<dl	<dl	<dl	<dl
Total	88.55	89.15	91.21	94.1	93.79	89.76	85.18	97.48
Ca	1.05	1.03	1.05	1.04	1.05	1.06	1.06	1.06
K	0.00	0.00	0.00	0.00	0.00	0.00	0.01	0.00
S	0.98	0.99	0.98	0.99	0.98	0.98	0.98	0.98
Ba	0.00	0.00	0.00	0.00	0.00	0.00	0.00	0.00

Sample	33-03	39-03
Group?	Gypsum	Barite
CaO	39.11	<dl
K2O	<dl	<dl
SO3	51.51	35.31
BaO	<dl	62.01
Total	90.62	97.32
Ca	1.06	0.00
K	0.00	0.00
S	0.98	1.02
Ba	0.00	0.94

Tourmalines

Sample	56-03	56-03	56-03	56-03	56-03	56-03	56-03	56-03
SiO2	36.47	35.74	36.41	34.88	36.02	36.73	36.45	36
TiO2	<dl	0.49	<dl	<dl	0.65	0.68	0.25	0.58
Al2O3	32.2	28.48	28.89	27.17	29.69	30.54	28.16	30.17
FeO	7.09	10.6	10.71	12.97	9.35	8.29	10.89	8.65
MgO	7.96	7.99	7.09	7.13	7.68	8.17	7.6	8.05
CaO	0.4	1.57	0.98	1.07	1.06	1.18	1.35	1.05
Na2O	2.76	2.64	2.91	2.73	2.63	2.68	2.85	2.8
Total	86.88	87.51	86.99	85.95	87.08	88.27	87.55	87.3

Sample	56-03	56-03	56-03	56-03	56-03	56-03
SiO2	36.56	36.03	36.08	36.07	36.82	37.01
TiO2	0.36	0.58	<dl	0.77	<dl	0.33
Al2O3	30.49	28.51	31.74	30.04	32.59	31.67
FeO	11.1	12.73	9.06	8.71	7.33	8.64
MgO	7.11	6.7	7.2	8.36	8.4	7.65
CaO	0.54	0.5	0.59	1.17	0.61	0.54
Na2O	3.12	3.13	3.06	2.67	2.93	2.75
Total	89.28	88.18	87.73	87.79	88.68	88.59

Ore Minerals

Sample	39-01	39-01	39-01	39-01	39-01	39-01
Group	mo	mo	cpy	hes	mo	mo
Mo	38.68	36.01	<dl	12.39	68.40	67.88
S	67.04	64.55	35.47	10.16	38.56	39.92
Cu	<dl	<dl	33.65	5.28	<dl	<dl
Fe	<dl	<dl	31.13	5.06	<dl	<dl
Ag	<dl	<dl	<dl	52.61	<dl	<dl
Te	<dl	<dl	<dl	28.56	<dl	<dl
Bi	<dl	<dl	<dl	<dl	<dl	<dl
Se	<dl	<dl	<dl	<dl	<dl	<dl
Zn	<dl	<dl	<dl	<dl	<dl	<dl
Cd	<dl	<dl	<dl	<dl	<dl	<dl
Pb	<dl	<dl	<dl	<dl	<dl	<dl
Total	105.72	100.56	100.25	114.06	106.96	107.80

Abbreviations:
Ag = Native silver
Bi = Native bismuth
bis = Bismuthinite
cla = Clausthalite
cpy = Chalcopyrite
Cu = Native copper
gre = Greenokite
gua = Guanajuatite
hes = Hessite
mo = Molybdenite
py = Pyrite
tbi = Tellurobismuthite

Sample	39-01	39-01	39-01	39-01	39-01	39-01
Group	???	tbi	???	???	???	cpy
Mo	<dl	<dl	<dl	<dl	<dl	<dl
S	16.55	4.56	20.77	14.82	17.41	34.63
Cu	<dl	<dl	1.55	<dl	1.52	32.62
Fe	2.41	1.53	1.45	2.05	1.53	30.57
Ag	20.03	<dl	11.03	7.45	16.35	<dl
Te	<dl	35.19	<dl	7.96	<dl	<dl
Bi	56.61	57.31	63.99	60.09	65.99	<dl
Se	<dl	<dl	<dl	3.24	<dl	<dl
Zn	<dl	<dl	<dl	<dl	<dl	<dl
Cd	<dl	<dl	<dl	<dl	<dl	<dl
Pb	<dl	<dl	<dl	<dl	<dl	<dl
Total	95.60	98.59	98.79	95.61	102.80	97.82

Abbreviations:
Ag = Native silver
Bi = Native bismuth
bis = Bismuthinite
cla = Clausthalite
cpy = Chalcopyrite
Cu = Native copper
gre = Greenokite
gua = Guanajuatite
hes = Hessite
mo = Molybdenite
py = Pyrite
tbi = Tellurobismuthite

Sample	39-01	39-01	39-03	39-03	39-03	39-03
Group	tbi	tbi	cpy	py	py	cpy
Mo	<dl	<dl	<dl	<dl	<dl	<dl
S	4.68	5.81	34.97	54.14	55.35	35.29
Cu	<dl	<dl	35.17	<dl	<dl	34.74
Fe	1.91	0.71	30.24	46.25	47.42	30.26
Ag	<dl	<dl	<dl	<dl	<dl	<dl
Te	35.98	28.91	<dl	<dl	<dl	<dl
Bi	59.16	55.57	<dl	<dl	<dl	<dl
Se	<dl	<dl	<dl	<dl	<dl	<dl
Zn	<dl	<dl	<dl	<dl	<dl	<dl
Cd	<dl	<dl	<dl	<dl	<dl	<dl
Pb	<dl	<dl	<dl	<dl	<dl	<dl
Total	101.73	91.00	100.38	100.39	102.77	100.29

Abbreviations:
Ag = Native silver
Bi = Native bismuth
bis = Bismuthinite
cla = Clausthalite
cpy = Chalcopyrite
Cu = Native copper
gre = Greenokite
gua = Guanajuatite
hes = Hessite
mo = Molybdenite
py = Pyrite
tbi = Tellurobismuthite

Sample	41-01	41-01	41-01	56-03	56-03	56-03
Group	cpy	bis?	bis?	tbi	tbi	cpy
Mo	<dl	<dl	<dl	<dl	<dl	<dl
S	34.62	13.76	13.86	4.67	4.75	35.16
Cu	32.79	<dl	<dl	<dl	<dl	34.12
Fe	31.42	<dl	1.75	1.05	1.50	30.82
Ag	<dl	27.66	27.25	<dl	<dl	<dl
Te	<dl	<dl	<dl	34.28	34.57	<dl
Bi	<dl	54.67	53.25	58.66	59.90	<dl
Se	<dl	6.16	4.95	<dl	<dl	<dl
Zn	<dl	<dl	<dl	<dl	<dl	<dl
Cd	<dl	<dl	<dl	<dl	<dl	<dl
Pb	<dl	<dl	<dl	<dl	<dl	<dl
Total	98.83	102.25	101.06	98.66	100.72	100.10

Abbreviations:
Ag = Native silver
Bi = Native bismuth
bis = Bismuthinite
cla = Clausthalite
cpy = Chalcopyrite
Cu = Native copper
gre = Greenokite
gua = Guanajuatite
hes = Hessite
mo = Molybdenite
py = Pyrite
tbi = Tellurobismuthite

Sample	56-03	56-03	56-03	56-03	56-03	56-03
Group	cpy	hes-bis	bis	Ag	Ag	Cu
Mo	<dl	<dl	<dl	<dl	<dl	<dl
S	35.66	15.89	18.21	0.90	1.34	<dl
Cu	34.48	<dl	<dl	<dl	<dl	101.03
Fe	31.61	1.04	<dl	<dl	<dl	<dl
Ag	<dl	28.00	<dl	96.81	98.97	<dl
Te	<dl	<dl	<dl	<dl	<dl	<dl
Bi	<dl	54.67	81.70	<dl	<dl	<dl
Se	<dl	1.60	<dl	<dl	<dl	<dl
Zn	<dl	<dl	<dl	<dl	<dl	<dl
Cd	<dl	<dl	<dl	<dl	<dl	<dl
Pb	<dl	<dl	<dl	<dl	<dl	<dl
Total	101.75	101.20	99.91	97.71	100.31	101.03

Abbreviations:
Ag = Native silver
Bi = Native bismuth
bis = Bismuthinite
cla = Clausthalite
cpy = Chalcopyrite
Cu = Native copper
gre = Greenokite
gua = Guanajuatite
hes = Hessite
mo = Molybdenite
py = Pyrite
tbi = Tellurobismuthite

Sample	56-03	56-03	56-03	58-03	58-03	58-03
Group	Cu	cpy	cpy	gua	gre	hes
Mo	<dl	<dl	<dl	<dl	<dl	<dl
S	<dl	35.21	34.98	1.12	21.83	<dl
Cu	98.82	33.88	33.72	<dl	<dl	<dl
Fe	<dl	31.14	32.23	<dl	0.71	<dl
Ag	<dl	2.43	<dl	<dl	<dl	48.23
Te	<dl	<dl	<dl	6.03	<dl	31.62
Bi	<dl	<dl	<dl	77.63	<dl	1.39
Se	<dl	<dl	<dl	14.95	<dl	0.94
Zn	<dl	<dl	<dl	<dl	6.86	<dl
Cd	<dl	<dl	<dl	<dl	65.90	<dl
Pb	<dl	<dl	<dl	<dl	<dl	<dl
Total	98.82	102.66	100.93	99.73	95.30	82.18

Abbreviations:
Ag = Native silver
Bi = Native bismuth
bis = Bismuthinite
cla = Clausthalite
cpy = Chalcopyrite
Cu = Native copper
gre = Greenokite
gua = Guanajuatite
hes = Hessite
mo = Molybdenite
py = Pyrite
tbi = Tellurobismuthite

Sample	58-03	58-03	58-03	58-03	58-03	58-03
Group	tbi	hes	cla	hes	Bi	hes
Mo	<dl	<dl	<dl	<dl	<dl	<dl
S	<dl	<dl	<dl	<dl	<dl	<dl
Cu	<dl	<dl	<dl	<dl	<dl	<dl
Fe	<dl	<dl	<dl	<dl	<dl	<dl
Ag	<dl	63.16	13.59	62.39	2.80	64.82
Te	32.62	38.61	11.61	37.40	1.50	38.23
Bi	54.09	<dl	13.03	<dl	86.47	<dl
Se	5.83	<dl	18.40	<dl	<dl	<dl
Zn	<dl	<dl	<dl	<dl	<dl	<dl
Cd	<dl	<dl	<dl	<dl	<dl	<dl
Pb	<dl	<dl	43.86	<dl	<dl	<dl
Total	92.54	101.77	100.49	99.79	90.77	103.05

Abbreviations:
Ag = Native silver
Bi = Native bismuth
bis = Bismuthinite
cla = Clausthalite
cpy = Chalcopyrite
Cu = Native copper
gre = Greenokite
gua = Guanajuatite
hes = Hessite
mo = Molybdenite
py = Pyrite
tbi = Tellurobismuthite

Sample	66-04	66-04	66-04	66-04	66-08	66-08
Group	cpy	py	cpy	cpy	bis	bis
Mo	<dl	<dl	<dl	<dl	<dl	<dl
S	35.61	52.83	34.51	33.83	16.24	18.55
Cu	35.58	<dl	34.52	34.36	1.11	1.58
Fe	30.53	45.54	30.34	30.16	1.13	1.05
Ag	<dl	<dl	<dl	<dl	<dl	<dl
Te	<dl	<dl	<dl	<dl	1.77	<dl
Bi	<dl	<dl	<dl	<dl	77.79	81.45
Se	<dl	<dl	<dl	<dl	1.04	<dl
Zn	<dl	<dl	<dl	<dl	<dl	<dl
Cd	<dl	<dl	<dl	<dl	<dl	<dl
Pb	<dl	<dl	<dl	<dl	<dl	<dl
Total	101.72	98.37	99.37	98.35	99.08	102.63

Abbreviations:
Ag = Native silver
Bi = Native bismuth
bis = Bismuthinite
cla = Clausthalite
cpy = Chalcopyrite
Cu = Native copper
gre = Greenokite
gua = Guanajuatite
hes = Hessite
mo = Molybdenite
py = Pyrite
tbi = Tellurobismuthite

Sample	66-08	66-08	66-08
Group	gua	Bi	cpy
Mo	<dl	<dl	<dl
S	4.54	<dl	34.78
Cu	1.13	<dl	34.74
Fe	1.39	<dl	30.47
Ag	0.98	<dl	<dl
Te	<dl	<dl	<dl
Bi	78.65	99.71	<dl
Se	12.66	<dl	<dl
Zn	<dl	<dl	<dl
Cd	<dl	<dl	<dl
Pb	<dl	<dl	<dl
Total	99.35	99.71	99.99

Abbreviations:
Ag = Native silver
Bi = Native bismuth
bis = Bismuthinite
cla = Clausthalite
cpy = Chalcopyrite
Cu = Native copper
gre = Greenokite
gua = Guanajuatite
hes = Hessite
mo = Molybdenite
py = Pyrite
tbi = Tellurobismuthite

Appendix D

Isotope Sample Descriptions

HAM-29B-08:

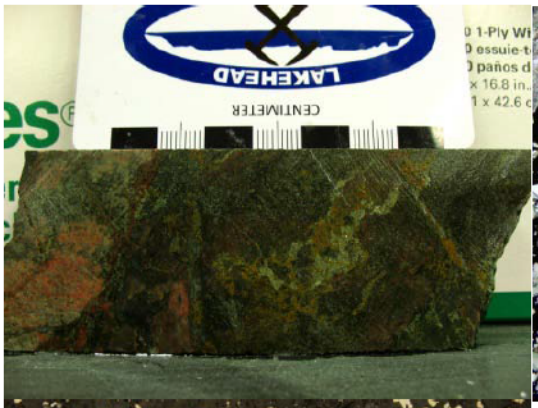

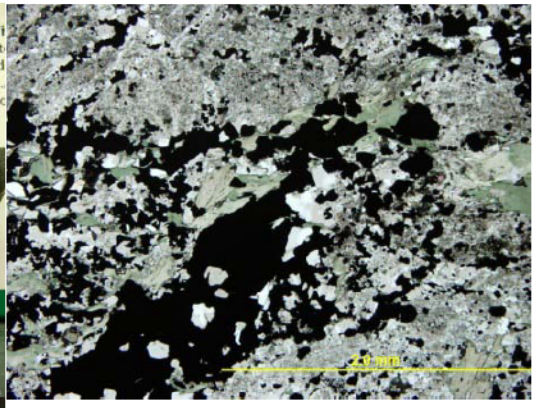

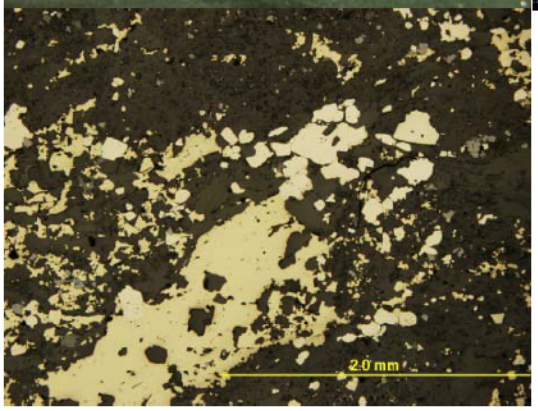

Hole ID: HAM06-29B

Depth: 47.0m

Rock type: brecciated felsic metavolcanics

Chlorite: 0.1-0.5mm blades of pale green weakly foliated chlorite in matrix of breccia, very little biotite present

Magnetite: present in trace amounts, not analyzed

Pyrite: aggregates of subhedral 0.1-1.0mm grains in matrix of the breccia, making up 1-2% of the rock

Chalcopyrite: anhedral stringers up to 5cm in the matrix of the breccia making up 3-5% of the rock

Pyrrhotite: not present

HAM-31-05:

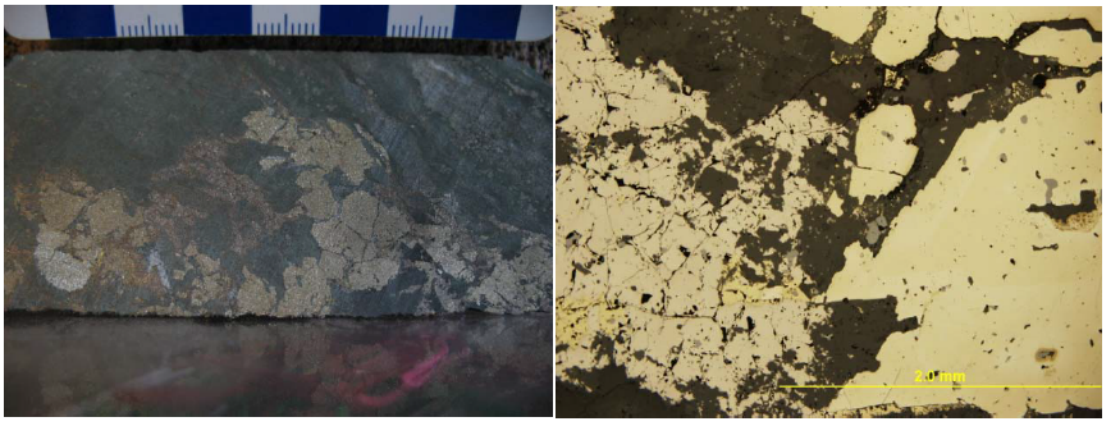

Hole ID:	HAM06-31
Depth:	73.5m
Rock type:	altered mafic metavolcanics
Chlorite:	present in abundance, not analyzed
Magnetite:	present in trace amounts, not analyzed
Pyrite:	aggregates of subhedral grains up to 1.0cm in size, making up 10-15% of the rock
Chalcopyrite:	present as trace anhedral stringers in pyrrhotite, not analyzed
Pyrrhotite:	wispy anhedral stringers up to 3.0cm long, making up 3-5% of the rock

HAM-31-06:

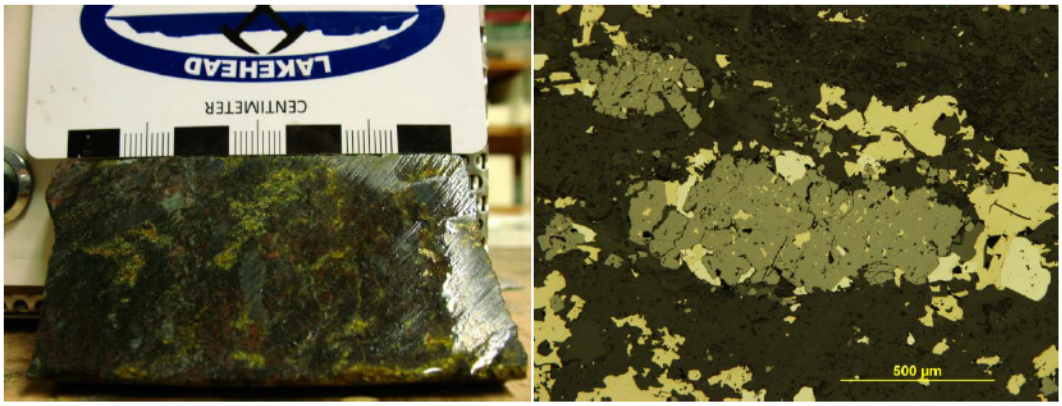

Hole ID: HAM06-31

Depth: 156.0m

Rock type: brecciated felsic metavolcanics

Chlorite: present in the matrix of the breccia, not analyzed

Magnetite: anhedral masses in the matrix of the breccia, up to 1.0mm in size, often containing intergrown chalcopyrite and pyrite, makes up 3-5% of the rock

Pyrite: subhedral grains in the matrix of the breccia, usually <0.5mm in size, makes up <1% of the rock

Chalcopyrite: anhedral stringers up to 2.0cm in the matrix of the breccia making up 3-5% of the rock

Pyrrhotite: not present

HAM-32-06:

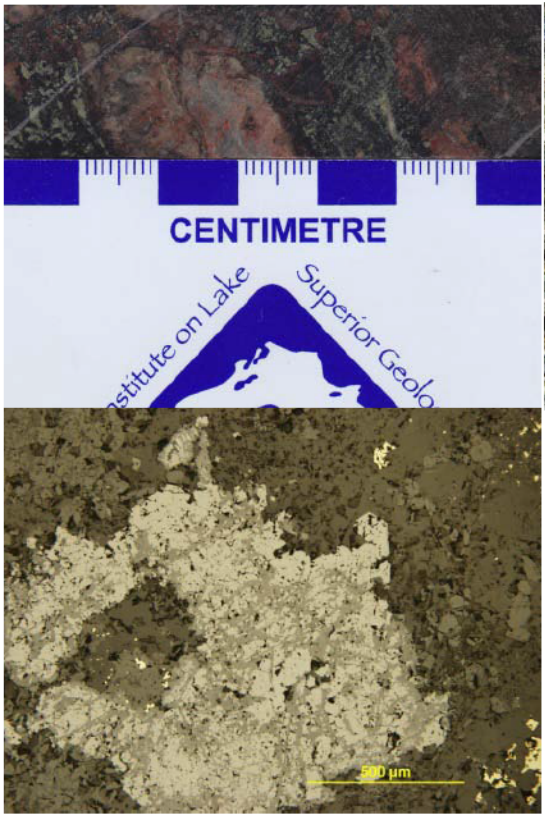

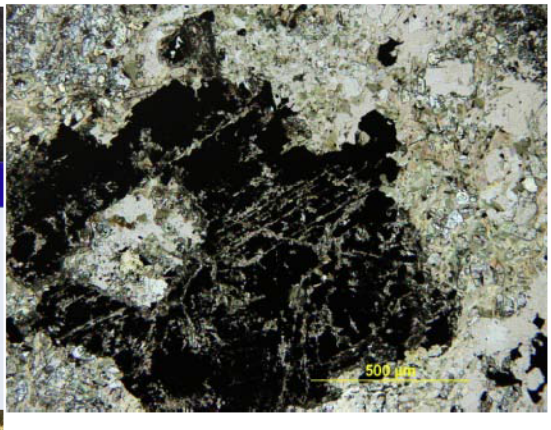

Hole ID: HAM06-32

Depth: 166.5m

Rock type: brecciated felsic metavolcanics

Chlorite: in the matrix of the breccia as pale green blades that often transition to biotite, grains are 0.1-0.5mm in size, biotite is very abundant and isolation of chlorite from biotite is extremely difficult, therefore not analyzed

Magnetite: anhedral masses in the matrix of the breccia, up to 1.0mm in size, often exhibiting replacement by sphene along cleavage planes (see image), makes up 3-5% of the rock

Pyrite: present in trace amounts, not analyzed

Chalcopyrite: present in trace amounts, not analyzed

Pyrrhotite: not present

HAM-33-06:

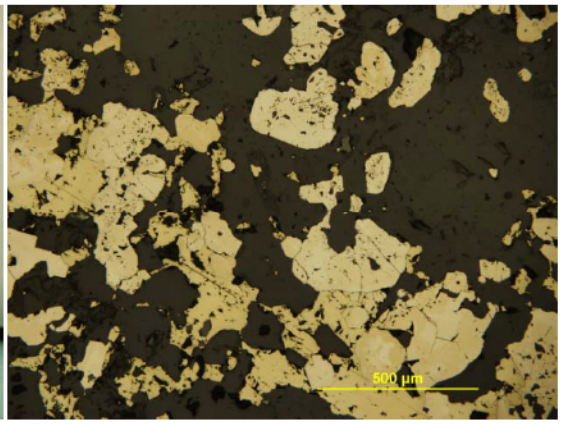

Hole ID:	HAM06-33
Depth:	220.5m
Rock type:	brecciated felsic metavolcanics
Chlorite:	present in the matrix of the breccia, not analyzed
Magnetite:	present in trace amounts, not analyzed
Pyrite:	subhedral rounded grains in the matrix of the quartz breccia, 0.5-1.0cm in size, makes up 2-3% of the rock
Chalcopyrite:	anhedral stringers in the quartz breccia, 0.5-1.0cm in size, makes up 2-3% of the rock
Pyrrhotite:	not present

HAM-33-07:

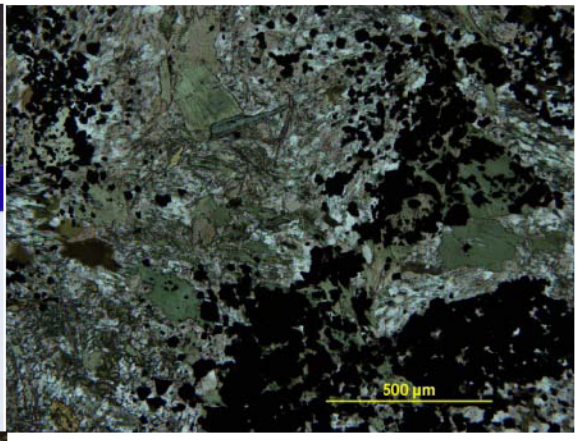

Hole ID: HAM06-33

Depth: 70.5m

Rock type: brecciated felsic metavolcanics

Chlorite: in the matrix of the breccia as pale to dark green blades, grains are 0.1-0.5mm in size, biotite is present but usually isolated from chlorite.

Magnetite: aggregates of subhedral grains disseminated throughout the matrix of the breccia, <0.5mm in size, makes up 3-5% of the rock

Pyrite: present in trace amounts, not analyzed

Chalcopyrite: present in trace amounts, not analyzed

Pyrrhotite: not present

HAM-39-08:

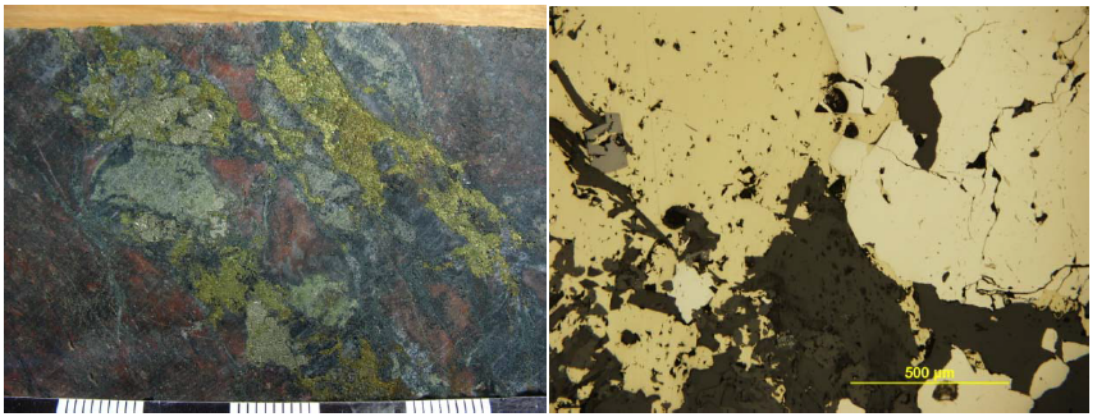

Hole ID:	HAM06-39
Depth:	247.0m
Rock type:	brecciated felsic metavolcanics
Chlorite:	present in the matrix of the breccia, not analyzed
Magnetite:	present in trace amounts, not analyzed
Pyrite:	anhedral to subhedral masses in the matrix of the breccia, size varies from 1.0mm to 1.0cm, makes up 3-5% of the rock
Chalcopyrite:	anhedral stringers up to 5.0cm in the matrix of the breccia, making up 3-5% of the rock
Pyrrhotite:	not present

HAM-41-06:

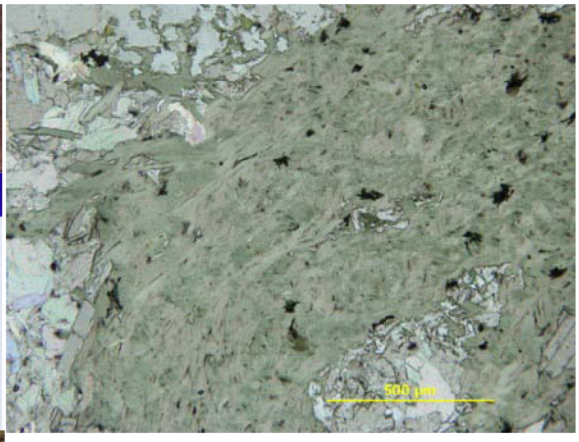

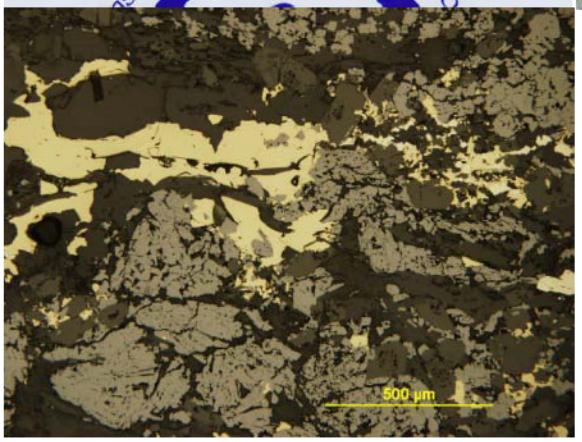

Hole ID: HAM06-41

Depth: 123.1m

Rock type: brecciated felsic metavolcanics

Chlorite: present in the matrix of the breccia as aggregates of pale green blades, grains are 0.1-0.5mm in size, but form continuous weakly foliated masses throughout the matrix, biotite is only present in trace amounts

Magnetite: anhedral to subhedral masses assembled with chalcopyrite, bladed form is common, grain size is 0.5-1.0mm, makes up 1-2% of the rock.

Pyrite: present in trace amounts, not analyzed

Chalcopyrite: present at trace to 1%, not analyzed

Pyrrhotite: not present

HAM-43-05:

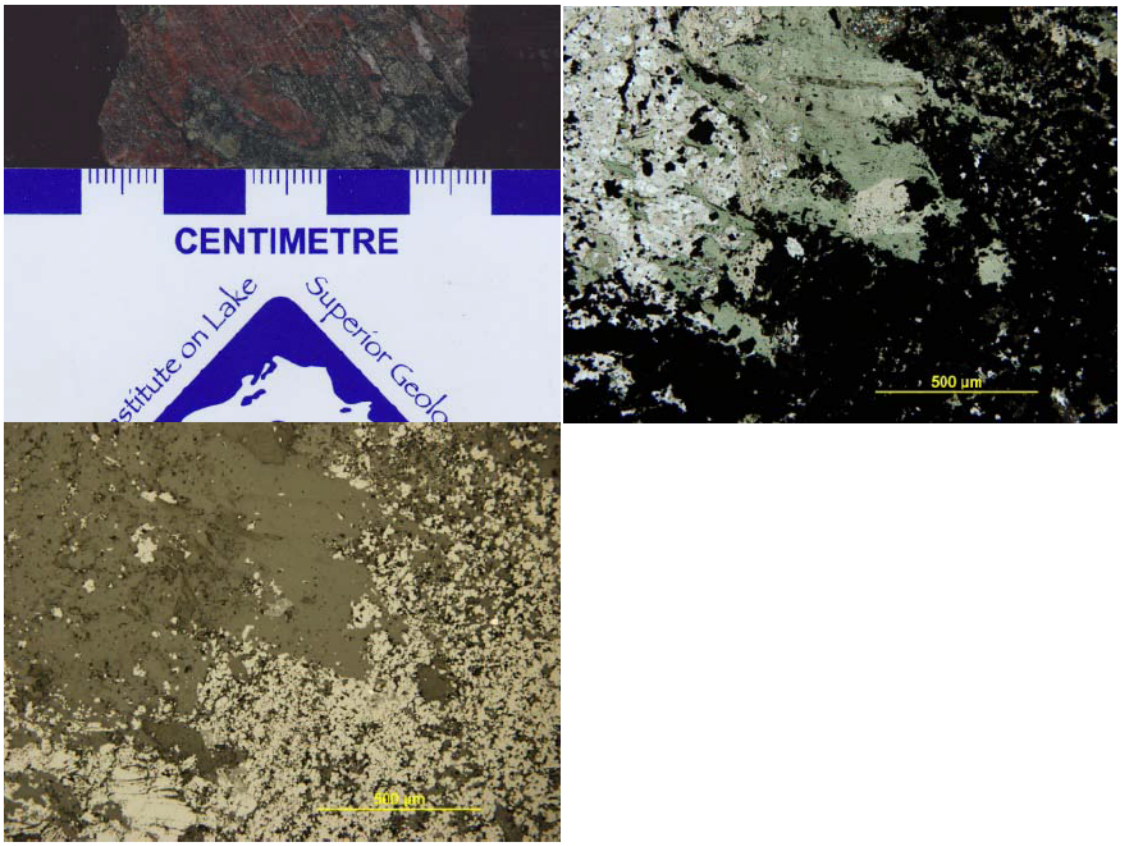

Hole ID: HAM06-43

Depth: 134.9m

Rock type: brecciated felsic metavolcanics

Chlorite: present in the matrix of the breccia as pale to dark green blades, grains are 0.1-1.0mm in size, biotite is only present in trace amounts and usually isolated from chlorite

Magnetite: aggregates of subhedral grains disseminated throughout the matrix of the breccia with chlorite, disseminations are <0.1mm in size, but larger (up to 0.5mm) "blades" of magnetite are common, makes up 5-7% of the rock

Pyrite: present in trace amounts, not analyzed

Chalcopyrite: present in trace amounts, not analyzed

Pyrrhotite: not present

HAM-55-02:

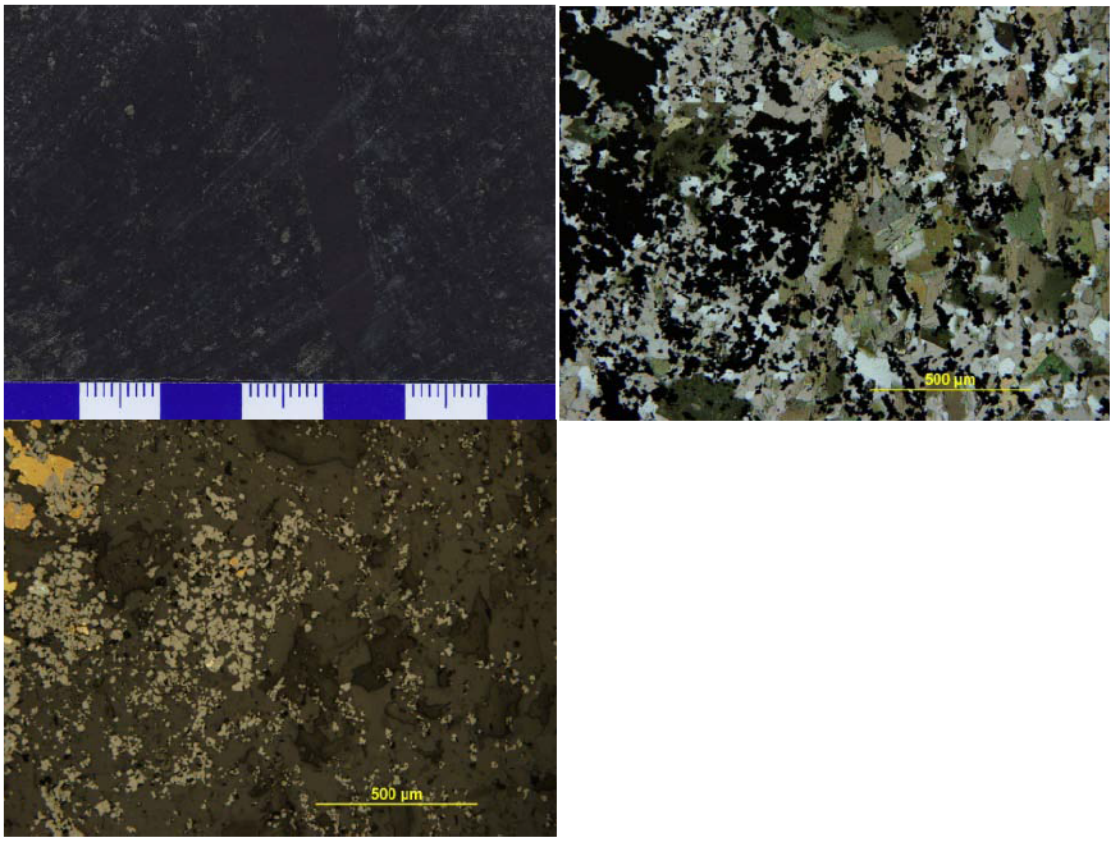

Hole ID: HAM06-55

Depth: 107.0m

Rock type: brecciated metadiorite

Chlorite: present in the groundmass of the rock as dark green blades, grains are 0.5-1.0mm in size, biotite present in equal amounts but usually separate from grains of chlorite

Magnetite: present as aggregates of subhedral grains disseminated throughout the groundmass (<0.1mm) with chlorite and biotite, as well as veins of massive magnetite up to 1.0cm wide

Pyrite: present in trace amounts, not analyzed

Chalcopyrite: present in trace amounts, not analyzed

Pyrrhotite: not present

HAM-57-06:

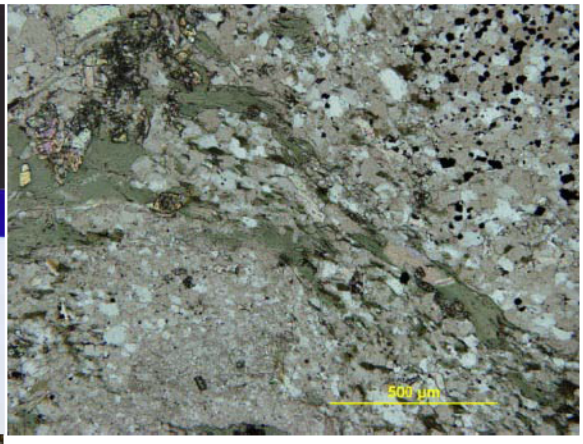

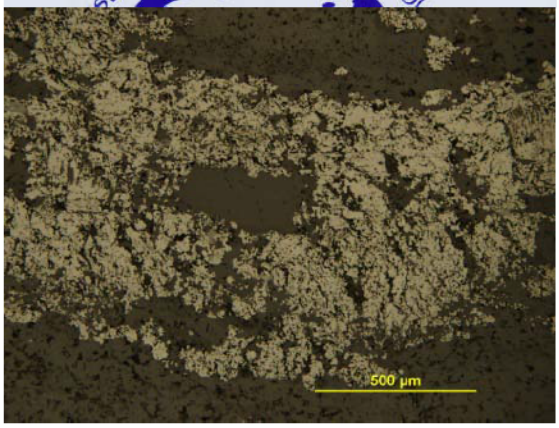

Hole ID: HAM06-57

Depth: 272.1m

Rock type: brecciated felsic metavolcanics

Chlorite: present in the matrix of the breccia as pale green blades, grains are 0.1-0.5mm in length and weakly foliated, biotite is only present in trace amounts

Magnetite: masses of subhedral grains throughout the matrix of the breccia up to 5.0cm in length, disseminations of subhedral to euhedral grains are also common and usually <0.1mm in size, makes up 3-5% of the rock

Pyrite: present in trace amounts, not analyzed

Chalcopyrite: present in trace amounts, not analyzed

Pyrrhotite: not present

HAM-61-03:

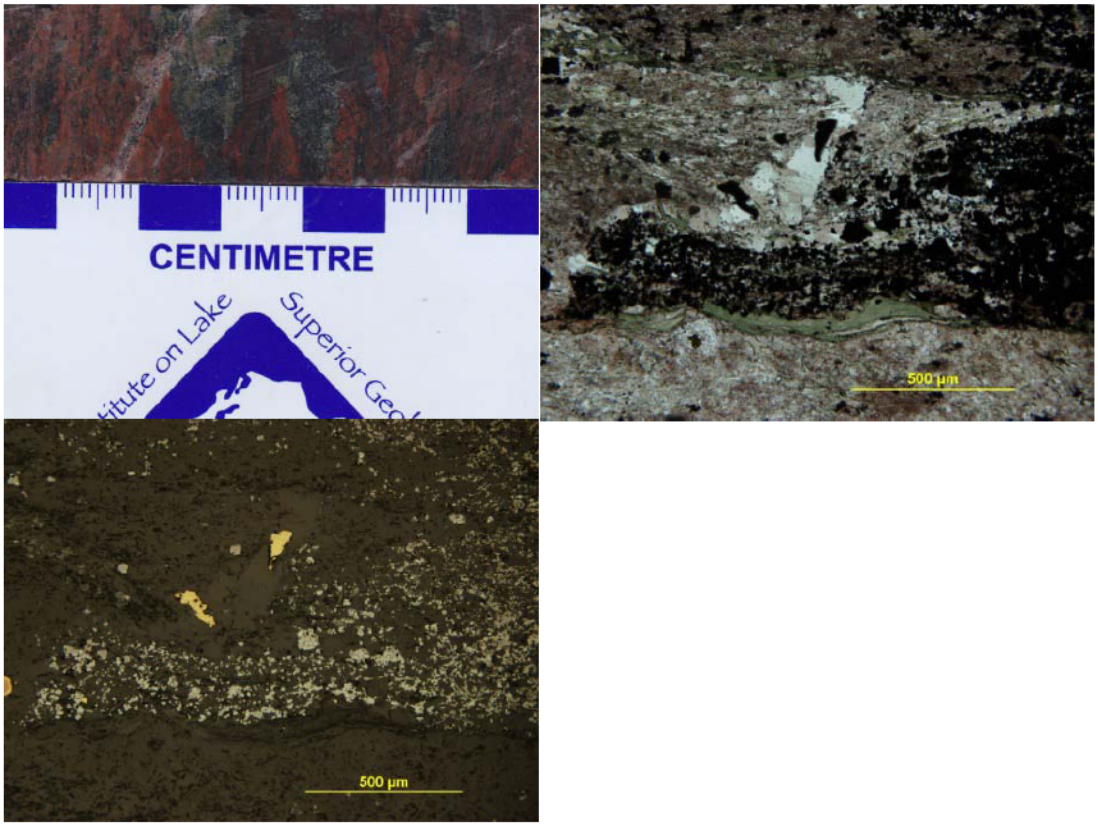

Hole ID: HAM09-61

Depth: 203.0m

Rock type: brecciated felsic metavolcanics

Chlorite: present in the matrix of the breccia as weakly foliated pale green blades, often vein-like along the margins of the matrix, grains are 0.1-1.0mm in length, biotite is only present in trace amounts

Magnetite: disseminations of subhedral grains throughout the matrix of the breccia, grains are usually <0.1mm in size, makes up 1-2% of the rock

Pyrite: present in trace amounts, not analyzed

Chalcopyrite: present in trace amounts, not analyzed

Pyrrhotite: not present

HAM-62-07:

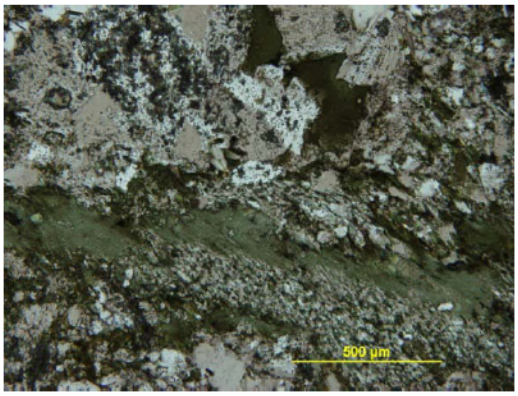

Hole ID: HAM09-62

Depth: 319.5m

Rock type: polymictic breccia

Chlorite: present in the matrix of the breccia as pale to dark green masses, often vein-like in habit, weakly foliated, grains are 0.5-1.0mm in length, biotite abundant and many chlorite grains are transitional to biotite, however sample purity is not an issue

Magnetite: present in trace amounts, not analyzed

Pyrite: present in trace amounts, not analyzed

Chalcopyrite: present in trace amounts, not analyzed

Pyrrhotite: not present

HAM-63-14:

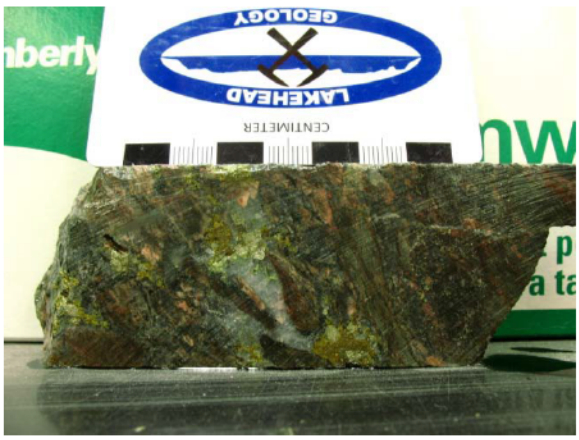

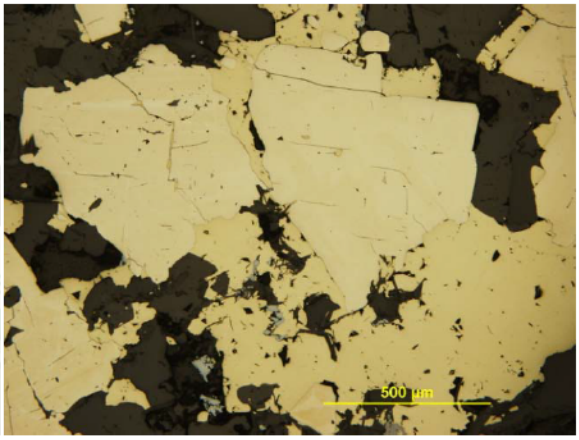

Hole ID:	HAM10-63
Depth:	236.0m
Rock type:	brecciated felsic metavolcanics
Chlorite:	present in the matrix of the breccia, not analyzed
Magnetite:	present in trace amounts, not analyzed
Pyrite:	subhedral grains in the matrix of the quartz breccia, 0.5-1.0cm in size, makes up 1-2% of the rock
Chalcopyrite:	anhedral masses in the quartz breccia, minor molybdenite present, 0.5-1.0cm in size, makes up 1-2% of the rock
Pyrrhotite:	not present

HAM-63-15:

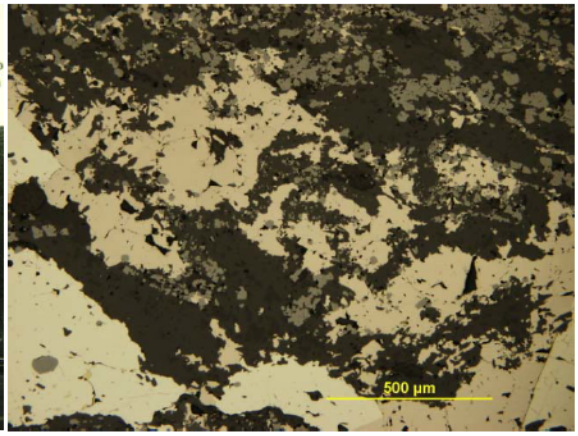

Hole ID: HAM10-63

Depth: 92.0m

Rock type: altered mafic metavolcanics

Chlorite: present in abundance, not analyzed

Magnetite: present in abundance, not analyzed

Pyrite: aggregates of anhedral to subhedral grains up to 0.5cm in size, making up 3-5% of the rock

Chalcopyrite: present as anhedral stringers in pyrite, not analyzed

Pyrrhotite: wispy anhedral stringers up to 3.0cm long, making up 5-7% of the rock

HAM-65-02:

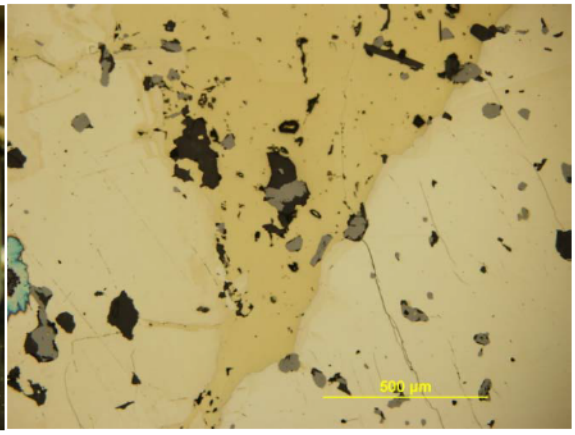

Hole ID:	HAM10-65
Depth:	302.0m
Rock type:	brecciated felsic metavolcanics
Chlorite:	present in the matrix of the breccia, not analyzed
Magnetite:	present, not analyzed
Pyrite:	anhedral to subhedral masses, which form stringers throughout the vuggy matrix along with chalcopyrite, size varies from 1.0mm to 1.0cm, makes up 3-5% of the rock
Chalcopyrite:	anhedral stringers in the matrix of the breccia along with pyrite, stringers are up to 2.0cm in length, making up 5-7% of the rock
Pyrrhotite:	not present

Appendix E

Thermodynamic Data and fo_2 vs. pH Diagrams

Thermodynamic Data

Description	Reaction	log K					
		300°C	320°C	340°C	360°C	380°C	400°C
H_2S^0/ HS^-	$H_2S^0 = HS^- + H^+$	-6.828	-6.964	-7.11	-7.263	-7.425	-7.596
HSO_4^-/ SO_4^{2-}	$HSO_4^- = SO4^{2-} + H^+$	-5.318	-5.576	-5.834	-6.092	-6.349	-6.608
H_2S^0/ HSO_4^-	$H_2S^0 + 2O_2(g) = HSO_4^- + H^+$	54.388	51.601	48.98	46.508	44.171	41.956
H_2S^0/ SO_4^{2-}	$H_2S^0 + 2O_2(g) = SO_4^{2-} + 2H^+$	49.07	46.025	43.146	40.417	37.822	35.349
HS^-/ SO_4^{2-}	$HS^- + 2O_2(g) = SO_4^{2-} + H^+$	55.898	52.989	50.255	47.68	45.247	42.944
hematite/magnetite	$4Fe_3O_4 + O_2(g) = 6Fe_2O_3$	30.966	29.451	28.034	26.704	25.453	24.274
pyrrhotite/magentite(H_2S^0)	$3FeS + 3H_2O + 0.5O_2(g) = Fe_3O_4 + 3H_2S^0$	9.519	9.452	9.398	9.361	9.34	9.334
pyrrhotite/pyrite(H_2S^0)	$FeS + 0.5O_2(g) + H_2S^0 = FeS_2 + H_2O$	19.565	18.495	17.489	16.542	15.649	14.805
pyrite/hematite(H_2S^0)	$2FeS_2 + 4H_2O = Fe_2O_3 + 4H_2S^0 + 0.5O_2(g)$	-27.623	-25.781	-24.04	-22.392	-20.829	-19.342
pyrite/magnetite(H_2S^0)	$3FeS_2 + 6H_2O = Fe_3O_4 + 6H_2S^0 + O_2(g)$	-49.176	-46.034	-43.068	-40.264	-37.606	-35.081
magnetite/pyrrhotite(HS^-)	$3FeS + 3H_2O + 0.5O_2(g) = Fe_3O_4 + 3HS^- + 3H^+$	-10.965	-11.442	-11.931	-12.428	-12.936	-13.454
pyrrhotite/pyrite(HS^-)	$FeS + 0.5O_2(g) + HS^- + H^+ = FeS_2 + H_2O$	26.393	25.459	24.598	23.805	23.074	22.401
pyrite/magnetite(HS^-)	$3FeS_2 + 6H_2O = Fe_3O_4 + 6HS^- + 6H^+ + O_2(g)$	-90.143	-87.82	-85.726	-83.843	-82.157	-80.656
hematite/pyrite(HSO_4^-)	$2FeS_2 + 4H_2O + 7.5O_2(g) = Fe_2O_3 + 4HSO_4^- + 4H^+$	189.929	180.624	171.88	163.641	155.857	148.484
pyrite/magnetite(HSO_4^-)	$3FeS_2 + 6H_2O + 11O_2(g) = Fe_3O_4 + 6HSO_4^- + 6H^+$	277.152	263.573	250.811	238.785	227.422	216.657
hematite/pyrite(SO_4^{2-})	$2FeS_2 + 4H_2O + 7.5O_2(g) = Fe_2O_3 + 4SO_4^{2-} + 8H^+$	168.657	158.319	148.543	139.274	130.459	122.052
pyrite/magnetite(SO_4^{2-})	$3FeS_2 + 6H_2O + 11O_2(g) = Fe_3O_4 + 6SO_4^{2-} + 12H^+$	245.245	230.115	215.806	202.235	189.326	177.01

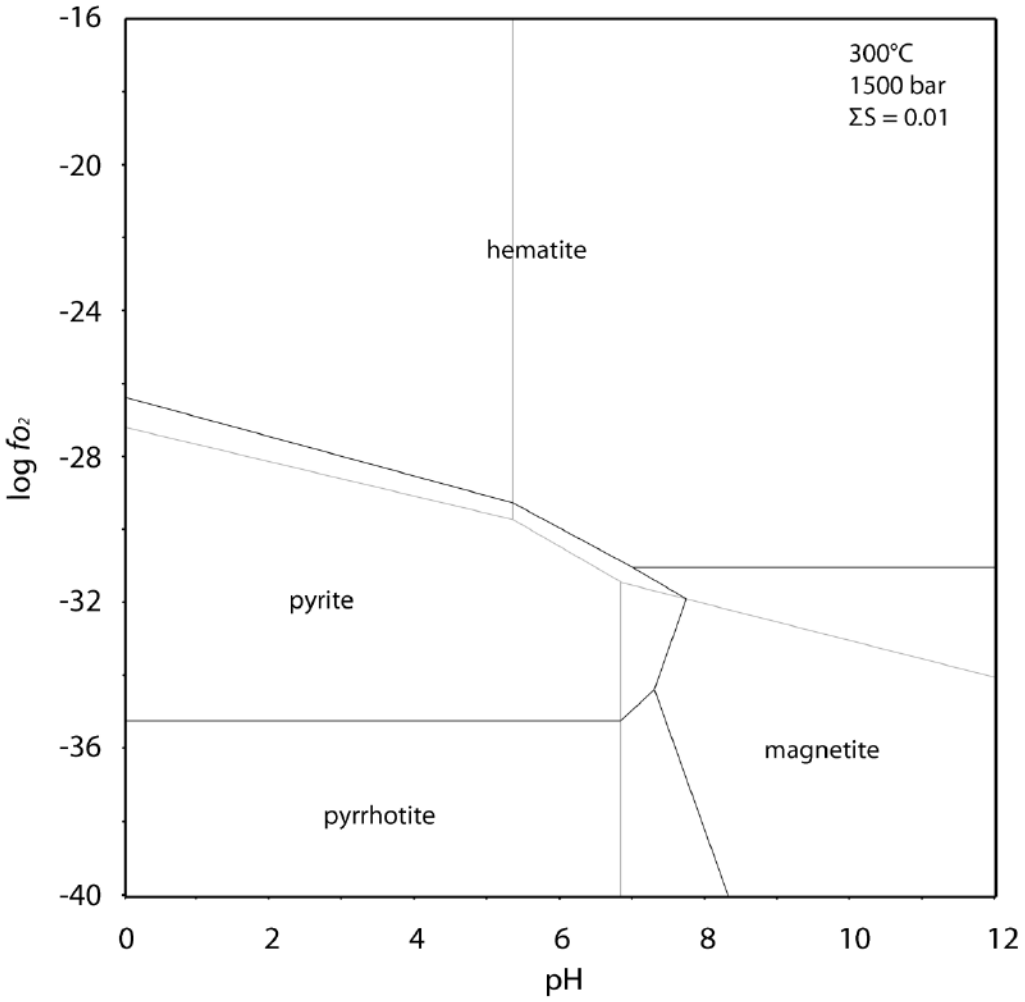
300°C
1500 bar
ΣS = 0.01
hematite
pyrite
magnetite
pyrrhotite
log fo2
pH
-16
-20
-24
-28
-32
-36
-40
0
2
4
6
8
10
12

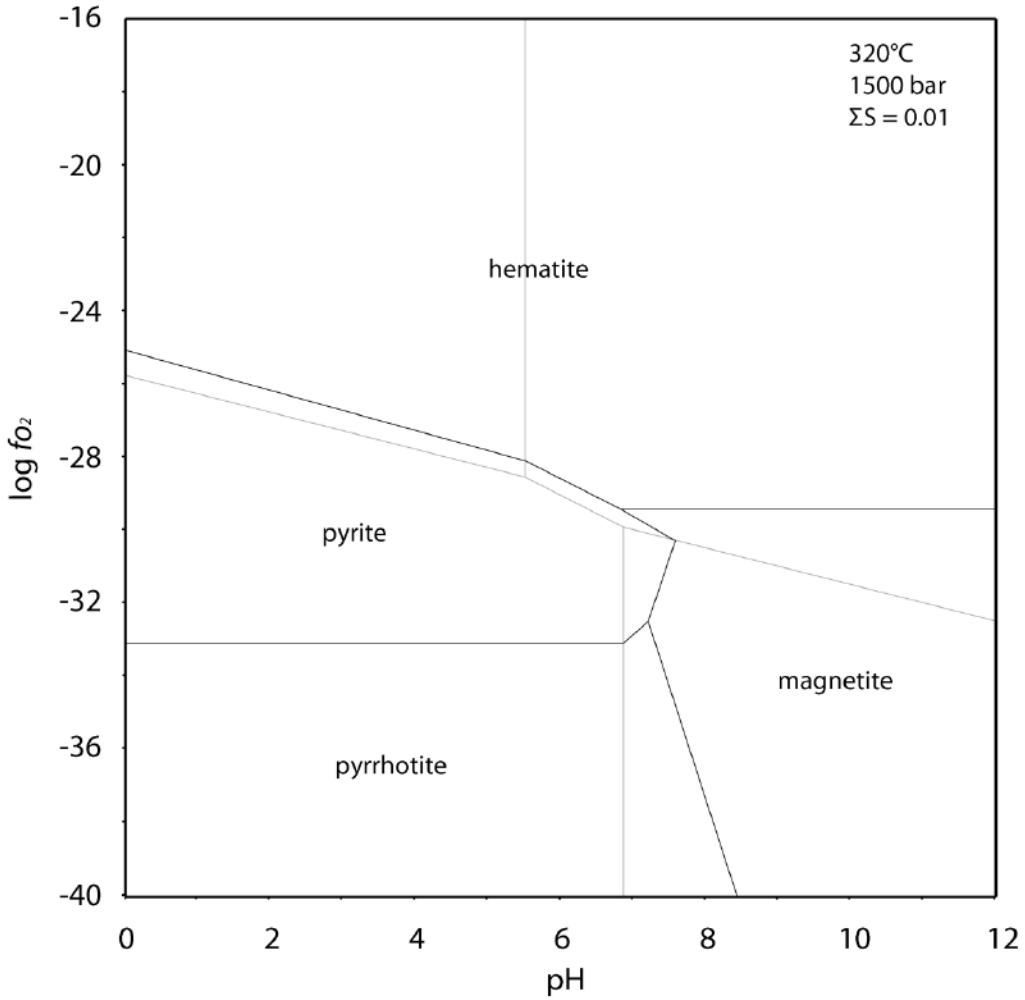
320°C
1500 bar
ΣS = 0.01
hematite
pyrite
magnetite
pyrrhotite
log fo2
pH
-16
-20
-24
-28
-32
-36
-40
0
2
4
6
8
10
12

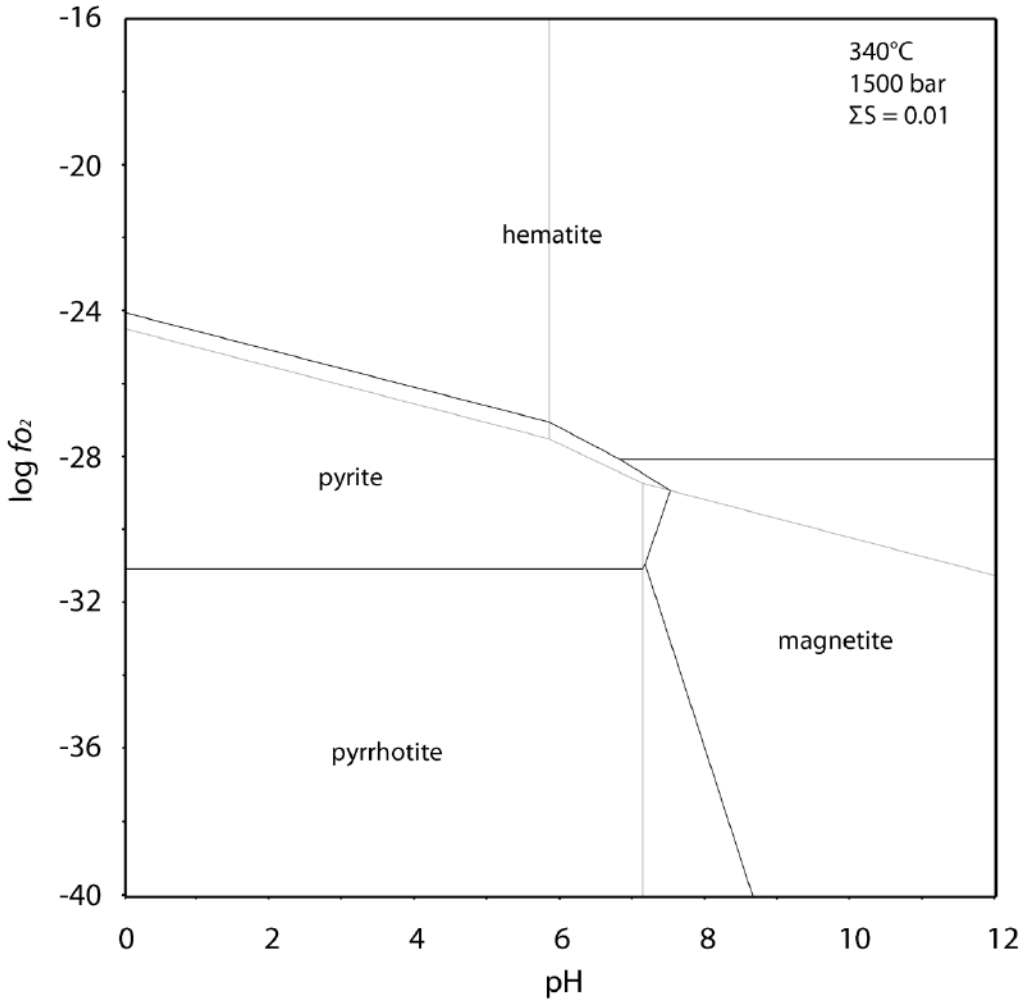
340°C
1500 bar
ΣS = 0.01
hematite
pyrite
magnetite
pyrrhotite
-16
-20
-24
-28
-32
-36
-40
log fo2
0
2
4
6
8
10
12
pH

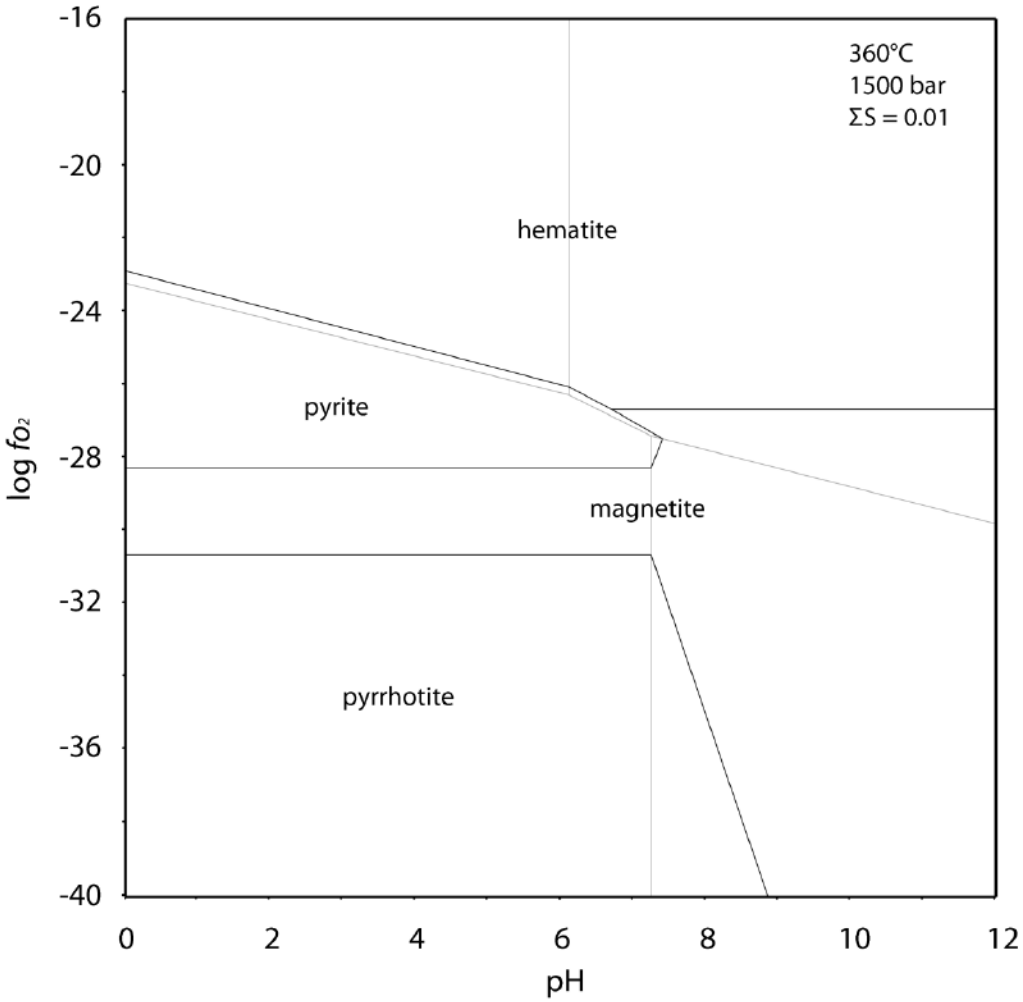
360°C
1500 bar
ΣS = 0.01
hematite
pyrite
magnetite
pyrrhotite
log fo2
pH
-16
-20
-24
-28
-32
-36
-40
0
2
4
6
8
10
12

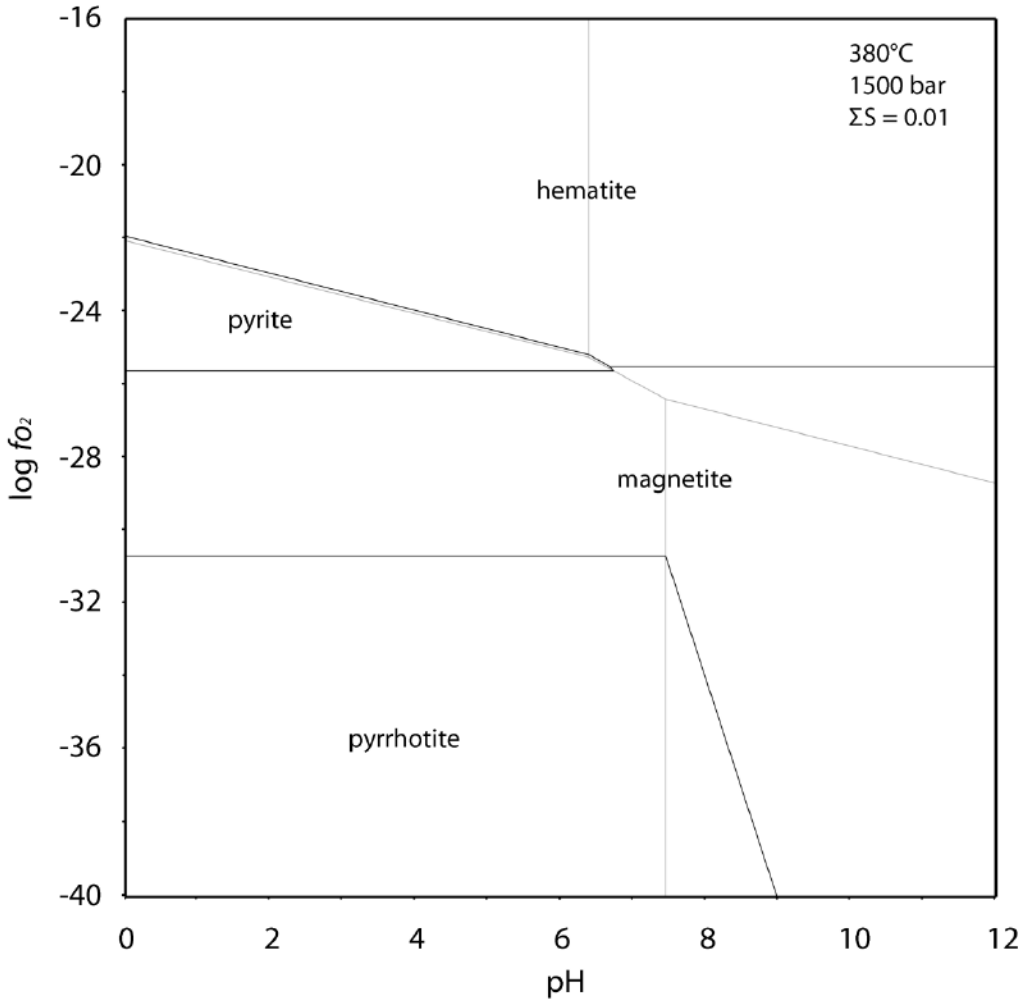
380°C
1500 bar
ΣS = 0.01
hematite
pyrite
magnetite
pyrrhotite
log fo2
pH
-16
-20
-24
-28
-32
-36
-40
0
2
4
6
8
10
12

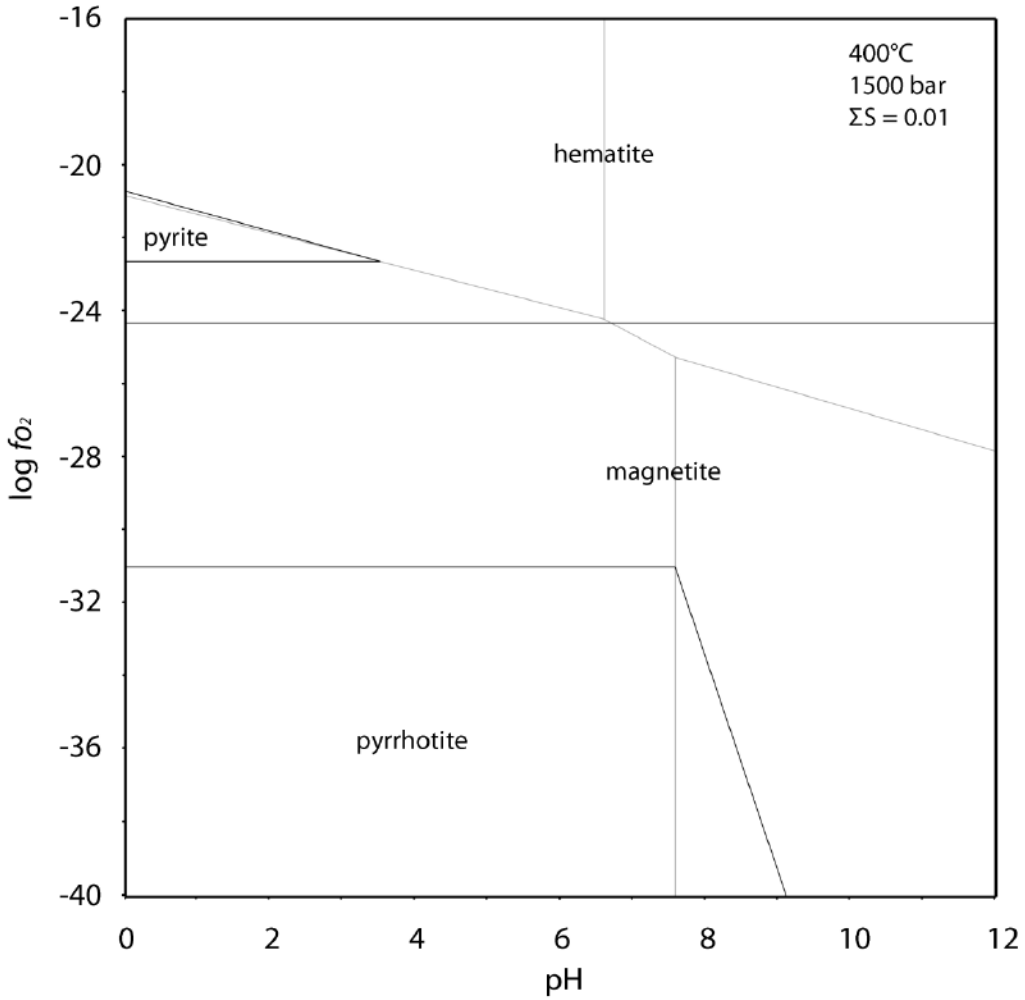
400°C
1500 bar
ΣS = 0.01
hematite
pyrite
magnetite
pyrrhotite
log fo2
pH
-16
-20
-24
-28
-32
-36
-40
0
2
4
6
8
10
12